Title
Structural and functional biological materials : abalone nacre, sharp materials, and abalone foot adhesion

Author
Lin, Albert Yu-Min

Publication Date
2008

Peer reviewed|Thesis/dissertation

UNIVERSITY OF CALIFORNIA, SAN DIEGO

STRUCTURAL AND FUNCTIONAL BIOLOGICAL MATERIALS: ABALONE NACRE, SHARP MATERIALS, AND ABALONE FOOT ADHESION

A Dissertation submitted in partial satisfaction of the requirements

for the degree of Doctor of Philosophy

in

Materials Science and Engineering

by

Albert Yu-Min Lin

COMMITTEE IN CHARGE:

Professor Marc André Meyers (Chair)

Professor Michael J. Heller

Professor Sungho Jin

Professor Joanna McKittrick

Professor Frank Eberhard Talke

2008

The dissertation of Albert Yu-Min Lin is approved and it is acceptable in quality and form for publication on microfilm:

_____

_____

_____

_____

_____

Chair

University of California, San Diego

2008

Dedicated to my Grandfathers

Oh! A bare, brown rock stood up in the sea,
The waves at its feet dancing Merrily.

A little bubble once came sailing by,
And thus to the rock did it gaily cry,

Ho! Clumsy brown stone, Quick, make way for me:
I'm the fairest thing that floats on the sea.

See my rainbow-robe, see my crown of light,
My glittering form so airy and bright.

O'er the waters blue, I'm floating away,
To dance by the shore with the foam and spray.

Now, make way, make way; for the waves are strong,
And their rippling feet bear me fast along.

But the great rock stood straight up in the sea:
It looked gravely down and said pleasantly

Little friend, you must go some other way;
For I have not stirred this many a long day.

Great billows had dashed, and angry winds blown;
But my sturdy form is not overthrown.

Nothing can stir me in the air or sea;
Then, how can I move, little friend, for thee?

Then the waves all laughed, in their voices sweet;
And the sea-birds looked, from their rocky seat,

At the bubble gay, who angrily cried,
While its round cheek glowed with a foolish pride

You shall move for me; and you shall not mock
At the words I say, you ugly, rough rock.

Be silent, wild birds! While stare you so?
Stop laughing, rude waves, And help me to go!

For I am the queen of the ocean here,
And the cruel stone cannot make me fear.

Dashing fiercely up, with a scornful word,
Foolish bubble broke; but the Rock never stirred.

Then said the sea-birds, sitting in their nests
To the little ones leaning on their breasts,

Be not like the bubble, headstrong, rude and vain,
Seeking by violence your object to gain;

But be like the rock. Steadfast, true and strong,
Yet cheerful and kind and firm against wrong.

Heed, little birdlings, and wiser you'll be
For the lessons learned today by the sea.

-

Louisa May Alcott

TABLE OF CONTENTS

SIGNATURE PAGE…….……iii

DEDICATION……...iv

EPIGRAPH…….v

TABLE OF CONTENTS……vi

LIST OF FIGURES: x

ACKNOWLEDGEMENTS xxi

VITA xxiii

FIELD OF STUDY xxiii

LIST OF PUBLICATION xxiv

INTERNATIONAL CONFERENCE PRESENTATIONS xxv

ABSTRACT OF THE DISSERTATION xxvi

CHAPTER 1 1

CHAPTER 2 7

2.1 Structure & Mechanical Properties 7

2.1.1 Biomimetics 26

2.2 Growth: Biomineralization 29

2.3 Functional Biological Materials 45

2.3.1 Sharp Materials: 45

2.3.2 Attachment Devices: 45

CHAPTER 3 59

EXPERIMENTAL METHODS 59

3.1 Live Specimen Culturing Facilities 59

3.2 Structural Characterization 61

3.2.1 Scanning Electron Microscopy Observations on the Structure of Nacre: 61

3.2.2 EDTA Demineralization of Nacre: 62

3.2.3 Atomic Force Microscopy: 63

3.2.4 Heating: 64

3.2.5 Deproteination: 64

3.2.6 Transmission Electron Microscopy: 64

3.2.7 X-ray Diffraction: 65

3.2.8 Raman Spectroscopy: 66

3.2.9 Critical Point Drying: 66

3.3 Mechanical Testing of Nacre 67

3.3.1 Nanoindentation: 67

3.3.2 Quasi-static Mechanical Testing: 68

3.3.3 Dynamic Mechanical Testing: 71

3.4 Growth Implantation: Flat Pearl and Trepanning Techniques 71

3.4.1 Flat Pearl: 71

3.4.2 Trepanning: 72

3.4.3 Crystal Nucleation: 74

3.5 Attachment Measurements 75

3.5.1 Bulk Mechanical Testing: 75

3.5.2 Structural Characterization of Abalone Foot: 77

3.5.3 Preparation of Single Seta: 78

3.5.4 Force Estimation of a Single Seta During PerpendicularPull: 80

CHAPTER 4 82

RESULTS AND DISCUSSION 82

4.1 Structure and Mechanical Properties 82

4.1.1 The Nacre of the Abalone: 82

4.1.1.1 Quasi-static Compression and Tension 82

4.1.1.2 Hardness and Nanoindentation 89

4.1.1.3 Relationship to Structure 91

4.1.1.4 Tile-Tile Interface 95

4.1.1.5 Strength of Individual Tile 118

4.1.1.6 Mesolayers 121

4.1.2 Comparative Study: 124

4.1.2.1 Conch shell 124

4.1.2.2 Giant Clam shell 126

4.1.2.3 Characterization of Damage 133

4.1.2.4 Hydration Effects 138

4.2 Growth (Biomineralization) 140

4.2.1 Implantation Experiments: 143

4.2.2 Transmission Electron Microscopy: 151

4.3 Functional Biological Materials 160

4.3.1 Sharp Materials: 160

4.3.1.1 Plants: Razor grass 160

4.3.1.2 Insects: Mosquito and Bee 161

4.3.1.3 Fish teeth 163

4.3.1.4 Mammal Incisors 168

4.3.2 Attachment Device (Abalone foot): 169

4.3.2.1 Characterization and theoretical evaluation 169

4.3.2.2 Bulk mechanical testing of pull-off force of the abalone foot 175

4.3.2.3 Force estimation of a single seta during perpendicular pull-off using an AFM 176

4.3.2.4 Attachment hierarchy 178

4.3.3 Attachment Devices (Tree Frog, Scinax perereca): 181

CHAPTER 5 187

SUMMARY AND CONCLUSIONS 187

REFERENCES 192

LIST OF FIGURES:

Figure 1.1 Schematic representation of (a) contributing scientific fields and (b) constraints/components in the study of biological systems (modified from E. Artz [4], and Meyers et al. [5]). 2

Figure 2.1 Structure of typical mollusk shell (adapted from Zaremba et al. [31]). 7

Figure 2.2 The various levels of structural hierarchy in nacre; macro scale mesolayers, 10 μm by 0.5 μm aragonite tiles, the nanostructure defined within the interface between tiles. 9

Figure 2.3 Weibull analysis of abalone nacre in; (a) quasi-static, and (b) dynamic compressive loading (Menig et al. [32]). 12

Figure 2.4 Mechanisms of damage accumulation in nacreous region of abalone through plastic microbuckling (Menig et al. [32]). 14

Figure 2.5 Experimental shear stress-shear strain curve for nacre (Menig et al. [32]). 15

Figure 2.6 Application to shell microbuckling (from Menig et al. [32]) of (a) Argon [42] analysis for kink stress formation and (b) Budiansky [43] formalism for the kink-band thickness prediction. 17

Figure 2.7 (a) Cross section of abalone shell showing how a crack, starting at the left is deflected by viscoplastic layer between calcium carbonate lamellae. (b) Schematic drawing showing arrangement of calcium carbonate in nacre, forming a miniature "brick and mortar" structure (Meyers and Chawla [46]). 18

Figure 2.8 Mechanisms of damage accumulation in nacreous region of abalone through tile pullout: (a) SEM micrograph; (b) schematic representation (Lin and Meyers [35]). 20

Figure 2.9 Various models for the proteinaceous layer. 21

Figure 2.10 (a) SEM of protein chain stretching at tile interface, (b) force extension curve of organic component via AFM probe [75]. 22

Figure 2.11 Unit cell of aragonite showing schematic position of (Asp-Y)n and β sheet. Notice protruding calcium ions on (001) face; black atoms: Ca; small black: carbon; gray atoms: oxygen. (Courtesy of K. S. Vecchio, UCSD [64]). 24

Figure 2.12 TEM of nacre platelets showing transition from single crystal aragonite to amorphous calcium carbonate at the edge of each tile (Nassif et al. [65]). 25

Figure 2.13 Metallic-intermetallic laminate inspired from abalone nacre [198]. 27

Figure 2.14 "Christmas tree" observed on growth surface of steady state tiled aragonite. 30

Figure 2.15 Free energy of nucleation as a function of cluster size (Mann [27]). 31

Figure 2.16 Structural control by organic matrix-mediated nucleation (Mann [27]). 32

Figure 2.17 Representation of activation energies of nucleation in the presence and absence of an organic matrix for two nonspecific polymorphs (Mann [27]). 33

Figure 2.18 AFM images showing: (a) pure calcite growth hillock; (b-d) growth hillocks after the addition of supersaturated solutions of (b) glycine, an achiral amino acid,;(c and d) aspartic acid enantiomers (Orme, Fig. 1 [100]). 35

Figure 2.19 Hypothetical growth mechanism with periodic injection of proteins arresting growth in "c" direction. (a,b) protein deposition causing the arrest of

crystallographic growth in the “c” direction; (c) second growth spurt after deposition of beta sheet and nucleation; (d) first aragonite plates are butted together while growth of second layer continues in “a,b” direction; (e) nucleation of third layer as second layer growth continues in “a” direction (Lin and Meyers [35]). 36

Figure 2.20 Schematic of growth mechanism showing intercalation of mineral and organic layers. 39

Figure 2.21 Schematic representation of mineral bridges connecting sequential aragonite tiles layers. 40

Figure 2.22 (a) TEM view of mineral bridges on tile surfaces (Song et al. [73,74]), (b) AFM image of mineral bridge remnants on tile surface (Schäffer et al. [105]). 41

Figure 2.23 Tile separation occurs; (a) in a gastropod (abalone) shells where tiles are formed in columns, and (b) in a bivalves (pearl oyster) shells where tile location is offset from preceding layers (Wang et al. [66]). 42

Figure 2.24 Growth sequence in bivalve nacre (Cartwright and Checa [121]). 43

Figure 2.25 (a) TEM micrograph of a cross-section of nacre, (b-g) SAD diffraction patterns of various tiles as labeled (Feng et al. [122]). 44

Figure 2.26 Setae and distal spatulae fly *Callifora vicina*. Van der Waals forces at spatula-surface interface generate attachment forces as 20N (Arzt [126]). 46

Figure 2.27 SEM micrographs showing the detail of (a) satae; and (b) spatulae (Courtesy of E. Artz and G. Huber). 47

Figure 2.28 Idealized arrangement of attachment system with spherical tip shape (radius R and spacing 2Λ) (Spolenak et al.[128], Fig. 2). 48

Figure 2.29 Idealized arrangement of attachment system with spherical tip shape (radius R and spacing 2Λ) (from Artz et al. [127]). 50

Figure 2.30 Partial adhesion map for a spherical tip shape; thin lines are contours of equal apparent contact strength; oval section represents regime of bioattachments [128]. 50

Figure 2.31 Pull-off forces of spatulae on glass with varying humidity [129]. 52

Figure 2.32 Force diagram of the toe pad of a gecko [142]. 53

Figure 2.33 Force of single seta pulled parallel to surface (preload of 15 μN) [123]. 55

Figure 2.34 Shapes of attachment devices in nature and their hypothetical evolution paths indicated by arrows (Arzt et al. [133]). 56

Figure 2.35 Synthetic gecko tape. (a) Scanning electron micrographs of microfabricated polyimide hairs in a 1cm2 array, (b) re-attachable dry adhesives based on the gecko principle applied to a spider-man toy allowing it to cling to a horizontal glass plate. The toy weighed approximately 40g (Geim et al. [135]). 57

Figure 2.36 Nanomolding PGSA pillarse by photocuring the prepolymer under UV. 58

Figure 3.1 Abalone culturing facilities at: (a) MAE department of UCSD; (b) the Scripps Institution of Oceanography, at UCSD. 60

Figure 3.2 Demineralized nacre in Sodium Ethylene Diaminetetreacetic Acid (EDTA). 63

Figure 3.3 Ion milled 3 mm diamter TEM sample of nacre perpendicular to growth bands, a copper support grid can be seen through the sample. 65

Figure 3.4 Critical point drying apparatus at Scripps Institution of Oceanography. 66

Figure 3.5 Sample container for nanoindentation. 67

Figure 3.6 Testing set up of nacre being pulled in tension parallel to the plane of growth. 69

Figure 3.7 Shear testing mount, specimens are placed in the space indicated above. 69

Figure 3.8 Dog-bone mechanical tensile tests on abalone nacre: (a) dog-bone shaped sample of nacre hydrated in saltwater; (b) dog-bone shaped testing mount. 70

Figure 3.9 Drilling of trepanning holes in live abalone using a coring drill while being irrigated with chilled sea water. 73

Figure 3.10 Implantation methods for growth experiments..... 74

Figure 3.11 Bulk mechanical testing of live abalone pull-off force using Instron screw driven tensile testing device. 76

Figure 3.12 Bulk mechanical testing of live abalone pull-off force in tank. 77

Figure 3.13 Preparation of a single seta: (a) removal of tissue; (b) attachment of seta onto AFM cantilever; (c) SEM image of single seta on cantilever beam. 79

Figure 3.14 Force-distance measurements used to determine the pull-off force. 81

Figure 4.1 Compressive strength of nacre perpendicular to layered structure. 84

Figure 4.2 Weibull distribution of tensile strength perpendicular to layered structure [49]. 85

Figure 4.3 Weibull distribution of tensile loading parallel to layered structure. 87

Figure 4.4 Weibull distribution of compressive loading parallel to layered structure..... 87

Figure 4.5 Strength of nacre with respect to loading direction, parrallel lines represent growth bands. 88

Figure 4.6 Nanoindentation data for dry polished nacre parallel to growth plane. 90

Figure 4.7 Nanoindentation data for dry polished nacre perpendicular to growth plane. 91

Figure 4.8 (a) SEM of cross section of abalone, showing protein layer (darker regions) and its virtual absence where tiles on same plane join; (b) schematic drawing of stacking of abalone tiles and their separation under tension..... 92

Figure 4.9 (a) SEM microscopy of polished cross-section after plastic deformation under tension; notice fracture by tile "pullout"; (b) plot showing distribution of step lengths. 94

Figure 4.10 Schematic diagram showing pull-out of overlapping tile layers. 95

Figure 4.11 Schematic diagram of nacre in tension: (a) at the scale of an individual tile; (b) as oriented in a single dogbone shaped sample. 97

Figure 4.12 Sketch of shear test configuration acting on a cube of abalone shell. 98

Figure 4.13 Stress-strain curves of abalone samples, tested within a single mesolayer... 99

Figure 4.14 Weibull distribution of shear strength of nacre. 100

Figure 4.15 (a) Interface between tiles (before deproteination) with organic matrix surrounding mineral bridges; (b) tile surface (before deproteination) with regions where organic matrix "A" remains; (c) mineral bridges (marked by arrows) between aragonite tiles after 9 hours of hydrazine deproteination; (d) asperities, many of which are remnants of mineral bridges, concentrated at the center of a aragonite tile after 9 hours of Hydrazine deproteination. 102

Figure 4.16 Transmission electron micrograph of nacre crossection showing mineral bridges between tile interfaces. 103

Figure 4.17 Tensile strength of mineral as a function of size. 105

Figure 4.18 Calculated number of mineral bridges per tile as a function of bridge diameter required to provide tensile strength prependicular to surface of 3 MPa. . 107

Figure 4.19 (a) Asperities (a fraction of which are remnants of mineral bridges) and (b) mineral bridges (marked by arrows) between tile layers. 108

Figure 4.20 Different models for sliding between tiles; inter-tile layer formed by (a) asperities; (b) organic layer acting as visco-elastic glue; (c) mineral bridges; (d) combination of three mechanisms. 110

Figure 4.21 Top growth surface six weeks after implantation. Light regions represent apexes of terraced cones and streaks marked by arrows are due to folding of organic interlayer. 111

Figure 4.22 (a) Side view of intermediate tile growth through organic layers on flat pearl five weeks after implantation; (b) Schematic showing terraced growth and organic membrane sagging under its own weight..... 112

Figure 4.23 Calculated (a) stress, and (b) elastic modulus of organic layer as a function of deflection for two circle radii (assumed shape between sagging points of the membrane) are considered: 2.5 and 5 μm. 115

Figure 4.24 Atomic force micrograph of organic layer; (a) magnification showing outline of tiles; (b) high magnification showing linear chains and holes with ~30 nm diameter [49]. 117

Figure 4.25 Critical stress as a function of flaw size *a* [K_{IC} = 1 $MPam^{1/2}$] [35]. 119

Figure 4.26 Schematic model of the nanoscale structural effect on the propagation of cracks through a material, flaw is represented by penny shaped crack. 120

Figure 4.27 Nacre which has been demineralized with EDTA (ethylenedi-amine tetraacetic acid) leaving exposed mesolayer. 122

Figure 4.28 Schematic representation of (a) the macrostructure of nacre including the mesolayers, (b) macrostructure of a non-laminate aragonite, (c) the effect of macro structure on the material response to bending showing reduction in stress concentration, (d) the stress concentrations which develop in bending of a non-laminate material. 123

Figure 4.29 Schematic drawing of the crossed-lamellar structure of *Strombus gigas*. Each layer also consists of first-, second-, and third-order lamella [161]. 125

Figure 4.30 Schematic representation and SEM image of *Tridacna gigas* shell outer region. 127

Figure 4.31 Optical microscopy of polished cross-sectional specimen of *Tridacna gigas* shell (inner region), with continuous single crystal facilitating crack propagation. 128

Figure 4.32 Weibull analysis of; (a) *Strombus gigas*, (b) *T. gigas*, (c) *Haliotis rufescens* shells in quasi-static compressive loading. 130

Figure 4.33 Weibull analysis of; (a) *Strombus gigas*, (b) *T. gigas*, (c) *Haliotis rufescens* shells in dynamic compressive loading. 132

Figure 4.34 Crack propagation through middle section of *Strombus gigas* creating a zigzag pattern through second-order and third-order lamella [161]. 133

Figure 4.35 Fracture surface of *Strombus gigas* (a) parallel to growth direction, (b) perpendicular growth direction. 135

Figure 4.36 Fracture surface of *Tridacna gigas* under bending (a) perpendicular to growth bands, (b) parallel to growth bands 137

Figure 4.37 Stress-strain curves of compression on the giant clam parallel to growth layers. Samples were hydrated in salt water for: (a) one week; (b) two weeks; (c) three weeks..... 138

Figure 4.38 (a) Macrostructural view of a cross section of the *Haliotis rufescens* shell. Growth bands are observed separating larger regions of nacre, (b) SEM micrograph of fracture surface; direction of growth marked with arrow..... 141

Figure 4.39 Order of events during mesolayer growth in nacre. 142

Figure 4.40 Summary of sequential growth from flat pearl and trepanning experiments. 143

Figure 4.41 Schematic of the forces acting on the growth surface of the shell. 144

Figure 4.42 Raman spectra of implanted flat pearl one week after implantation. Raman bands verify the material to be aragonite..... 146

Figure 4.43 Growth on 15 mm slide after 24 days; (a) low magnification SEM; (b) high-magnification SEM; (c) Schematic drawing showing the same crystallographic orientation. 147

Figure 4.44 Growth of nacreous tiles by terraced cone mechanism; SEM of arrested growth showing partially grown tiles (arrow A) and organic layer (arrow B). 148

Figure 4.45 (a) Growth sequence through mineral bridges (b) Detailed view of mineral bridges forming through holes in organic membranes [120]..... 150

Figure 4.46 Transmission electron microscopy of tiled aragonite nacre with selected area diffraction..... 153

Figure 4.47 (a) Schematic representation of the growth of two adjacent "Christmas trees" with velocities V_c and V_{ab} along crystallographic axes (*a,b*) and *c* marked. (b) Measured tile sizes, d, for successive layers. 155

Figure 4.48 SEM micrograph of cross-sectional fracture surface of green abalone shell that has been cultured with environmentally-controlled variations in seawater content and feeding. 158

Figure 4.49. Tile configuration (on fractured surface) for shells having approximately 10, 100, and 200 mm length. 159

Figure 4.50. Pampas grass; note serrations at edges. 160

Figure 4.51 Scanning Electron Microscopy of mosquito proboscis; Top: proboscis covered with hairy sheath; bottom: serrated stylet designed to section tissue for dual needle penetration. 162

Figure 4.52 Bee (*Apis mellifera*) stinger 163

Figure 4.53 Dogfish and teeth. 164

Figure 4.54 Piranha Teeth: (a) hierarchical structure from jaw to single tooth to micro serrations; (b) and (c) Diagram of guillotine-like confinement of material during the biting action of a piranha. 165

Figure 4.55 Great white shark (*Carcaradon carcharinus*) teeth. 166

Figure 4.56 Mako Shark and tooth 167

Figure 4.57 Rodent incisors: (a) rabbit teeth; (b) schematic; (c) rat teeth. 168

Figure 4.58 The pedal foot of the red abalone: (a) optical image of bottom surface of foot; (b) abalone supporting its own hanging weight through single contact point; (c) scanning electron microscopy of foot tissue cross-section. 171

Figure 4.59 SEM characterization of abalone foot tissue: (a) seta lining the outer surface of the foot; (b) nanofibers uniaxially aligned on seta; (c) single nanofiber with hemispherical tip. 172

Figure 4.60 SEM image of cleaved section of pedal foot attached to kelp. 174

Figure 4.61 Nanofibrils uniaxially aligned along the outer surface of the foot tissue.... 175

Figure 4.62 Pull-off force as a function of relative humidity of a single seta on a hydrophobic and a hydrophilic substrate. 177

Figure 4.63 Schematic representation of how suction might generate attachment forces. 180

Figure 4.64 Schematic diagram of the structural hierarchy found in the toe pad of a Brazilian tree frog. 182

Figure 4.65 Scanning electron micrograph of the toe pad of a Brazilian tree frog; (a) low magnification view of single toe, (b) hexagonal subsections found on the contact surface of the toe pad. 183

Figure 4.66 Scanning electron micrographs of hexagonal subdivisions: (a) top down view; (b) side view. 184

Figure 4.67 High magnification of individual fibers comprising the larger hexagonal subdivisions..... 185

ACKNOWLEDGEMENTS

I would like to thank all of the members of the Marc Meyers group for their relentless support, especially Po-Yu Chen who largely contributed to this work both in content, friendship, and in inspiration. Dr. Hussam Jarmakani and Dr. Anuj Mishra will also be remembered for their endearing friendships that were born from the grueling process of graduate school.

Dr. Chris Orme and Professor Andrea Hodge offered both encouragement and guidance throughout the early stage of this study. Professors Joanna McKittrick, Lars Bjursten and K.S. Vecchio provided many insightful observations and support. Ryan Anderson's assistance at ITL facility at UCSD and E. Kisfaludy's expertise at the Laboratory facilities at the Scripps Institution of Oceanography are greatly acknowledge; for which this work would not have been possible. H.J. Walker offered the generous support of the Scripps Collections Facility. The assistance provided by Evelyn York with scanning electron microscopy was instrumental in this work. Tom Chalfant provided instrumental assistance with manufacturing of testing apparatus. I would also like to thank Norman Olson and Dr. Timothy S. Baker for their assistance at the Cryo-Electron Microscopy Facility at UCSD.

My friends and family have provided tremendous support over the last twenty eight years without which I would not have had this opportunity. The women in my life have kept me grounded while giving me power for which I am grateful. Special thanks

are extended to my parents who provided the foundation of my academic interests and nurtured my interests with their love and support.

Finally, Professor Marc A. Meyers, who provided extensive personal and professional mentorship over the last eight years, will forever be acknowledged as a major influence in my understanding of life. This research is supported by the National Science Foundation Grant DMR 0510138.

Content from the following published manuscripts were included in Chapter 4 of this dissertation:

Lin A, Meyers MA. Growth and structure in abalone shell. ***Materials Science and Engineering* A** 2005;390:27-41.

Lin AYM, Meyers MA, Vecchio KS. Mechanical properties and structure of Strombus gigas, Tridacna gigas, and Haliotis rufescens sea shells: A comparative study. ***Materials Science and Engineering C*** *2006;*16:1370-1389.

Lin AYM, Chen PY, Meyers MA. The Growth of Nacre in the Abalone Shell. ***Acta Biomaterialia*** 2008;4:131-138.

Lin AYM, Brunner R, Chen PY, Talke FE, Meyers MA. Abalone foot, underwater adhesion. Submitted

Meyers MA, Lin AYM, Chen PY, Muyco J. Mechanical strength of abalone nacre: role of the soft organic layer. ***Journal of the Mechanical Behavior of Biomedical Material***. 2008;1:76-85.

Meyers MA, Lin AYM, Lin YS, Olevsky EA, Georgalis S. The cutting edge: sharp biological materials. ***Journal of Metals*** March 2008;21.

VITA

6/2005-6/2008 Materials Science and Engineering Program, University of California, San Diego. Ph.D. in Materials Science, 2008 (Charles Lee Powell Foundation Fellow).

6/2004-6/2005 Materials Science and Engineering Program, University of California, San Diego. M.S. in Materials Science, 2005 (Charles Lee Powell Foundation Fellow).

9/1999-6/2004 Mechanical and Aerospace Engineering, University of California, San Diego. B.S. in Mechanical and Aerospace Engineering. 2004.

FIELD OF STUDY

Major: Materials science and engineering with an emphasis on biomimetics and the study of biological materials.

LIST OF PUBLICATIONS

1) Lin A, Meyers MA. Growth and structure in abalone shell. ***Materials Science and Engineering* A** 2005;390:27-41.
2) Lin AYM, Meyers MA, Vecchio KS. Mechanical properties and structure of Strombus gigas, Tridacna gigas, and Haliotis rufescens sea shells: A comparative study. ***Materials Science and Engineering C*** *2006;*16:1370-1389.
3) Lin AYM, Chen PY, Meyers MA. The Growth of Nacre in the Abalone Shell. ***Acta Biomaterialia*** 2008;4:131-138.
4) Lin AYM, Brunner R, Chen PY, Talke FE, Meyers MA. Abalone foot, underwater adhesion. Submitted
5) Meyers MA, Lin AYM, Chen PY, Muyco J. Mechanical strength of abalone nacre: role of the soft organic layer. ***Journal of the Mechanical Behavior of Biomedical Materials***. 2008;1:76-85.
6) Meyers MA, Chen PY, Lin AYM, Seki Y. Biological Materials: Structure and Mechanical Properties (REVIEW ARTICLE). ***Progress in Materials Science*** 2008;53:1-206.
7) Meyers MA, Lin AYM, Seki YS, Chen PY, Kad BK, Bodde S. Structural biological composites: an overview. ***Journal of Metals*** 2006;58:35-41.
8) Meyers MA, Lin AYM, Lin YS, Olevsky EA, Georgalis S. The cutting edge: sharp biological materials. ***Journal of Metals*** March 2008;21.

9) Chen PY, Lin AYM, Lin YS, Seki Y, Stokes AG, Meyers MA, McKittrick J. Structure and mechanical properties of selected biological materials. ***Journal of the Mechanical Behavior of Biomedical Materials*** in press.

10) Chen PY, Lin AYM, Mckittrick J, Meyers MA. Structure and mechanical properties of crab exoskeletons. ***Acta Biomaterialia*** 2008;4:587-597.

11) Chen PY, Lin AYM, Stokes AG, Seki Y, Bodde, SG, Mckittrick J, Meyers MA. Structural biological materials: overview of current research. ***Journal of Metals*** June 2008.

INTERNATIONAL CONFERENCE PRESENTATIONS

1. NBRM 2004, Stanford Linear Accelerator Center: "Characterization of the Bio-Nanostructure and Mechanical Properties of Nacre"
2. TMS 2005 Annual Meeting, San Francisco: "Growth and Structure in Abalone Shell"
3. TMS 2006 Annual Meeting, San Antonio: "Mechanical Properties and Structure of Haliotis Rufescens, Strombus Gigas, and Tridacna Gigas Sea Shells: a comparative study"
4. TMS 2007 Annual Meeting, Orlando: "Growth Sequence After Implantation: a study of the transition from growth bands to steady state growth"
5. MRS 2008 Spring Meeting, San Francisco: "The abalone foot, adhesion through van der Waals"

ABSTRACT OF THE DISSERTATION

STRUCTURAL AND FUNCTIONAL BIOLOGICAL MATERIALS: ABALONE NACRE, SHARP MATERIALS, AND ABALONE FOOT ADHESION

by

Albert Yu-Min Lin

Doctor of Philosophy in Materials Science and Engineering

University of California, at San Diego, 2008

Professor Marc André Meyers, Chair

A three-part study of lessons from nature is presented through the examination of various biological materials, with an emphasis on materials from the mollusk *Haliotis rufescens,* commonly referred to as the red abalone. The three categories presented are: structural hierarchy, self-assembly, and functionality.

Ocean mollusk shells are composed of aragonite/calcite crystals interleaved with layers of a visco-elastic protein, having dense, tailored structures with excellent mechanical properties. The complex nano-laminate structure of this bio-composite material is characterized and related to its mechanical properties. Three levels of structural hierarchy are identified: macroscale mesolayers separating larger regions of tiled aragonite, microscale organization of 0.5 μm by 10 μm aragonite bricks; nanoscale mineral bridges passing through 30 nm layers of organic matrix separating individual aragonite tiles.

Composition and growth mechanisms of this nanostructure were observed through close examination of laboratory-grown samples using scanning electron microscopy (SEM), Raman spectroscopy, and transmission electron microscopy (TEM). Glass slides and nacre pucks were implanted onto the growth surface of living abalone and removed periodically to observe trends in nacre deposition. Various deproteinization and demineralization experiments are used to explore the inorganic and organic components of the nacre's structure. The organic component of the shell is characterized by atomic force microscopy (AFM).

The functionality of various biological materials is described and investigated. Two specific types of functionality are characterized, the ability of some materials to cut and puncture through sharp designs, and the ability for some materials to be used as attachment devices. Aspects of cutting materials employed by a broad range of animals were characterized and compared. In respect to the attachment mechanisms the foot of the abalone and the tree frog were investigated. It is discovered that the foot of the abalone applies similar mechanics as that of the gecko foot to adhere to surfaces. Approximately 10^{11} 100 nm diameter fibers found at the base of the foot pedal are found to create Van der Waals interactions along with capillary and suction mechanisms to enable attachment. This reusable adhesive is found to exhibit strength of ~0.14 MPa. This represents an evolutionary convergence of design from two independent species (the gecko and the abalone) living in extremely dissimilar environments.

The presented work provides a summary of an effort to investigate materials found in nature with the hope of inspiring novel technological advances in design.

CHAPTER 1

INTRODUCTION AND OBJECTIVES

Natural selection provides a tool by which nature can process, improve, and refine biologically-based organisms over millions of years. Scientists can learn from these evolutionary refinements and develop technologies based on natural designs. To ignore these lessons of nature would be squandering the largest resource available to mankind. At present, even the simplest bio-mineralized structures cannot be synthesized in the laboratory without the use of living organisms. *Biomimetics* is a newly emerging interdisciplinary field in materials science and biology in which lessons learned from biology form the basis for novel material concepts. This field investigates biological structures, establishing relationships between properties and structures in order to develop; methods of processing, microstructural design, and functionality for new materials. The approach to such an undertaking requires an obvious synergy of a variety of fields. The foundational work by D'Arcy W. Thompson, first published in 1917, may be considered the earliest concerted effort towards this goal [1]. He examined the shape and form of various biological systems and related them to their engineering functions. This spawned the gradual flow of other investigations from a mechanistic, or at least non-biology, perspective. Work by Vincent lead to the publication of "Structural Biological Materials" [2], Currey's study of various biological materials resulted in the publication of the well known book "Bone" [3], and thus the field's momentum gained steam and the flood gates of intellectual insight were opened.

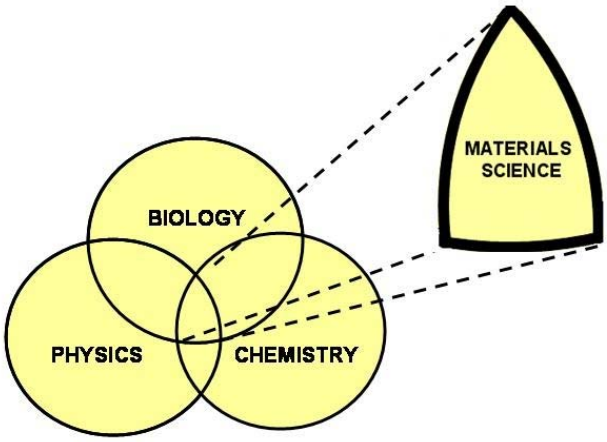

(a)

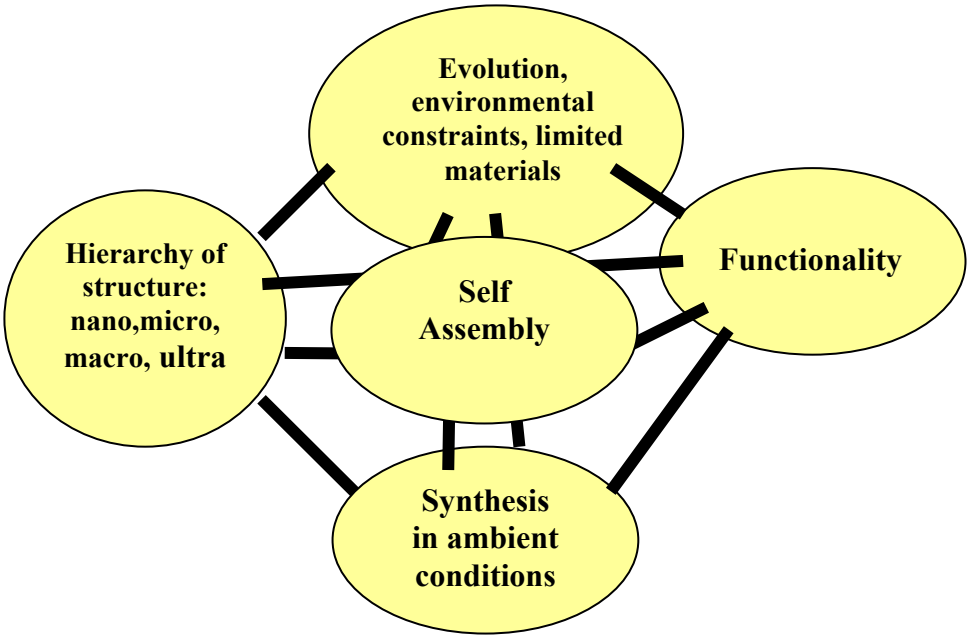

(b)

Figure 1.1 Schematic representation of (a) contributing scientific fields and (b) constraints/components in the study of biological systems (modified from E. Artz [4], and Meyers et al. [5]).

Arzt portrays the multidisciplinary nature of materials science at the intersection of physics, biology, and chemistry; this is represented in Figure 1.1 a [4]. The study of biological systems in materials science is further defined by a variety of constraints and requirements exhibited by the ruthless demands of nature; these are represented in Figure 1.1 b.

It can be seen that materials developed in nature must exhibit favorable mechanical properties and often exhibit multi-functionality. Furthermore, the intricate hierarchy of structural designs must self-assembled at ambient conditions, a process very different to the synthesis of synthetic materials. Thus the study of biological materials offers valuable insight towards both the future, and the past of materials science. Sarikaya [6] divides the emerging field into:

(a) *Biomimicking*: the understanding of these biological systems and application of concepts to synthetic materials using current technology.

(b) *Bioduplication:* a more advanced stage, in which new methodologies, such as genetic engineering, will be used to produce an entire class of new materials.

This study is focused on the first of these subcategories, *Biomimicking*. Basic inorganic materials found in nature (such as calcium carbonate, hydroxyapatite, and amorphous silicas) are, independently, very weak. However, when combined with proteins, and self-organized into highly ordered structures, and refined over long periods, these basic materials make very strong composites, sometimes increasing their strength by orders of magnitude [2,8]. There are numerous examples of biological materials with unique mechanical properties [8-13]: silk, antler, hedgehog spines [14], silica rods in sea sponges (possessing three times the flexural strength of monolithic/synthetic silica [15]),

pink conch (*Strombus Gigas*) shells [16], and abalone (*Haliotis*) shells [6,17-20]. These complex composites contain both inorganic and organic components in their macro-, micro-, and nano-structures [8, 21]. Understanding these structures and how their hierarchical organizations provide toughness and strength may lead to improvement of current synthetic materials. The mechanisms of energy absorption at many different scales are important to the bulk strength of any composite. An increase in strength due to structure can be seen in laminates as they form stronger materials from weak base materials; however the relative strength gain found in bio-composites remains unparalleled in synthetic materials. The complexity of these structures and their ability to self-assemble has drawn considerable attention [e.g. 6, 22, 23].

Biological materials are formed in ambient temperature and pressure, yet the simple organisms through which these inorganic materials form are able to create extremely precise and complex structures. Understanding the process in which living organisms' control the growth of structured inorganic materials could lead to significant advances in materials science, opening the door to novel synthesis techniques for multi-scale composites. Self-assembly is one of the manifestations of self-organization. Self-organization defies classical thermodynamics in that isolated systems reach equilibrium at maximum entropy; however, the criterion for thermodynamic stability in closed systems is the minimization of the free energy. The temporal evolution from simpler to more complex structures, nevertheless, leads inexorably to greater order and self-organization. This inherent contradiction has spawned some of the most creative thinking of the past thirty years. The seminal work of Prigogine (1977 Nobel Laureate) and co-workers [22,24], in particular, has reconciled thermodynamics with evolution. Most

systems are indeed open and off equilibrium, conditions under which, fluctuations can lead to self-organization. Thus, whereas the entire universe marches inexorably toward entropy maximization, isolated systems evolve, by self-organization and self-assembly, toward greater order. Nicolis and Prigogine [22] believe that "we can truly speak of a new dialogue of man with nature." Whitesides [23] laid down a broad foundation for future ventures in this direction.

Biomineralization [21, 25-27] involves the selective identification and uptake of elements and ionic molecules from the local environment and their incorporation into functional structures under strict biological mediation and control. It is possible (and indeed probable) that organic mediation accelerates the mineralization process. This is presented by Mann [27]. It is an important field of science and directly impacts materials of the future, especially in regards to the creation of nanostructures by self-assembly.

Learning from nature is not only limited to self assembly, mechanical properties, and structure of materials but the functionality of various biomaterials may also provide some extraordinary insights. Velcro™ is an example of an extremely successful biomimetic invention, inspired after an engineer by the name of Georges de Mestral found himself covered in wildflower burs after an afternoon walk with his dog [28]. Other, more advanced functions, such as turning solar energy into chemical energy through photosynthesis is present in every common plant, yet our ability to synthetically recreate the process with comparable efficiency is still far out of reach. These incredible designs from nature could inspire revolutionary advances in technology if properly understood.

The rise of the industrial revolution in the early part of the last century saw an explosion of technological advances, amongst which most were designed from a "top down" approach. However recent improvement in scientific tools has allowed scientists and engineers to examine and design at increasingly small scales. We are reaching a point at which the limitations of the previous paradigm of design principles are becoming obsolete. As Nobel Laureate, Richard P. Feynman proclaimed in his 1959 seminal talk entitled "There's Plenty of Room at the Bottom", we are entering an age in which this paradigm must shift from the "top down" to the "bottom up" [29]. The molecular building blocks with which nature builds intricate structures are the foundation of everything. Their structural designs incorporate a synergy of mechanism at every length scale. And the functionality of these materials is anchored in the principles of evolution, building from the bottom up.

CHAPTER 2

BACKGROUND

This chapter will attempt to provide a consolidated background of previous foundational works that are pertinent to this study.

2.1 Structure & Mechanical Properties

The abalone shell is composed of two defined layers: an outer prismatic layer (rhombohedral calcite) and an inner nacreous layer (orthorhombic aragonite) as observed by Nakahara et al. [30]. This shell acts as the primary mechanism of protection for the animal against predatory action. Figure 2.1 is a schematic of the overall structure of the shell as it is oriented around the animal's mantle and epithelium skin. In the figure the shell is upside down, with the bottom layer being the prismatic calcite, and the nacreous portion being represented by a tile like structure. Although the outer prismatic layer will indeed affect the over all response of the shell, the majority of the work carried out thus far has been on the inner nacreous layer; this is the focus of the following study.

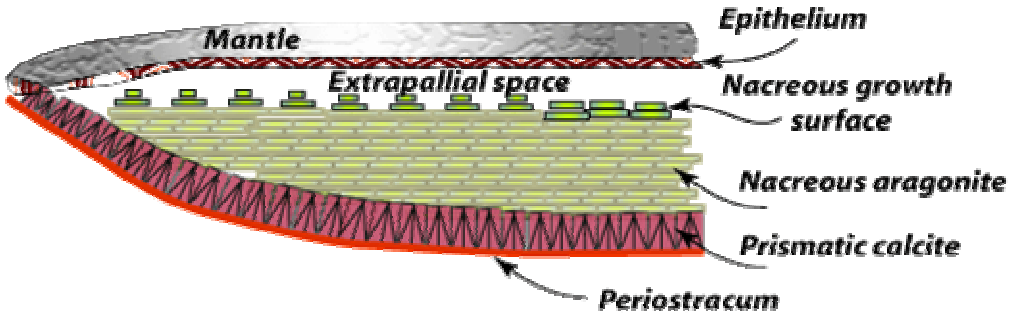

Figure 2.1 Structure of typical mollusk shell (adapted from Zaremba et al. [31]).

Aragonitic $CaCO_3$ constitutes the inorganic component of the nacreous ceramic/organic composite (95 wt.% ceramic, 5 wt.% organic material). This composite is comprised of stacked platelets (~0.5 μm thick and ~ 10 μm wide), arranged in a 'brick-and-mortar' microstructure with an organic matrix (20-50 nm thick) interlayer that is traditionally considered as serving as glue between the single platelets. A second element to the hierarchy exists as growth bands, or mesolayers. Layers of organic material with a thickness of about 20 μm separate the thicker mesolayers which are approximately 300 μm thick. These layers were identified by Menig et al. [32], Su et al. [33], Erasmus et al. [34], and Lin et al. [35] but are not often mentioned in other reports dealing with the mechanical properties of abalone. This is surprising considering the important role of the macrostructure of any material towards its mechanical response. Especially a macroscale feature as pronounced as the laminate nature of the mesolayers. It is thought that these thick organic layers form in abalone during periods in which there is little mineral growth.

Figure 2.2 shows the various levels of structural hierarchy found within the nacre of abalone. The upper left hand corner of the image presents a photograph of the lustrous nacre or "mother of pearl" shell. Interestingly, the micro- and nano-structure is responsible for the colorful nature of the material for which this shell is famous. A scanning electron microscope (SEM) image of the individual tiles of aragonite can be seen below the photo. These tiles are exactly 0.5 μm in thickness, a structural element which not only is responsible for the strength of the material (as shown later) but also the diffraction of light across the visible spectrum, resulting in the shells famous lustrous appearance. A schematic representation of the ordered arrangement of these tiles is

shown in the bottom right hand section of image. The tiles are found to be pseudo-hexagonal, a feature that can be modeled by a simple Voronoi tessellation [36] in which a discrete set of points in a plane can be decomposed into subsections of the over all plane due to the spatial distance between neighboring points. Thus, if all the tiles originate from individual points on a plane and then expand outward they would abut at their boundaries forming the hexagonal tile shapes explained by Voronoi's mathematical model.

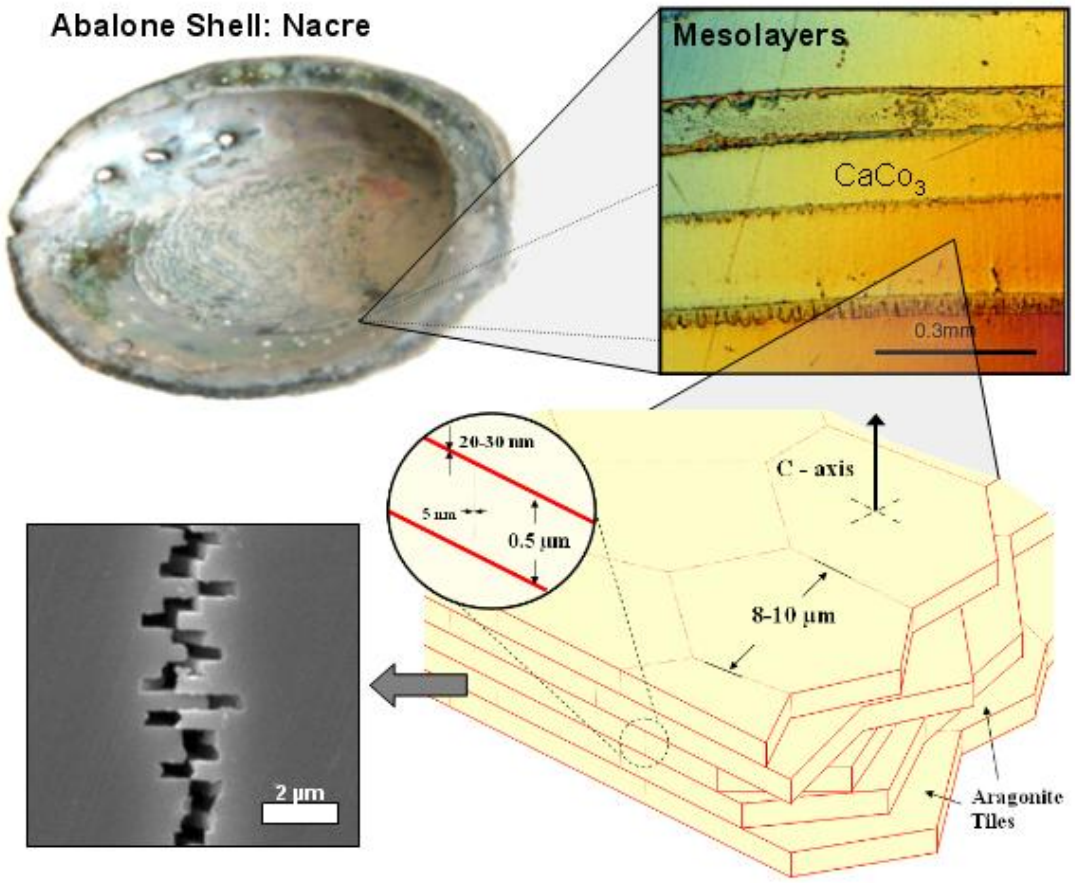

Figure 2.2 The various levels of structural hierarchy in nacre; macro scale mesolayers, 10 µm by 0.5 µm aragonite tiles, the nanostructure defined within the interface between tiles.

Mesolayers can be seen in an optical micrograph on the upper right hand corner of Figure 2.2. The darker lines mark the regions of inorganic deposition interruption, while the thicker uniform sections are composed of the tiled aragonite.

As a result of this highly ordered hierarchical structure nacre exhibits excellent mechanical properties. The following shall describe previous studies of, the mechanical characteristics of the shell, each scale of structural design, and how they contribute to the strength and toughness of nacre described above.

Currey [37] was the first to perform measurements of mechanical properties of nacre from a variety of bivalves, gastropods and cephalopods. He concluded that the fracture strength in bending varied between 56 and 116 MPa. This was followed by Jackson et al. [38] who used nacre from the shell of a bivalve mollusk, *Pinctada*. They report a Young's modulus of approximately 70 GPa for dry and 60 GPa for wet samples; the tensile strength of nacre was found to be 170 MPa for dry and 140 MPa for wet samples. The work of fracture varied from 350 to 1240 J/m^3, depending on the span-to-depth ratio and the degree of hydration, wet nacre showing superior toughness by associated introduction of plastic work. In contrast, monolithic $CaCO_3$ showed a work-of-fracture that was approximately 3000 times less than that of the composite nacre material [37].

It should be noted that this work-of-fracture is not identical to the toughness measured by Sarikaya et al. [39]. The work-of-fracture is the area under the stress-strain curve and is deeply affected by gradual, graceful fracture, whereas the fracture toughness does not incorporate this entire process. Thus, one should be careful when considering this number. Early studies show indications of the low span-to-depth ratios of tiles

contributing to fracture toughness [40]. Jackson et al. [38] concluded that water affects the Young's modulus and tensile strength by reducing the shear modulus and shear strength of the organic matrix which comprises less than 5 wt% of the total composite. The toughness is enhanced by water, which plasticizes the organic matrix, resulting in greater crack blunting and deflection abilities. In contrast with more traditional brittle ceramics, such as Al_2O_3, or high toughness ceramics, such as ZrO_2, the crack propagation behavior in nacre reveals that there is a high degree of tortuosity.

Sarikaya et al. [39] conducted mechanical tests on *Haliotis rufescens* (red abalone) with square cross-sections. They performed fracture strength σ_f (tension) and fracture toughness K_{IC} tests on single straight notched samples in 4-point and 3-point bending modes, respectively, in transverse direction, i.e. perpendicular to the shell plane. A fracture strength of 185±20 MPa and a fracture toughness of 8±3 $MPam^{1/2}$ was found. This is an eight-fold increase in toughness over monolithic $CaCO_3$. The scatter is explained by natural defects in the nacre and the slight curvature of the layers. The K_{IC} and σ_f value of synthetically produced monolithic $CaCO_3$ is 20–30 times less than the average value of nacre. The specific flexural strength of $CaCO_3$ is 10 MPa/gcm^{-3}.

Previous work at the University of California at San Diego by Menig et al. [32] on the mechanical response of abalone nacre was conducted in concurrence with the above mentioned studies. This effort represented the foundation of the current study described here.

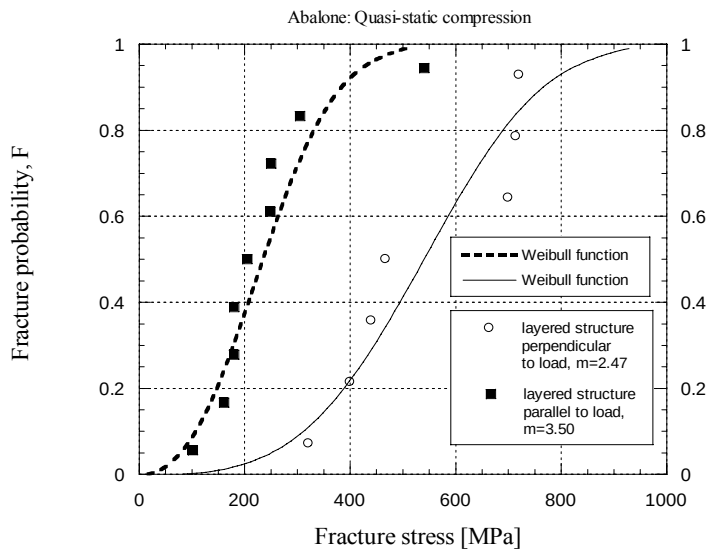

(a)

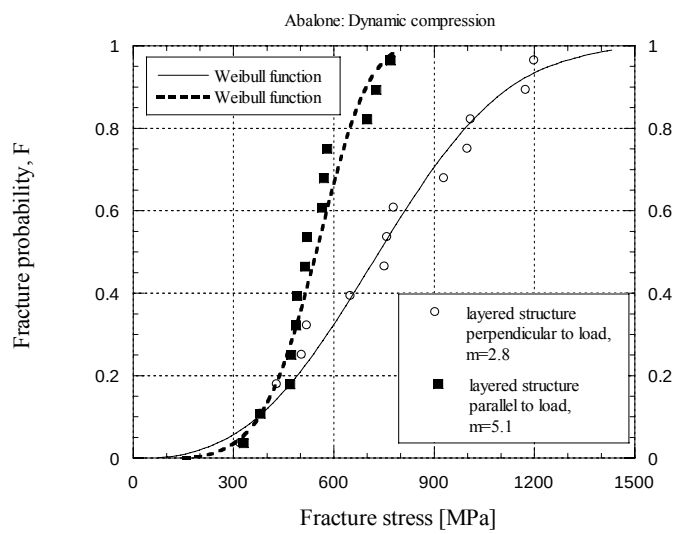

(b)

Figure 2.3 Weibull analysis of abalone nacre in; (a) quasi-static, and (b) dynamic compressive loading (Menig et al. [32]).

Menig et al. [32] measured the compressive strength of red abalone and found considerable variation. Weibull statistics [41] were successfully applied to characterize the results. Presented in Figure 2.3 are the statistical summaries of their mechanical tests on abalone nacre (a) in quasi-static compression, with failure probabilities of 50% being reached at 235 MPa and 540 MPa with loading parallel and perpendicular to layered structure, respectively, and (b) dynamic compression with 50% failure probabilities for the abalone shell found at 548 MPa and 735 MPa with the layered structure parallel and perpendicular to loading, respectively. This is within the range for synthetic ceramics. As will be discussed in Chapter 4, the tensile strength of nacre perpendicular to layered structure was found to be approximately 5 MPa. This dramatic difference will be expalined in terms of structure.

The abalone exhibits orientation dependence of strength as well as significant strain-rate sensitivity; the failure strength at loading rates of 104 GPa/s was approximately 50% higher than the quasi-static strength. This may be explained by the visco-elastic nature of the organic component of the nacre, which is evidently quite influential despite its low volume fraction within the material. Compressive strength when loaded perpendicular to the shell surface was approximately 50% higher than parallel to the shell surface. Quasi-static compressive failure in both shells occurred gradually, in “graceful failure”. The shear strength of the organic/ceramic interfaces of Haliotis rufescens was determined by means of a shear test and was found to be approximately 30 MPa. Considerable inelastic deformation of these layers (up to a shear strain of 0.4) preceded failure.

Upon compression parallel to the plane of the tiles, an interesting phenomenon observed previously in synthetic composites was seen along the mesolayers: plastic microbuckling. This mode of damage involves the formation of a region of sliding and of a kinking knee. Figure 2.4 shows a plastic microbuckling event, which is a mechanism to decrease the overall strain energy, and was observed in a significant fraction of the specimens. Plastic microbuckling is a common occurrence in the compressive failure of fiber-reinforced composites when loading is parallel to the reinforcement. The coordinated sliding of layer segments of the same approximate length by a shear strain γ produces an overall rotation of the specimen in the region with a decrease in length. Figure 2.4 shows a characteristic microbuckling region. The angle α was measured and found to be approximately 35°. The ideal angle, which facilitates microbuckling according to Argon, is 45° [42].

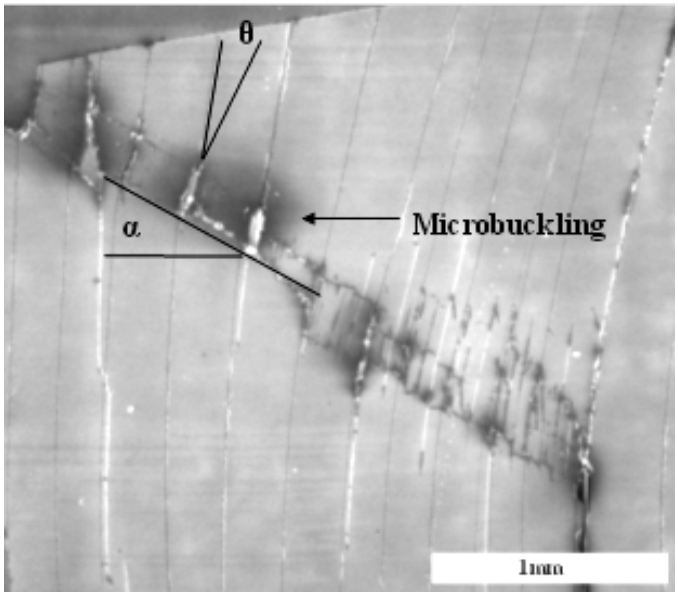

Figure 2.4 Mechanisms of damage accumulation in nacreous region of abalone through plastic microbuckling (Menig et al. [32]).

The angle θ (Figure 2.4) varies between approximately 25° and 15° and is determined by the interlamellar sliding. This angle is consistent with the shear strain of 0.45 between lamellae observed in Figure 2.5.

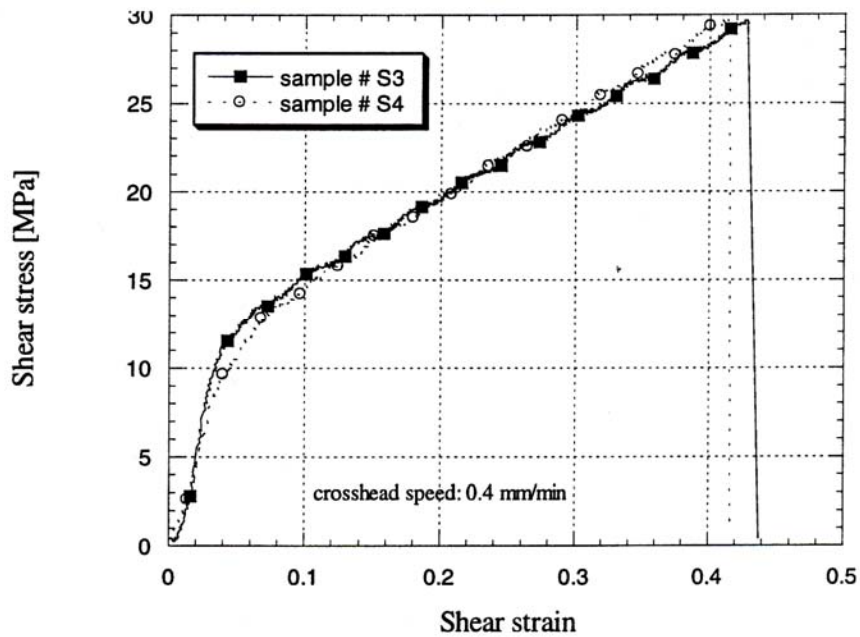

Figure 2.5 Experimental shear stress-shear strain curve for nacre (Menig et al. [32]).

The shear strain associated with the rotation θ in Figure 2.4 is tan $\theta = \gamma = 0.47$. Hence, the rotation θ in kinking is limited by the maximum shear strain, equal to 0.45. If this kinking rotation were to exceed 0.45, fracture along the sliding interfaces would occur. The shear strain γ_0 is:

$$\gamma_0 = \frac{\gamma}{f} \tag{2.1}$$

where f is the fraction of organic layer, which has an approximate value of 5 wt %, providing $\gamma_0 \cong 9$. The results by Menig et al. [32] are of the same order of magnitude as the ones reported by Sarikaya [39] and were applied to existing kinking theories (Argon [42], Budiansky [43]).

The Argon [42] formalism for kinking based on an energetic analysis, can be applied. The plastic work done inside the band (W) is equated to the elastic energy stored at the extremities (ΔE_1) of the band and the energy outside the band (ΔE_2) that opposes its expansion:

$$\Delta E_1 + \Delta E_2 - W = 0 \tag{2.2}$$

This leads to:

$$\sigma \cong \frac{\tau}{\theta_o}\left[1 + \frac{bG_c\Delta\theta}{2\pi a\tau(1-\nu)}\ln\left(\frac{2\pi a\tau(1-\nu)}{bG_c\Delta\theta}\right) + \frac{E_r\Delta\theta}{48\tau}\left(\frac{t_r}{b}\right)^2\right] \tag{2.3}$$

where τ is the shear strength of the matrix, θ is the angle between the reinforcement and the loading axis, E_r is Young's modulus of the reinforcement, t_r is the lamella thickness, G_c is the shear modulus of the composite, υ is Poisson's ratio, and a and b are the kink nucleus dimensions. Fleck et al. [44] and Jelf and Fleck [45] further developed this treatment.

Budiansky [43], using a perturbation analysis, developed the following expression for the ratio between the thicknesses of kink bands and the spacing between reinforcement units (w/d):

$$\frac{w}{d} = \frac{\pi}{4}\left(\frac{2\tau_y}{CE}\right)^{-1/3} \tag{2.4}$$

where E is the Young's modulus of the fibers and C is their volume fraction. It is interesting to note that Eqn. 2.4 predicts a decrease in *w/d* with increasing τ_y.

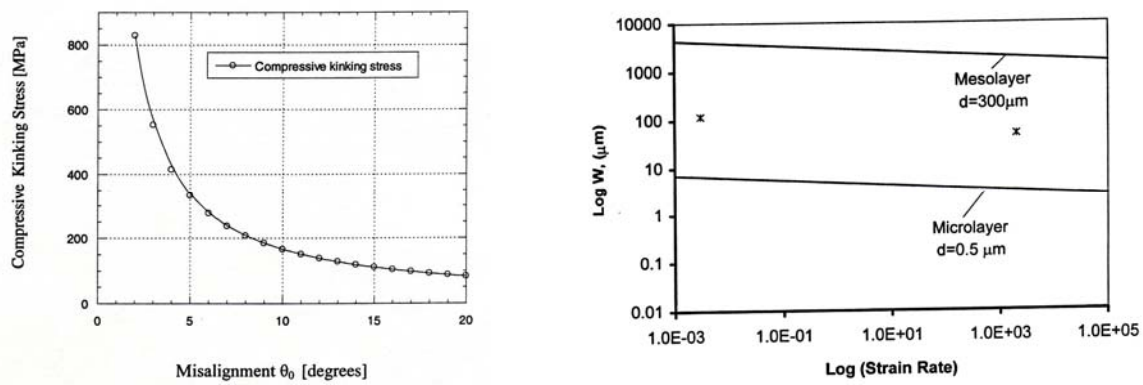

(a) **(b)**

Figure 2.6 Application to shell microbuckling (from Menig et al. [32]) of (a) Argon [42] analysis for kink stress formation and (b) Budiansky [43] formalism for the kink-band thickness prediction.

These formalisms for microbuckling were applied to abalone and enable some conclusions to be drawn regarding the kink stress and spacing of the slip units. Figure 2.6 (a) shows the predicted compressive kinking stress for abalone as a function of misalignment angle. It can be seen that the strength is highly sensitive to the angle α. Figure 2.6 (b) using the Budiansky equation adapted to the abalone geometry shows the kink band thickness (*w*) as a function of strain rate. The results by Menig et al. [32], carried out at different strain rates, confirmed the Budiansky prediction. Two parameters were used: the mesolayer and microlayer thicknesses. The experimental results, shown in

Figure 2.6 (b), fall in the middle proving both the mesolayers and platelets (microlayers) take part in kinking.

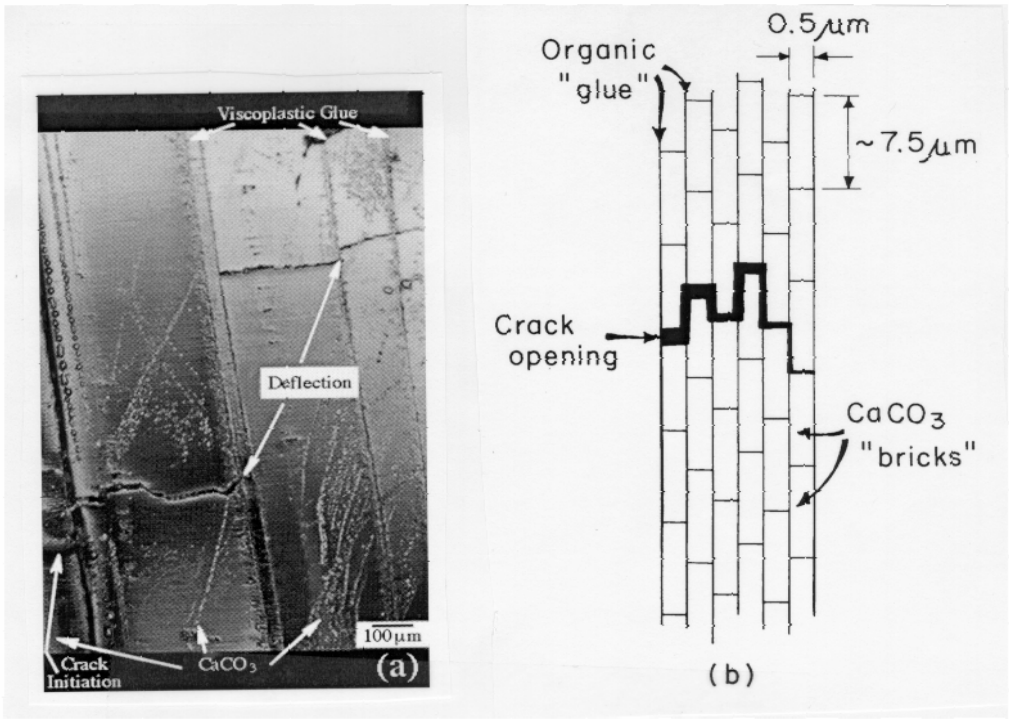

Figure 2.7 (a) Cross section of abalone shell showing how a crack, starting at the left is deflected by viscoplastic layer between calcium carbonate lamellae. (b) Schematic drawing showing arrangement of calcium carbonate in nacre, forming a miniature "brick and mortar" structure (Meyers and Chawla [46]).

Another significant mechanism of toughening is crack deflection at both the meso- and micro-scale. The effect of the visco-elastic organic interruptions between mesolayers or even individual aragonite tiles is to provide a crack deflection layer that

creates an impediment in the propagation of cracks through the composite. Therefore the composite is superior to the monolithic material, in which a propagating crack has no barriers. Jackson et al. [40] correctly recognized that the increase in path length, created through deflection of cracks is responsible for enhanced work-of-fracture. The two levels of the structure presented in Figure 2.7 can be seen engaging in this mechanism: (a) mesolayers provide crack deflection, (b) at a smaller scale the tile layers force cracks in a tortuous path. This and several other toughening mechanisms have been proposed [39] including: (a) crack blunting/branching, (b) microcrack formation, (c) plate pull out, (d) crack bridging (ligament formation), and (e) sliding of $CaCO_3$ layers. The high degree of crack tortuosity in these shells may be due mainly to crack blunting and branching. However, it is reported that the many orders of magnitude increase in toughness cannot be caused by tortuosity alone. Therefore, it is possible that the major toughening mechanisms are sliding and ligament formation [17].

Figure 2.8 shows tensile failure along the direction of the tiles. The tensile strength of the tiles is such that they do not exclusively break nor slide along their interfaces; rather it is a combination of the two. It has been suggested though personal communications with Sir Ashby [47] that this is in fact an important observation into the optimization techniques employed in this material. If the tiles were significantly stronger than the shear strength of their interfaces the strength of the material could be characterized by the interface alone. On the other hand, if the tiles are considerably weaker than the interface shear strength then the usefulness of the structure at those interfaces is essentially negated. Thus an optimization of a balance between the tile strength and the interface strength is needed, and this is what is observed.

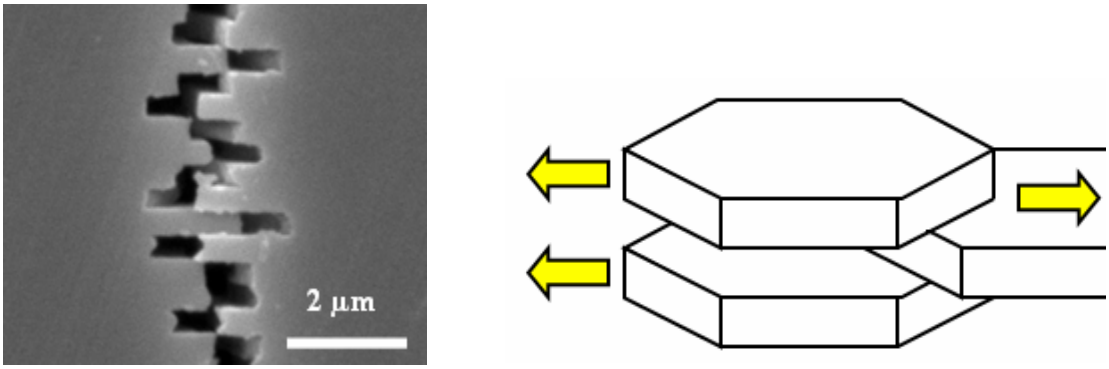

(a) (b)

Figure 2.8 Mechanisms of damage accumulation in nacreous region of abalone through tile pullout: (a) SEM micrograph; (b) schematic representation (Lin and Meyers [35]).

Tile sliding is represented in Figure 2.8 (b). This is accomplished by the viscoplastic deformation of the organic layer and/or by the shearing of the mineral ligaments traversing the organic phase. The organic phase is not a monolithic material but possesses an important and complex structure. Both of these aspects will be discussed in great detail throughout this dissertation. The center region is structurally more rigid with high chitin content. Aspartic acid is a major constituent of the acid soluble components. Other constituents are glutamic acid, serine, glycine, alamine. Shen et al. [48] reported the characterization of the cDNA coding for "Lustrin A" which is a protein they have identified within the nacreous layer of red abalone.

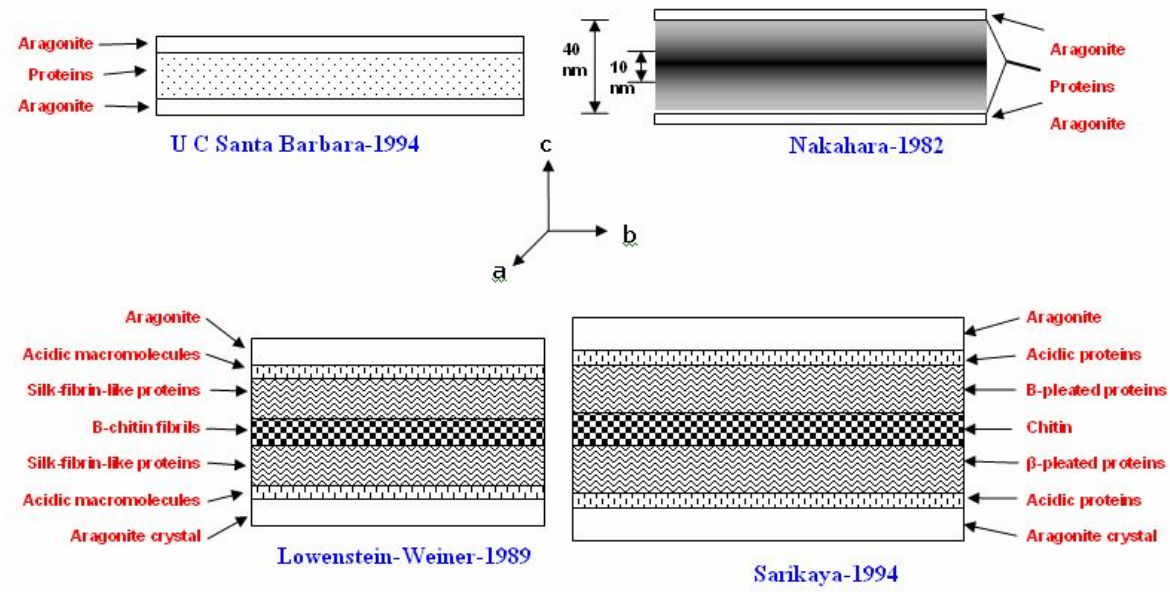

Figure 2.9 Various models for the proteinaceous layer.

Figure 2.9 is a representation some of the different structures proposed for the organic layer. The most concerted effort in identification of this layer can be arguably credited to the group at the University of California, Santa Barbra [51], however various models have both preceded and followed their work [18, 21, 30]. Early models indicate the presence of a thin protein sheet (10-40 nm thick) sandwiched between the aragonite tiles. More complex models attempt to represent the composition of the organic matrix with a central β-chitin sheet sandwiched between β-pleated proteins which are in turn covered in acidic proteins which act as the interface between the organic and inorganic. Belcher and Gooch (Figure 15.9) [51] quote a value of $\varepsilon_{max} = 3$ (equivalent to a maximum stretch $\lambda = \varepsilon + 1 = 4$). The calculations confirm that the organic layer material has a very small stiffness and is highly stretchable.

Smith et al. [75] used an atomic force microscope to pull the organic layer from a freshly cleaved section of nacre. Their results presented in Figure 2.10 show a "saw-tooth" pattern of deformation in which it is possible that sacrificial bonds may absorb energy through protein unfolding, increasing the toughness of the composite. They found a breaking force on the order of 100-400 pN in their curves, and stated that the work done on the shell was irreversibly dissipated as heat. There have been other various studies on the organic matrix between tiles [52-57]. Furthermore, investigations on the interface between the organic-mineral junction have added considerable insight into the process of tile sliding, and the deformation mechanism of the overall composite [58,59].

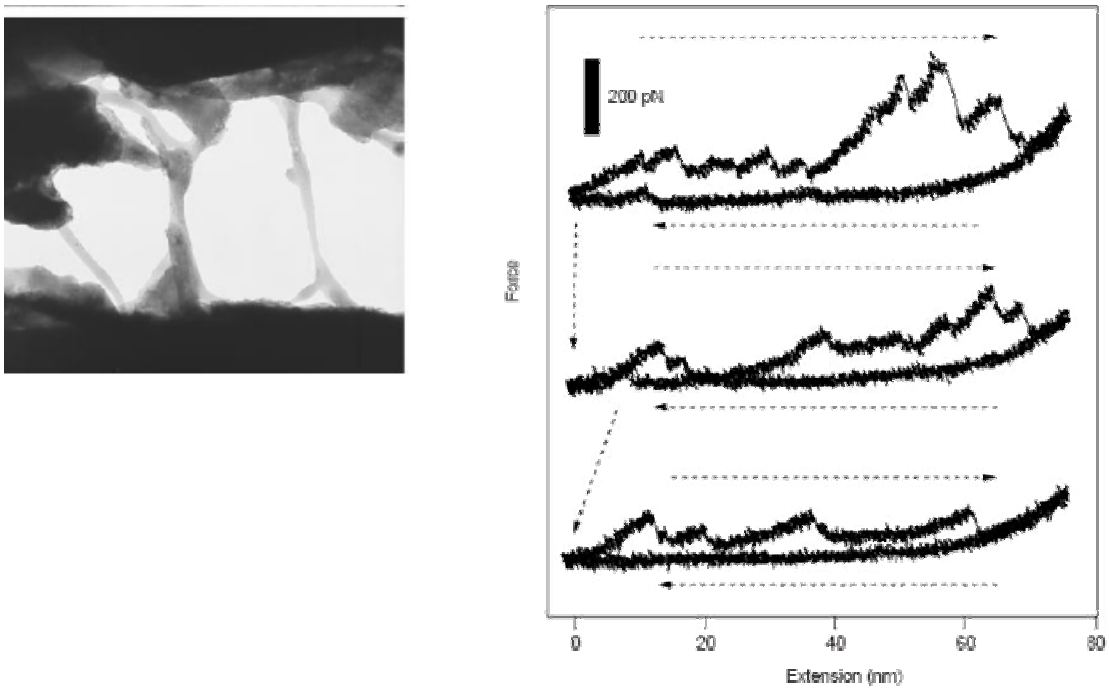

(a) **(b)**

Figure 2.10 (a) SEM of the organic membrane stretching at tile interface, (b) force extension curve of organic component via AFM probe [75].

The interface between the organic phase and the aragonite may be critical in the shear strength of the laminate components. Figure 2.11 (courtesy of K.S. Vecchio [64]) shows the unit cell. The (001) plane is the top surface. The calcium atoms are black; the carbon atoms are black and smaller; the oxygen atoms are gray. As described by Weiner and coworkers [60-62] Figure 2.11 shows the aspartic acid-rich protein $(Asp\text{-}Y)_n$,where Y is an amino acid bonding to the Ca^{+2} ions of the aragonite structure. These proteins, in turn, bond to the more rigid beta sheets. Addadi and Weiner [63] describe the phenomenon of stereoselectivity in considerable detail and provide three possible explanations for it. They suggest that the aspartic acid- rich protein binds to calcium atoms preferentially. Indeed the (001) plane of aragonite is characterized by protruding calcium atoms.

The nanostructure of these organic layers is still not well known; however, as will be later shown a network of protein chains has been identified through atomic force microscopy. It will also be shown that the elastic modulus of the organic matrix is so low that any significant impact of on the mechanical response will likely be limited to dampening, or crack deflection, and the majority of its influence is in the process of mineral mediation during biomineralization. This will also be discussed in greater length throughout *Chapter 4*.

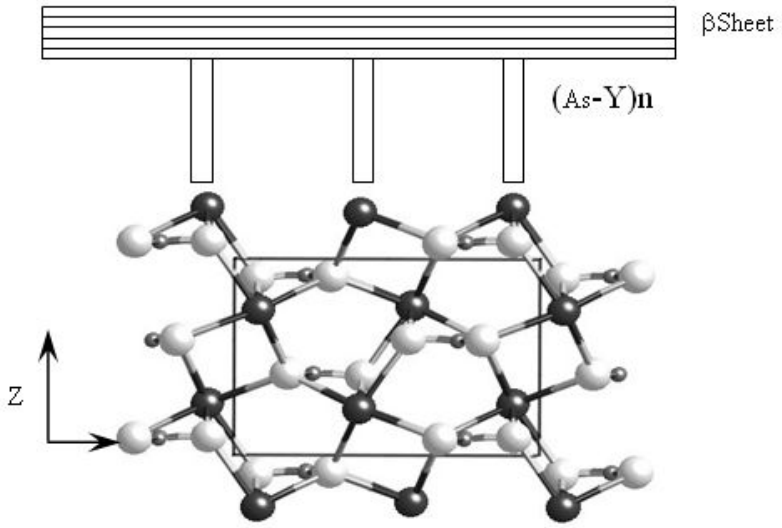

Figure 2.11 Unit cell of aragonite showing schematic position of (Asp-Y)n and β sheet. Notice protruding calcium ions on (001) face; black atoms: Ca; small black: carbon; gray atoms: oxygen. (Courtesy of K. S. Vecchio, UCSD [64]).

In contradiction to the proposed model in Figure 2.11, Nassif et al. [65] recently showed evidence of an amorphous layer of $CaCO_3$ surrounding each aragonite platelet. They used high-resolution transmission electron microscopy (HRTEM) to expose the crystallographic structure of a single tile from the shell of the abalone *Haliotis laevigata*. Figure 2.12 shows their results, it can be seen that at the edge of the tile there is a transition from the single crystal aragonite structure to an amorphous calcium carbonate layer. This work will be discussed in further detail as to its impact on the understanding of growth mechanisms, however here it introduces an interesting alternative. They suggest that the carbonate sites at disordered surfaces would not allow bonding of proteins. If this is the case, there would be little interaction between the mineral and the organic because of the lack in epitaxial match up.

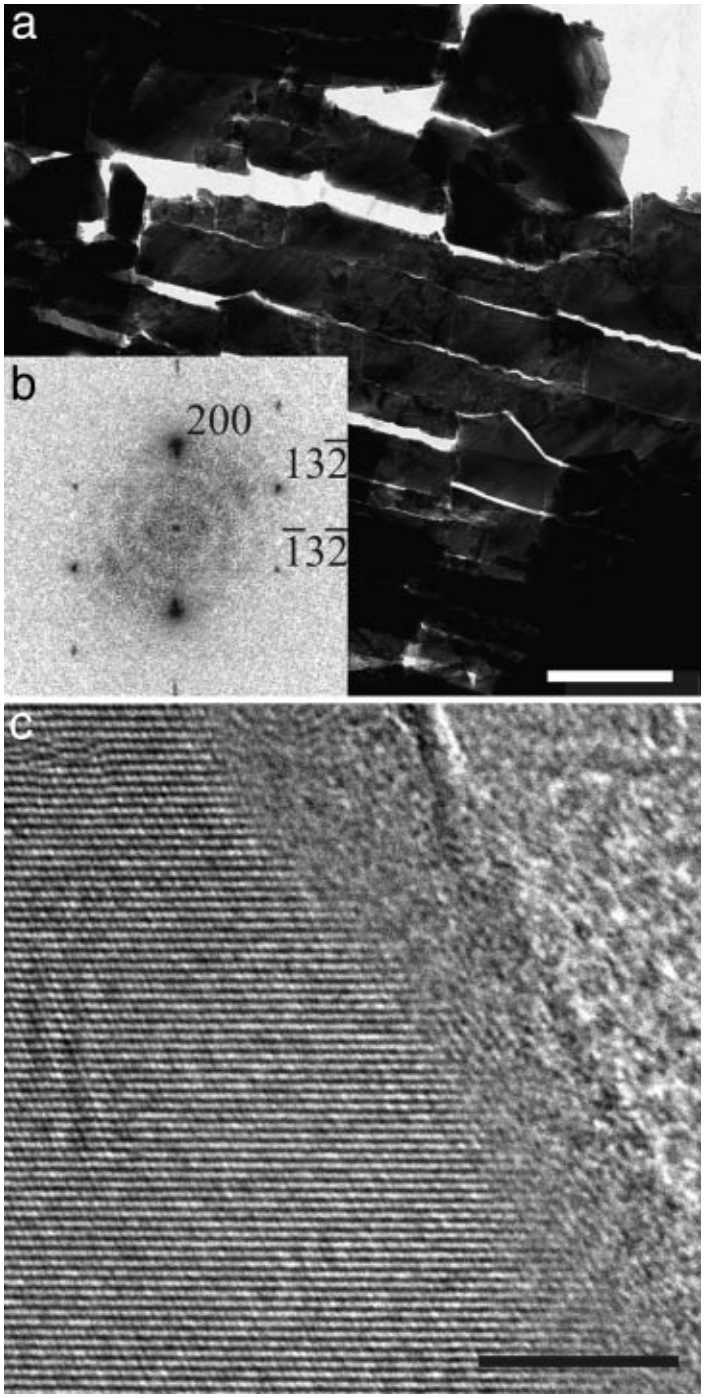

Figure 2.12 TEM of nacre platelets showing transition from single crystal aragonite to amorphous calcium carbonate at the edge of each tile (Nassif et al. [65]).

Evans et al. [67] and Wang et al. [66] proposed an alternative toughening mechanism: that nano-asperities on the aragonite tiles are responsible for the mechanical strength. These nano-asperities create frictional resistance to sliding, in a manner analogous to rough fibers in composite material. They developed a mechanism that predicts the tensile mechanical strength based on these irregularities. These nano-asperities were modeled by Barthelat et al. [68], who carried out nanoindentation and FEM analysis of the aragonite crystals. Bruet et al. [69] obtained, through nanoindentation and atomic force microscopy, local measurements of the mechanical properties of the aragonite tiles: E = 79 and 92 GPa and compressive strengths of 11 and 9 GPa for dry and seawater soaked tiles, respectively. This strength is much higher than that observed by Menig et al. [32] in compression tests (~540 MPa); yet, the Young's modulus is consistent with values reported in literature [35,40]. The source of inter-tile shear resistance is still a subject of significant debate.

2.1.1 Biomimetics

The motivation of the presented studies on the structure of nacre is to develop novel material concepts which may be implemented into synthetic materials. By examining structural components one may ascertain the secrets of a material's its strength. These secrets can then be applied to existing materials, further optimizing their mechanical properties (eg. [106, 107]). Inspired from the nacre of abalone, researchers have begun to develop new composite laminates which attempt to mimic the incredible natural structure [198].

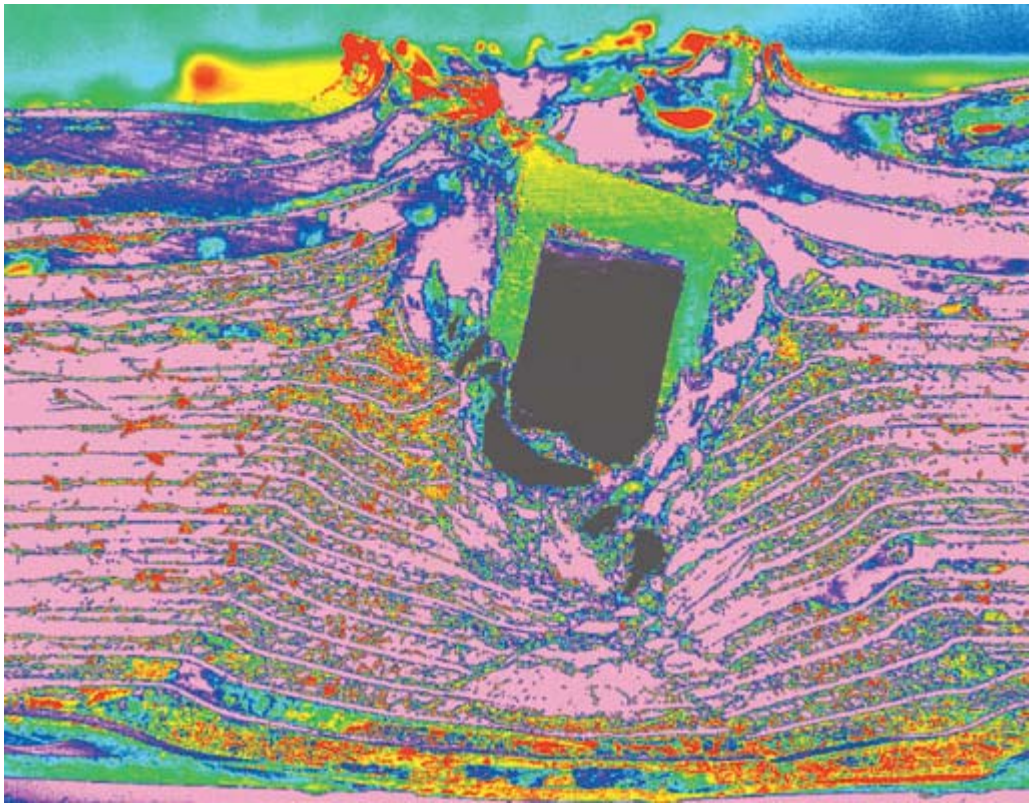

Figure 2.13 Metallic-intermetallic laminate inspired from abalone nacre [198].

Figure 2.13 shows a Ti-TiAl laminate composite which was inspired from the structure of nacre. The hard ceramic-like intermetalic layer of titanium aluminide represents the hard mineral phase in the shell structure, while the pliable layer of residual titanium alloy plays the role of the compliant protein layers.

Another example, attachable hexagonal ceramic plates have even been introduced as possible armor designs for military vehicles [199]. The plates were designed to be attached externally via layers of Velcro®. These attempts at biomimicktry are valiant efforts, however still lack the ability to harnesses the tiny scales of complexity employed in natural materials.

Another more advanced flattery of nature is to mimic its ingenuity by attempting to grow or produce biomimetic materials using the same mechanisms of growth as those found in nature. Significant efforts in recent years have been conducted towards this goal from leading scientists around the world [108-112]. Heuer's and coworkers [110] heavily cited article entitled "Innovative Materials Processing Strategies: A Biomimetic Approach" reviewed the way in which living systems fabricate biocomposites, and highlighted some of the efforts to exploit the basic principles involved. They concluded that the control of complex composite microstructures in natural materials has a greater influence on ceramic functional properties then the chemistry behind the ceramic itself. Thus they suggested that efforts to design new materials should be focused the mimicry of the fabrication process used in nature to manipulate the formation of microstructure. *Section 2.2* will discuss in greater detail the processes of biomineralization which occurs in the course of nacre formation with the hope of gaining insight into this complex and sophisticated processing technique.

2.2 Growth: Biomineralization

The growth of the red abalone shell has been the subject of considerable study starting in as early as the 1950's with Wada [76,77], continuing with Watabe and Wilbur [78], Bevelander and Nakahara [79] and followed by many others [80-82]. The work by the UC Santa Barbara group [31,33,51,83-88] represents one of the most comprehensive efforts. Nacre is one of the many materials (ie. dentin [113], enamel [114], cartilage [115], bone[119], and eggshells [116-118]) which may shed light on the basic principles of biomineralization [110]. It is a material which is formed in an aqueous solution of approximate 17 degrees Celsius temperature, with roughly 1 atm of pressure using nothing more then the ingenious fingers of molecular manipulation. To this day the complete picture of shell growth is not entirely understood; however, the information presented below is a review of the foundational knowledge base which lays the groundwork for a significant section of this doctorial study.

Shell growth begins with the secretion of proteins that mediate the initial precipitation of calcite, followed by a phase transition from calcite to aragonite. There are at least seven proteins involved in the process. As steady-state tiled aragonite growth is reached, nacre deposition occurs through the successive arrest of mineral deposition by means of a protein-mediated mechanism; this is followed by the subsequent re-initiation of mineral growth on the new surface layer through the existence of mineral bridges which form through the organic matrix. This takes place in the "Christmas-tree pattern" as seen in SEM image of a fractured edge of the growth surface of nacre presented in Figure 2.14.

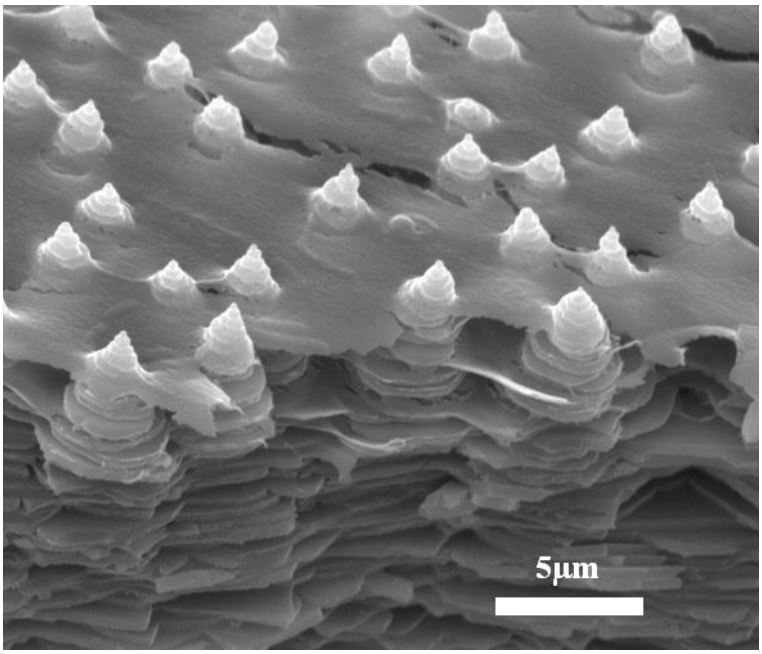

Figure 2.14 "Christmas tree" observed on growth surface of steady state tiled aragonite.

To understand this progression we must first examine the process of biomineralization. Organic molecules in solution can influence the morphology and orientation of inorganic crystals if there is molecular complementarity at the crystal-additive interface. Phase transformations are believed to occur by surface dissolution of precursors which mediate the free energies of activation of interconversions. Yet these principles are yet to be well developed. Mann states that in order to address the question of nanoscale biologically induced phase-transformations and crystallographic control we must understand the bonding and reactivity of extended organized structures under the mediation of organic chemistry [88].

The control of nucleation of inorganic materials in nature is achieved by the effect of activation energy dependency on organic substrate composition. Inorganic

precipitation is controlled by the kinetic constraints of nucleation. Homogeneous nucleation occurs with a spontaneous formation of nuclei in the bulk of the supersaturated solution; heterogeneous nucleation occurs due to formation of nuclei on a substrate in an aqueous solution. In biomineralization, heterogeneous nucleation is the norm, due to the strong dependence of nucleation and critical nucleus size on the interfacial energy. The aggregate grows against the gradient of free energy (required to create the new solid-liquid interface). When the expenditure of the interfacial energy (ΔG_i) is balanced by the energy released in the formation of bonds in the aggregate (ΔG_b) a stable nucleus is attained (see Figure 2.15 [27]). The effect of the organic substrate, on which nucleation occurs, is to lower the activation energy of nucleation ($\Delta G^{\#}$) by lowering the interfacial energy.

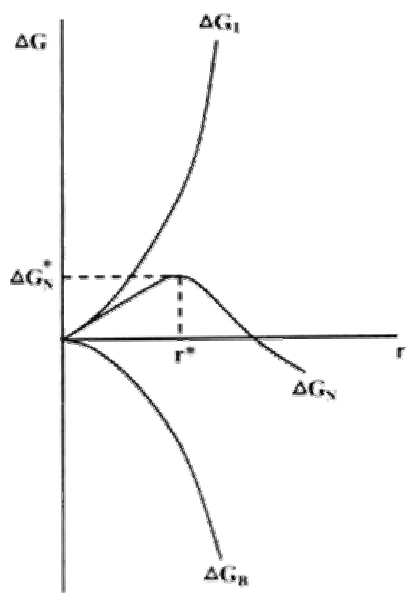

Figure 2.15 Free energy of nucleation as a function of cluster size (Mann [27]).

This activation energy may also depend on the two-dimensional structure of different crystal faces, indicating that there is a variation in complementarily of various crystal faces and the organic substrate.

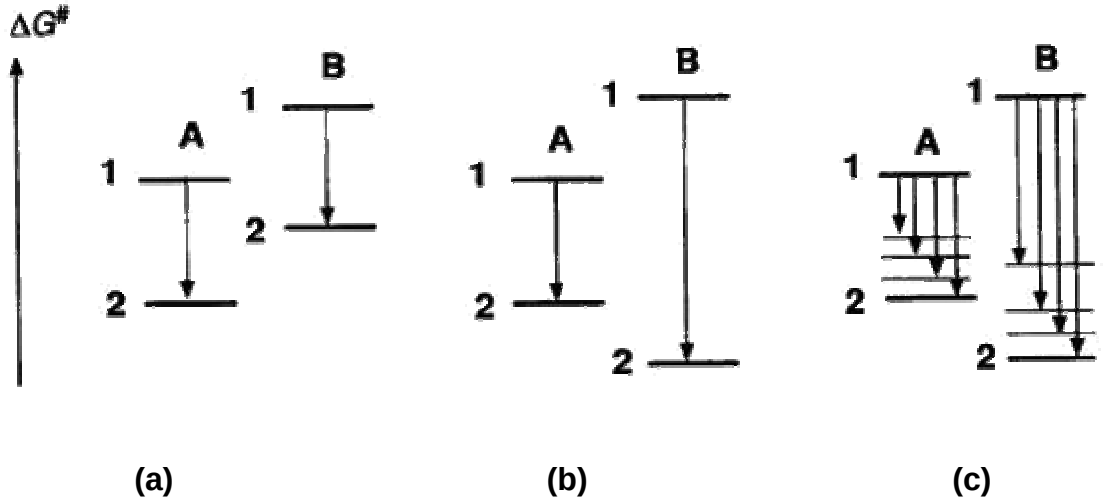

Figure 2.16 Structural control by organic matrix-mediated nucleation (Mann [27]).

The morphology of the inorganic material created in nucleation is controlled through the interaction with the organic matrix. Activation energies can be influenced in the presence of an organic matrix in three possible ways. Figure 2.16 describes the possibilities of polymorphic nucleation [27]. The activation energies of two nonspecific polymorphs, "A" and "B", are shown in the presence (state 2) and absence (state 1) of the organic matrix. If "A" is more kinetically favored in the absence of the organic matrix then it is possible to examine the possibilities of organic effect on the activation free energy ($\Delta G^{\#}$) of various polymorphs with respect to each other. In the first case both polymorphs are affected equally, thus "A" remains kinetically favorable. In the second case the effect on the "B" polymorph is much larger than for "A" and thus, when in the

presence of the organic matrix, "B" is kinetically favorable. In the last case we see a combination of the two earlier cases, in which the kinetic favorability of the two polymorphs is influenced by genetic, metabolic, and environmental processes.

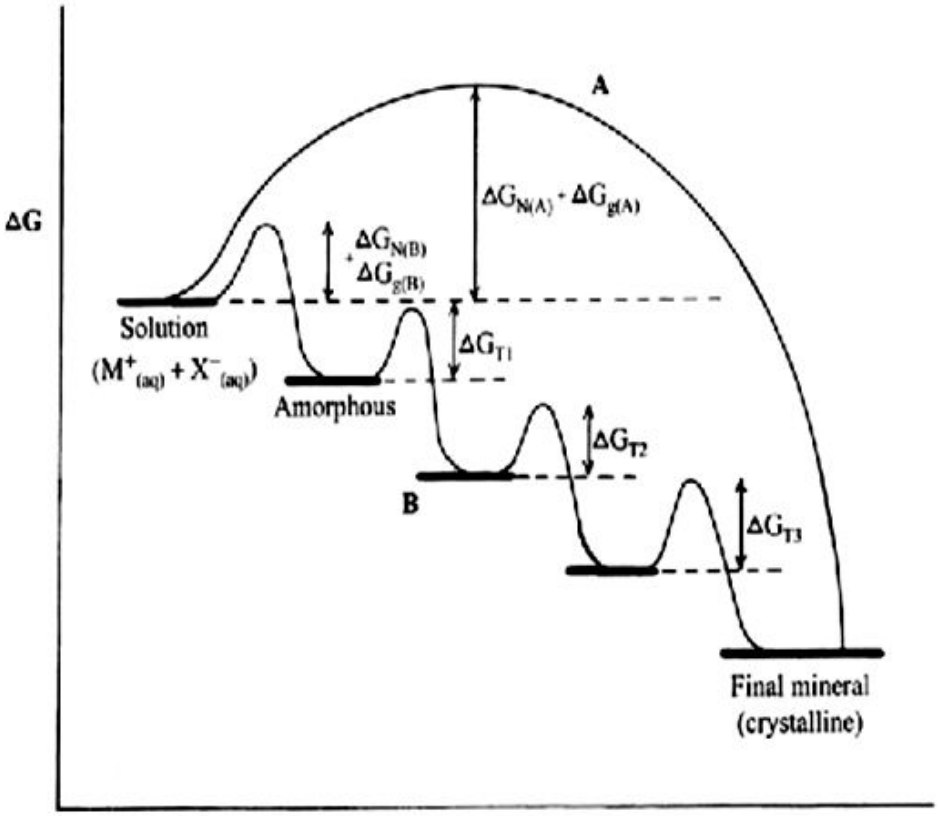

Figure 2.17 Representation of activation energies of nucleation in the presence and absence of an organic matrix for two nonspecific polymorphs (Mann [27]).

The selection of the polymorph will also be determined by a transformation. This starts, in Figure 2.17, with an amorphous mineral and continues through a series of intermediate structures that have the same composition but decreasing free energy (increasing thermodynamic stability [27]). This cascade is shown in Figure 2.17. The

system will either follow the one step route (A) or travel along a sequential transformation route (B) depending on the activation energies of nucleation, growth, and transformation. Addadi et al. [63,95,96] proposed that the role of the solid-state amorphous precursor phase could be fundamental in the biomineralization process.

Thus an animal which is able to control its emission of molecular precursors (organic matrix, or soluble protein) will be able to control the growth and structure of its inorganic biocomposite. Addadi and Weiner [63] and Addadi et al. [95,96] demonstrated the steroselective adsorption of proteins in the growth of calcite crystals resulting in a slowing down of growth in the *c* direction and altering the final shape of the crystal. This evidence of the influence of organics on inorganic crystal growth led them to examine the influence of proteins on the morphology of crystal growth.

The findings by Nassif et al. [65] further confirm this transition period by exposing a thin amorphous calcium carbonate layer surrounding each aragonite tile. This, as suggested by Nassif, would confirm that nacre is built by mesoscale transformations from amorphous colloidal intermediates, as described by Politi et al. [98] and Colfen and Mann [99] , and not by an epitaxial match between the organic and inorganic interfaces.

Belcher et al. [83] showed that a controlled phase transition between aragonite and calcite in nacre could be obtained in the laboratory with the use of soluble polyanionic proteins. They showed that biological phase transformation did not require the deposition of an intervening protein sheet, but simply the presence of soluble proteins. This was directly observed by Hansma et al. [97] through atomic force microscopy. Mann et al. [88] explained the role of soluble proteins as effective agents to the reduction of interfacial energies on the surface of the inorganic. An increase in

hydrophobicity of the additive reduces its ability to control morphology and phase transition during crystallization. The effectiveness of the soluble proteins in the process of morphology control depends on their interaction with crystal surfaces in a way which is identical to that of an organic matrix (protein sheet). Thus, the effect of the protein sheet is the control of crystal orientation with respect to bonding energies of specific crystal phases.

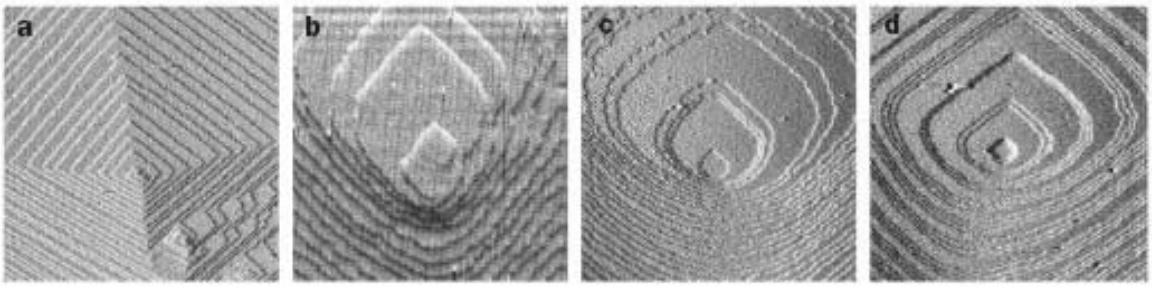

Figure 2.18 AFM images showing: (a) pure calcite growth hillock; (b-d) growth hillocks after the addition of supersaturated solutions of (b) glycine, an achiral amino acid;(c and d) aspartic acid enantiomers (Orme, Fig. 1 [100]).

Orme et al. [100] and Teng et al. [101] reported a dependency of calcite growth morphology on the selective binding of amino acids on the crystal step-edges. Through in-situ atomic force microscopy they were able to show that in solution amino acids bind to geometric and chemically-favored step-edges, changing the free energy of the step edge. Figure 2.18 (a) shows the AFM image of pure calcite growth hillocks. When a supersaturated solution of glycine is introduced into the growth solution, it can be observed in Figure 2.18 (b) that the two acute steps become curved. By modifying the free energy of step edges, preferential attachment of calcium ions onto specific locations

can be controlled, thus resulting in macroscopic crystal shape manipulation. Similar results were obtained following the addition of aspartic acid enantiomers Figure 2.18 (c) and (d). The importance of this observation is the verification of such theories as those proposed by Mann et al. [27], proving that the addition of various organic growth modifiers can change the rate and location in which calcite attaches onto surfaces. In essence, this is an in-situ observation of nature's hand laying the bricks of self organization and biomineralization.

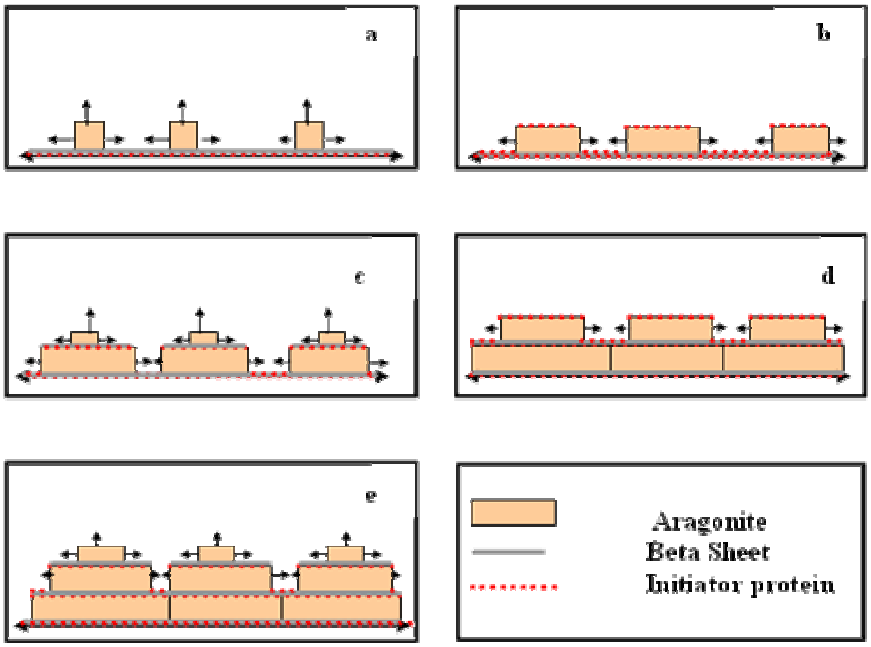

Figure 2.19 Hypothetical growth mechanism with periodic injection of proteins arresting growth in "c" direction. (a,b) protein deposition causing the arrest of crystallographic growth in the "c" direction; (c) second growth spurt after deposition of beta sheet and nucleation; (d) first aragonite plates are butted together while growth of second layer continues in "a,b" direction; (e) nucleation of third layer as second layer growth continues in "a" direction (Lin and Meyers [35]).

Figure 2.19 shows a hypothetical description of the sequence of tile growth, as it has been thought to occur during steady state deposition of nacre [35]. This is an earlier model by Lin and Meyers [35], later superseded by the 'bridge' growth mecahanism. First, a proteinaceous layer (possibly, the beta conformation of Addadi et al. [95]) is deposited. The identification of the proteins involved has only been partially done to this date, although there is work to draw upon that has succeeded in extracting protein from shells and causing precipitation from supersaturated solutions of Ca^{2+} and CO_3^{2-}. This work indeed provides a valuable database for this study. As described above, Shen *et al*. [48] reported the characterization of the cDNA coding for "Lustrin A" which is a protein they have identified within the nacreous layer of *Haliotis rufescens*. Aspartic acid, glutamic acid, serine, glycine, alamine are some of the constituents of this organic phase. Addadi and Weiner [63] describe the phenomenon of stereoselectivity in considerable detail and provide three possible explanations for it:

a) The aspartic acid-rich protein that they used for in-vitro experiments binds to calcium atoms preferentially. Indeed the (001) plane of aragonite is characterized by protruding calcium atoms, as shown in Figure 2.19. The (001) plane is the top surface. The calcium atoms are black; the carbon atoms are black and smaller; the oxygen atoms are gray.

b) The relative position of calcium and carbonate ions creating a favorable electric charge on the (001) face for the adsorption of protein.

c) Carboxylate groups (CO_3^-) are oriented perpendicular to the (001) face and therefore complete the coordination around the protein-bound calcium atoms.

Based on this, it has been proposed that the aspartic acid- rich protein attaches itself preferentially to the (001) plane of the aragonite [35] as shown previously in Figure 2.11.

New aragonite tiles grow on the subsequent organic films, with a characteristic spacing. They have the orthorhombic structure with the "*c*" direction is perpendicular to the protein plane [9]. In the absence of proteins, this is the rapid growth direction. It was speculated by Lin and Meyers [35] that the host animals produce the proteins that arrest growth in the "*c*" direction in a periodic manner. Thus, the (001) growth is periodically arrested. It was earlier thought that new aragonite tiles nucleate at the growth surfaces, on the beta conformation layer. This occurs in parallel with lateral growth.

More recent advances show that aragonite does not nucleate on the beta layer, rather mineral growth continues through pores in the organic membrane, allowing sites on which new tiles can form. This is developed fully in *Section 4.2*. In this fashion, successive "terraces" are formed and propagate. The resulting configuration is the "Christmas tree" morphology reported by Simkiss and Wilbur [25] and in greater detail by Belcher [84] and Fritz et al. [86].

These organic layers covering each tile layer may also play an important role in the providing the scaffolding for formation, not just as an arresting component. First observed and described by Nakahara et al. [102,103], they exist and are in place before the growth of aragonite tile is complete. Figure 2.20 represents the possible environment surrounding aragonite tiles with the presence of the organic scaffolding. The calcium and carbonate ions can penetrate through the organic layer deposited by the epithelium.

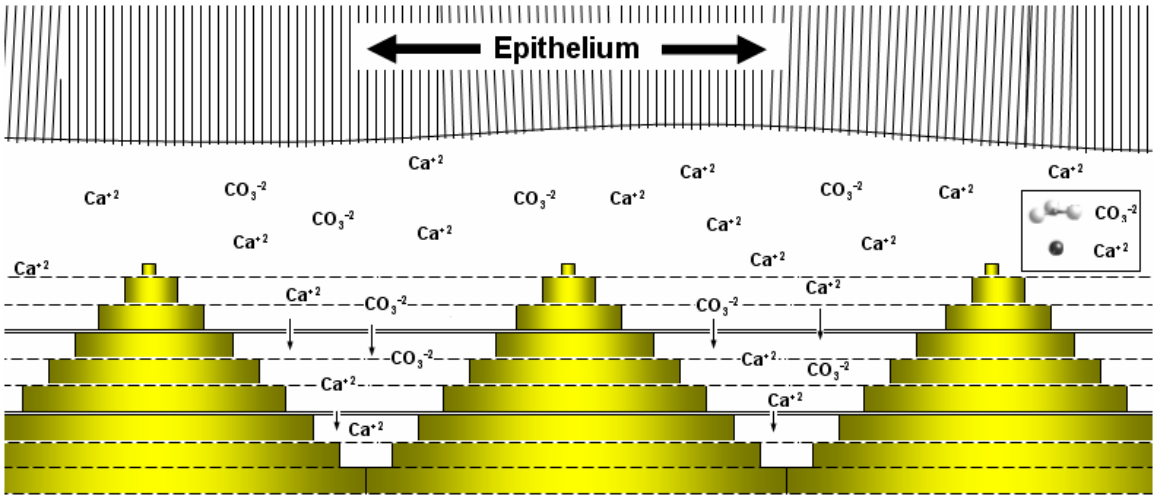

Figure 2.20 Schematic of growth mechanism showing intercalation of mineral and organic layers.

Initially, Sarikaya [104] reported a central core along the "Christmas tree" trunk. This central core would be responsible for triggering lateral growth. Song et al. [73,74], on the other hand, report a large number of bridges in each tile. The bridges traverse the organic layers, which are porous. They observed a higher concentration of bridges in the central region of the tiles; this is shown schematically in Figure 2.21. Having been first described by Schäffer et al. [105], they are responsible for transmitting the crystallographic orientation from layer to layer.

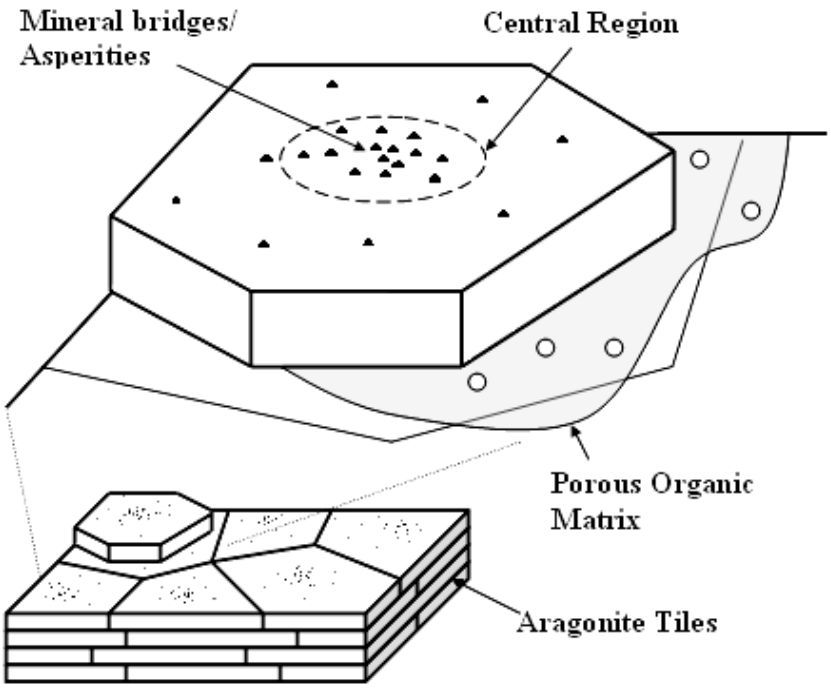

Figure 2.21 Schematic representation of mineral bridges connecting sequential aragonite tiles layers.

Atomic force microscopy [105], transmission electron microscopy [74,120], and scanning electron microscopy [120] have been used to observe the existence of mineral bridges in abalone nacre; the results are presented in Figure 2.22 (a & b). Figure 2.22 (a) shows a TEM of a tile with the lighter region marked by arrows being identified by Song et al. [74] as bridges. Figure 2.22 (b) shows the tiles (boundaries dark). The small white spots are supposedly remnants of bridges; however, it may be possible that they are artifacts developed during ion milling.

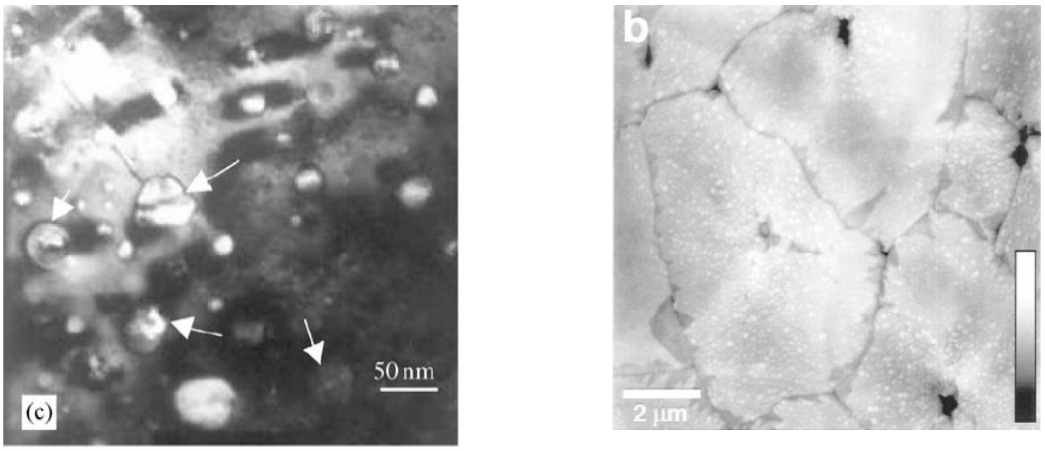

(a) **(b)**

Figure 2.22 (a) TEM view of mineral bridges on tile surfaces (Song et al. [73,74]), (b) AFM image of mineral bridge remnants on tile surface (Schäffer et al. [105]).

While in gastropods the nucleation of aragonite tiles occurs in the Christmas tree pattern described above, bivalve mineralization takes place with tablets offset with respect to layers above and below them. Figure 2.23 from Wang et al. [66] compare the two nacre structures as tile separation occurs: (a) in gastropod (abalone) shell where columns of white markings (identified with white arrows) indicate separation, and (b) in bivalves (pearl oyster) shell where tile location is offset from preceding layers and separation is more random.

In the case of the abalone nacre it is clear from the image that tile stacking occurs in an ordered fashion, with each tile located above its predecessor. This implies that during the process of deposition, there remains some kind of connection between layers, even through the existence of the organic matrix.

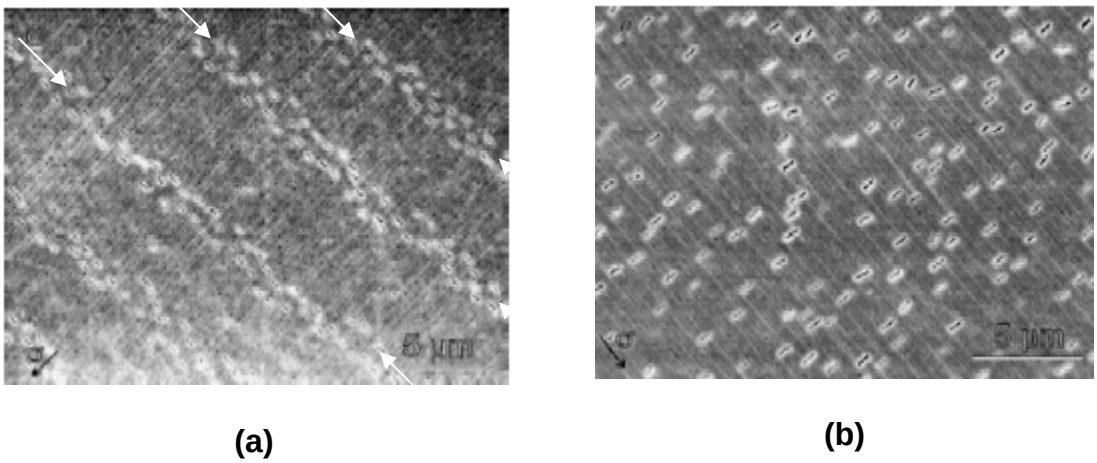

Figure 2.23 Tile separation occurs; (a) in a gastropod (abalone) shells where tiles are formed in columns, and (b) in a bivalves (pearl oyster) shells where tile location is offset from preceding layers (Wang et al. [66]).

Cartwright and Checa [121] compare differences in microstructures between gastropods and bivalves and attribute them to variations in growth dynamics. In gastropods there are a large number of holes that enable the growth, therefore a "Christmas tree" or terraced cone stacking of tiles is possible. In bivalves a smaller number of holes exist, most of which are filled with proteins and not mineral. There appears to be no direct evidence of mineral bridges. However heteroepitaxy is required for the tiles to retain the same orientation. Cartwright and Checa [121] suggest that there are more widely spaced bridges in bivalves, as shown in Figure 2.24. There are two bridges per tile, causing the heteroepitaxial growth to dictate a random stacking of subsequent tiles.

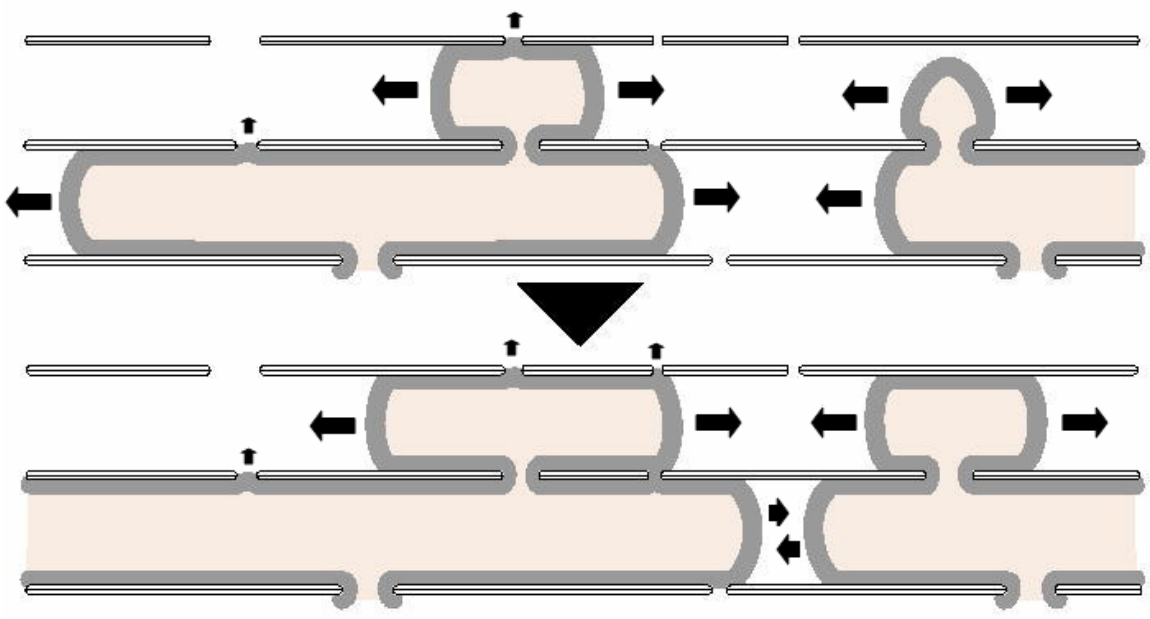

Figure 2.24 Growth sequence in bivalve nacre (Cartwright and Checa [121]).

There is a very high degree of crystallographic texture characterized by a nearly perfect "c-axis" alignment normal to the plane of the tiles as shown by Feng et al. [122] through a series of selected area diffraction patterns. Figure 2.25 (a) is a transition electron micrograph of the brick like microstructure with accompanying SAD patterns shown in Figure 2.25 (b-g).

The six tablets shown have a single orientation of [151]. This would confirm a mineral connection between layers of calcium deposition in the form of the mineral bridges described above. These results are significant in understanding the relationship between protein secretion and mineral deposition.

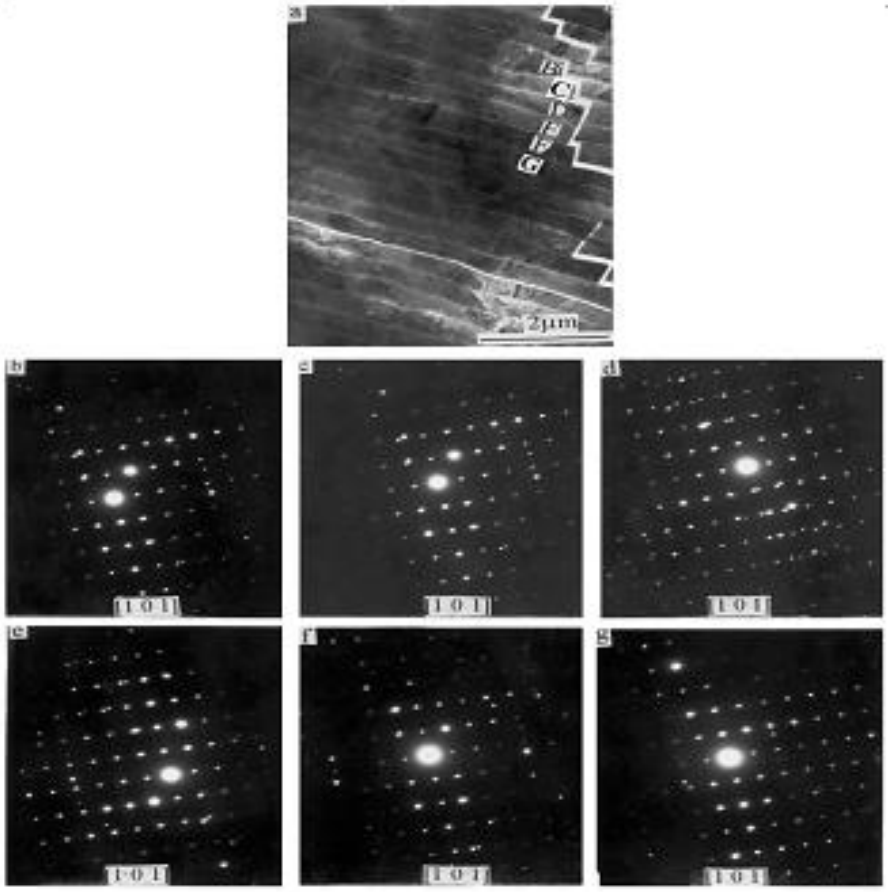

Figure 2.25 (a) TEM micrograph of a cross-section of nacre, (b-g) SAD diffraction patterns of various tiles as labeled (Feng et al. [122]).

The macroscale components of structure are also mediated through protein secretion. Growth bands occurring intermittently between large (~500μm) regions of tiled aragonite are thought to form during seasonal environmental variations. During this period mineral deposition is ceased, and a larger organic layer is deposited (~15 μm). The inorganic $CaCO_3$ undergoes morphological changes before and after the interrupting growth bands [88].

2.3 Functional Biological Materials

Some materials in nature have shown remarkable functionality. It seems, in fact, obvious that all materials in nature should serve some important and essential function, of which without its necessity would fade away with the filtering fingers of evolution. Here we look at various biological materials which exploit interesting mechanisms of physics to exhibit extraordinary functionality.

2.3.1 Sharp Materials:

Biological organisms produce composites that are organized in terms of composition and structure, containing both inorganic and organic components in complex structures. These unique aspects are illustrated in this section by focusing on one function of biological materials: their ability to puncture, cut, and shred materials which are often times much stronger then their own constituents [89-94]. The fact that serrations and needles are present in many species and in diverse configurations is direct evidence that they developed independently, by a mechanism that anthropology calls convergent evolution.

2.3.2 Attachment Devices:

The gecko feet present a fascinating problem of adhesion [123] which has puzzled great minds since antiquity. In the 4th century B.C., Aristotle pondered the gecko's ability to "run up and down a tree in any way, even with the head downwards". Only recently has it has been shown that the gecko employs a mechanism of accumulated van der Waals interactions along with capillary forces created by nanosized fibers neatly

organized along the bottom of its toes. This attachment system has first recognized by Ruibal and Ernst [124]. Indeed, there are several biological systems in which the attachment to surfaces uses similar principles: flies, beetles, and spiders. Preliminary results show that the tree frog might be included in this category [125]. Novel experimental techniques coupled with analysis are revealing these mechanisms in a variety of animals, including the abalone.

This section is intended to provide the reader with the necessary background for the understanding of the attachment mechanism of the abalone foot. It will be later shown that the abalone exploits the same mechanism of adhesion as that used by the gecko foot, in which nanofiber rods create intimate molecular and capillary contacts with a given surface which in turn accumulate into a significant macro adhesive force.

The fly and gecko feet are made of a myriad of thin rods, called setae, terminated by spatulas, with submicron diameters. These are shown for the fly *Calliphora vicina* in Figure 2.26.

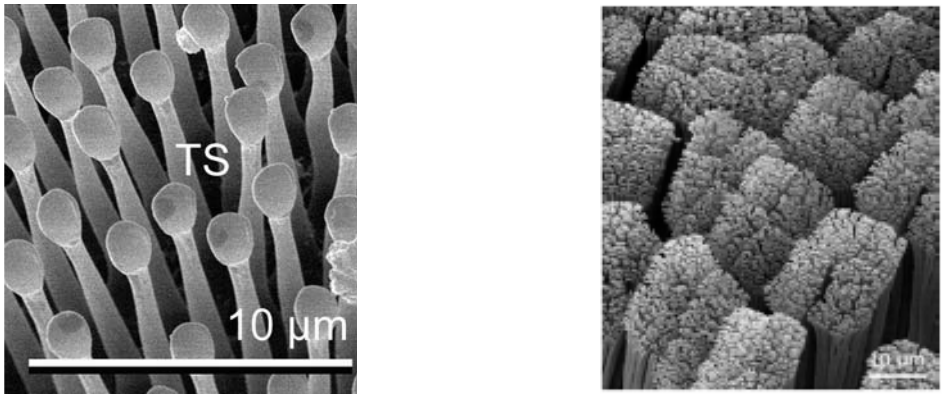

Figure 2.26 Setae and distal spatulae fly *Callifora vicina*. Van der Waals forces at spatula-surface interface generate attachment forces as 20N (Arzt [126]).

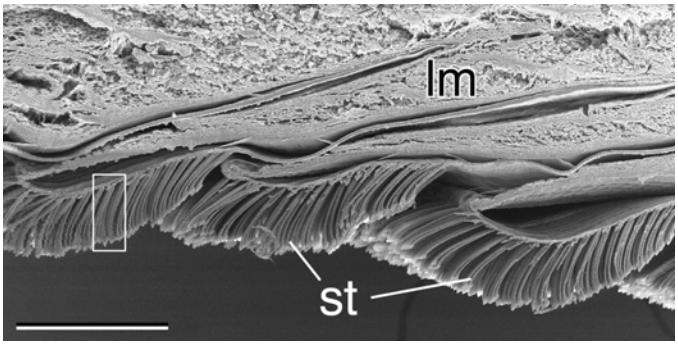

(a)

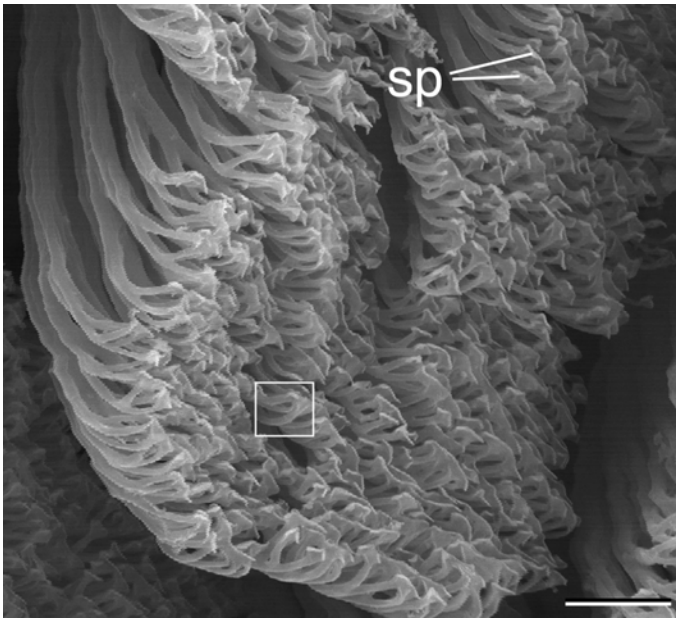

(b)

Figure 2.27 SEM micrographs showing the detail of gecko (a) satae, marked *st*; and (b) spatulae, marked *sp* (Courtesy of E. Artz and G. Huber).

Figure 2.27 (a) shows a cross section of the gecko foot with setae marked (st). Each seta has, at its tip, a number of spatulae, marked (sp) in Figure 2.27 (b). Arzt et al. [126,127] and Spolenak et al. [128] calculated the stress required to pull off a contact. This calculation is based on the van der Waals forces combined with Hertzian contact stresses. For simplicity, spatulae are assumed to have semi-spherical extremities as a first approximation, as shown in Figure 2.28. It will later be shown that the shape of the contact point has a significant impact on the adhesion forces which can be generated.

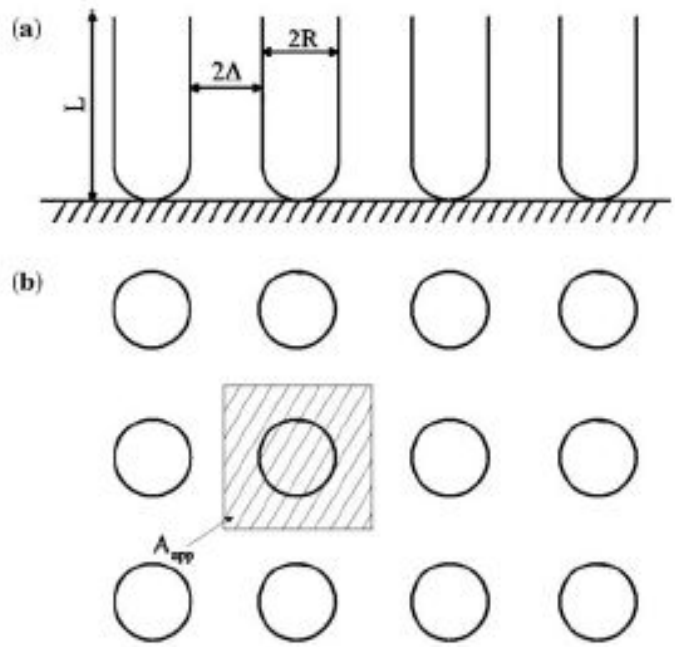

Figure 2.28 Idealized arrangement of attachment system with spherical tip shape (radius R and spacing 2Λ) (Spolenak et al.[128], Fig. 2).

The Hertzian stress is given by:

$$d^3 = \frac{12RF}{E^*} \tag{2.1}$$

Where R is the radius of the spatula, d is the contact area, F is the adhesion force, and E^* is a biaxial elastic modulus. The attractive interfacial adhesion energy per unit area, γ, was added to the calculation (Johnson, Kendall, and Roberts [160]) leading to the pull-off force F:

$$F = \frac{3}{2}\pi R\gamma \tag{2.2}$$

Where γ is the adhesion energy per area (calculated through the implementation of the Hamaker constant for a given material). The stress required to pull off a spatula is the force F divided by the apparent area (see Figure 2.28).

$$\sigma_{app} = \frac{3}{2}\frac{f\gamma}{R} \tag{2.3}$$

Where f is the fraction of the area covered by setae:

$$f = \frac{\pi R^2}{A_{app}} \tag{2.4}$$

It can be seen that the pull-off stress is inversely proportional to R. Thus, the larger the mass of the biological system, the smaller R has to be. This is confirmed by the experimental plot of Figure 2.29 from Artz et al. [127]. They found that number density of attachments, proportional to R^{-2}, increases with the mass. For geckos, that have a mass of approximately 100g, it is equal to 1000 setae per 100μm^2, or 10 setae per μm^2. This is in full agreement with Figure 2.27, which shows spatulae having an approximate diameter of 0.2 μm.

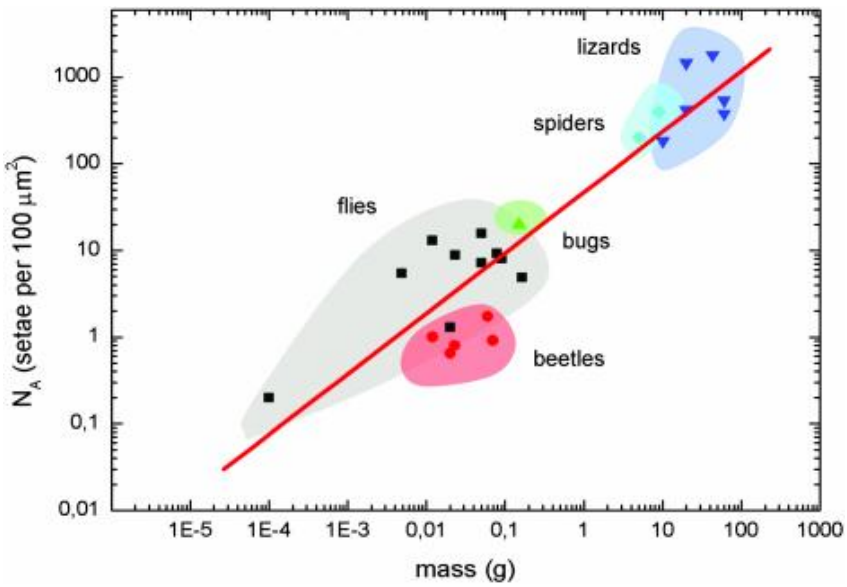

Figure 2.29 Idealized arrangement of attachment system with spherical tip shape (radius R and spacing 2Λ) (from Artz et al. [127]).

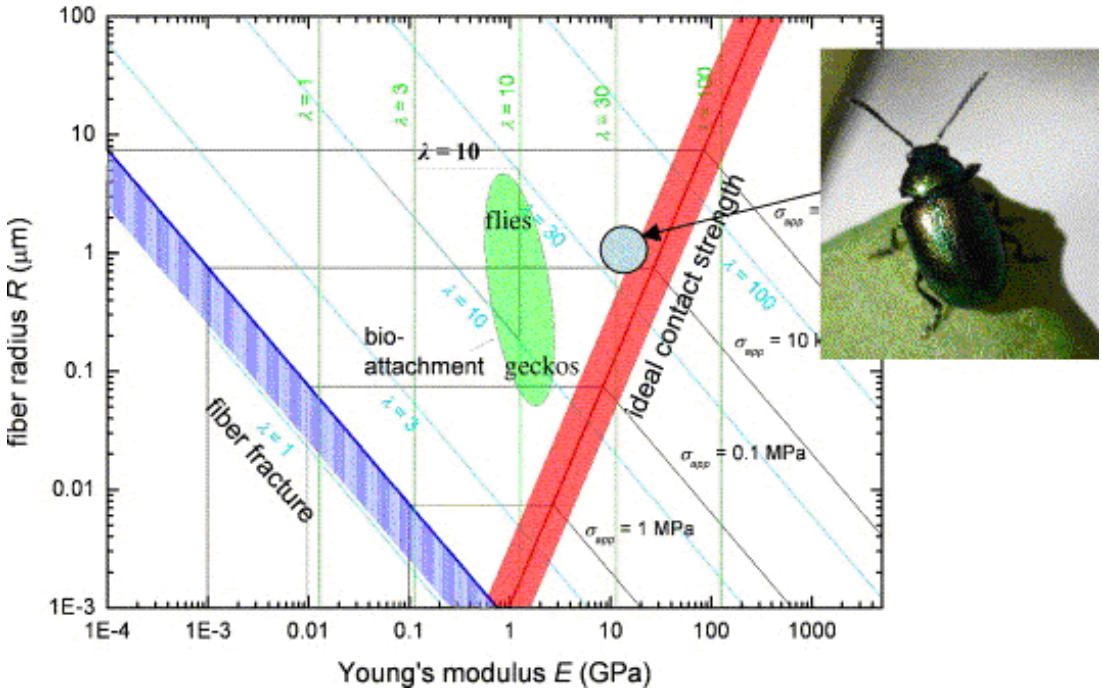

Figure 2.30 Partial adhesion map for a spherical tip shape; thin lines are contours of equal apparent contact strength; oval section represents regime of bioattachments [128].

Spolinek et al. [128] developed a design map that incorporated both the tensile strength of setae and the ideal contact strength. This plot is shown in Figure 2.30. It represents the fiber radius in the ordinate plotted against the Young's modulus in the abscissa. Two major lines define an inverted cone in which the system should be. The line with negative slope represents the failure of setae by tension and is obtained from the application of the theoretical strength (σ_{th}=E/10) to Eqn. 2.7. This results in:

$$R \geq \frac{3\gamma}{2\sigma_{th}} = \frac{15\gamma}{E} \tag{2.5}$$

The second line, on the right side, represents the ideal contact strength and is given by:

$$R \geq kE^2 \tag{2.6}$$

k is a parameter incorporating several dimensions. Indeed, the biological systems fall within the V region of the plot, showing that the calculations bracket the requirements well.

The biomimicking of this attachment principle is being implemented in synthetic systems. Whereas the paws of a gecko can generate adhesion forces of tens of N, much greater forces will be hopefully achieved in synthetic systems, and Spiderman is in the realm of reality.

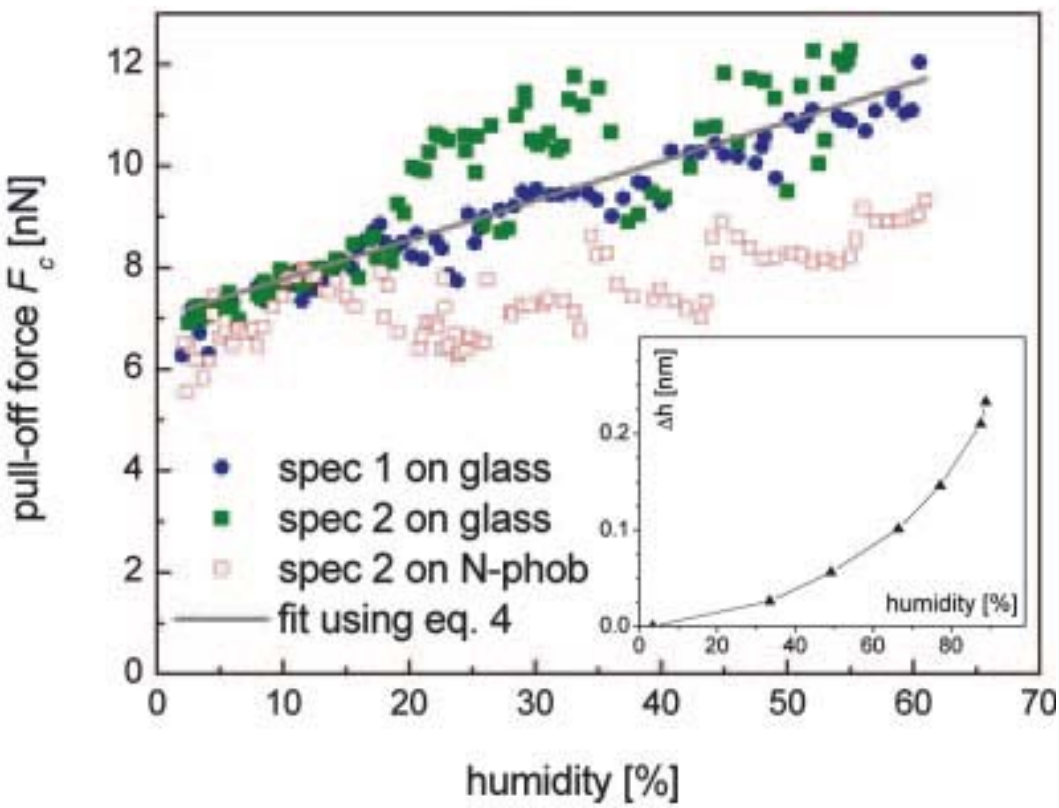

Figure 2.31 Pull-off forces of gecko spatulae on glass with varying humidity [129].

However, van der Waals forces are not complete story, and capillarity plays a role. The adhesion force of exerted by a single gecko spatula was measured by Huber et al. [129] after modifying the substrates. The seta of a gecko was glued to an AFM cantilever. Although work by Autumn et al. [123] indicated that the pull-off force did not increase with humidity, this is clearly evident in Figure 2.31. The results are expressed analytically as (eq. 4 in [129]):

$$F = F_{drag}\left(1 + 1.22Hg\sqrt{\frac{A_W}{A_S}}\right) \tag{2.7}$$

Where H is the humidity, g is a geometrical parameter (~1.2), A_W (3.7×10^{-20} J) and A_S (6.5×10^{-20} J) are the Hamaker constants for water and the substrate, respectively. They are represented as the straight line in Figure 2.31 which correlates very closely to the data points for the various spatula specimens. It can be seen that the pull off force increases linearly with the relative humidity, a clear indication that the capillarity plays a role in the adhesive force. It should be noted that at zero percent humidity there is still a significant force observed; this would indicate that van der Waals forces are present throughout the range of humidity variation, and that the effect of capillarity is seen by the additional adhesion thereafter.

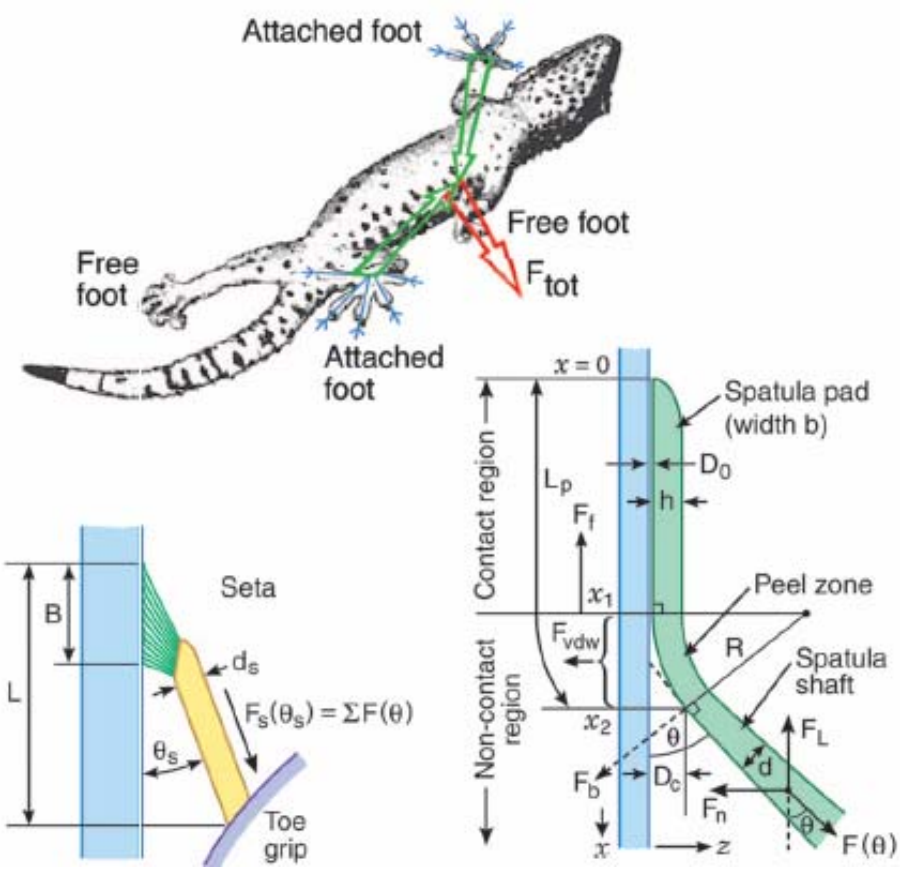

Figure 2.32 Force diagram of the toe pad of a gecko [142].

Another angle was introduced, as researchers began to examine the frictional effect which became obvious when looking at the natural loading pattern of the animal [130-132, 142]. Although a strong adhesive force could be created directly perpendicular to a given surface, the gecko often loads its toe pads parallel to a surface. Thus in addition to a "normal adhesion force" researchers began taking into account the "lateral friction force" imposed when the spatulae slide across a surface. Figure 2.32 taken from Tian et al. [142] provides a schematic representation of the various forces imposed during friction. They take into account the possibility of a peeling mode, which had been previously identified and characterized through the Kendall peeling model [133, 143-145] and incorporates an element of friction. Their results showed that by controlling the position and angle of loading a gecko could change both its lateral and normal adhesive force by up to three orders of magnitude. Figure 2.33 provides some experimental results from Autumn et al. [123] on the adhesive force parallel to a surface. It can be seen that a parallel maximum parallel force is obtained at around 200 μN.

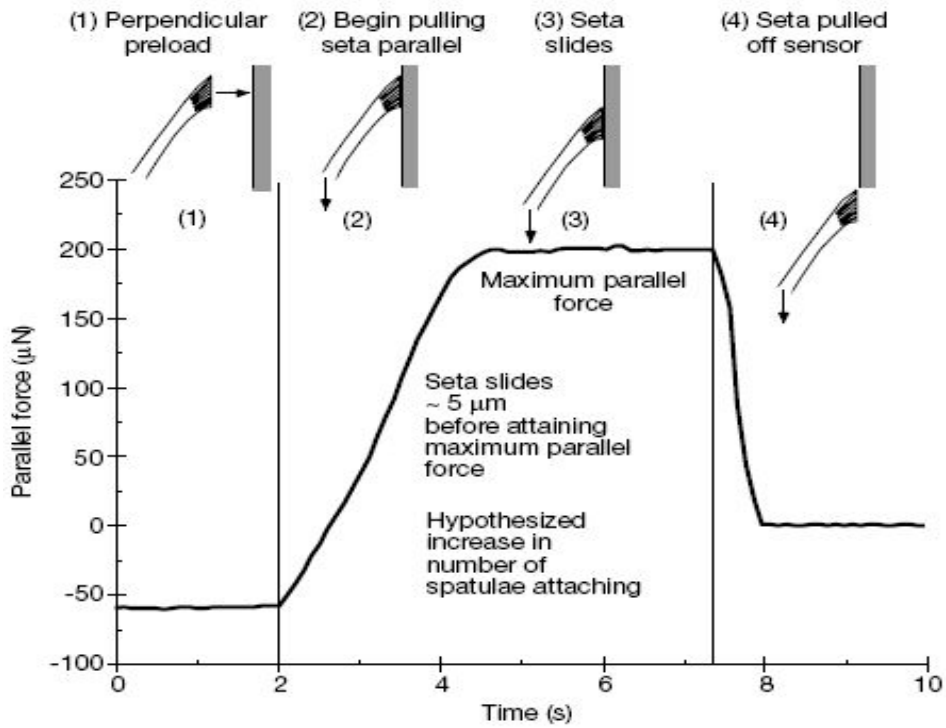

Figure 2.33 Force of single seta pulled parallel to surface (preload of 15 μN) [123]

Spolenak et al. [133] and del Campo et al. [134] further developed the initial models by correctly highlighting the effects of contact shape on the scaling of biological attachments. After conducting a series of theoretical assessments on various contact shapes they concluded that designs such as the toroidal contact geometry found in beetles and flies could in fact lead to better attachment. Figure 2.34 provides a series of images and schematic diagrams of contact shapes for various biological organisms and their possible evolutionary paths from the simple spherical extension of the bug *Pyrrhocoris apterus* to a more sophisticated suction cup employed by the male beetle *Dytiscus marginatus* on the vertical side of the foreleg tarsi.

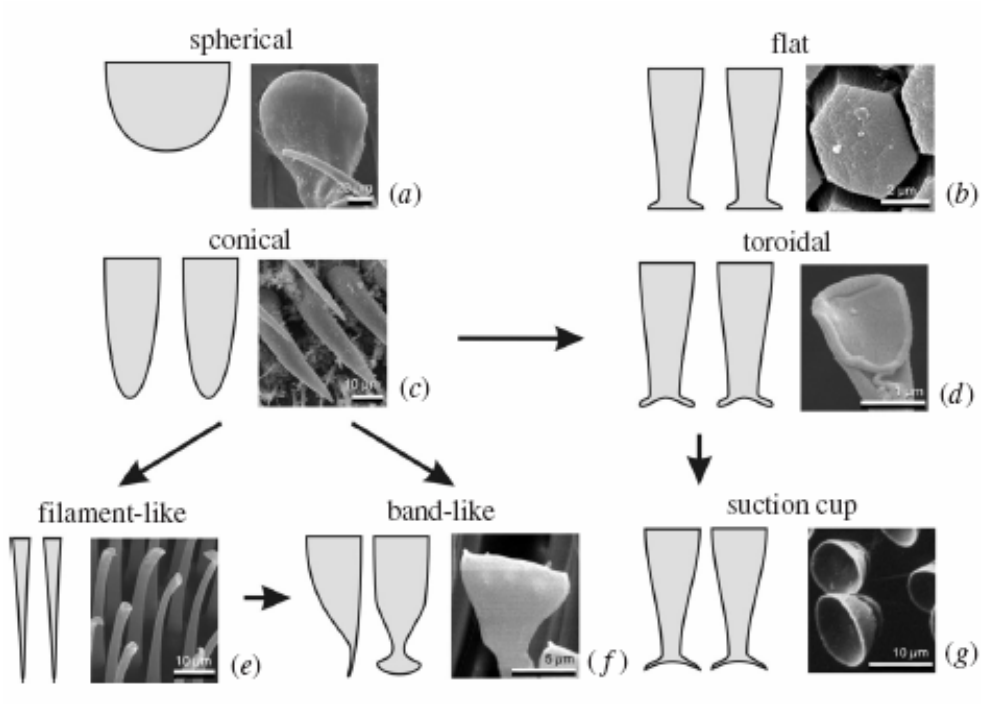

Figure 2.34 Shapes of attachment devices in nature and their hypothetical evolution paths indicated by arrows (Arzt et al. [133]).

The study of this attachment mechanism in nature has spawned a multitude of biomimetic advances employing the same nanofibrial contact mechanics but using synthetic materials [135-148]. In 2003 Geim et al. [135] microfabricated polyimide hairs (Figure 2.35 a) into a 1cm^2 organized array that was able to support approximately 3 N using the same mechanisms as that described above, van der Waals. Their first application was, of course, the attachment of a "spider-man" toy onto a horizontal glass surface (Figure 2.35 b). Although humorous, this initial proof of concept showed that synthetic tapes could be developed to employ the same mechanisms as those found in nature, and that it might be possible to further optimize their structures towards a broad range of applications.

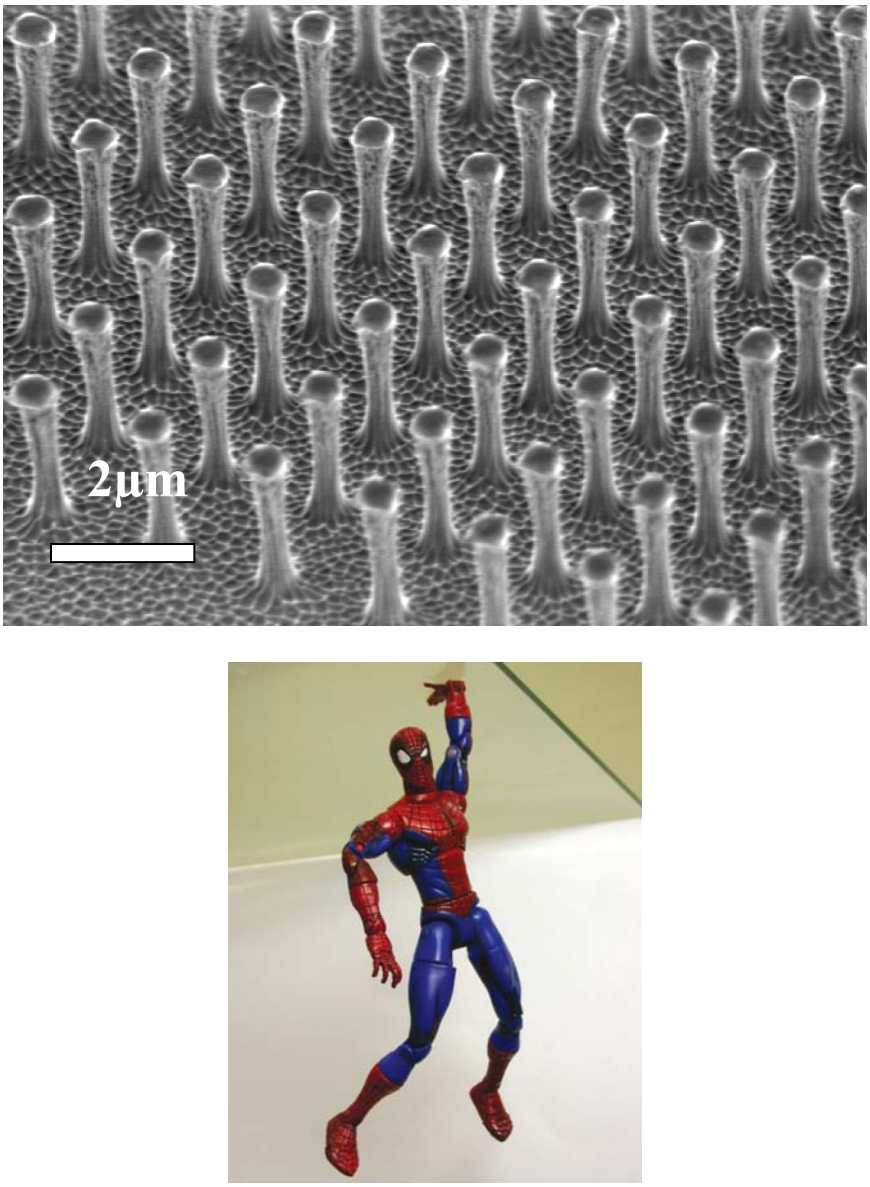

Figure 2.35 Synthetic gecko tape. (a) Scanning electron micrographs of microfabricated polyimide hairs in a 1cm^2 array, (b) re-attachable dry adhesives based on the gecko principle applied to a spider-man toy allowing it to cling to a horizontal glass plate. The toy weighed approximately 40g (Geim et al. [135]).

In the recent years this concept has become increasingly developed and will likely make a lasting impact on the science of adhesion. It will be seen in the following chapters that this mechanism is not only limited to dry applications, however may have useful contributions to wet environments, such as in biomedical or marine engineering. In fact efforts to create a biodegradable and biocompatible nanofibrial adhesive are already underway (see Figure 2.36 [200]).

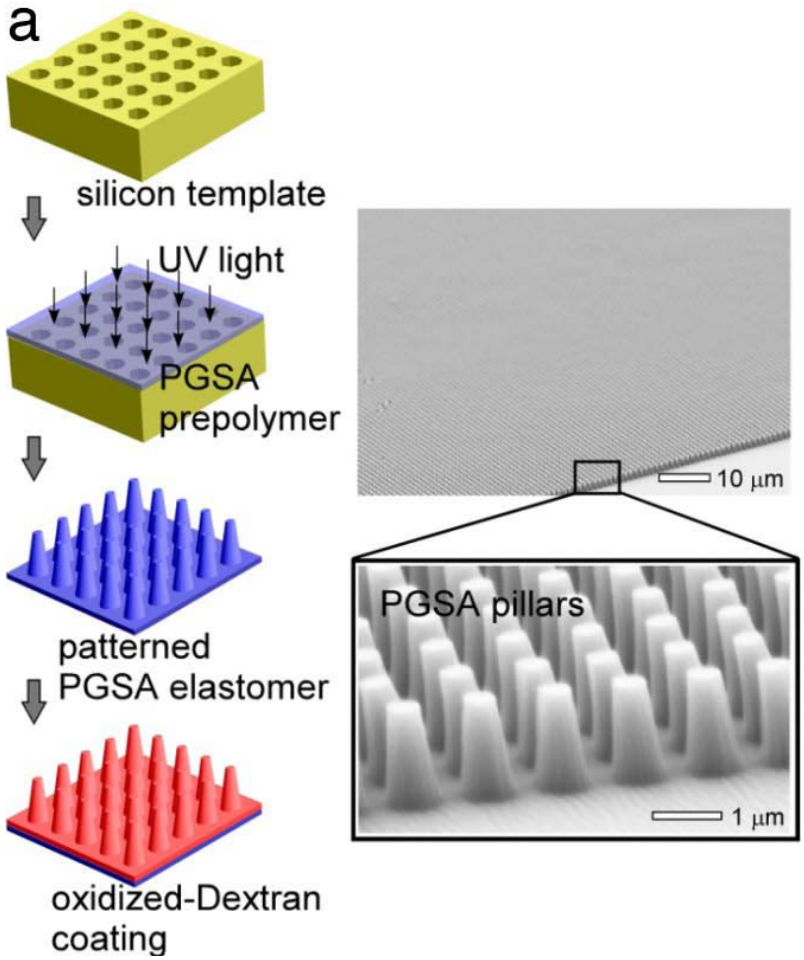

Figure 2.36 Nanomolding PGSA pillarse by photocuring the prepolymer under UV light followed by removal of the patternand subsequent spin coating of DXTA on the surface of the pillars (Karp et al. [200]).

CHAPTER 3

EXPERIMENTAL METHODS

This chapter will focus on the various experimental methods throughout the completion of this doctorial study.

3.1 Live Specimen Culturing Facilities

A 150-gallon tank with chilled salt water (~16^0 C) in a closed system was initially set up in the laboratory (Figure 3.1 (a)). Both red and green abalone were transported from the open water facility (Marine Bioculture, in Leucadia, CA) to the laboratory and subjected to experiments. The abalones were fed *microcistus* and *agregia* seaweed on a regulated schedule.

Within six months of this initial research a space in the Hubbs Hall laboratory at the Scripps Institution of Oceanography was acquired. The animals were then transported from the closed water system into a larger open water system (Figure 3.1 (b)), where sea water is directly cycled from the Pacific Ocean. These tanks were subdivided into pods which were used separate and house individual animals. The animals continue to be fed giant kelp (*Macrocystis pyrifera*) on a regular schedule which is collected courtesy of Mr. E. Kisfaludy from the Pacific Ocean. The holding tanks are curtained, limiting the exposure to exterior lighting, creating a similar ambiance to the natural habitat of both red and green abalone (10-30 meters below sea level). Wild abalones were collected from the Pacific Ocean courtesy of Mr. E. Kisfaludy from the Scripps Institute of Oceanography.

(a)

(b)

Figure 3.1 Abalone culturing facilities at: (a) MAE department of UCSD; (b) the Scripps Institution of Oceanography, at UCSD.

3.2 Structural Characterization

3.2.1 Scanning Electron Microscopy Observations on the Structure of Nacre:

A major component of this research was structural observations enabled through a Phillips XL30 environmental scanning electron microscopy (ESEM). Thus it becomes relevant to discuss some of aspects of this technique, its limiting factors, and how it was used to characterize the various biological materials studied here.

SEM images are generated through the detection of secondary and backscattered electrons as they are emitted from a sample which is bombarded with a highly focused scanning electron beam. Thus it is necessary for the sample to be conductive; this is either facilitated through a metallization of the sample with gold plating (invisible to the SEM detector) or the use of water vapor, as done in Environmental or Low Vacuum SEM. Localized heating of the observation site is often a limiting factor with organic samples, and often lead to structural damage. This was negated through increased metallization, or the use of ESEM. A backscatter detector can be enabled to provide atomic density characterization, in these samples the lighter images have higher atomic density.

Initial observations were conducted on cross sectional samples of nacre that were prepared from shells varying in length from 10 mm to 50 mm and finally 200 mm. These shells were fractured through blunt impact (a hammer) and mounted on using electrically conductive tape SEM sample holders. Samples were then coated with a thin film of gold using a gold sputtering machine. Some of the cross sectional samples were polished before examination; however many were examined along the natural fracture surface.

To observe mineral bridges between individual tiles, nacre was fractured in tension parallel to the direction of growth. Cylindrical pucks were drilled with 3 mm diameters from fresh nacre and glued onto tensile testing platens using J-B weld epoxy resin and left to cure for 24 hours. After fracture by tension a common deproteination technique was applied to remove the organic component of the shell. This will be discussed in *Section 3.2.5.*

In order to study the growth characteristics of nacre under varying feeding and environmental characteristics, a selected number of animals were subjected to starvation for certain periods of time. Specimens from this group were removed from the holding tank for a period of less then an hour before SEM examination. The animals were removed from their shells and the shells were sectioned using a Struers high speed diamond saw. These samples were observed along the cross section (aragonite *a* and *b* axes) as well as growth surface (aragonite *c* growth axis).

Further characterization of growth interruption periods were conducted through SEM observations on flat pearl and trepanning samples; this technique is described in detail in *Section 3.4.*

Both an environmental SEM (FEI) at Scripps Institute of Oceanography (SIO) with accelerating voltages of 15-20 kV and a field emission SEM (FEI) with EDS at the Nano3 Laboratory in CalT2 were used for characterization.

3.2.2 EDTA Demineralization of Nacre:

A common process of demineralization was employed using Sodium Ethylene Diaminetetreacetic Acid (EDTA). Thin slices of nacre were sectioned from freshly

collected abalone shells and placed in a solution of 1g EDTA in 200ml buffer solution of pH 7. These samples were placed in glass beakers and left on a rocker table for up to 4 weeks. Fully demineralized samples can be seen in Figure 3.2; the larger strips represent the organic growthbands separating mesolayers of tiled aragonite.

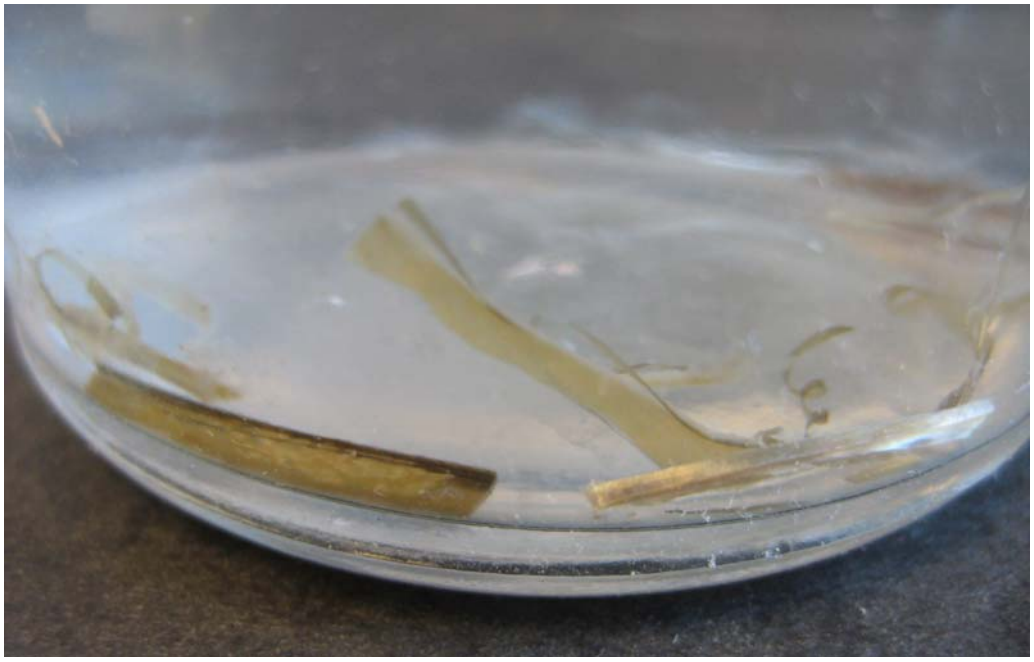

Figure 3.2 Demineralized nacre in Sodium Ethylene Diaminetetreacetic Acid (EDTA)

3.2.3 Atomic Force Microscopy:

Samples were prepared from both demineralized nacre, and implanted growth surfaces for observations through Atomic Force Microscopy. Two instruments were used; a Veeco Scanning Probe Microscope located at the Nano3 Laboratory in CalT2, and an Atomic Force Microscope in Dr. Christine Orme's Laboratory at the Lawrence Livermore National Laboratory (LLNL) with the help of Ph.D. candidate Julia Muyco.

3.2.4 Heating:

5mm cubic samples of nacre were heated to varying temperatures ranging from 150°C-750°C at a rate of 20°C/min using a Centurion VPM vacuum furnace in Professor Joanna Mckittrick's laboratory at UCSD. They were held at the maximum temperature for five minutes and then brought back down to ambient temperature. Each sample was taken from naturally grown abalone shells which were collected off the shores of Southern California (courtesy of Eddie Kisfaludy). They were air dried then cut into approximately 5 mm cubes along the nacreous region. The outer surface of shell was polished off by hand. Each sample was weighed and measured before heating.

3.2.5 Deproteination:

The fracture surface was immersed directly into 10 ml of hydrazine (98.5%) at room temperature for periods of 1, 2, and 9 hours to remove the organic component of the tiled structure. The samples were then serially diluted with absolute ethanol under 5 min increments of increasing concentrations of ethanol at 50%, 75%, 87.5% and then 100%. After air drying, the samples were gold plated and observed by SEM.

3.2.6 Transmission Electron Microscopy:

Transmission electron microscopy was conducted on nacre perpendicular to the direction of growth. Thin slices of nacre were sectioned using a high-speed diamond saw, then ground into 3 mm diameter circular slides by hand. They were mechanically dimpled to a minimum thickness of 100 μm using a model D500 Dimpler © then glued onto copper support grids using super glue. Ion milling then polished the samples to perforation using an ion mill with a voltage of 5.5 kV and a current of 0.5 mA.

Observations were made using a FEI 200 kV Sphera microscope. Both transmission images and selected area diffraction patterns were obtained. Figure 3.3 shows a typical sample after preparation. The copper support grid can be seen through the thin translucent nacre, while growth bands are still prominently identifiable as the dark lines running through the sample.

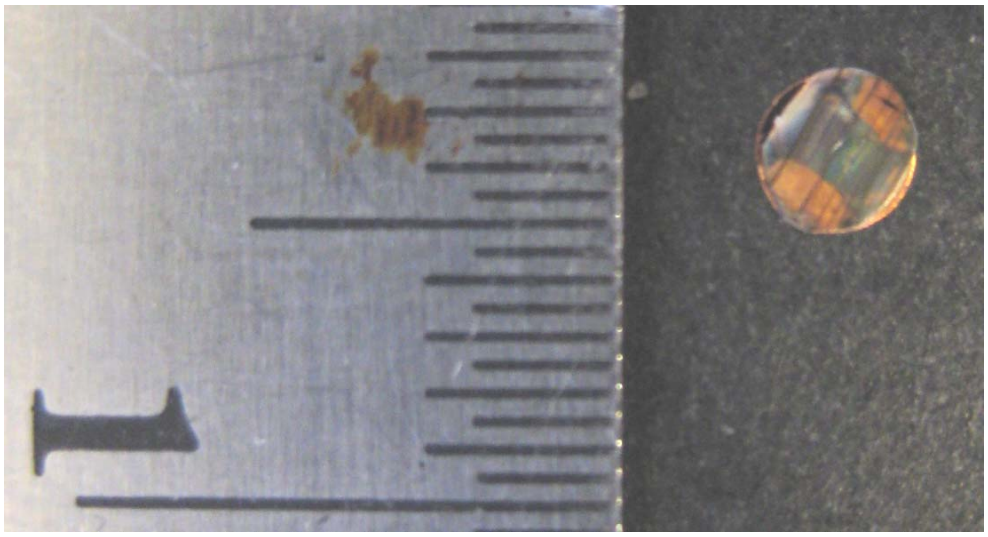

Figure 3.3 Ion milled 3 mm diamter TEM sample of nacre perpendicular to growth bands, a copper support grid can be seen through the sample.

3.2.7 X-ray Diffraction:

Nacre samples were ground into a powder, first using a ball mill, then by hand with a mortar/pistol. X-ray diffraction was carried out on these powders to confirm the elemental compounds present in nacre.

3.2.8 Raman Spectroscopy:

A Renishaw Raman Spectrometer in Professor Frank Talke's laboratory at the Center for Magnetic Research and Recording (CMRR), at UCSD was used to determine the composition of the various biological materials. Samples were placed under a 514.4 nm wavelength laser with a beam energy of 1 mW.

3.2.9 Critical Point Drying:

Samples of abalone tissue were sectioned from live abalone and placed in 10% formaldehyde for 2 days. They were then flushed with 20%, 40%, 60%, 80%, and 100% Ethanol for periods exceeding 45 minutes at each stage. They were then placed in a critical point drying machine (see Figure 3.4) and soaked in liquid CO_2 under high pressure. The temperature of the critical point chamber was then raised to the point in which liquid CO_2 instantaneously turned into vapor, leaving dried but not deformed tissue.

Figure 3.4 Critical point drying apparatus at Scripps Institution of Oceanography.

3.3 Mechanical Testing of Nacre

3.3.1 Nanoindentation:

Nanoindentation was carried out both in "wet mode" and in "dry mode" for demineralized and dry polished samples respectively in Dr. Andrea Hodge's Laboratory at the Lawrence Livermore National Laboratory (LLNL).

Wet samples of demineralized nacre were sectioned and attached with *SuperGlue*® to a plastic substrate. The sample was kept hydrated in a buffer solution of a pH of approx 7 within a raised container depicted bellow in Figure 3.5.

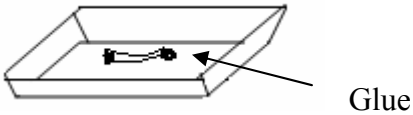

Figure 3.5 Sample container for nanoindentation.

Samples of dry nacre were tested in two directions of growth (a) parallel to the growth direction (along the a/b-axis), and (b) perpendicular to the growth direction (indenting into the c-axis). They were removed from freshly sacrificed animals and mounted in an epoxy mold to be polished to the 0.3 μm wheel.

Nanoindentation and nanoscratch tests were also carried out in Professor Talke's Laboratory in the Center for Magnetic Research and Recording at UCSD with the help of Ralf Brunner. Samples from freshly removed growth implantations were subjected to scratch tests with the aim of producing nanoscale shear measurements of individual tiles.

3.3.2 Quasi-static Mechanical Testing:

An Instron screw driven testing frame was used to obtain the mechanical properties of bulk nacre. Sections of the tiled aragonite region of nacre were carefully cut into compression, tension, shear, and dog-bone samples using a Struers high speed diamond saw. Great care was taken to ensure parallel planes on opposing sides of compression samples. The samples were tested in compression with a strain rate control of 0.05 min^{-1}.

To measure the tensile strength of the shell in the direction perpendicular to the planes of growth 3mm diameter pucks were drilled out of fresh nacre using a diamond coring drill. This was done under continuous irrigation with chilled water. The calcite layer was ground away until the entire thickness consisted exclusively of aragonite tiles. Two methods were used for tensile testing of the nacre with loading perpendicular to the plane of the tiles. The upper and lower surfaces of the specimens were glued to aluminum holders using JB weld and allowed to cure for 24 hours with the loading assembly in place (sample can be seen in Figure 3.6). The assembly was either mounted in an Instron testing machine through two adjustable clamps or at the extremity of a cantilever beam so that no bending was applied to the specimen. The breaking load was determined and the surfaces characterized directly afterward through SEM.

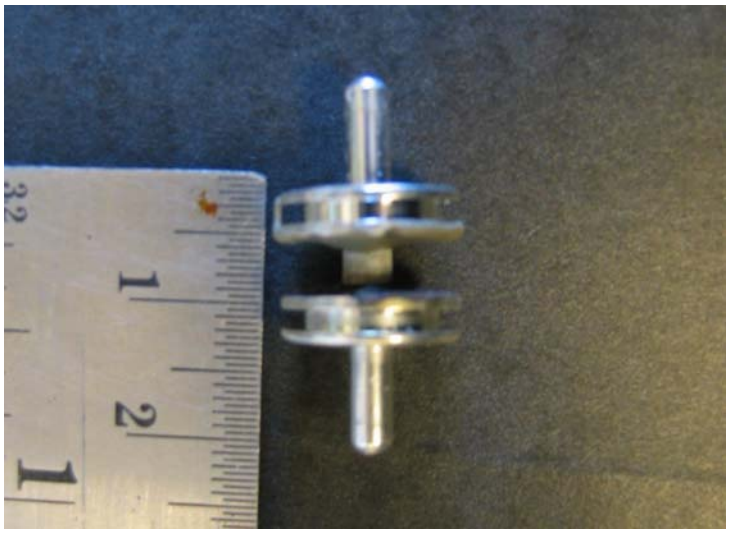

Figure 3.6 Testing set up of nacre being pulled in tension parallel to the plane of growth.

Shear tests were developed to complement previous work by Menig et al [32]. A shear testing mount was designed with an "S" spacing of less then 300µm so that the material was tested between the mesolayers and not across them. The steel mount can be seen in Figure 3.7, it is composed of two sliding pistons within a cylindrical sleeve. The specimen is loaded in the empty cubic space in the center of the device, with the growth planes parallel the direction of loading.

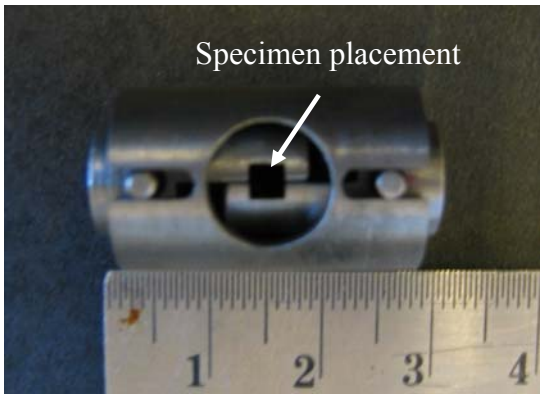

Figure 3.7 Shear testing mount, specimens are placed in the space indicated above.

Dog-bone samples were created to test the nacre in parallel to the planes of growth. These samples were made by carefully polishing the nacre section of the shell into flat plates. Two methods were implemented to obtain the dog-bone shape; plates were first sectioned into individual rectangles and either placed: (a) between a steel mold of a dog-bone sample silhouette, or (b) taken to a laser cam machine to be laser cut. The silhouette was sanded down with a small hand file, resulting in a nacre dog bone sample. The laser cuts however resulted in localized heating of the sample and loss of mechanical properties. These were left in sea water before testing to maintain hydration (see Figure 3.8 a). Each sample was then mounted in the device seen in Figure 3.8 b to be pulled in tension.

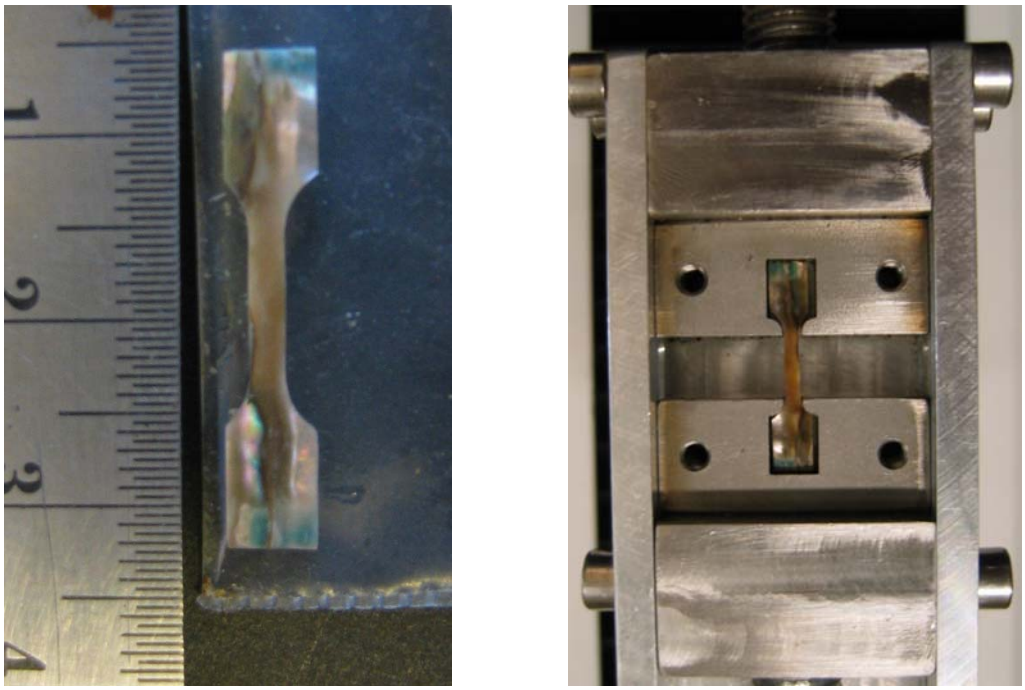

(a) (b)

Figure 3.8 Dog-bone mechanical tensile tests on abalone nacre: (a) dog-bone shaped sample of nacre hydrated in saltwater; (b) dog-bone shaped testing mount.

3.3.3 Dynamic Mechanical Testing:

Samples were cut into rectangular prisms of approximately 6.6 x 6.6 x 10 mm in different orientations with respect the shell layers. A Hopkinson bar with pulse-shaping [149] courtesy of KS Vecchio was used to perform high strain rate loading. Strain rates were between 200 and 500 s^{-1}.

3.4 Growth Implantation: Flat Pearl and Trepanning Techniques

Both the "flat pearl" technique, first introduced by Wada et al. [76,77] then further developed by the UC Santa Barbara group [86], and the "trepanning" technique in which foreign sections of nacre are introduced into the growth surface were used to observe the various formations and morphological transitions following steady state growth interruption [120].

3.4.1 Flat Pearl:

Glass slides 15 mm in diameter and TEM grids (nickel grid with Formvar coating) 3 mm in diameter were glued (only one spot using 5 minute epoxy or superglue®) to the growth surface of the shells. Various locations were selected throughout the shell to observe any position dependency. The growth surface of each shell was exposed by gently pushing back the mantle layer in the inside of the shell using a flat stainless steel scalpel with rounded, dull edges. No copper was used in the process because of the negative reaction abalones have with the metal. It was observed that the retracted mantle, exposing the extrapallial space, took a few days to relax back to its original position covering the glass slides. The growth was monitored by extracting glass

slides and TEM grids after three separate periods of embedment: 7, 14, and 24 days. Several days are required before the mantle reposition itself over the glass slide. Hence, the numbers above should be corrected for this time, which is typically 2-4 days. SEM observation slides were examined immediately after removal in order to maintain hydration of the organic matrix. Before examination each slide was washed in purified water to remove salt build up. (Note: it was observed that the coloration of slides after prolonged SEM observation changed from translucent to transparent).

3.4.2 Trepanning:

A second implantation experiment was carried out simultaneously in which a foreign substrate of abalone nacre was polished, destroying its original growth surfaces, and implanted onto the growth surface of a live abalone. Pucks of nacre, 3 mm in diameter, were drilled from fresh abalone shells using a diamond coring drill. Holes, slightly larger than 3 mm were then drilled in the shells of live abalone allowing a press fit of samples into designated positions along the growth surface. During this process the drilled area was continuously irrigated and cooled with chilled sea water (see Figure 3.9). Care was taken to physically retract the living tissue of the animal from the drilling site; this was done using a flat stainless steel scalpel. Multiple samples were placed in each shell so that they could be sequentially removed at one week intervals.

Figure 3.9 Drilling of trepanning holes in live abalone using a coring drill while being irrigated with chilled sea water.

This method of trepanning provided a natural substrate on which growth could restart. Although the implant surfaces were polished the surface activation energy of the implant and host nacre are similar being that they are the same material. The pucks were then left for periods of one to six weeks before being removed simultaneously with the above mentioned flat pearls.

Figure 3.10 illustrates both the flat pearl and the trepanning techniques on the shell of an abalone**.** In the upper left hand quadrant of the figure a fractured glass slide is depicted. These slides were glued onto the outer edge of the shell using beads of superglue®. The lower portion of the figure shows a 3mm puck sample as it is implanted into drilled holes along the shell growth surface.

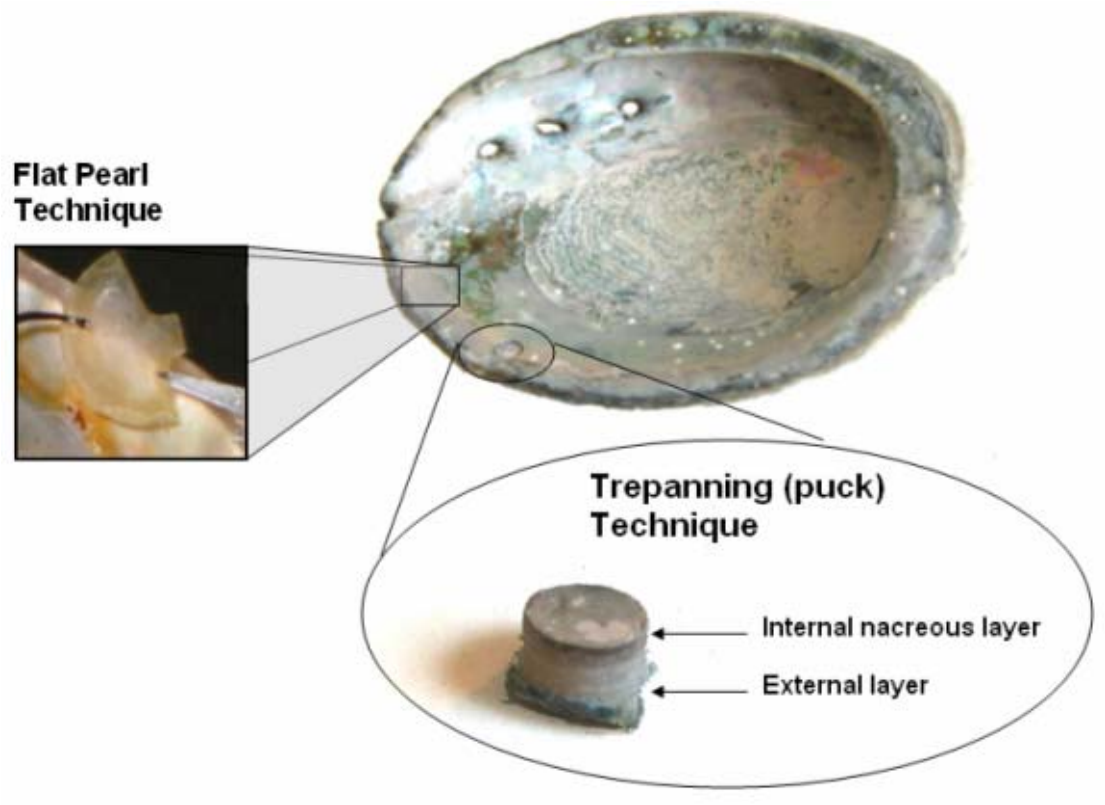

Figure 3.10 Implantation methods for growth experiments.

3.4.3 Crystal Nucleation:

Crystal nucleation was attempted in a supersaturated solution of $CaCO_3$ on demineralized surfaces. This was done by placing organic material in a solution and allowing the solution to "crash" out of saturation. This was not found in initial runs but could have been attributed to traces of phosphate buffer on organic material. Phosphate reacts poorly with $CaCO_3$.

3.5 Attachment Measurements

3.5.1 Bulk Mechanical Testing:

Live red abalone were held in an open water facility in the Hubbs Hall Laboratory at the Scripps Institute of Oceanography, La Jolla, CA prior to bulk mechanical testing of the pull-off force. Two techniques were used to measure the pull-off force of a single live abalone. A three-pronged steel jaw was used to clamp the shell of abalones which averaged 5.5 x 10^{-3} meters^2 foot area. Initially animals were transferred into a testing chamber which was filled with chilled sea water. This chamber could be attached as an instillation on the bottom platen of an Instron screw driven tensile testing frame. The three-pronged jaw could also be attached to the upper platen of the testing frame. Animals were securely clamped to the jaw device and lowered onto the bottom surface (made from acrylic) of the testing chamber. When the abalone came into contact with the bottom surface it was allowed to "set" for an approximately 30 seconds before the load cell was placed in high strain rate tension. The setup in which a live abalone is submerged into a saltwater filled testing chamber can be seen in Figure 3.11. The dynamic nature of abalone attachment loading was such that the quasi-static screw driven device was overly sensitive to obtain any significant results. Furthermore, localized warming of the chamber resulted in an abnormal environment for the animal; thus, specimens became lethargic and unsuitable for testing before measurements were taken. It quickly became clear that the animals needed to be tested in their natural environment, or at least in the environment in which they had adapted to.

Figure 3.11 Bulk mechanical testing of live abalone pull-off force using Instron screw driven tensile testing device.

A second technique was used in which the pronged steel jaw was clamped the shell of abalones while they remained in their permanent holding facility at Hubbs Hall. This proved to provide a more accurate assessment technique for attachment, as the subjects were allowed to remain undisturbed before testing. The other end was attached to a cable that was fed through a pulley to a platform on which the weights were incrementally placed. The schematic illustration in Figure 3.12 shows the configuration

of the testing setup. The detachment force was measured on a smooth, painted tank in which the abalone had been held for over a year before testing.

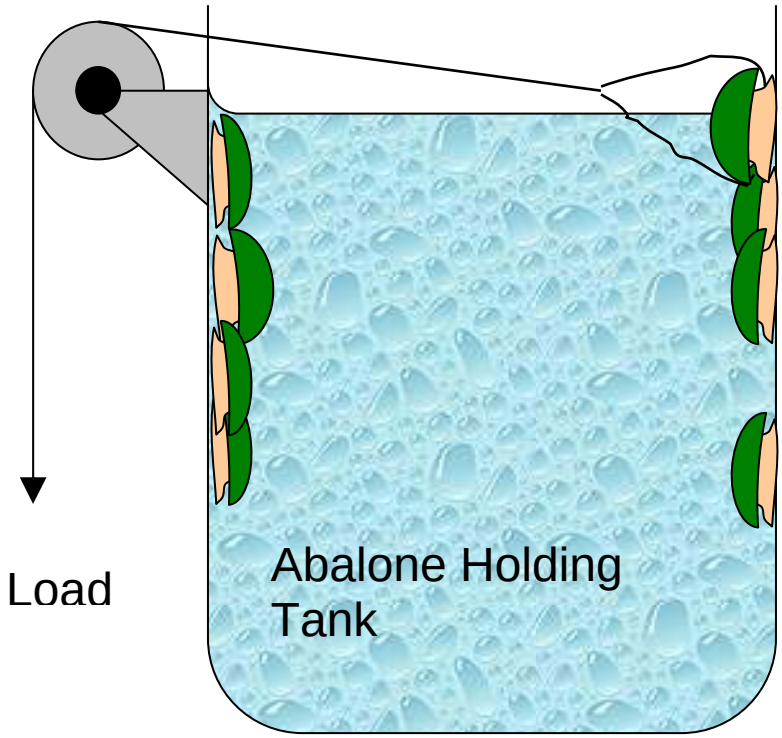

Figure 3.12 Bulk mechanical testing of live abalone pull-off force in tank.

3.5.2 Structural Characterization of Abalone Foot:

Tissue from the foot of the red abalone was removed from live or freshly sacrificed specimens and fixed in formaldehyde. Samples were removed from both freshly detached animals, or animals still attached to kelp. The later was done by allowing an abalone to attach itself to a kelp leaf while alive, then scooping it out of its shell and sacrificing it in its attached state. It should be noted that animals could still

exert a significant attachment force onto kelp, post mortem. After the muscle had relaxed the kelp and foot tissue were sectioned together and fixed (while still attached) in formaldehyde. All samples were then critically point dried and examined using SEM.

3.5.3 Preparation of Single Seta:

Samples of tissue from the foot of the abalone were removed from live abalone and fixed in formaldehyde, then dried through Critical Point Drying (a process in which the liquid to vapour transition is negated, allowing preservation of sample structure (Figure 3.13 a)). Single abalone setae were attached to AFM cantilevers using an optical microscope and micrometer stage. Each seta was glued to the end of a calibrated cantilever (Veeco NP-20). The following procedure was used for testing. First, the AFM tip was brought into contact with the tip of a needle covered with UV-hardening glue, allowing glue to cover the tip of the cantilever. Thereafter, the tip of the cantilever was positioned over a single seta on the abalone foot tissue, Figure 3.13 b. When the seta was in contact with the cantilever tip, UV light was used to harden the glue, thereby firmly connecting the seta to the cantilever tip. Finally, the seta was sheared off the abalone foot. An SEM image of a single seta on a cantilever beam is shown in Figure 3.13 c.

(a)

(b)

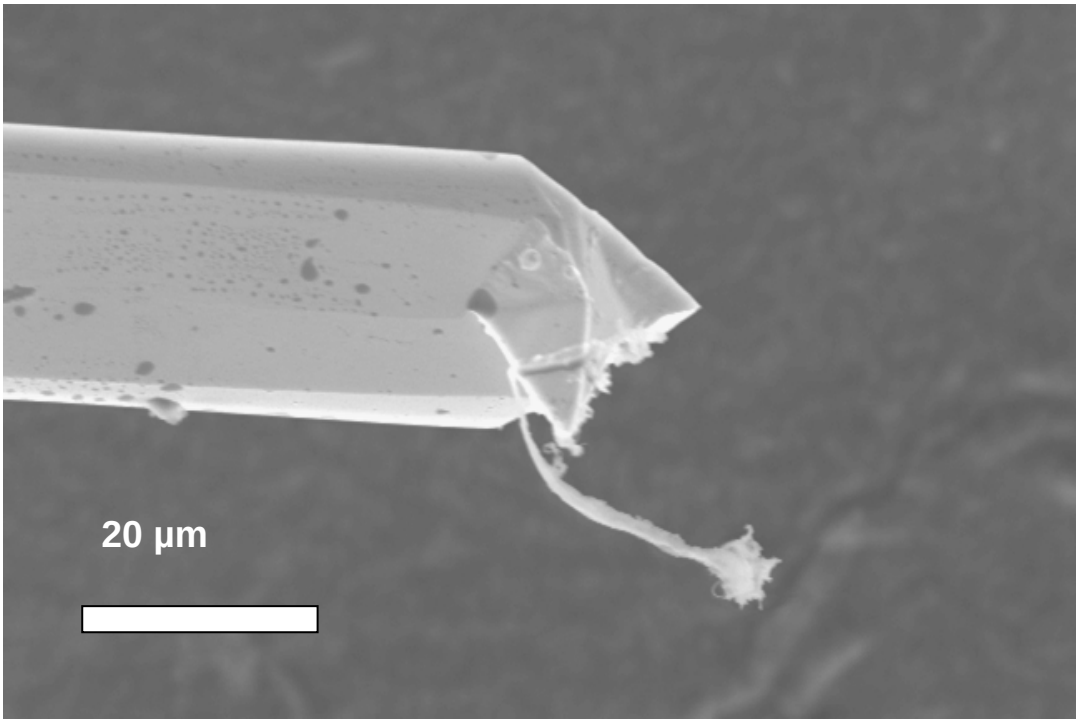

(c)

Figure 3.13 Preparation of a single seta: (a) removal of tissue; (b) attachment of seta onto AFM cantilever; (c) SEM image of single seta on cantilever beam.

3.5.4 Force Estimation of a Single Seta During PerpendicularPull:

The pull-off force perpendicular to the substrate surface was measured using a contact silicon cantilever. The spring constant of the cantilever was 0.58 N/m. The AFM was placed in a sealed enclosure to allow controlled humidity variation within testing environment.

Force-distance measurements were used to determine the pull-off force as follows (typical test results shown in Figure 3.14). First, the seta was brought into close proximity to the testing surface. This distance was reduced (points A–B) until the AFM tip "snaps" into contact (point B). Further approach of the AFM tip towards the surface causes perpendicular preloading of the seta onto the silicone substrate (point C). After reaching point C, the tip was retracted from the surface until the pull-off force exceeds the adhesion force between the seta and the surface (point E). At that point the AFM tip separates from the surface (line E-F). The cantilever deflection between E and F can provide a qualitative measure for the adhesion force at the interface.

Measurements were conducted for values between 10% and 74% humidity to study the effect of humidity on possible capillary forces. Dry nitrogen was introduced in the sealed AFM chamber to reduce the humidity. A hygroscope was placed close to the sample to measure humidity throughout testing. Testing perpendicular to a hydrophilic (silicon oxide) and a hydrophobic (carbon coated thin film disks) substrate was measured using a contact silicon cantilever with a spring constant of 0.58 N/m.

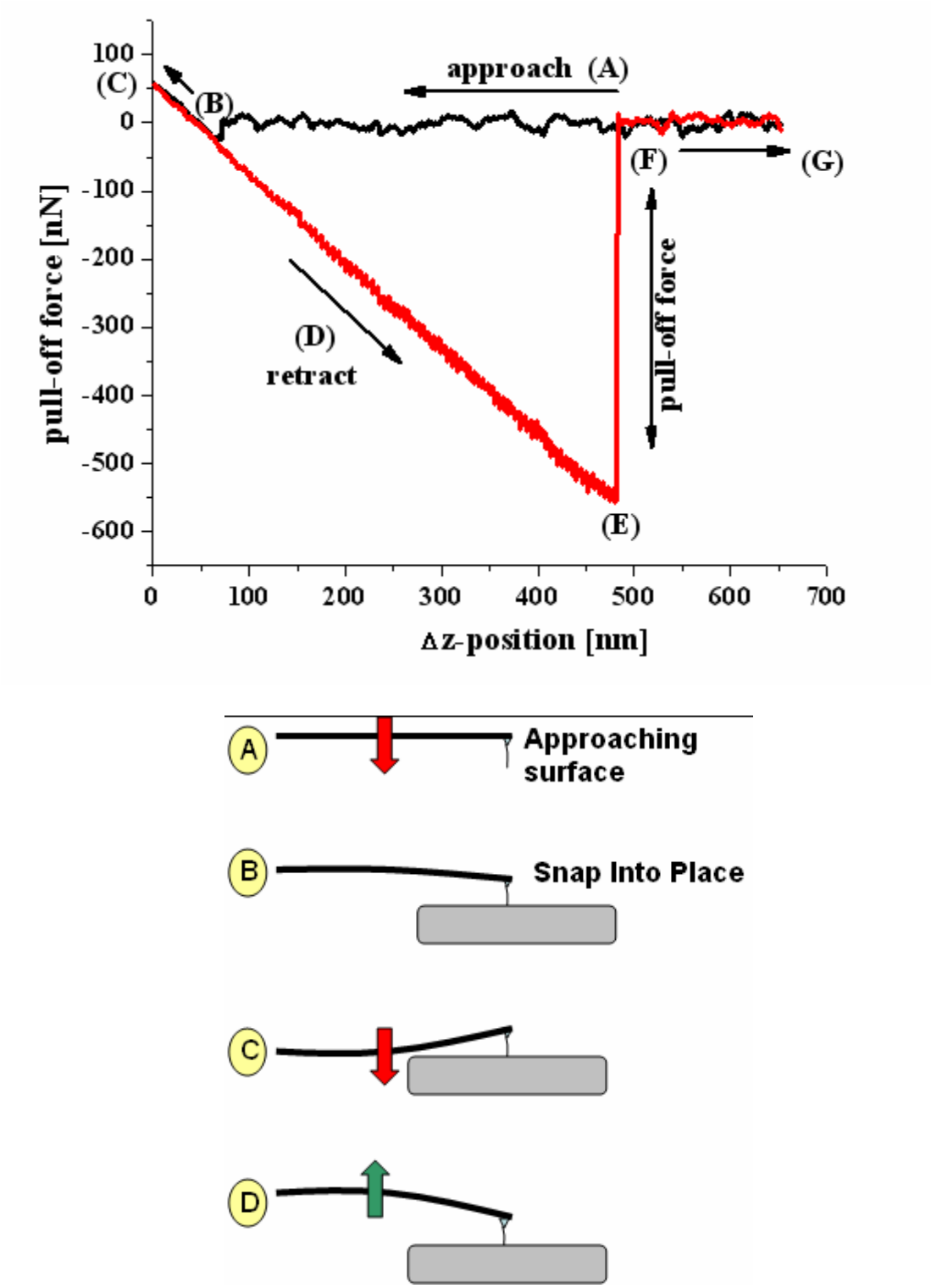

Figure 3.14 Force-distance measurements used to determine the pull-off force.

CHAPTER 4

RESULTS AND DISCUSSION

Because of the broad nature of this study the following chapter has been sectioned into three main components: structure and mechanical properties of various biological materials, growth and biomineralization, and functional biological materials. An analysis and discussion of the results is presented within each subsection.

4.1 Structure and Mechanical Properties

4.1.1 The Nacre of the Abalone:

This section will describe the results of various mechanical tests performed on nacre and will attempt to identify the specific structural elements which may be responsible for the remarkable strength of this biological material. It will become clear that this composite material relies on its advanced structural hierarchy to create a level of strength and toughness that far exceeds its constituent materials.

4.1.1.1 Quasi-static Compression and Tension

Compression tests were conducted to confirm the results from previous studies by Menig et al. [32]. Figure 4.1 shows the Weibull analysis of nacre in quasi-static compression with load perpendicular to layers. When performing mechanical tests on natural materials such as mollusk shells, scatter in the experimental results is expected due to natural variations in microstructure and defects. Irregularities may include shell thickness, micro and macro cracks, invasion by burrowing organisms, curvature and variation in growth layers, cracks introduced by sample preparation, the age of the

material being tested, and structural differences due to location within the shell. Thus, it is necessary to use a statistical analysis to quantitatively evaluate the mechanical properties of these and other biological materials. While the Weibull distribution [41] is usually used for flexural strength and is representative of extreme-value statistics, here it is applied to a variety of quasi-static and dynamic compression data with intention of creating a clear picture from a scattered range of data points. The Weibull analysis [41] was applied by means of the equation:

$$F(V) = 1 - \exp\left[-\left(\frac{\sigma}{\sigma_0}\right)^m\right] \tag{4.1}$$

which can be transformed into:

$$\ln\ln\left[\frac{1}{1-F(V)}\right] = m(\ln\sigma - \ln\sigma_o) \tag{4.2}$$

F(V) is the failure probability, *m* is the Weibull modulus and σ_o is a characteristic strength. The parameters σ_o and *m* are experimentally obtained by plotting the two sides of Eqn. 4.2 and finding the value of lnσ when lnln(1/1-F) equals zero, and taking the slope the best fit line, respectively. The Weibull curve yields an S-shaped distribution from which the failure probability at a certain stress can be computed. In general we can describe the 50% failure probability as the characteristic strength of the material.

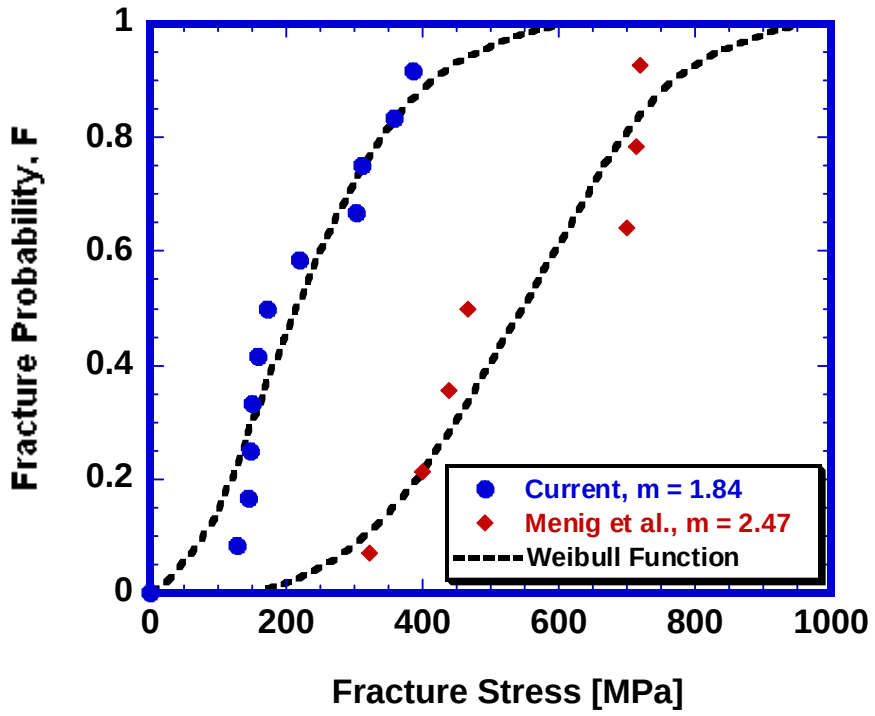

Figure 4.1 Compressive strength of freshly sectioned nacre perpendicular to layered structure.

The current results, presented in Figure 4.1, predict a 50 percent failure probability occurring at approximately 250 MPa for compression perpendicular to the layered structure. This is lower than previous results by Menig et al. [32] of approximately 540 MPa; however, both results are within one order of magnitude. It is not clear why the variation in results exists; yet, the tests were conducted on two separate testing apparati and samples were prepared from different sources such as fresh live abalone in this work, and older store bought shells in the previous study. Results from both tests are presented in the figure, the diamond makers represent the previous study [32], and the circular markers represent the current results. The dotted lines represent the

statistical Weibull curve that would correlate to these data points, a Weibull function "m" is found for each data point, 1.84 and 2.47 for the current and past studies respectively.

Figure 4.2 shows the Weibull analysis of nacre in tension perpendicular to the layered structure. This represents the results from the mechanical tests described in ***Section 3.3.2*** in which pucks of nacre were removed from the shell and mounted in cement glue then tested in tension. It should be noted that because of the nature of this loading direction, the results represent the weakest link between consecutive tile layers. Thus, a true average strength in this direction of loading will be shifted to the right of the plot by some unspecified amount, dependent on the strength variation between individual tile layers.

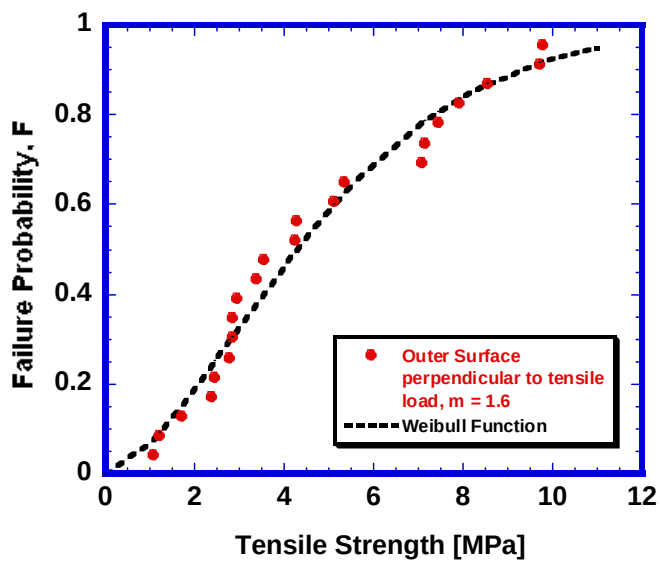

Figure 4.2 Weibull distribution of tensile strength perpendicular to layered structure [49].

The 50% failure probability was determined at only 3 MPa. The Weibull moduli in tension and compression are similar: 2 and 1.8–2.47, respectively. However, the difference in strength is dramatic and much higher than in conventional brittle materials. The ratio between compressive and tensile strength is on the order of 100, whereas brittle materials varies between 8 and 12. This difference is indeed striking, especially if one considers the tensile strength parallel to the layer plane found in previous studies is on the order of 140–170 MPa [38], which is approximately two-thirds the compressive strength. Other work by Barthelat et al. [68] found the tensile strength of nacre to be closer to 100 MPa, which is still just below one fifth the compressive strength.

New tensile tests were performed parallel to tile planes in quasi-static loading at a strain rate of 0.05 mm/min. "Dog-bone" shaped samples were sectioned from regions in which the shell had minimal curvature. Figure 4.3 shows the Weibull statistical analysis of the results obtained. The Weibull parameter was found to be 1.8. The plot shows a 50% failure probability when a load of approximately 65 MPa was applied. This is lower then the value of 170 MPa found through bending by Jackson et al. [38] and the value of 100 MPa found by Barthelat et al. [68] which may be due to imperfections introduced during sample preparation; however, it is still within reason to the previous studies and still only 3.6 times less then the compressive strength. It can be concluded that the shell sacrifices tensile strength in the perpendicular direction to the tiles to use it in the parallel direction.

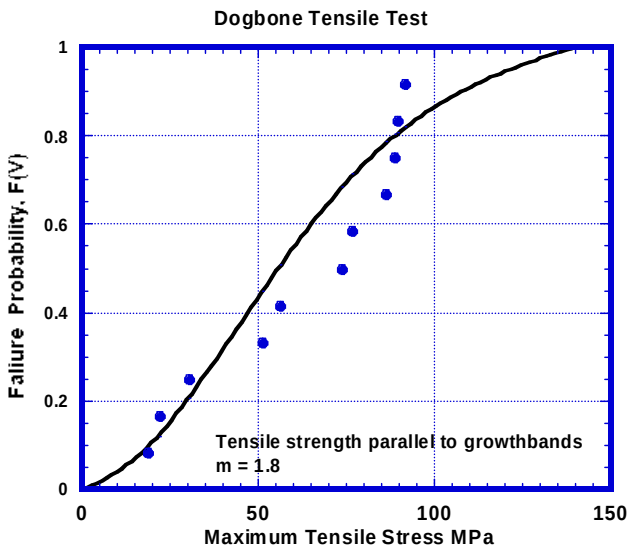

Figure 4.3 Weibull distribution of tensile loading parallel to layered structure.

In compression parallel to growth bands, a 50% failure probability of approximately 235 MPa was found; this is shown in Figure 4.4 .

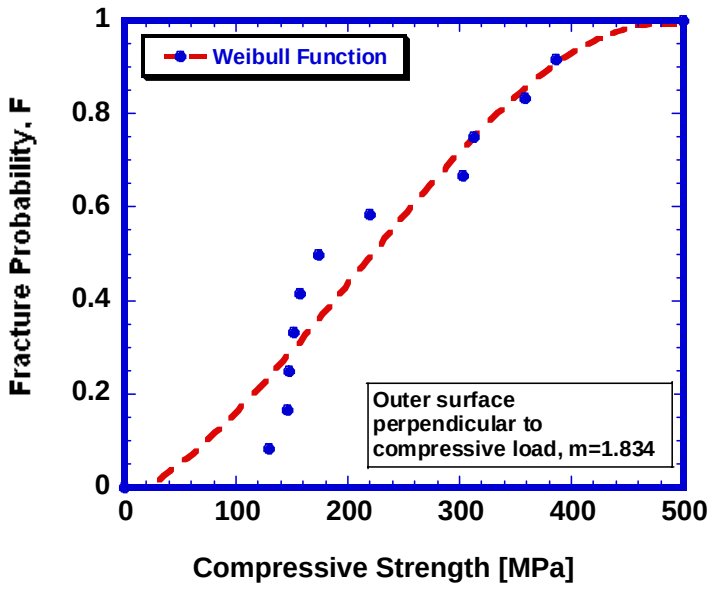

Figure 4.4 Weibull distribution of compressive loading parallel to layered structure.

This, in combination with the results previously described in *Section 2.1* provides a general picture of the mechanical anisotropy of nacre, summarized in Figure 4.5. The lines along the cube represent the growth bands which exist in naturally grown shells.

The unique strength anisotropy perpendicular to the layers (3-5 MPa vs. 540 MPa) is remarkable and will be discussed throughout this section. Another marked characteristic is the greater compressive strength when loading is applied perpendicular rather then parallel to the tiles. This is due to the phenomenon of axial splitting and microbuckling (kinking) when loading is applied parallel to the tiles; this was described earlier by Menig et al. [32] and discussed in *Section 2.1*. The relatively small difference in tensile and compressive strength (65-170 MPa vs. 235 MPa) in this direction of loading is directly related to the high toughness through tile interface shear. Both these aspects are discussed below.

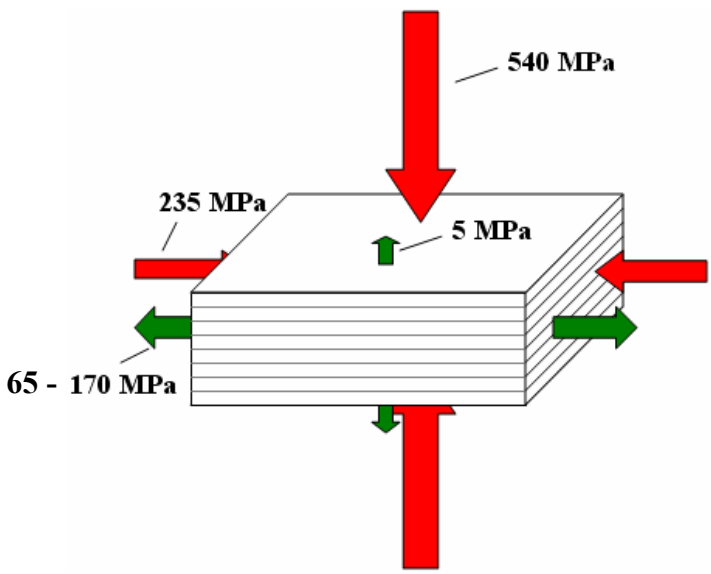

Figure 4.5 Strength of nacre with respect to loading direction, parallel lines represent growth bands (results are from freshly sectioned specimens).

4.1.1.2 Hardness and Nanoindentation

Nanoindentation was conducted along various sections of polished cross-sections of nacre. The nacre was tested in two directions of growth (a) parallel to the growth direction (along the a/b-axis), and (b) perpendicular to the growth direction (indenting into the c-axis). They were mounted and polished to the 0.3 μm wheel.

Figure 4.6 shows the data of a sample which has undergone nanoindentation parallel to the growth surface across various interfaces of a mesolayer. These interfaces have been broken into regions labeled A-E across the polished surface. Tile growth occurs from region "A" towards region "E". The sharp line between region A and B represents the uniform termination of tiled aragonite deposition followed by a large organic period (12 μm in thickness for the specific band seen in Figure 4.6. The mechanical response of the material is very consistent throughout the tiled aragonite region (region "A") with an elastic modulus of 94 GPa, approximately ten times that found in region "B" (9.8 GPa). This confirms the presence of an organic region, or at least a much softer region. The mean hardness in region "A" was also significantly higher then in region "B"; the values were found to be 3.12 GPa and .56 GPa, respectively. Regions "C" through "E" represent the transition section between amorphous aragonite nucleation into spherulitic aragonite bundles and finally into the steady state aragonite tiles. The mean modulus and mean hardness directly adjacent to the organic band were found to be 84 GPa and 3.1 GPa, respectively; however this region also showed the most variation in results as indicated with the relatively high standard deviation for both results. Moving to the left towards the re-initiation of steady state aragonite tile growth the mean modulus fluctuates between 60 and 80 GPa and the

hardness between 1.3 and 3.2 GPa yet these values remain close to an order of magnitude larger then those found in region “A”.

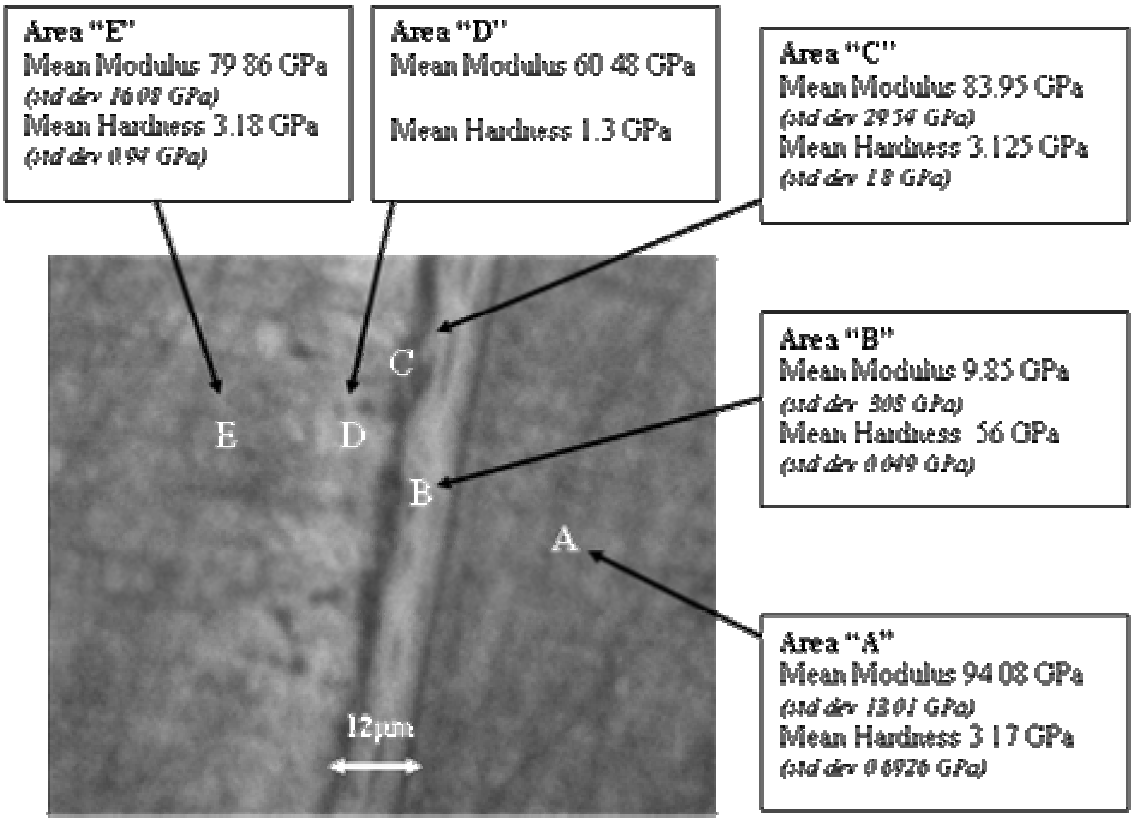

Figure 4.6 Nanoindentation data for dry polished nacre parallel to growth plane: region A and E represent tiled aragonite, while region B consists of the thick organic mesolayer. Region C and D represent the transitional period following mineral growth interruption.

Figure 4.7 shows the data for a sample which has undergone indentation perpendicular to the growth surface along a section which exposes the cross-section of a mesolayer. Two sections were tested in bulk runs, one across the interface and the other along the interface. This was done looking for any large deviations in average properties through this thin layer of organic material. Along the direction of growth (crossing

through the organic band) the mean modulus and the mean hardness were found to be approximately 70 GPa and 4.4 GPa respectively. When the bulk run of indentations was conducted parallel to the growth direction and along the organic band the two results dropped dramatically reconfirming the results described above. The mean modulus and the mean hardness in this case were approximately 22 GPa and 1.2 GPa.

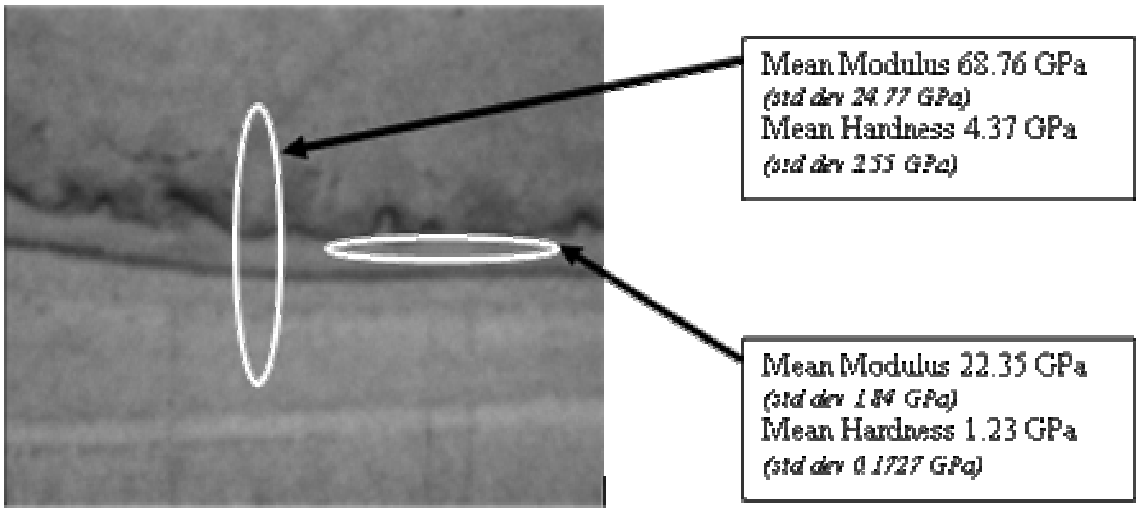

Figure 4.7 Nanoindentation data for dry polished nacre perpendicular to growth plane.

4.1.1.3 Relationship to Structure

Understanding of the individual components of the shell structure on all levels of hierarchy is necessary to explain the above results. As described in *Section 2.1* several toughening mechanisms have been proposed [18] including: (a) crack blunting/branching, (b) microcrack formation, (c) plate pull out, (d) crack bridging (ligament formation), and (e) sliding of $CaCO_3$ layers. The first of these mechanisms that will be discussed is plate

pullout. This represents a possible toughening mechanism within the steady state tiled aragonite region, and does not yet describe any macroscale mechanisms.

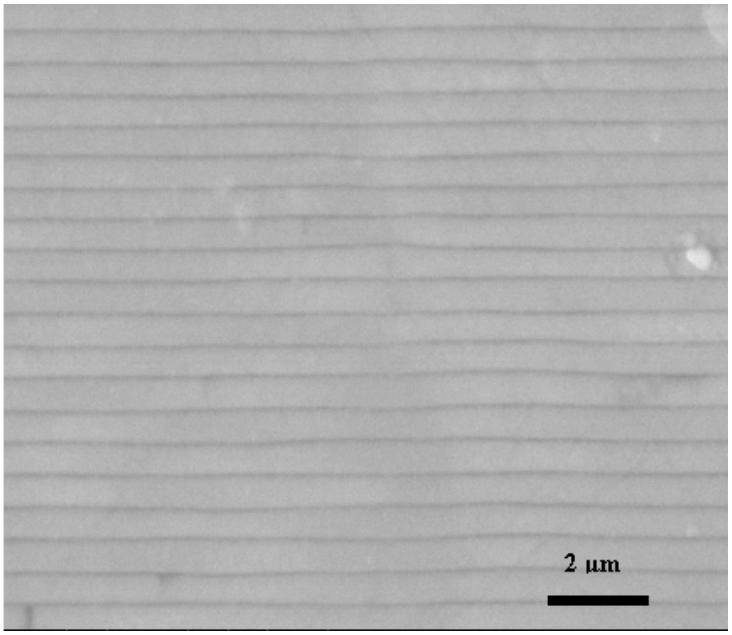

(a)

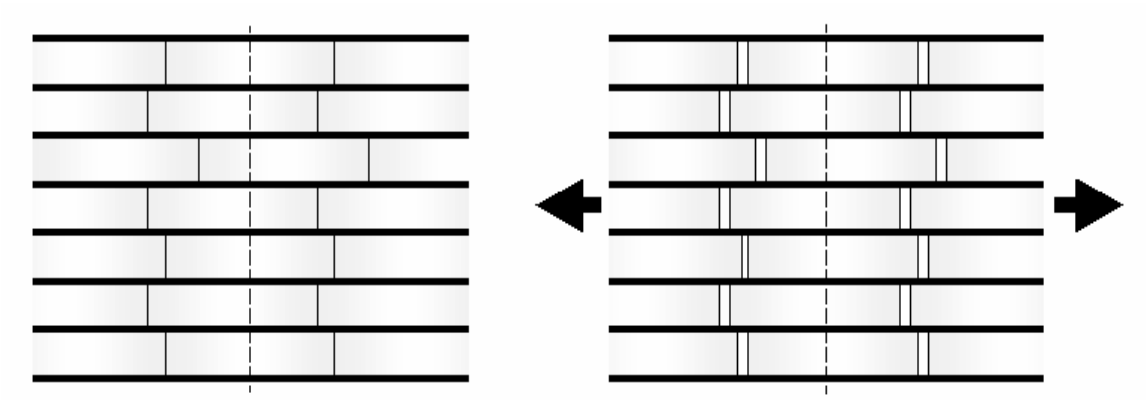

(b)

Figure 4.8 (a) SEM of cross section of abalone, showing protein layer (darker regions) and its virtual absence where tiles on same plane join; **(b)** schematic drawing of stacking of abalone tiles and their separation under tension.

Figure 4.8 (a) provides a view of a polished cross-section of nacre before deformation. It is observed that the majority of protein deposition, identified as dark lines, is present only in the planar direction of the tiles. The regularity in tile thickness can be clearly seen and is indeed striking. Very little organic material is observed at the abutment of tiles.

Figure 4.8 (b) is a schematic representation of tile stacking with the organic layers marked by thicker lines. Upon being subjected to tension parallel to the tile plane, the tiles slide rather than fracture. The absence of organic glue along the lateral surfaces of the tiles, where they abut, contributes to the sliding mechanism. If the edges were glued, there would be a greater tendency for fracture of the individual tiles, with less energy absorption. The schematics also show an axis along which consecutive tiles may grow, this stacking arrangement is due to the 'Christmas tree' growth pattern that was described in *Section 2.2.*

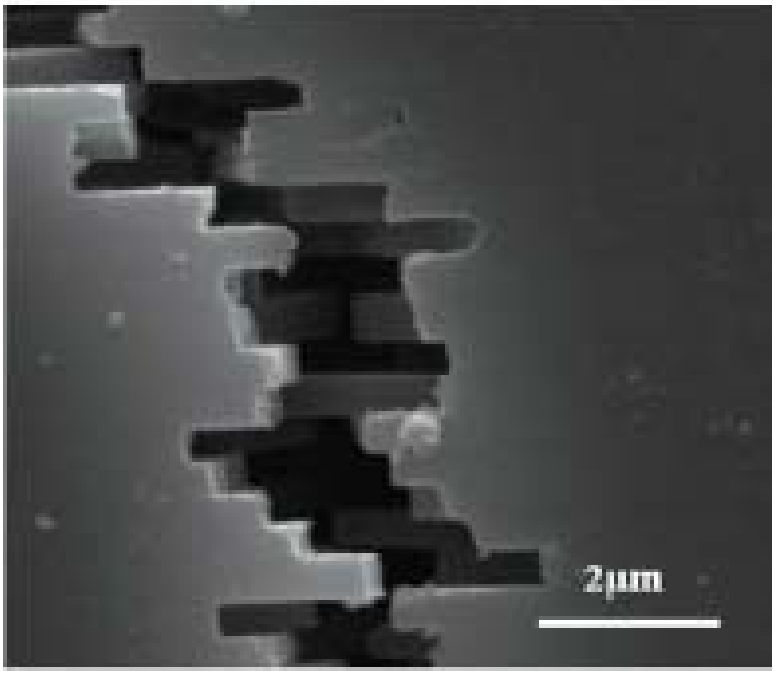

(a)

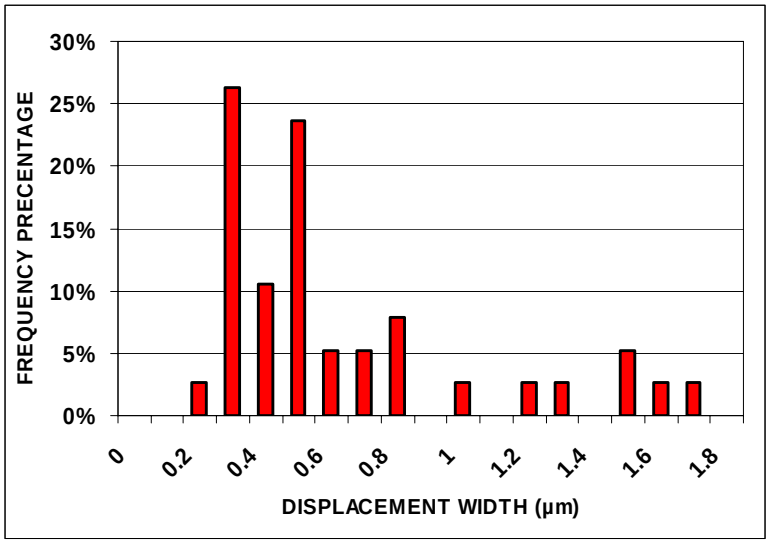

(b)

Figure 4.9 (a) SEM microscopy of polished cross-section after plastic deformation under tension; notice fracture by tile "pullout"; **(b)** plot showing distribution of step lengths.

Figure 4.9 (a) shows SEM image of a specimen subjected to tension in the same direction as that represented in the schematic of Figure 4.8 (b). The dark rectangular features are gaps that opened between tiles during tension. The tiles slide past each other rather than fracturing. The overlap of tiles was estimated from direct measurements along fracture surfaces, as shown in Figure 4.9 (b). An average step overlap of 0.63 μm is observed. It can be observed that the tiles are pulled out and the step height corresponds to the overlap. A conclusion can be made that only a slight majority of tiles do not break but rather separate through pullout. An optimization of strength ratios between the tensile strength of an individual tablet and the shear strength of the interface between overlapping tiles accounts for this observation as predicted by Ashby [47]. Thus, it becomes important to investigate both, we will begin with the interface between tiles.

4.1.1.4 Tile-Tile Interface

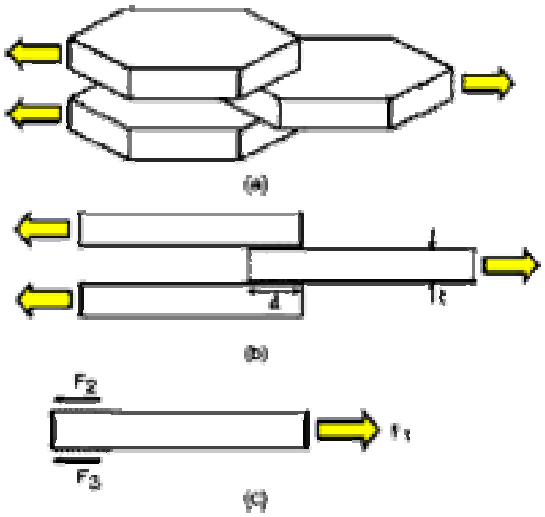

Figure 4.10 Schematic diagram showing pull-out of overlapping tile layers.

Figure 4.10 shows the schematic representation of tile overlap. In Figure 4.10 (a) three tiles are shown, subjected to tension. A simpler two-dimensional representation is shown in Figure 4.10 (b). Taking the equilibrium of forces in Figure 4.10 (c):

$$\mathbf{F_1 = F_2 + F_3} \tag{4.3}$$

This can be calculated terms of tensile stress on tile, σ_t, and shear stress on organic interfaces, τ_s:

$$\boldsymbol{\sigma_t t = 2\tau_s S} \tag{4.4}$$

Where *S* is step size of the tile overlap between consecutive layers and t is the tile thickness. From Figure 4.9 (b) we can assume that *S* = 0.63 μm and t = 0.5μm:

$$\boldsymbol{\sigma_t/\tau_s = 2S/t = 2.5} \tag{4.5}$$

Thus, the tensile strength of the ceramic should be, at least, equal to two and a half times the shear strength of the organic layer.

Thus, it is possible from the data obtained during then dog-bone shaped tensile tests to produce a first hand approximation of the shear stresses experienced by the individual tile interfaces during pullout. If one assumes that failure in tension occurs by plate pull-out, as seen in Figure 4.9 (a), then a shear force between tiles can be approximated through Eqn 4.5. Figure 4.11 provides a schematic of nacre in tension: (a) at the individual aragonite tile; (b) and as a dog-bone sample.

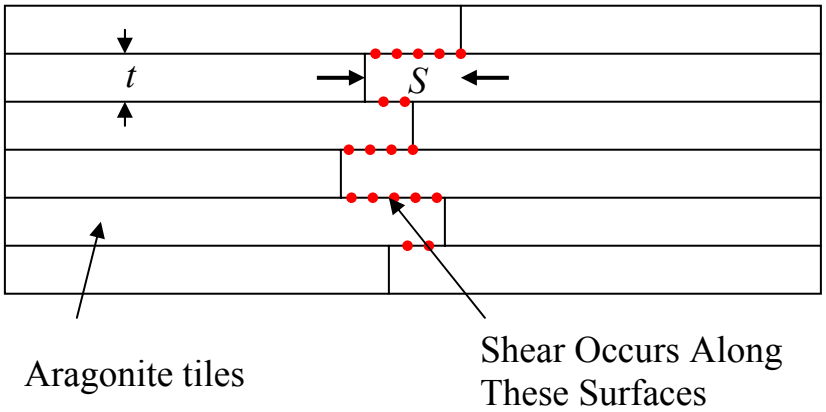

(a)

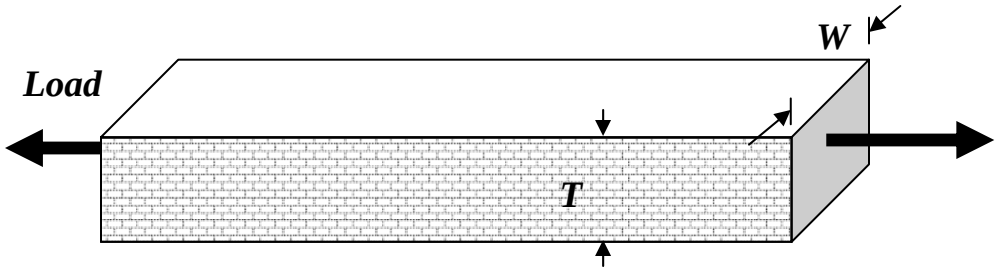

(b)

Figure 4.11 Schematic diagram of nacre in tension: (a) at the scale of an individual tile; (b) as oriented in the necking section of a dog-bone shaped sample.

Using Eqn. 4.5, the 50% failure probability tensile stress of 65 MPa (shown in Figure 4.3) can be correlated to a shear stress of 26 MPa.

Direct shear tests parallel to the layered structure were conducted on eight small cubes of nacre with average dimensions 2x2x2 mm. This was done to support previous work by Menig et al. [32], and to improve upon their effort by scaling down the dimensions of the test set up in the hopes of confining the test to the regions of tiled aragonite that exist within the 300 μm mesolayers. The previous work had shown shear

with an elastic region ending at around 12 MPa followed by a linear plastic region which increased until a maximum shear strength was reached, at a shear stress of 30 MPa and shear strain of approximately 0.45 [32]. Their test however had a gap "S" (identified in Figure 4.12) which was equal to 2mm; thus, the shear action occurred across the macro and micro structure. In the present study a new, smaller testing device was created in which the gap "S" was 200 μm, limiting the shearing action to the region within a given mesolayer.

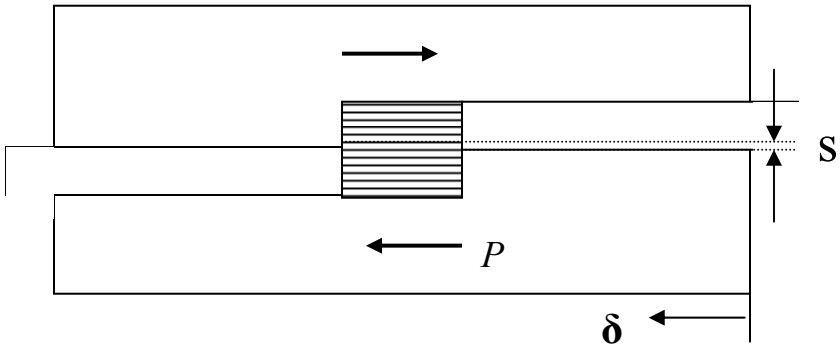

Figure 4.12 Sketch of shear test configuration acting on a cube of abalone shell.

The shear strain is given by the equation:

$$\gamma = \frac{\delta}{s} \tag{4.6}$$

in which δ is the axial displacement, and s is the gap which defines the region in which shearing action occurs. The shear stress is simply given by:

$$\tau = \frac{P}{A} \tag{4.7}$$

Where P is the load and A is the area under which shear occurs.

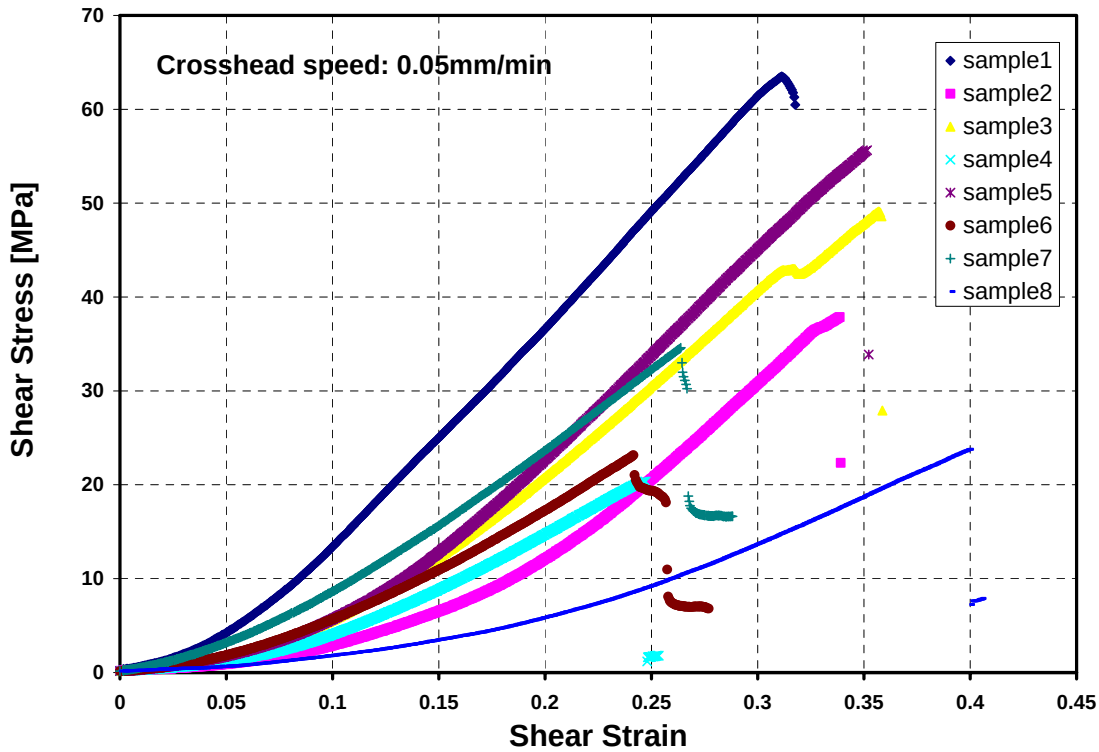

Figure 4.13 Stress-strain curves of abalone samples, tested within a single mesolayer.

The stress-strain curves of shear tests on eight samples are presented in Figure 4.13. The average shear strength of 36.9 ± 15.8 MPa was found (also shown through the Weibull distribution in Figure 4.14) with an average maximum shear strain of approximately 0.3. This is remarkably consistent with the results by Menig et al. [32] however, unlike their tests there is no observed transition from an elastic to linearly plastic region. Furthermore, this is in close agreement to the approximated shear strength

per tile interface (26 MPa) calculated from the results of the dog-bone shaped samples. This slight discrepancy may be due to the fact that the theoretical shear strength calculated from dogbone samples assumed that no tiles broke and that shearing occurred through sliding at the interface only.

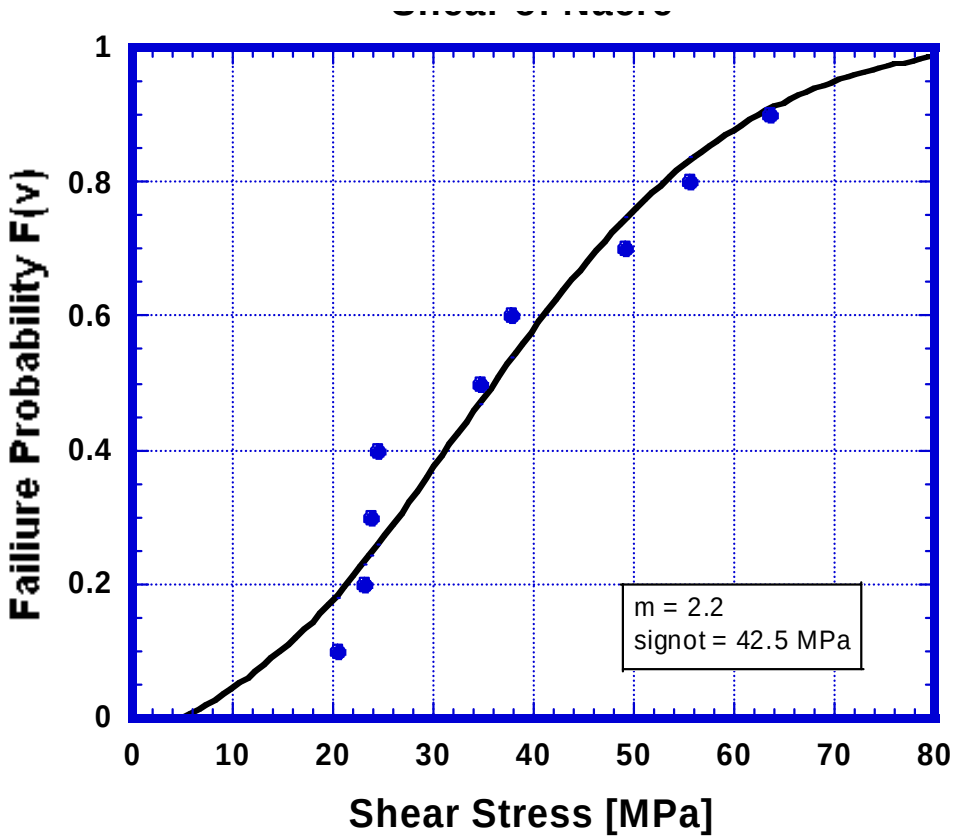

Figure 4.14 Weibull distribution of shear strength of nacre.

Various methods were employed to investigate the two specific components of the tile interface; the organic and the inorganic connections. To directly observe mineral bridges between individual tiles, nacre was fractured in tension parallel to the direction of growth. Figure 4.15 shows fracture surfaces exposed by tension tests with the force application direction parallel to the c-axis. Irregular features, the remnants of the organic

layer and mineral bridges, can be seen attached to these mineral surfaces of freshly fractured nacre in Figure 4.15 (a). Figure 4.15 (b) shows some regions (marked A) containing fabric of the organic layer, where other regions (marked B) are characteristic of the mineral.

In order to ascertain that some of these features are indeed mineral bridges, the organic component of the nacre was removed through the hydrazine-deproteination process described in *Section 3.2.5.* The fracture surfaces following deproteination are presented in Figure 4.15 (c and d). Arrows mark the location of remaining mineral bridges while a gap between tile layers can be clearly seen to exist in the absence of the organic matrix. The gap is approximately 50 nm in thickness; the asperities appear to have a diameter of 50 nm. Seen in Figure 4.15 (d), asperities pepper the surface of the tiles with greater concentration in the center region of individual tiles. The absence of the organic matrix provides a clear picture of the structure of the inorganic component at the tile interface.

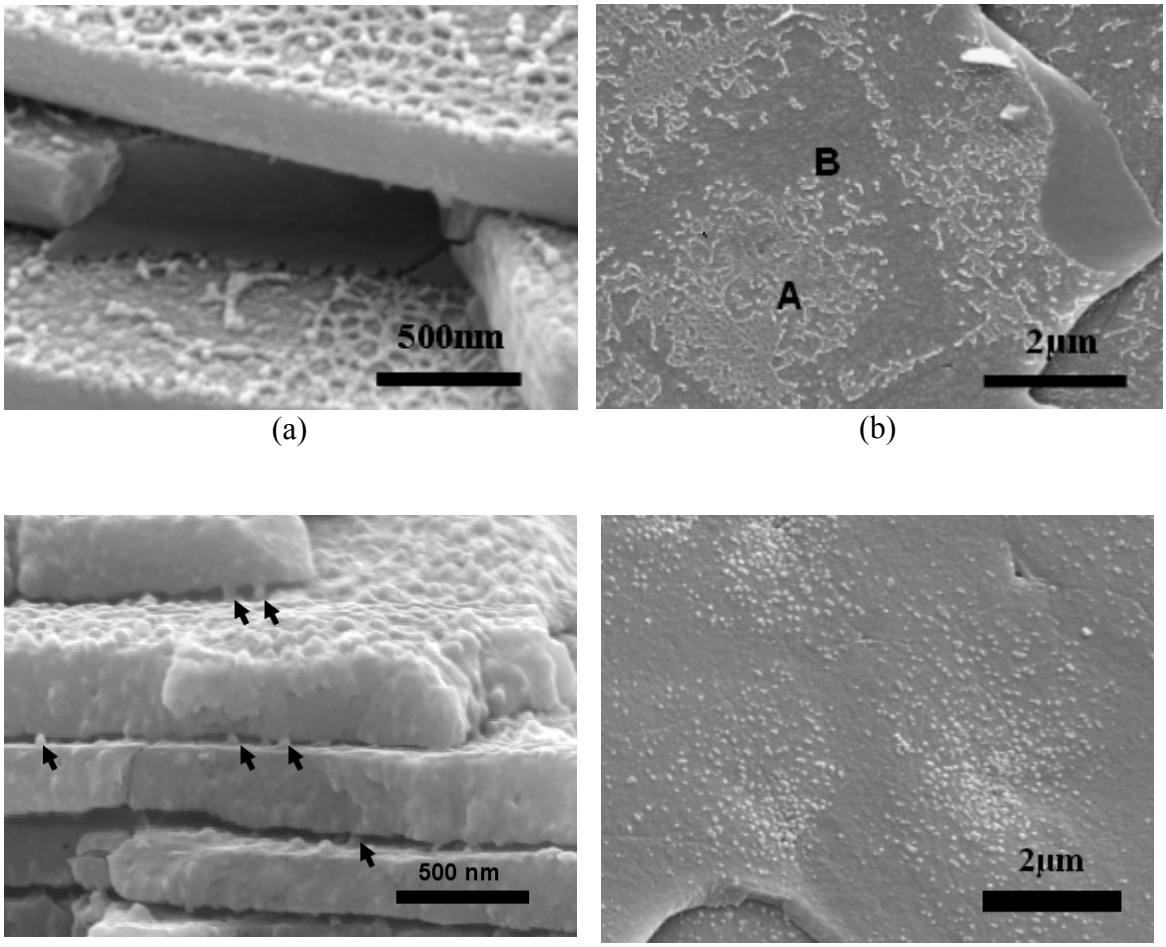

(a) (b)

(c) (d)

Figure 4.15 (a) Interface between tiles (before deproteination) with organic matrix surrounding mineral bridges; (b) tile surface (before deproteination) with regions where organic matrix "A" remains; (c) mineral bridges (marked by arrows) between aragonite tiles after 9 hours of hydrazine deproteination; (d) asperities, many of which are remnants of mineral bridges, concentrated at the center of a aragonite tile after 9 hours of hydrazine deproteination.

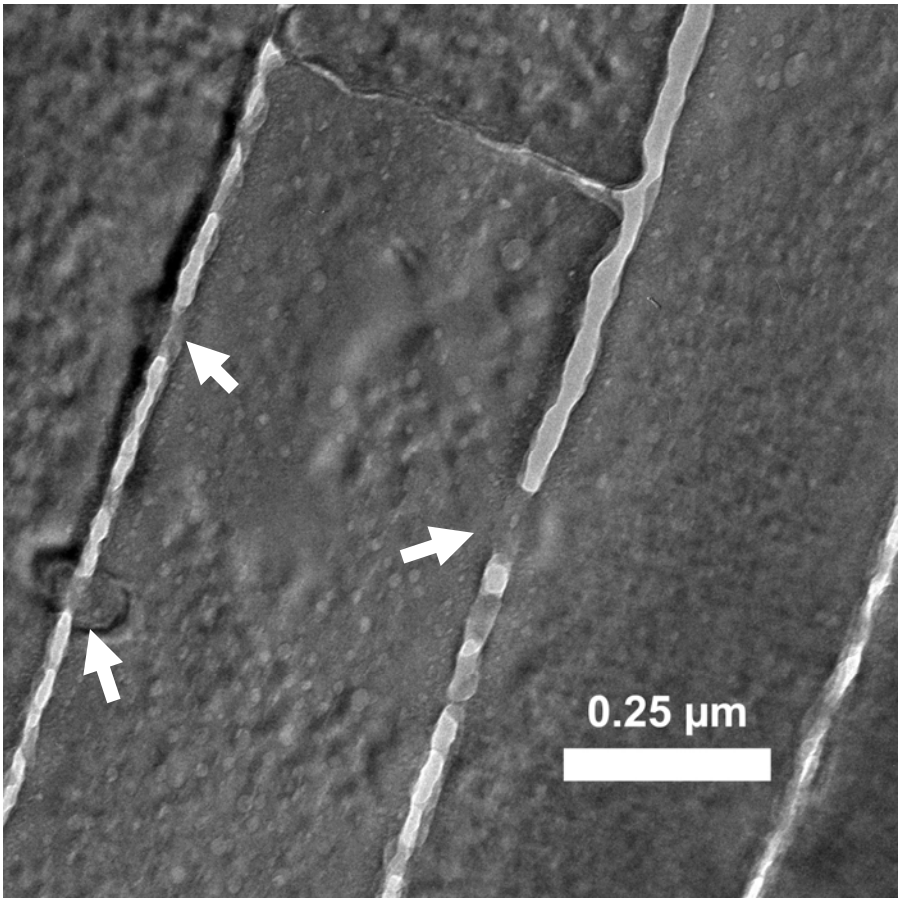

Figure 4.16 Transmission electron micrograph of nacre crossection showing mineral bridges between tile interfaces.

Figure 4.16 provides further evidence of mineral bridge formation (marked with arrows) through a TEM cross-sectional image. The aragonite surrounding individual mineral bridges seems to have semicircular bands emanating from the bridge. It has been suggested that this corresponds to a higher degree of protein absorption during the process of mineral bridge formation [150]. It may also be possible that the emanating rings are artifacts of stress concentrations surrounding the localized structural supports;

however neither of these hypotheses have been investigated in detail. From the image one can ascertain an approximate bridge diameter of 50 nm.

Observations were made indicating that the organic layer, while playing a pivotal role in the growth of the aragonite crystals in the *c* direction (perpendicular to tile surface), may have a minor role in the mechanical strength. The relatively weak tensile strength observed in the direction perpendicular to the layered structure can be explained by the presence of the identified mineral bridges. These bridges, having a diameter of approximately 50 nm, have a tensile strength not determined by the critical crack size, but by the theoretical strength. Their number is such that the tensile strength of the tiles (parallel to the tile/shell surface plane) is optimized for the tile thickness of 0.5 μm, as shown by Lin and Meyers et al. [35]. A higher number of bridges would result in tensile fracture of the tiles with loss of the crack deflection mechanism. This is a viable explanation for the small fraction of asperities that are bridges.

We estimate the tensile strength of the individual mineral bridges by applying the fracture mechanics equation to aragonite [49]. Consistent with recent analyses by Gao et al. [70], Ji and Gao [71], and Ji et al. [72], the mineral bridges have sizes in the nanometer range. The maximum stress, σ_{fr}, as a function of flaw size, $2a$, can be estimated, to a first approximation, to be:

$$\sigma_{fr} = \frac{K_{Ic}}{\sqrt{\pi a}} \tag{4.8}$$

where K_{Ic} is the fracture toughness. However, the strength is also limited by the theoretical tensile strength, which can be approximated as [70]:

$$\sigma_{th} = \frac{E}{30} \tag{4.9}$$

We assume that K_{Ic}= 1 MPa·m$^{1/2}$, E =100 GPa, and that 2a=D, where D is the specimen diameter. Figure 4.17 shows the two curves given by Eqn. 4.8 and Eqn. 4.9. They intersect for a = 28 nm (D = 56 nm). This is indeed surprising, and shows that specimens of this and lower diameter can reach the theoretical strength. This is in agreement with the experimental characterization results: the holes in the organic layer (obtained through AFM and presented below) and asperities/bridge diameters (shown above through SEM) are around 50 nm. Recent analyses [70,73,74] also arrive at similar values.

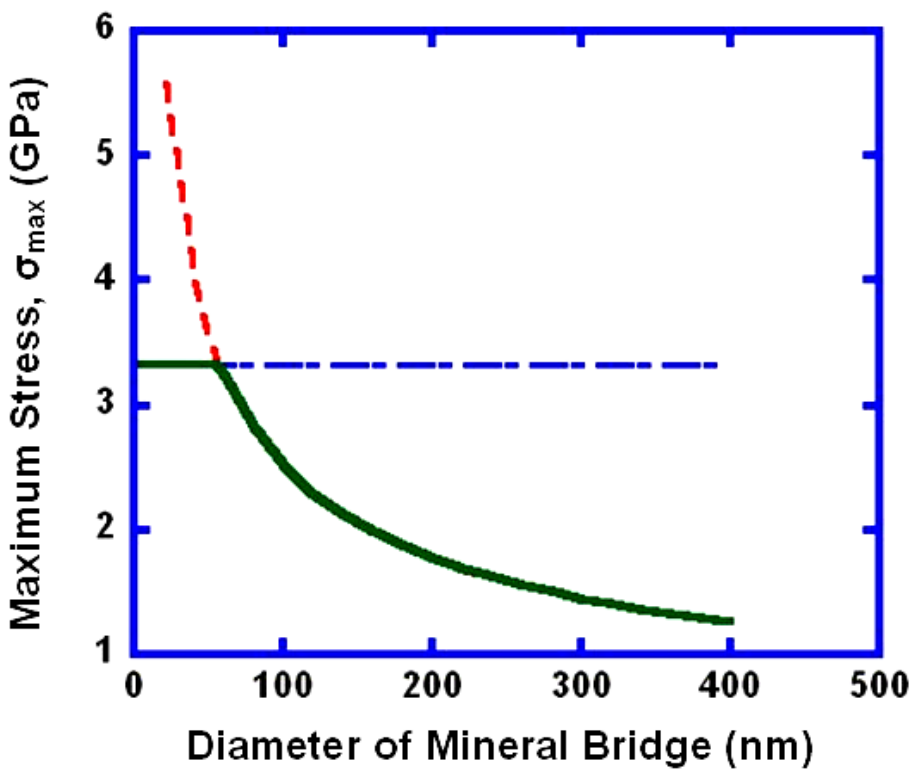

Figure 4.17 Tensile strength of mineral as a function of size**.**

It is possible to calculate the fraction of the tile surface consisting of mineral bridges, *f*. Knowing that the tensile strength is σ_t and assuming that the bridges fail at σ_{th}, we have:

$$f = \frac{\sigma_t}{\sigma_{th}} \tag{4.10}$$

The number of bridges per tile, *n*, can be calculated from:

$$f = \frac{nA_B}{A_T} \tag{4.11}$$

Where A_B is the cross-sectional area of each bridge and A_T is the area of a tile. Thus:

$$n = \frac{\sigma_t A_T}{\sigma_{th} A_B} \tag{4.12}$$

Assuming that the tiles have a diameter of 10 μm and that the bridges have a diameter of 50 nm (the approximate observed value), one obtains, for $\sigma_t = 3$ MPa (the value found by Meyers et al.) [49], $\sigma_{th} = 3.3$ GPa, and *n*=36, a mineral bridge density of approximately 2.25/μm^2 per tile. These results are of exact agreement with the experimental results described previously in which nacre was loaded in tension perpendicular to the tiles. Thus fracture occurs at the mineral bridges in this loading direction. Figure 4.18 shows the relationship between mineral bridge diameter and the number of mineral bridges predicted through Eqn. 4.12. The relationship is that as mineral bridge diameter increases the number of existing bridges should decrease.

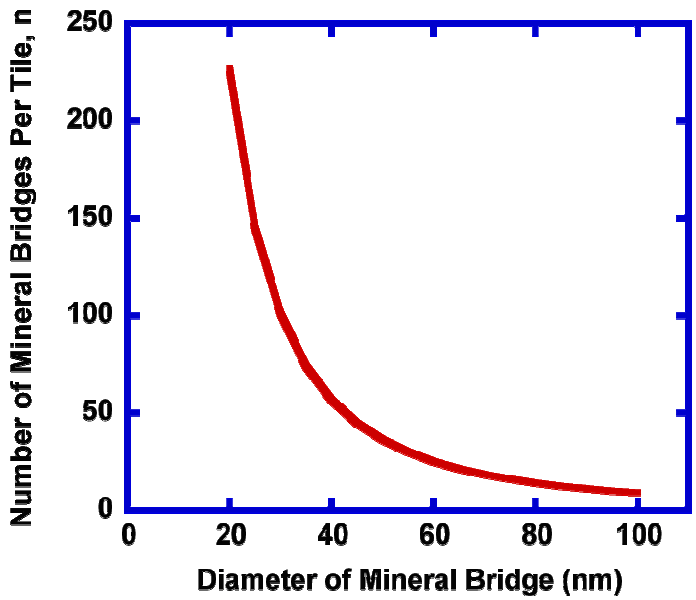

Figure 4.18 Calculated number of mineral bridges per tile as a function of bridge diameter required to provide tensile strength prependicular to surface of 3 MPa.

The number of asperities seen in Figure 4.19 exceeds considerably the values for bridges calculated herein. While the calculated density is 2.25/μm^2 the SEM analysis shows an estimated density closer to 60/μm^2. The density measured by Song et al. [73,74] is 105/μm^2, 1680 mineral bridges per tile. The fact that the shear strength of the interface (~50 MPa) exceeds significantly the tensile strength (~3 MPa) supports a hybrid mechanism of strength by the bridges and asperities, by which the continuous bridges (with a density of approximately 2.5/μm^2) provide the tensile strength, while both bridges and asperities (density of 60/μm^2) provide shear strength. The presence of asperities confirms results by Wang et al. [66] and Evans et al. [67] who suggested that the rough nature of tile surface asperities leads to inter-tile friction. They hypothesize that friction is the principal source of shear resistance between tiles, completely ignoring the cross

layer connection. Their assumption may not be correct; however, it is possible that friction providing asperities and mineral bridges both exist and both provide the inter-tile shear mechanism responsible for shear strength.

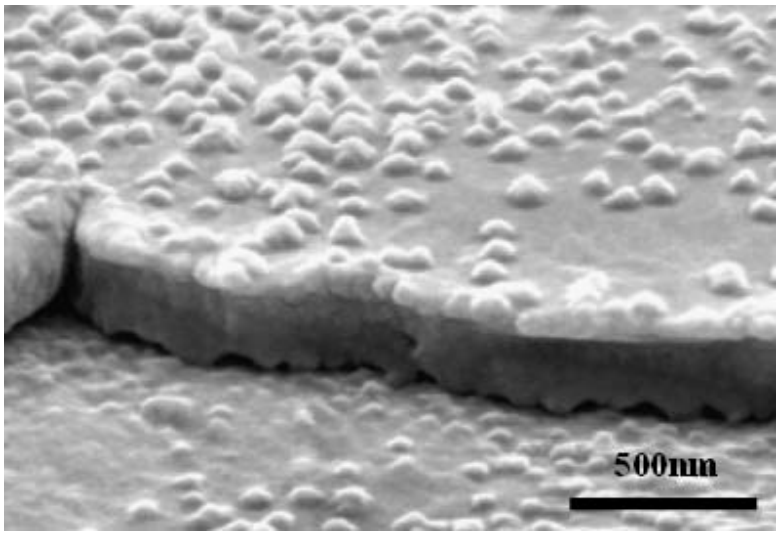

(a)

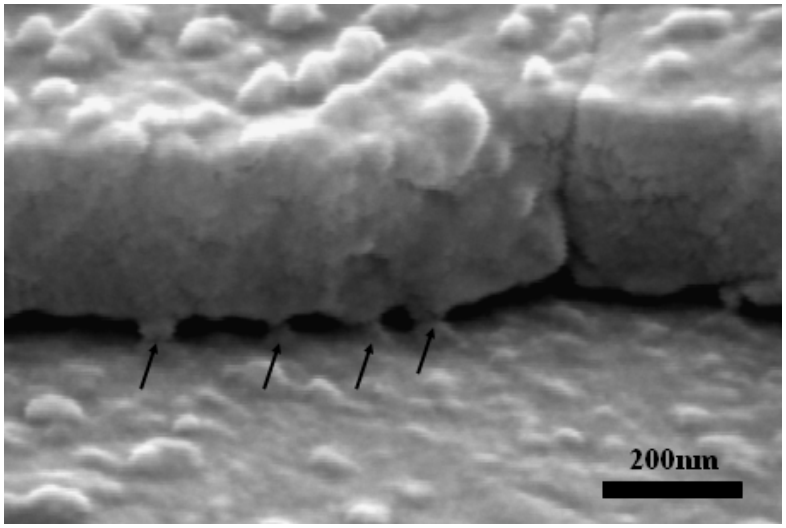

(b)

Figure 4.19 (a) Asperities (a fraction of which are remnants of mineral bridges) and (b) mineral bridges (marked by arrows) between tile layers.

The interface between tiles is critical to the mechanical response and thus several theories have developed and are summarized below:

(a) Evans et al. [73] and Wang et al. [66] suggest that the rough nature of tile surface asperities leads to inter-tile friction not mineral bridges. They hypothesize that friction is the principle source of shear resistance between tiles. Here mineral bridges between tile interfaces are not considered.

(b) Other studies suggest the impressive mechanical response of the aragonite tiles is attributed to the thin (20-30 nm) organic matrix which exists within the tile interfaces. The proteins consisting of beta-pleated sheets folded into a cross-linked polymer-like glue would adhere to tiles and provide toughness through the many sacrificial bonds between proteins [75].

(c) Mineral bridges could be the primary factor in the mechanical response of the system as described by Song et al. [73,74] and Meyers et al. [49]. They would mechanically link layers of aragonite tile. Toughening would then be increased through crack propagation and deflection along the resulting weaker tile interfaces. However the existence of interlamellar mineral bridges is still debated.

It is suggested here that the true mechanism of toughening is the combination of all three of these theories in a synergetic and harmonious collaboration. At the onset of plastic deformation, broken mineral bridges may play a role in forming the asperities that subsequently resist shear. This, in combination with the presence of the organic glue, results in the mechanical response of the mortar portion of the brick and mortar structure. Figure 4.20 presents schematics of the various inter-tile toughening theories.

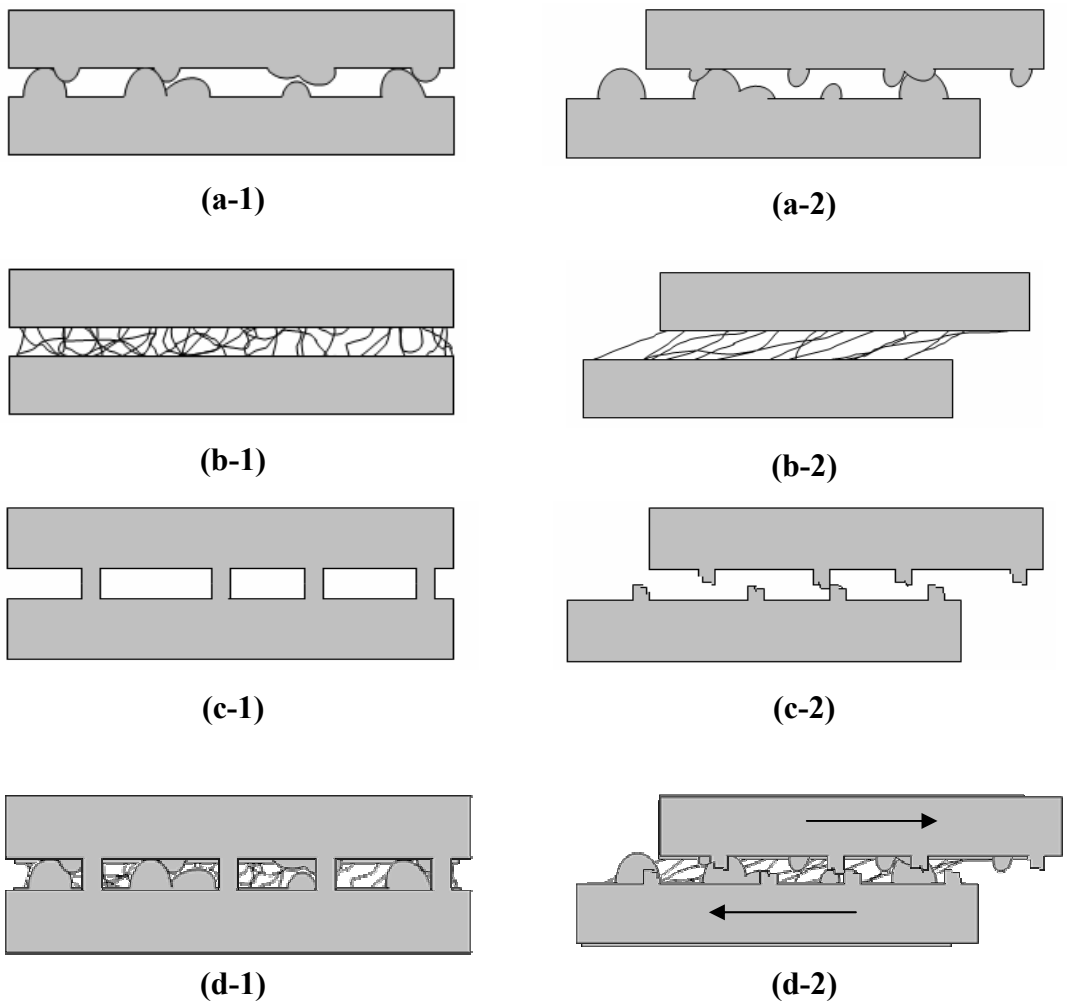

Figure 4.20 Different models for sliding between tiles; inter-tile layer formed by (a) asperities; (b) organic layer acting as visco-elastic glue; (c) mineral bridges; (d) combination of three mechanisms.

The column marked a-1 through c-1 represents the tile interface before deformation, the column marked a-2 through c-2 represents the inter-tile damage mechanisms which might exist for the various theories. Note how the process of going from c1-c2 creates a surface structure similar to the proposed mechanism in a1-a2. It

seems likely that mineral bridges exist, and after they break provide an added resistance to shear through a frictional component. The combination of all mechanisms is described in d-1 and d-2.

The organic layer that separates individual tiles was once thought to be the major factor in the inter-tile mechanism of toughening. The following analysis shows that the organic layer is actually quite weak and can only barely support its own weight.

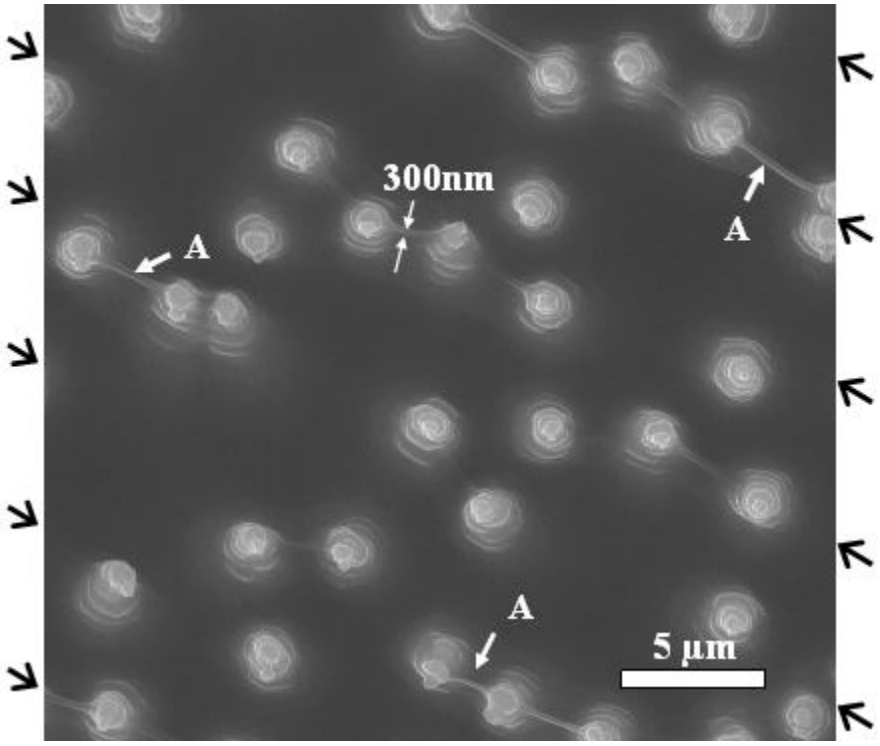

Figure 4.21 Top growth surface six weeks after implantation. Light regions represent apexes of terraced cones and streaks marked by arrows are due to folding of organic interlayer.

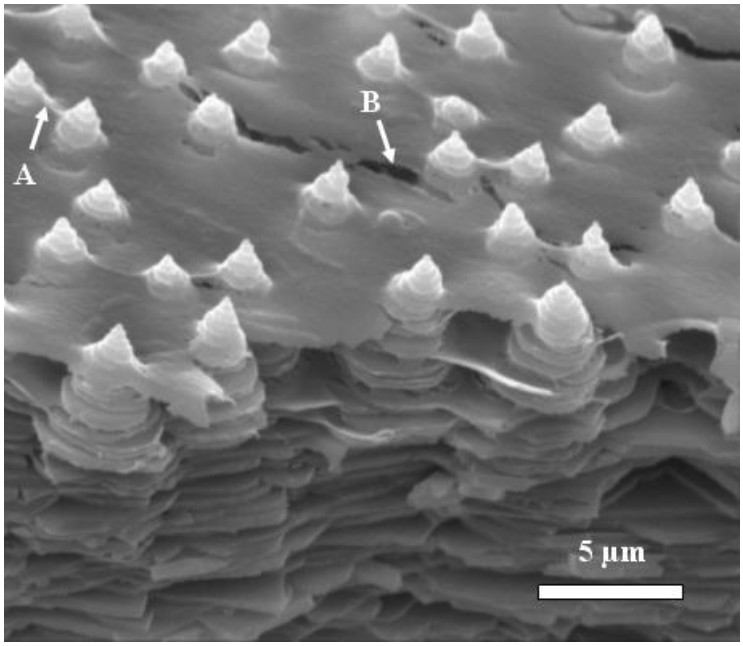

(a)

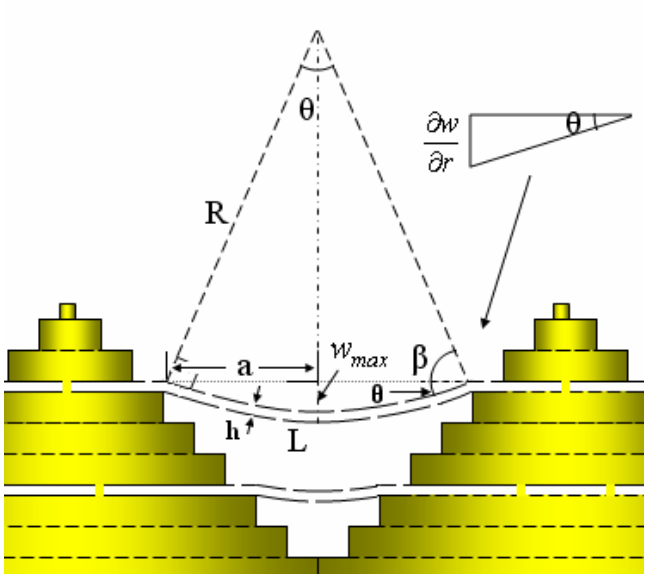

(b)

Figure 4.22 (a) Side view of intermediate tile growth through organic layers on flat pearl five weeks after implantation; (b) Schematic showing terraced growth and organic membrane sagging under its own weight.

The sagging of the organic layer, shown in Figure 4.21 and Figure 4.22, can be used to estimate its stiffness. The fact that the organic membrane undergoes substantial sagging from the sole effect of its weight suggests that its stiffness is very low. The sagging of a membrane is a classical mechanics problem and observations from its deflection can be used to give a first hand approximation of the mechanical strength of the membrane. We present here a solution applicable to the simple boundary conditions. The membrane is assumed to be circular and fixed along the circle. Its deflection as a result of its weight is calculated. The radial forces are considered to be zero at zero deflection. The equilibrium diagram is shown in Figure 4.22 (b). The following parameters are defined: a, radius of the membrane (assumed to be circular); w, deflection; p_z, vertical load; h, thickness of the membrane; σ, radial stress on membrane. One finds that w_{max}, the maximum deflection, can be expressed in terms of known parameters (e. g., Ugural [151]; Szilard [152]):

$$w_{max} = \frac{\rho h g a^2}{4N} \tag{4.13}$$

ρ is the density; N is the tensile force per unit length which is represented by stress multiplied by unit thickness:

$$N = \sigma h \tag{4.14}$$

The biaxial stress in a membrane under its own weight is:

$$\sigma = \frac{\rho g a^2}{4 w_{\max}} \tag{4.15}$$

The nominal biaxial strain is defined as:

$$\varepsilon = \frac{L - 2a}{2a} \tag{4.16}$$

For the calculation of the strain, we assume θ is small. Thus:

$$\sin\theta \cong \tan\theta = \frac{\partial w}{\partial r} = \frac{w_{\max}}{a} \tag{4.17}$$

$$L = 2\pi R\frac{\theta}{180^\circ} = 2\pi\frac{a^2}{w_{max}}\frac{\theta}{180^\circ} \tag{4.18}$$

We assume the density of the organic layer to be 1.5 g/cm^3. The thickness of the membrane is taken to be 30 nm, in accordance with several measurements reported in the literature and our own approximate evaluation. Two circle radii (assumed shape between sagging points of the membrane) are considered: 2.5 and 5 μm. This is consistent with tile size of approximately 5-10 μm.

Figure 4.23 (a) shows the stresses calculated using Eqn. 4.15. The deflection (found at the center of the sagging points) is varied from 0 to 0.6 μm. The corresponding biaxial modulus, obtained by dividing Eqn. 4.15 by Eqn. 4.16 is plotted in Figure 4.10 (b). An approximate value of the deflection can be estimated from Figure 4.22 (a): 0.5 μm. For this value one obtains a biaxial elastic modulus of 100 Pa, considering a tile spacing of 10 μm (a = 5 μm), this is indeed a very low value. This value would contradict the hypothesis that the shear strength of the nacre is obtained from the organic glue, rather the organic matrix has little to do with inter-tile mechanical strength and that its role is limited to the mediation of inorganic ions as they crash into solid state crystals, this will be discussed in *Section 4.2*.

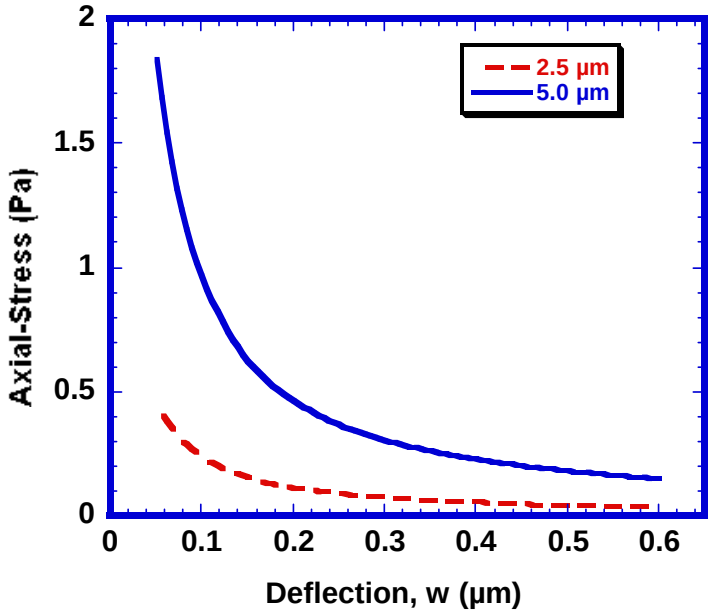

(a)

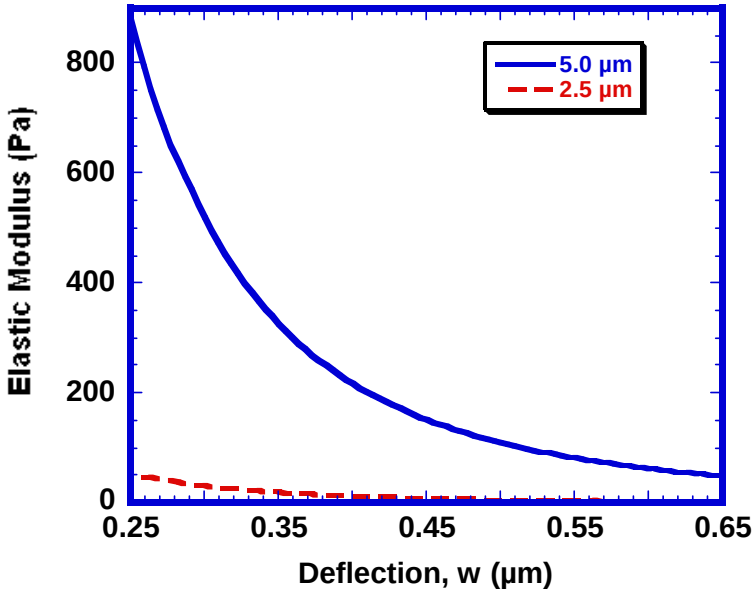

(b)

Figure 4.23 Calculated (a) stress, and (b) elastic modulus of organic layer as a function of deflection for two circle radii (assumed shape between sagging points of the membrane) are considered: 2.5 and 5 µm.

Atomic force microscopy of nacre following EDTA demineralization exposes the structure of the organic matrix, Figure 4.24. The foot prints of pseudo-hexagonal tiles of approximately 10 μm diameter can be seen in Figure 4.24 (a). As described above, Meyers et al. [49] obtained a biaxial elastic modulus of 100 Pa, by measuring the sagging of the membrane between a tile spacing of 10 μm, indeed a very low value. This low value can only be explained if the random network of protein chains seen in Figure 4.24 (b) can slide when tension is applied to the membrane. The value of 100 Pa is an upper bound of this approximation, and the range of elastic moduli is comparable to that for living cells [50]. This value is also consistent with the high maximum tensile strains that the organic layer can undergo in tension.

Figure 4.24 (b) provides a 3 dimensional analysis of the organic material, the scale bar on the right side of the image corresponds to the z-height of the probing tip. This means that the dark regions are the lowest and the pink regions are raised to a maximum height of 50 nm. This agrees precisely with the height of the gap between tile layers observed in Figure 4.19 (b) of 50 nm. Furthermore, the holes created through the porosity of membrane are also approximately 50 nm in diameter. This too matches exactly with the SEM observations of mineral bridges which may have resided in these regions between cross-linked protein chains (note all mineral material had been removed through EDTA exposure prior to AFM characterization).

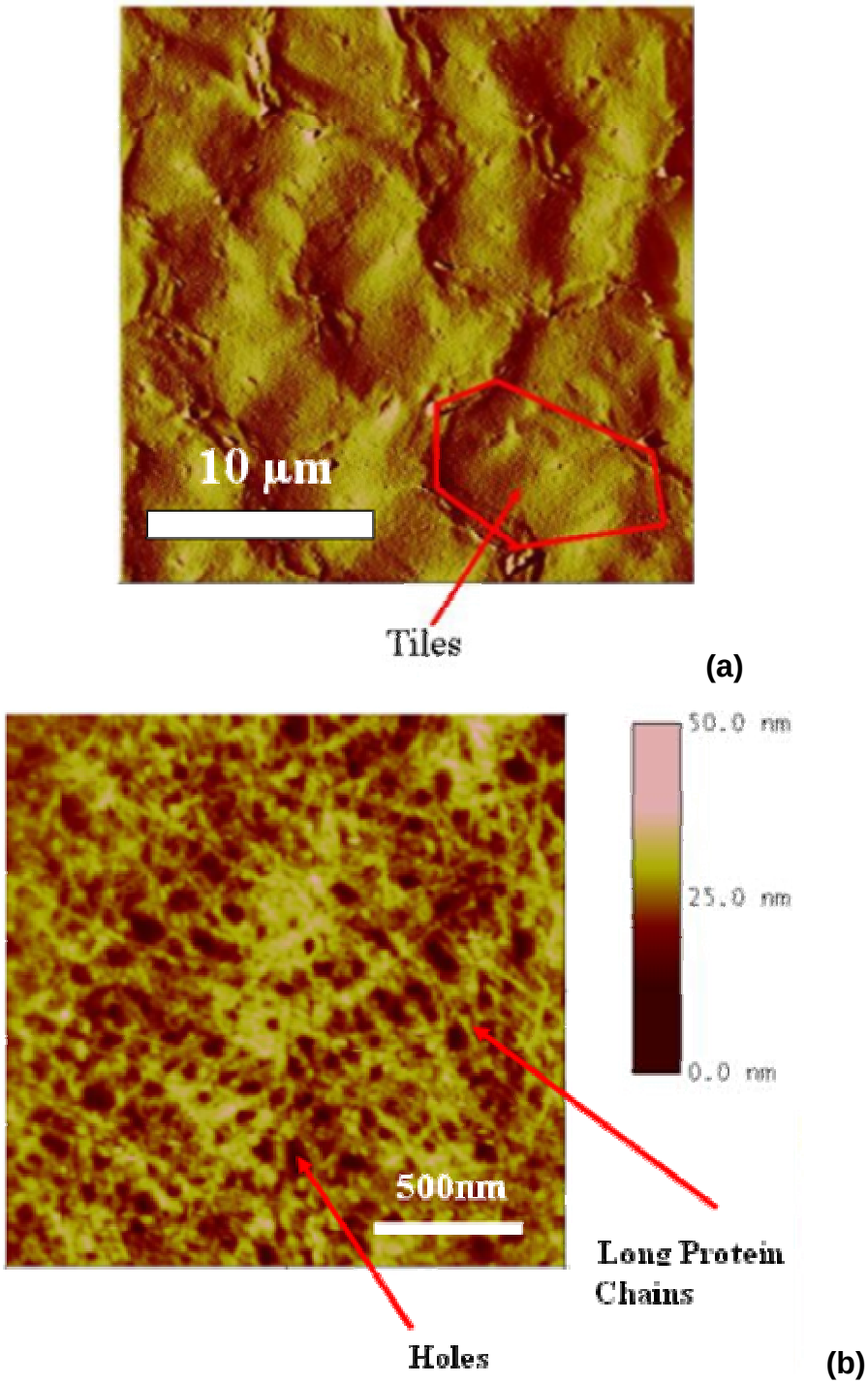

Figure 4.24 Atomic force micrograph of organic layer; (a) magnification showing outline of tiles; (b) high magnification showing linear chains and holes with ~30 nm diameter [49].

4.1.1.5 Strength of Individual Tile

Now that we have successfully identified the various toughening mechanisms within the interface between tiles it is relevant to discuss the strength of a single 0.5 μm by 10 μm aragonite tile. As discussed earlier, the relationship between these two forces, the tensile strength of a tile and the shear strength of the tile/tile interface created by nanoscale features, should be optimized and closely related.

Figure 4.25 shows the tensile strength of the aragonite phase as a function of crack size derived from the typical fracture toughness equation:

$$K_{IC} = \sigma\sqrt{\pi a} \tag{4.19}$$

The fracture toughness was taken as 1MPam$^{1/2}$. It can be seen that, if one considers the strength limited by flaw size, that it increases from values of ~50 MPa for large flaws to 250 MPa for a flaw the size of a tile (10 μm). The strength of tiles increases with decreasing size, and one can safely assume that it is higher than 250 MPa, for the given size. In fact, if one further considers the likely flaw path through an individual tile, it will tend to occur through the c-axis. This leaves us with a flaw size of 0.5 μm and a critical stress much higher then 250 MPa. Thus, the values of tensile strength obtained by Menig et al. [32] (180 MPa from flexure tests) and Wang et al. [66] (110MPa) may be explained by viscoplastic flow of organic matrix or plastic failure of mineral bridges at the tile interface, starting at 10 MPa and proceeding through gradual increase, until separation occurs. This would also explain why we tend to see fewer tiles broken and more tile pull-out during fracture.

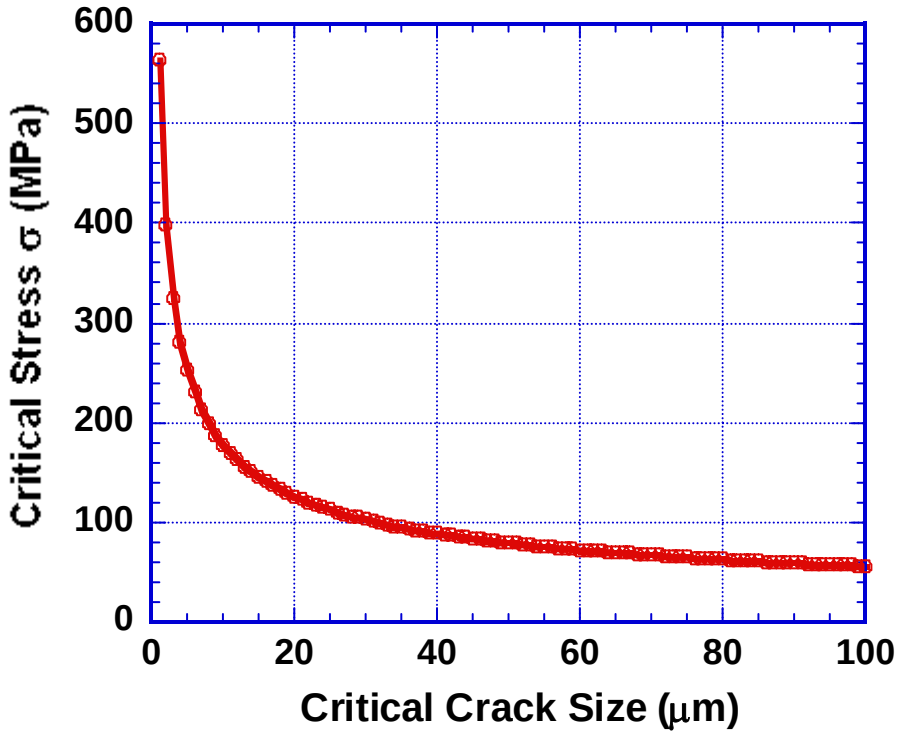

Figure 4.25 Critical stress as a function of flaw size *a* [K_{IC} = 1 $MPam^{1/2}$] [35].

This analysis provides a very interesting insight commentary on exploitation of nanoscale structures for macroscale effects. In this model the strength of the material is increased by sectioning the bulk material into subsections (in this case tiles) so that the size of internal flaws is limited by the size of the subsections, thus reducing the possibility of crack growth by necessitating a large critical stress to rupture. At the interface of each subsection a dampening effect is needed to provide crack deflection, for nacre this is represented by the presence of the visco-elastic organic matrix, and the staggered position of the adjacent tiles in a brick and mortar like fashion. Those two effects in essence provide a tortuous path for any crack to propagate. Thus by scaling down the size of the subsections, one can reach a point in which failure by crack growth

could be ignored and the theoretical limit of the material can be realized. This model of scaling effect for the case of nacre is represented in Figure 4.26. The figure shows three layers of tiles separated by a visco-elastic organic matrix. A flaw can be seen within the semi-transparent tile on the top right. It becomes clear that flaw sizes cannot exceed the dimensions of the tiles and thus the reduction in tile size leads to the inevitable reduction in possible flaw size. This is an effect which may be relevant to many synthetic composites and should be examined more thoroughly.

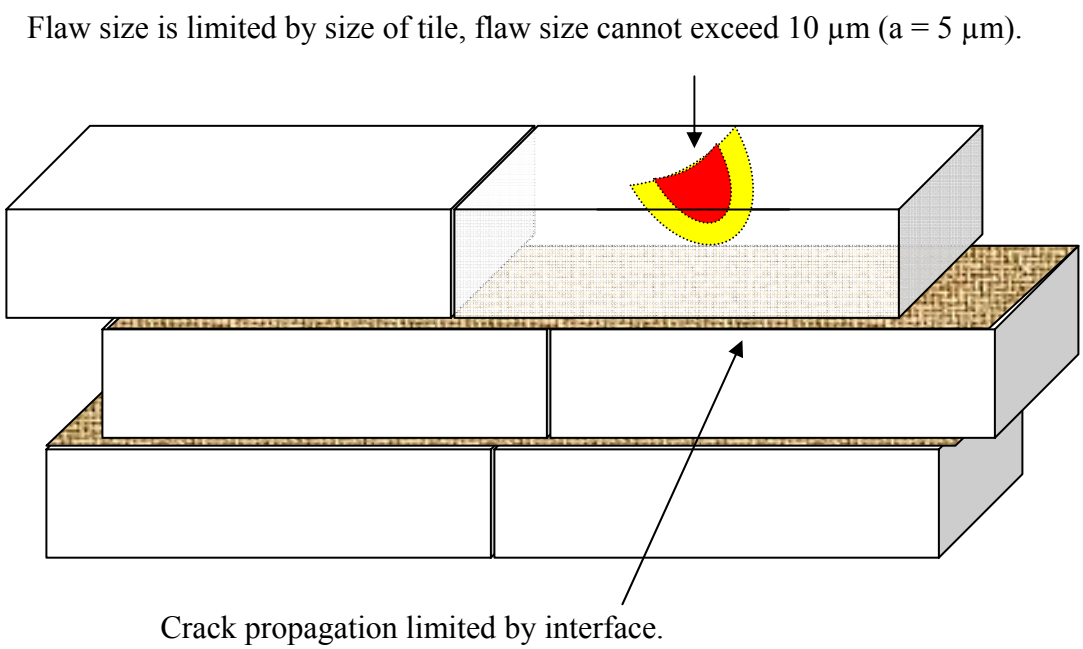

Figure 4.26 Schematic model of the nanoscale structural effect on the propagation of cracks through a material, flaw is represented by penny shaped crack.

4.1.1.6 Mesolayers

The final structural component of nacre which will be discussed is the macroscale effect of growth bands on the mechanical response of the shell. It is thought that interruptions in feeding patterns lead to the formation of growth bands or "mesolayers" within the nacre of the abalone shell. These are defined by the separation of the regular tiled aragonite sections into subsections of approximately 200-300 μm in thickness. The composition of the irregular separation planes was found to consist mostly of organic material. Figure 4.27 shows a section of partially demineralized abalone shell. The calcium carbonate component of the shell is removed by exposing the material to ethylenedi-amine tetraacetic acid (EDTA). Partially demineralized sections of tiled aragonite are seen below in the areas identified by arrows. Large sheets of organic material can be observed separating the remaining tiled aragonite sections.

It is proposed that these larger organic sheets introduce a visco-elastic component (confirmed by results in Figure 4.6) to the material at the macro level, and create a laminate-like structure that has major contributions to the mechanical response of the material in both bending and tension. It also affects the compressive failure by contributing enabling micro-buckling. A schematic representation of this mechanism is represented in

Figure 4.28.

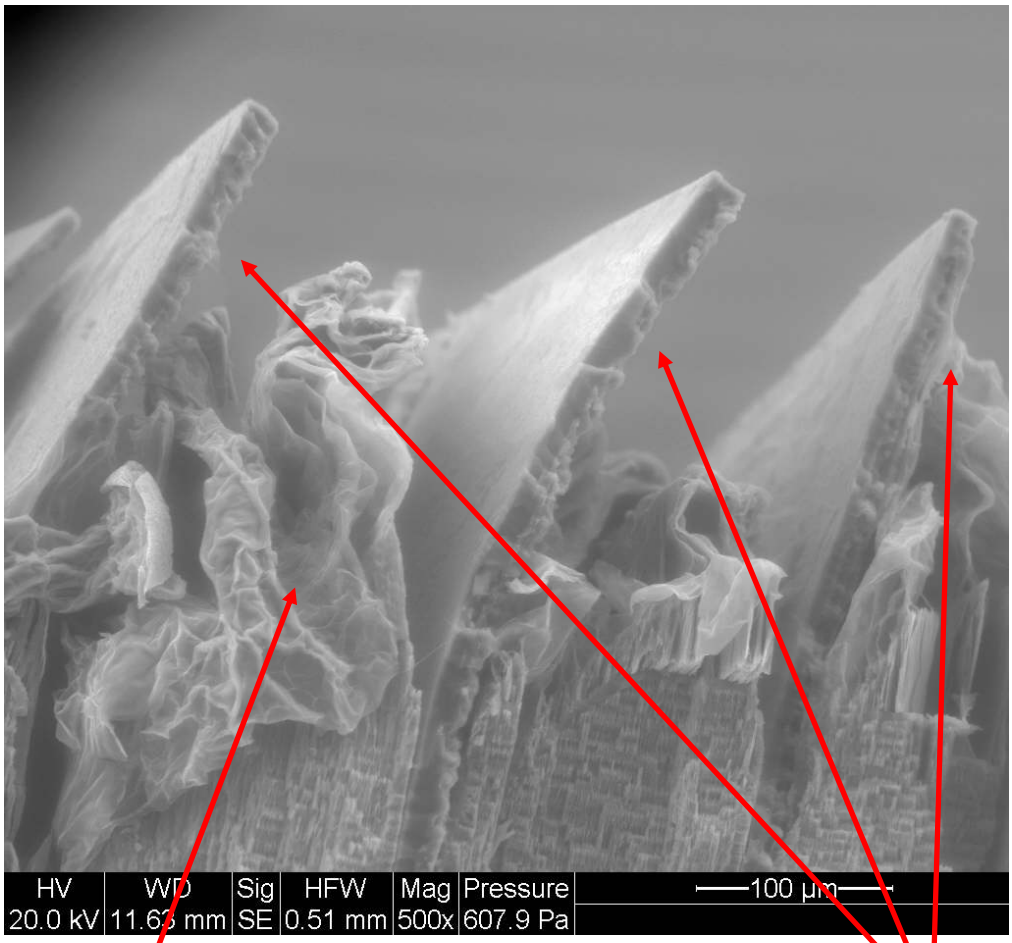

Partially deminerialized tile layers

Exposed viscoplastic organic material

Figure 4.27 Nacre which has been demineralized with EDTA (ethylenedi-amine tetraacetic acid) leaving exposed mesolayer**.**

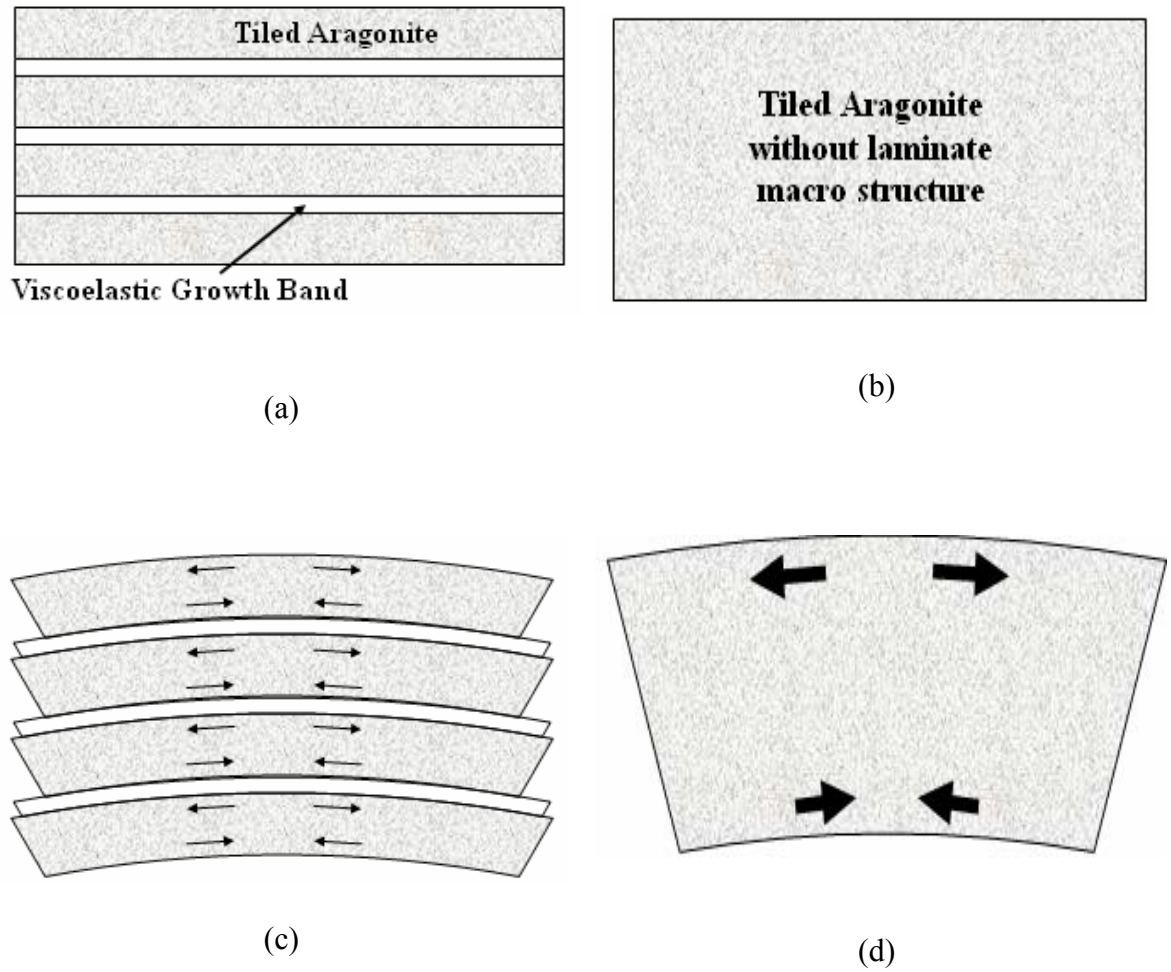

Figure 4.28 Schematic representation of (a) the macrostructure of nacre including the mesolayers, (b) macrostructure of a non-laminate aragonite, (c) the effect of macro structure on the material response to bending showing reduction in stress concentration**,** (d) the stress concentrations which develop in bending of a non-laminate material.

4.1.2 Comparative Study:

By investigating various shells with similar composition, but dissimilar structural organization, one can observe the impact of macro, micro, and nanostructural variation in the mechanical response of such biocomposites. The structure and mechanical response of the pink conch (*Strombus gigas*) [161], and the giant clam (*Tridacna gigas*) have been studied to provide a comparative discussion of biological materials [112] and the role of competing mechanisms involved in the process of strengthening and toughening composite designs. The two shells were chosen to highlight a composite with higher structural order and one with lower structural order, all of which are composed of primarily the same constituent material. It will be shown that an optimization of structural design is exhibited in the nacre of abalone.

4.1.2.1 Conch shell

The conch (*Strombus gigas)* shell, known for its logarithmic spiral shape, exhibits the highest level of organization in structure among the three shells described. Conch shells have a cross-lamellar structure consisting of lath-like aragonite crystals (99.9 wt-% of the shell) and an organic matrix (0.1 wt-% of the shell) [161,11]. As presented in Figure 4.29 (Taken from Menig et al. [161]), the lath-like aragonite crystals form 'plywood'-like structures composed of three macro-layers (outer, middle and inner). Each macro-layer is composed of first-order lamellae, which are in turn, formed from second-order lamella, which are further divided into third-order lamellae.

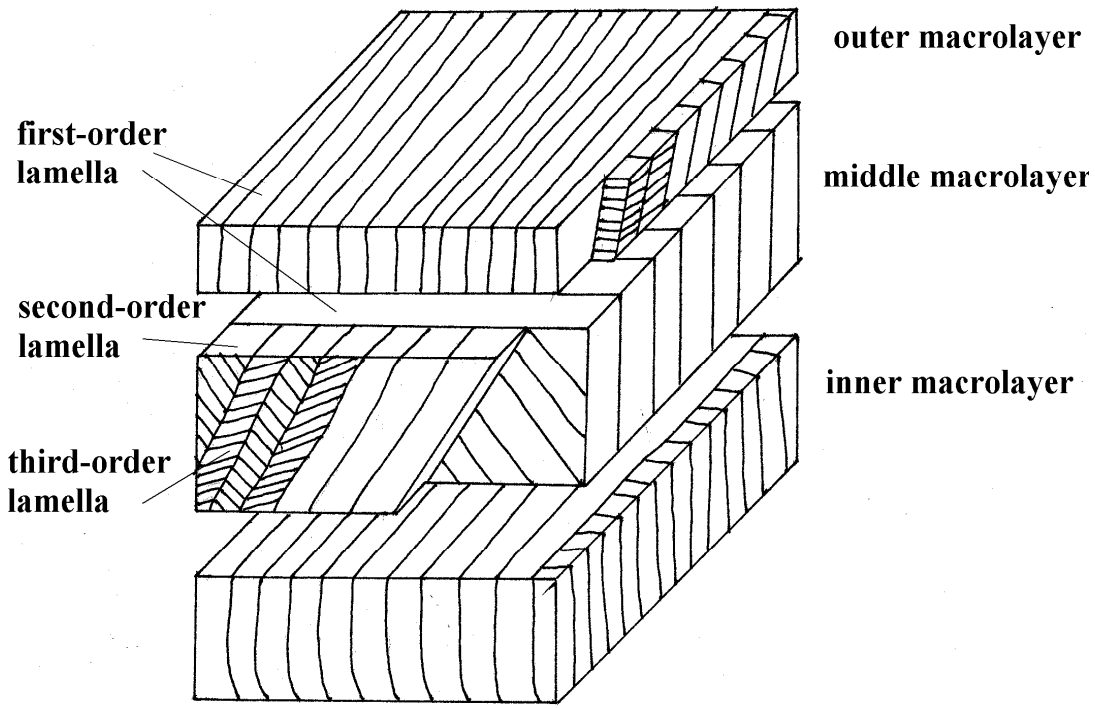

Figure 4.29 Schematic drawing of the crossed-lamellar structure of *Strombus gigas*. Each layer also consists of first-, second-, and third-order lamella [161].

This investigation is focused on the mechanical response of the middle macro-layer, yet it is important to note that the combination of all three layers is responsible for the mechanical response of the shell. The middle macro-layer shows parallel alignment of first order lamellae, which are composed of many single-crystal tiles (approx 10 μm thick x 150 μm wide) that are stacked upon each other, creating second order lamellae. The orientation of the tiles differs between rows of the second-order lamella in an alternating pattern of approximately ±35-45° rotations. The organic matrix has only been observed in TEM as an electron dense layer around each of the individual tiles [60].

4.1.2.2 Giant Clam shell

The giant clam (*Tridacna gigas*) can grow its shell to widths greater than 1 meter, with weights of over 340 kg [162]. The large amount of shell material produced has made the giant clam of interest in both contemporary, as well as historical context. Moir [163] documented the use of this shell as the raw material for applications such as blades for wood cutting tools in ancient and present day Takuu Atoll dwellers of Papua New Guinea. The structure of the shell has the lowest level of organization of the three materials in this investigation, yet its sheer mass results in a strong overall system. The protective shell consists of two distinct regions, an outer white region and an inner translucent region.

The outer region acts as the animal's first line of defense against the harsh environment. This region appears to comprise approximately one third of the shell thickness and is formed from dense structured layers of aragonite needles approximately 1-5μm in length [163]. Growth bands, which extend perpendicular to the direction of shell growth, are thought to contain a thin organic matrix, partially separating layers of crossed lamellar aragonite needles [164]. The structure of the outer region of the shell, presented in Figure 4.30, somewhat resembles the microstructure of the middle macro-layer of conch shell, yet a considerable decrease in organization is observed. Growth bands form first-order lamellae, separating layers of second and third-order lamellae perpendicular to the direction of growth. The second-order lamella is composed of planes, parallel to the growth direction, which separate planes of needles (third-order lamella) with alternating orientation. The directions of needles alternate between +60º and -60º to the direction of growth for each second-order lamella.

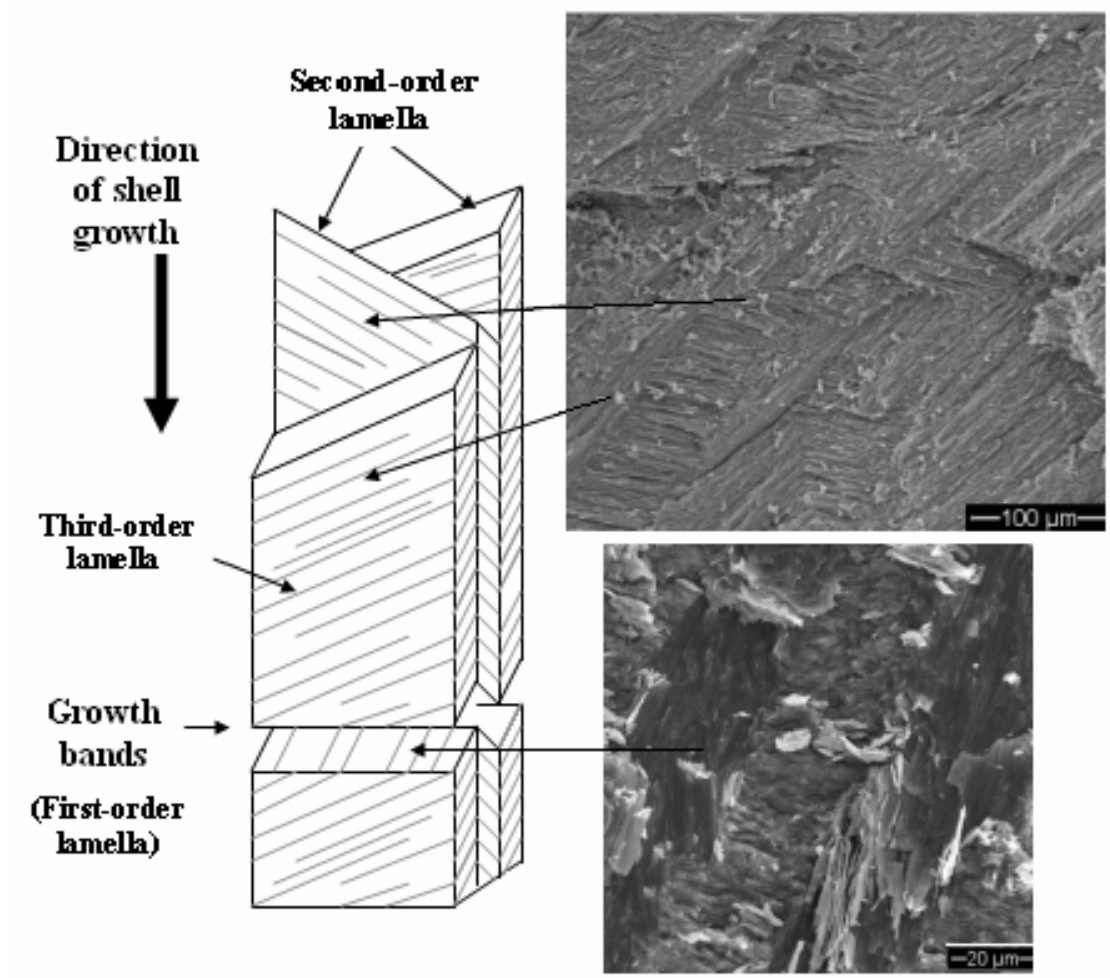

Figure 4.30 Schematic representation and SEM image of *Tridacna gigas* shell outer region.

Within the inner region of the shell, the microlayered structure is also observed as continuous planes of growth bands. These layers separate approximately 3-7µm of inorganic material and span normal to the direction of shell growth. Long single crystals of aragonite travel along the direction of growth and are not interrupted by growth bands. This inner region appears more transparent than the outer region and contains a high concentration of flaws traveling along the single columnar crystal interfaces. These

flaws, in the form of microcracks, travel along the direction of growth facilitating crack propagation along abutting interfaces of neighboring crystals. Figure 4.31 shows an optical micrograph of the microcracks along columnar crystal interfaces. The observed growth bands in the microstructure do not interrupt the growth of single crystals from one band to the next, and thus have a minimal effect on crack deflection.

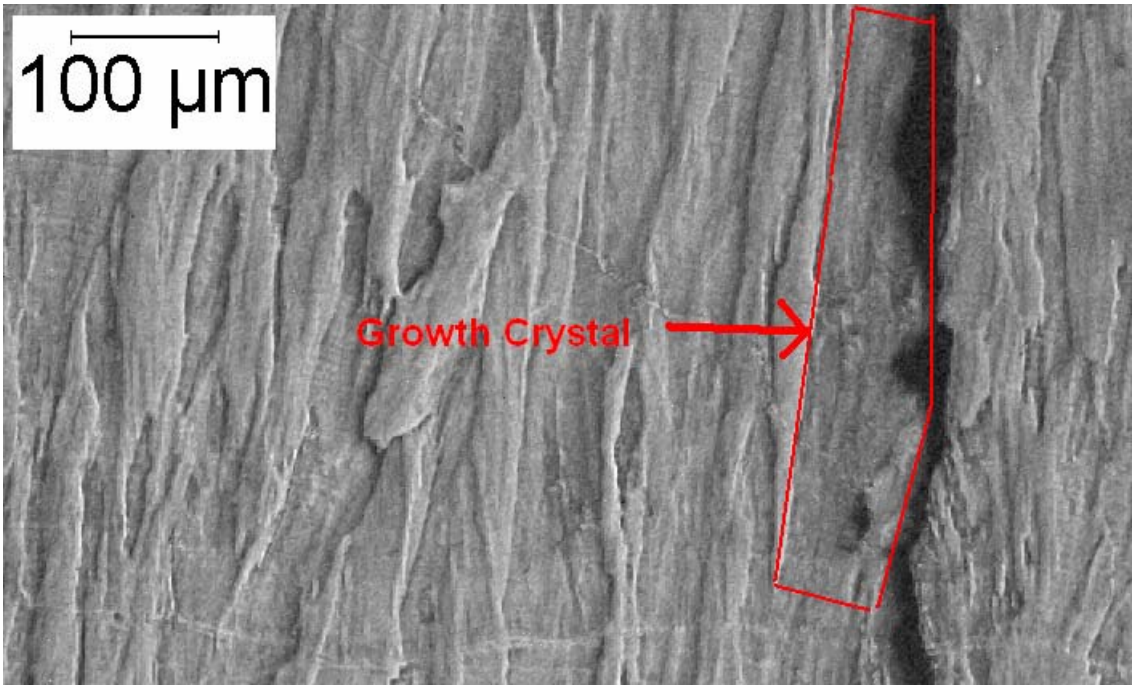

Figure 4.31 Optical microscopy of polished cross-sectional specimen of *Tridacna gigas* shell (inner region), with continuous single crystal facilitating crack propagation.

In all shells tested, there was a considerable dependence of the mechanical response on the direction of loading. Thus, the Weibull statistical plots for each shell

under specific loading conditions show two distinct curves. These curves correspond to compression perpendicular and parallel to the direction of the growth bands. In both the abalone and giant clam shells, it is observed that the compression strength of the material is greater in the perpendicular direction, yet the conch shell exhibits greater compressive strength parallel to the growth bands. This may be attributed to the tessellated "zigzag" pattern of the conch shell in which the direction of growth bands is not constant, creating a more isotropic microstructure and response.

Figure 4.32 (a-c) present the Weibull statistical analysis of conch, giant clam, and red abalone shell in quasi-static compression, respectively. For the conch shell, the failure probability of 50% [F(V)=0.5] is reached at 166 MPa and 218 MPa for the perpendicular and parallel direction of loading, respectively. This is approximately twice the compressive strength of the giant clam shell which showed 50% failure probability at 87 MPa and 123 MPa for loading parallel and perpendicular to layered structure, respectively. The abalone shell outperformed both the conch and the giant clam shells by over twice the compressive strength in quasi-static loading. With failure probabilities of 50% being reached at 235 MPa and 540 MPa with loading parallel and perpendicular to layered structure, respectively, the abalone also exhibits the highest difference in strength between loading directions, consistent with the level of microstructure anisotropy

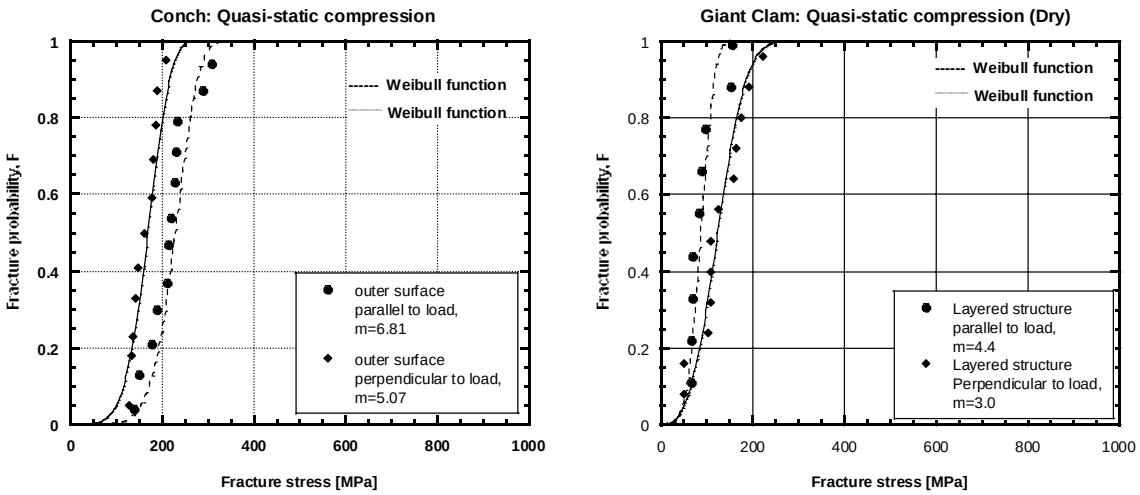

(a) **(b)**

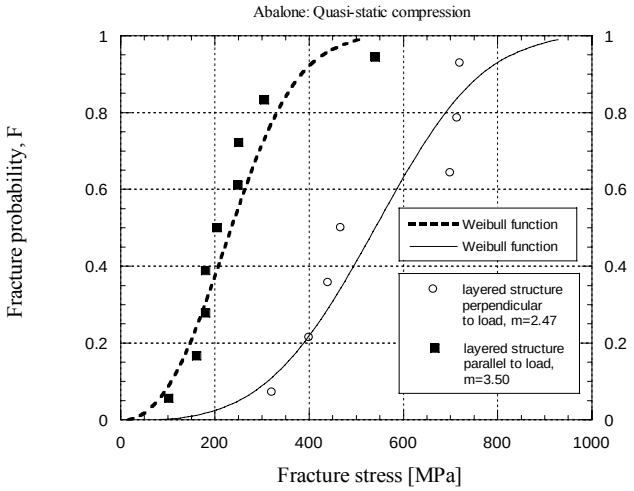

(c)

Figure 4.32 Weibull analysis of; **(a)** *Strombus gigas*, **(b)** ***Tridacna*** *gigas*, **(c)** *Haliotis rufescens* shells in quasi-static compressive loading.

Dynamic compression results for the three shells are presented in Figure 4.33(a-c), respectively. A similar trend in dynamic compression strength is observed with the compressive strength of abalone approximately twice that of the conch shell, and the conch shell having approximately twice the compressive strength of the giant clam shell. The 50% failure probabilities of the conch shell are found at 249 MPa and 361 MPa in dynamic loading perpendicular and parallel to layered structure, respectively. The 50% failure probabilities of giant glam in dynamic compression are found at 154 MPa and 202 MPa for parallel and perpendicular loading directions, respectively. As in quasi-static loading, the compressive strength of the abalone shell is superior in comparison to the conch and giant clam under dynamic loading. 50% failure probabilities for the abalone shell are found at 548 MPa and 735 MPa with the layered structure parallel and perpendicular to loading, respectively. It is clear that the materials all experience greater compressive strengths in dynamic loading than in quasi-static loading.

As in compression, the abalone shell is found to have the highest bending strength of the three shells. Surprisingly, the outer, white region of the giant clam shell slightly outperformed the conch shell. The loading direction dependency of the conch shell, with respect to its bending strength has large variations due to the tessellated “zigzag” pattern of the conch shell, in which the direction of growth bands is not immediately obvious and could be taken in either direction.

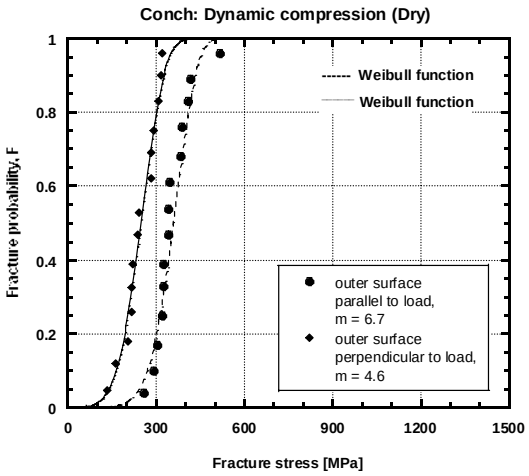

(a)

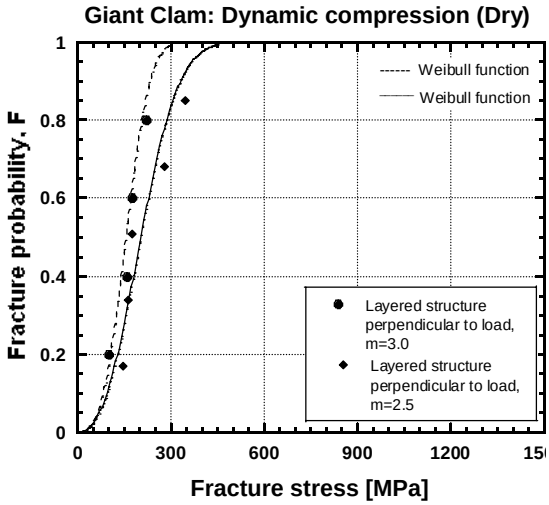

(b)

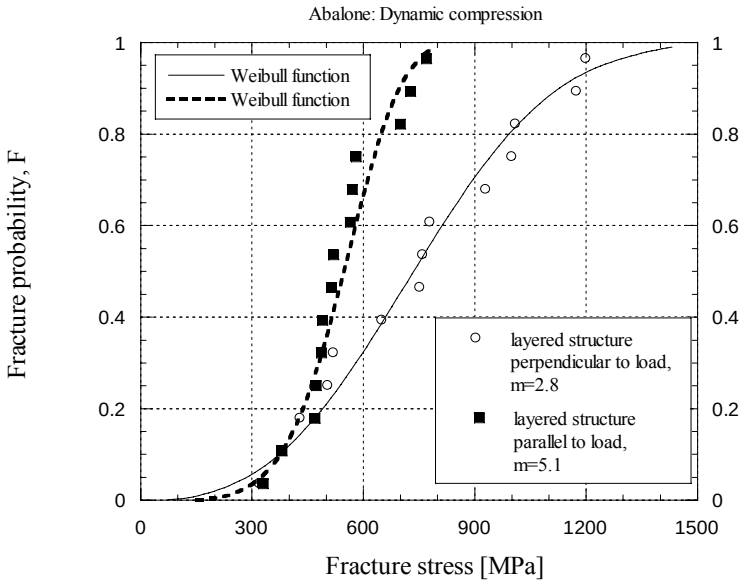

(c)

Figure 4.33 Weibull analysis of; **(a)** *Strombus gigas*, **(b)** *T**ridacna** gigas*, **(c)** *Haliotis rufescens* shells in dynamic compressive loading.

4.1.2.3 Characterization of Damage

Conch shell:

In most brittle materials under compressive loading, failure tends to occur as a result of an axial splitting mechanism, in which fracture occurs parallel to the loading direction (e.g. [46]), and the conch shell tested here fails in a similar manner. Through the middle macro-layer crack propagation is blunted along the organic-inorganic interface before traveling through second-order lamellae [161]. Figure 4.34 presents the resulting zigzag pattern created during failure. In this mode of failure, cracks are bifurcated and delocalized, increasing the toughness of the material.

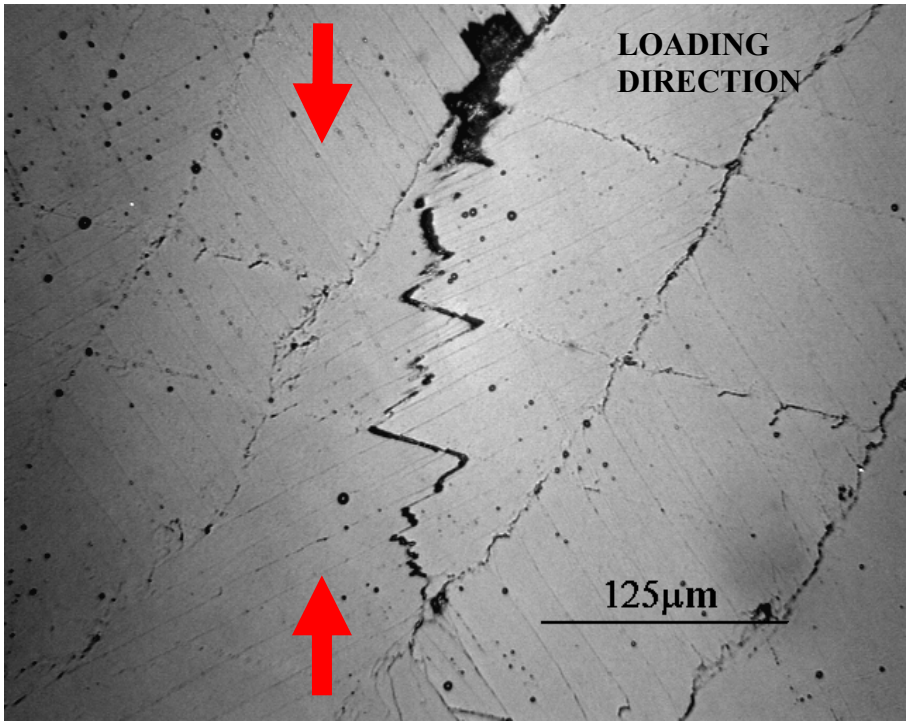

Figure 4.34 Crack propagation through middle section of *Strombus gigas* creating a zigzag pattern through second-order and third-order lamella [161].

Figure 4.35 shows scanning electron micrographs of the fracture surface of the conch shell: (a) parallel to the direction of growth, and (b) perpendicular to the direction of growth. The second and third-order lamellae of the shell structure and its cross-laminar structure of alternating directionality are shown in Figure 4.35 (a). Separation of the lamellae at both levels is observed as fracture travels along second-order lamella wandering between third-order lamellae aragonite crystal. This failure mechanism creates a step-like fracture described by Menig *et al.* [161], in which third-order lamellae fracture surfaces resembles the fibrous surface of broken wood.

The fracture surface of a sample under tension (created through bending) along the axis of shell growth is shown in Figure 4.35 (b). Separation along this axis exposes all three orders of lamellae as described in Figure 4.30. Planes of aragonite tablets in alternating orientation comprise the second order lamellae. The conch shell structure achieves its toughness through its hierarchical lamellae microstructure, in which single crack tips are delocalized by a large number of smaller cracks over a broader region, alternating direction at each lamellar level.

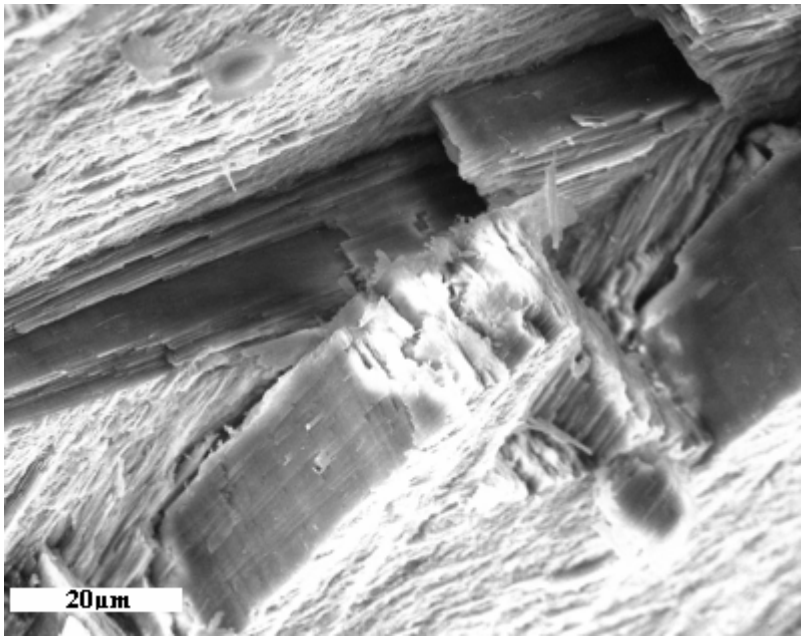

(a)

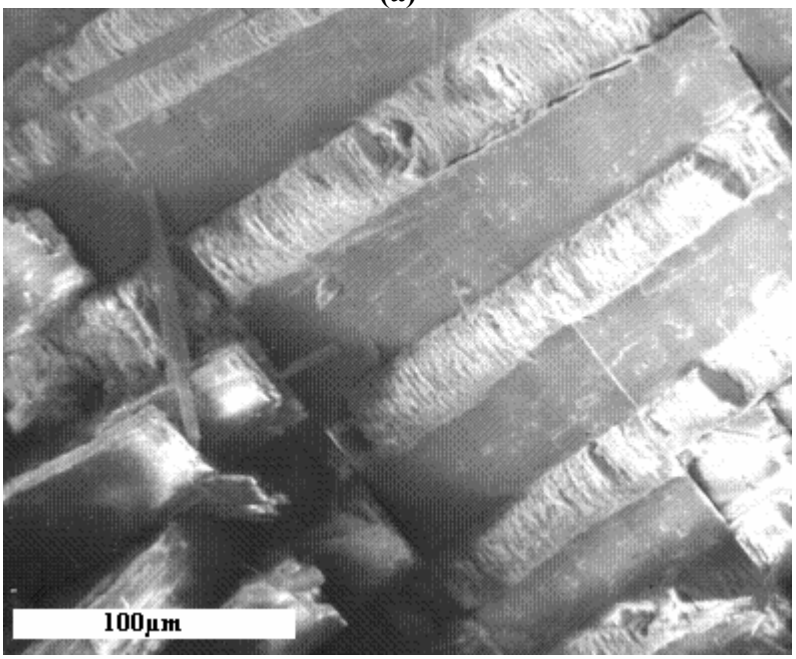

(b)

Figure 4.35 Fracture surface of *Strombus gigas* (a) parallel to growth direction, (b) perpendicular growth direction.

Giant clam shell:

The microstructure of the *Tridacna gigas* (giant clam) shell consists of both an inner, translucent brittle region, with relatively low organization, and an outer white, tougher region, which resembles the shell of the *Strombus gigas* (conch). The inner region fails at the crystal interfaces seen in Figure 4.30 through a mechanism of axial splitting. Initial microcracks within this region extend and coalesce under applied stress, resulting in the failure of the shell samples.

The material suffers in mechanical strength as a result of these flaws, resulting in weak properties in comparison to other shells, such as conch and abalone [161,32]. It is important to note that the mechanical strength of the outer solid white region of the clam shell is over ten times that of the inner translucent region. Figure 4.36 shows scanning electron microscopy of the fracture surfaces of the shell in bending (a) perpendicular to growth bands, and (b) parallel to growth bands. A cross lamellar structure can be seen in Figure 4.36 (a), in which the horizontal line marked with an arrow is a growth band extending perpendicular to the fracture surface. The alternating planes of fibrous crystals travel at 30 degree angles to the planes of the growth bands. Separation of material at the growth band interfaces occurred in shear during bending loading perpendicular to planes of growth interruption. Figure 4.36 (b) shows the fracture surface of a sample under tension in bending. Separation occurred across a single growth band, and second-order lamellae are observed as planes of fibers traveling perpendicular to the fracture surface and alternating in fiber angles. The surface separated cleanly at a single growth band across the entire sample. These observations indicate that separation occurs at the growth

band interfaces in both loading directions, parallel and perpendicular to the growth direction.

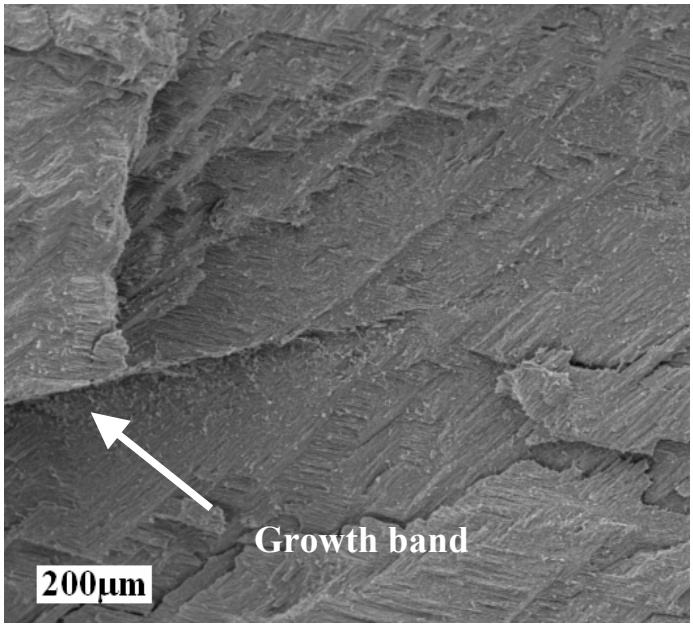

(a)

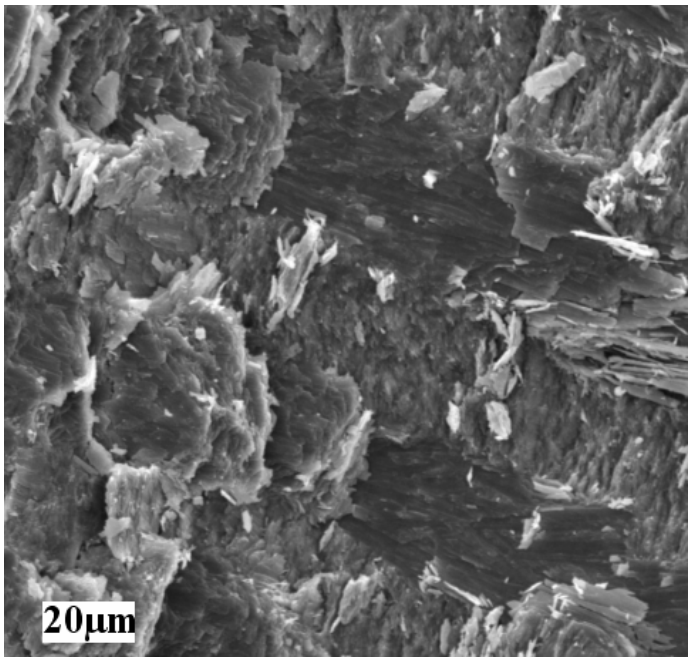

(b)

Figure 4.36 Fracture surface of *Tridacna gigas* under bending (a) perpendicular to growth bands, (b) parallel to growth bands

4.1.2.4 Hydration Effects

An investigation into the role of hydration was conducted on the shell of the giant clam to establish the importance of the visco-elastic organic matrix on the toughness of the overall system. Samples from a dried shell were sectioned into cubes for compression parallel to the growth layers and left in salt water for periods of one, two, and three weeks. The stress vs. strain curves for all three hydration periods can be seen in Figure 4.37. It can be seen that the area under the curve, representative of material toughness, increases with increasing hydration. If it is assumed that the majority of hydration absorption takes place in the organic component of the shell one can conclude from the trend in Figure 4.37 that the visco-elastic response of the organic matrix is a critical toughening mechanism in the over all system.

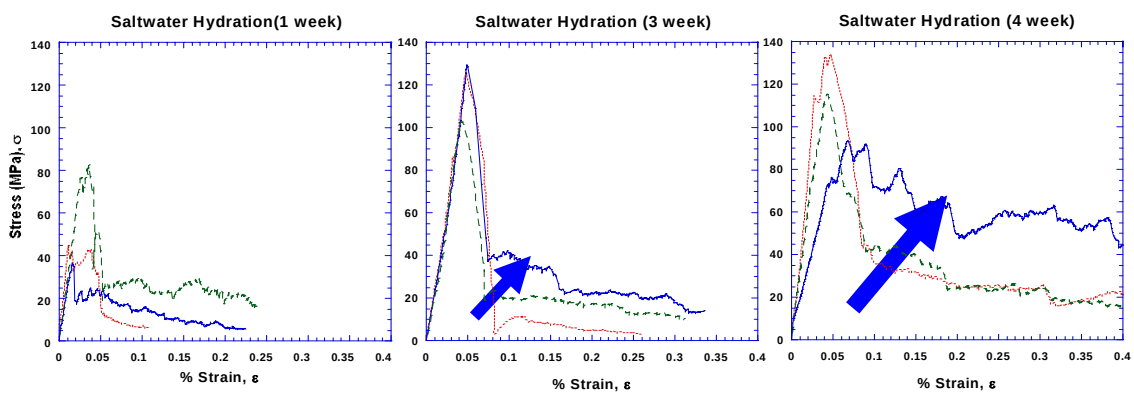

(a) (b) (c)

Figure 4.37 Stress-strain curves of compression on the giant clam parallel to growth layers. Samples were hydrated in salt water for: (a) one week; (b) two weeks; (c) three weeks. Each plot shows results from three individual samples represented by various curves.

From the observations and analysis within this study, it is clear that the micro-structure and macro-structure of these shells plays a significant role in increasing the toughness of an otherwise brittle base material, $CaCO_3$. In each shell, the viscoplastic deformation of the organic interfaces and the crack delocalization due to the layered microstructure of the inorganic aragonite lead to an increase in mechanical strength of the biocomposite above its base monolithic aragonite.

Of the three shells in this investigation, it was neither the most organized structure (conch shell) nor the least organized structure (inner section of giant clam shell) that exhibited the greatest mechanical strength, but rather the abalone, with its optimized hierarchically organized brick-and-mortar system. The abalone exhibited a compressive strength approximately twice that of conch shell and four times that of the giant clam shell, when loaded either quasi-statically or dynamically. The inner section of the giant clam is an order of magnitude weaker then the outer section of the same shell due to differences in microstructure. A strong dependence on loading direction with respect to microstructure was observed in all of these shells. It can be concluded that the microstructure of these biological materials determines the mechanical properties of each shell, with structures having an over-organized, under-organized, or optimized hierarchy.

4.2 Growth (Biomineralization)

The goal of the following study is to build upon the body of information surrounding the mechanism of biomineralization by investigating the processes involved in the natural formation of abalone nacre. This is done by investigating the various transition periods which occur during the process of shell formation.

The inorganic $CaCO_3$ undergoes morphological changes before and after the interrupting growth bands [120]. Figure 4.38 provides a macrostructural view of a cross section of the inner nacreous layer. Organic bands approximately 8 μm thick can be seen separating larger, 300 μm thick, regions of nacre. These "mesolayers" mark interruptions in nacre growth, and thus are therefore also called growth bands. In Figure 4.38 (a), the growth occurs from bottom to top. Prior to arrest of growth, the characteristic tiles are replaced by a block-like structure (B). This is followed by the massive deposition of the organic layer, which is initially intermediated with mineralized regions. At the end of the mesolayer, when mineralization starts again, a layer comprised of a spherulitic structure is observed. The inorganic $CaCO_3$ undergoes morphological changes before and after the interrupting growth bands [120]. As seen in Figure 4.38 (b), five regions can be identified (direction of growth marked by arrow): tiled (A); block-like aragonite (B); organic/inorganic mix (C); organic (D); and spherulitic (E). The growth sequence is described in greater detail by Lin and Meyers [35].

In Figure 4.38 (b), the growth occurs from bottom to top. Prior to arrest of growth, the characteristic tiles are replaced by a block-like structure (B). This is followed by the massive deposition of the organic layer, which is initially intermediated with

mineralized regions. At the end of the mesolayer, when mineralization starts again, a layer comprised of a spherulitic structure is observed.

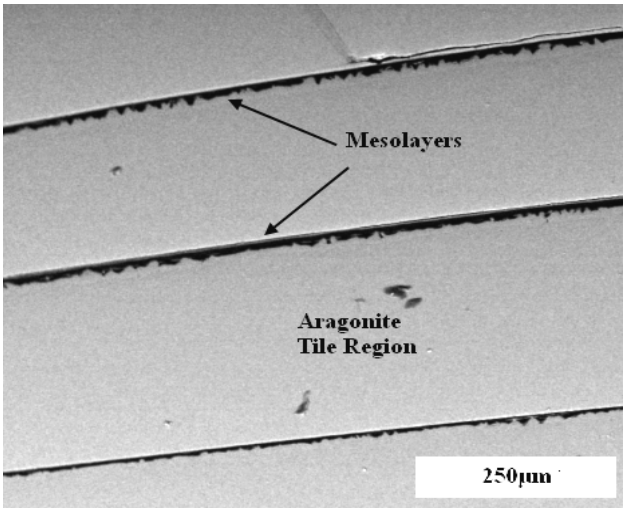

(a)

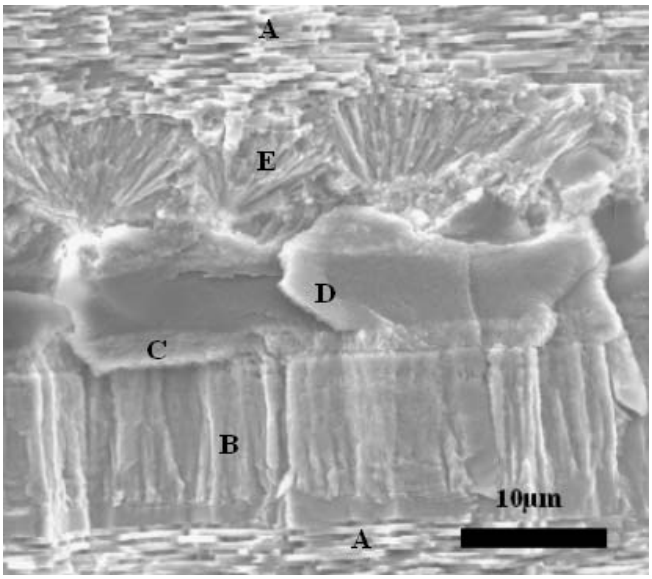

(b)

Figure 4.38 (a) Macrostructural view of a cross section of the *Haliotis rufescens* shell. Growth bands are observed separating larger regions of nacre, (b) SEM micrograph of fracture surface; direction of growth marked with arrow.

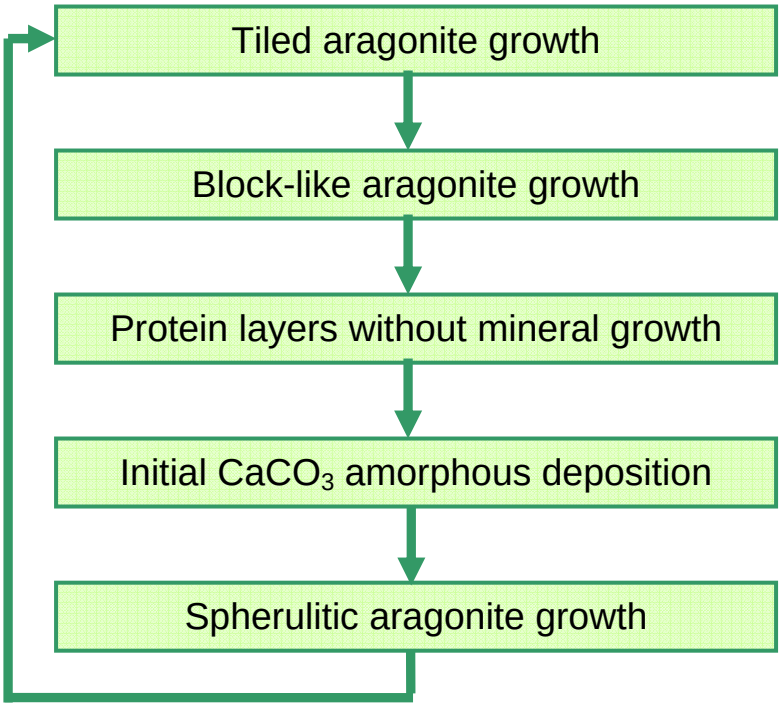

Figure 4.39 Order of events during mesolayer growth in nacre.

Figure 4.39 indicates the sequence of events which occurs during the formation of a mesolayer. The re-initiation of crystal growth following the period of interruption is of great interest. The process in which the scaffolding template for ordered tiled aragonite is developed from a plane of random amorphous nucleation provides insight into the mechanisms with which biomineralization may take place. By investigating the short period over which the organic symphony of proteins is able to develop this self perpetuating crystal growth we inch closer to the greater understanding of natures building tools.

4.2.1 Implantation Experiments:

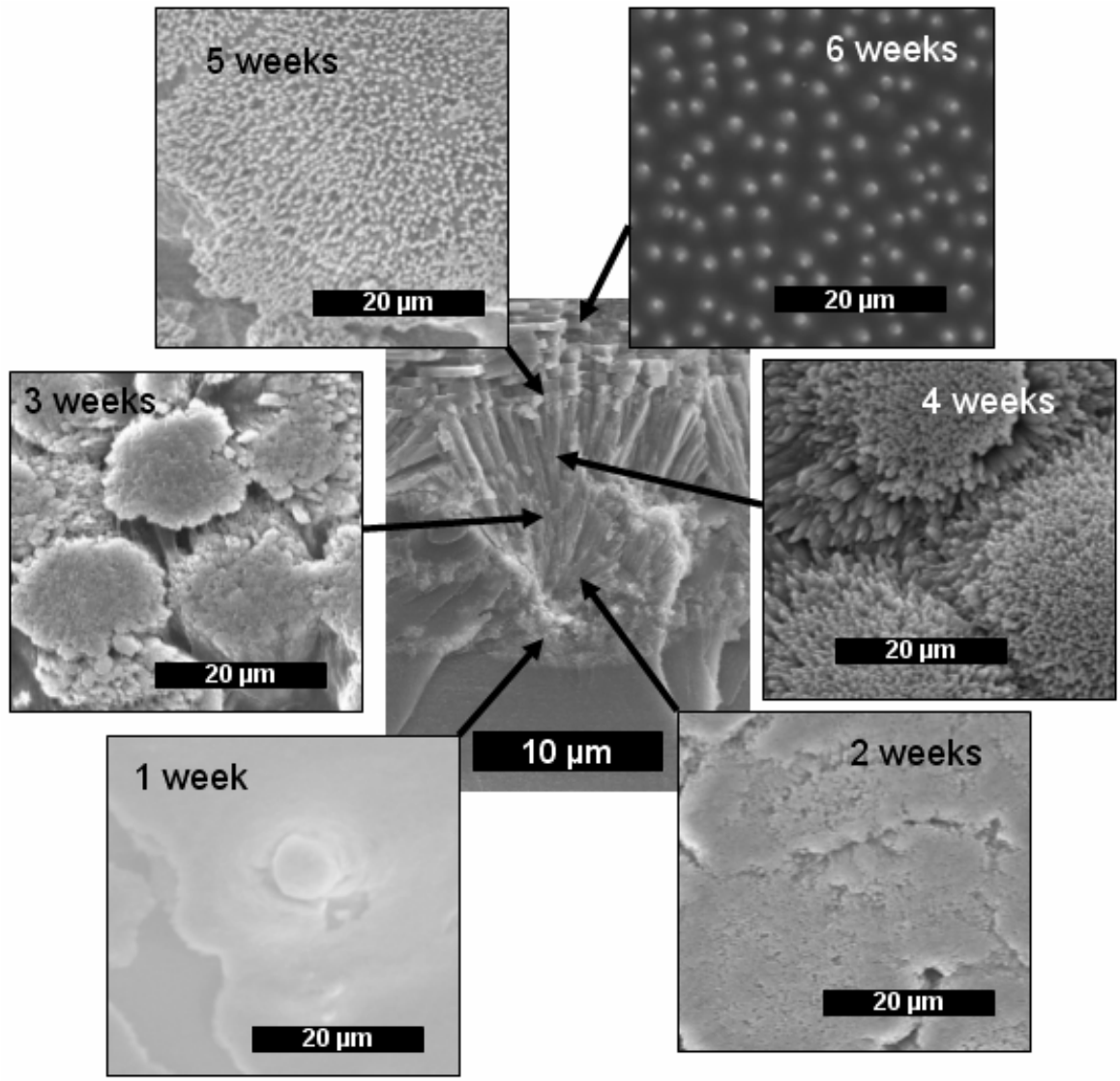

Figure 4.40 Summary of sequential growth from flat pearl and trepanning experiments.

Both the "flat pearl" technique and the "trepanning" technique are introduced into the growth to observe the various formations following steady state growth interruption. The results of the sequential growth study are presented in Figure 4.40. One week after implantation a precursor amorphous aragonite is begins to appear on the substrate. Two weeks after implantation, the precursor aragonite has spread across the entire substrate.

None of the original implantation is left exposed. As seen in the lower half of Figure 4.40, the morphology of deposited mineral transitions to spherulitic aragonite between the second and third week. It was earlier thought that the spherulitic layer was calcitic [31], but Su et al. [33] incontrovertibly identified it as aragonitic; this was also later reconfirmed by Lin et al. [120].

After three weeks of implantation the tops of each spherulitic bundle appear flattened. This is thought to be the result of a constant pressure or a rubbing force exerted by the mantle of the animal itself. It is proposed that the animal forms the structure of the shell through a mechanical-chemical action.

The self-assembly of aragonite in nacre does not translate into the overall architecture of the shell; the animal continuously molds it. The animal has the ability to apply a significant amount of binding force to keep itself attached to virtually any surface. This is action paired with a strong muscle contraction between the foot and the shell. This force translates to an approximately equal and opposite force applied normal to the growth surface of the shell as indicated in the schematic below.

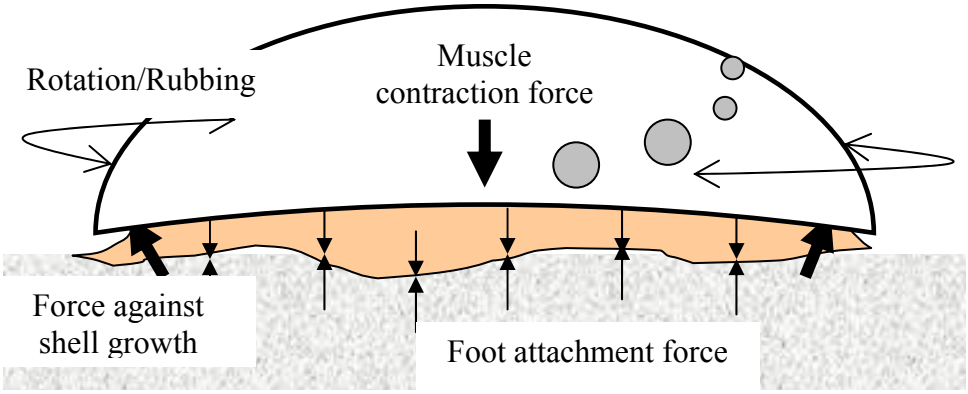

Figure 4.41 Schematic of the forces acting on the growth surface of the shell.

The epithelial layer of the mantle sits directly over the growth surface. As the animal moves along a rock or a wall it twists itself in a rotating manner. The epithelial skin slides back and forth along the shell producing a sanding effect over the growing mineral structures. This mechanical flattening of the growing surface occurs throughout the nacre deposition region and is evident in all SEM images.

After four weeks of implantation, the spherulites are fully formed as a result of the divergent growth of aragonite columns along the fast growing c-axis direction. The cross-sectional view of a growth band, shown in Figure 4.38, shows the divergent growth of these columns. They spread apart into a lower density as growth continues after five weeks of implantation.

Between five and six weeks of implantation the aragonite morphology transitions towards the regular tiled aragonite microstructure as shown at the top of Figure 4.40. It is hypothesized that this transition may occur as the ends of each spherulitic needle become nucleation sites for aragonite tiles. The intermittent deposition of the organic matrix which is believed to inhibit crystal growth [153] molds the spherulitic aragonite needles into an increasingly laminate structure, eventually reaching the steady-state aragonite tile formation. At six weeks the tops of the "Christmas tree" tile columns can be seen to protrude through intermittent thin organic sheets. They are spaced approximately 3-5 µm apart, indicating a density much less then the density of spherulitic needles.

The composition of the first mineral layers formed after one week of implantation. These were identified by Raman spectroscopy to be aragonite. The position of the Raman bands shown in Figure 4.42 coincides with those reported by Urmos et al. [75] for biogenic aragonite. The intense band, near 1086 cm^{-1} (A_{1g})

corresponds to the v_1 symmetric stretching of the carbonate ion. Further verification was provided through electron diffraction spectroscopy (EDS). These results are in concurrence with those described by Su et al. [33].

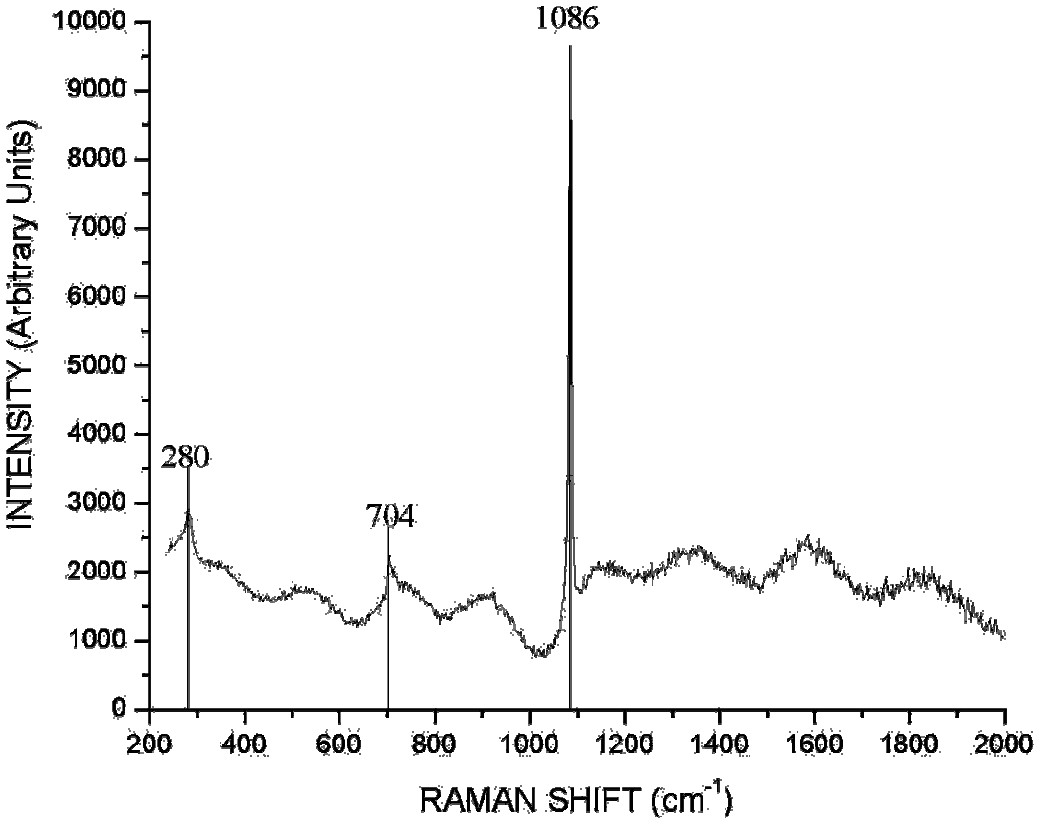

Figure 4.42 Raman spectra of implanted flat pearl one week after implantation. Raman bands verify the material to be aragonite.

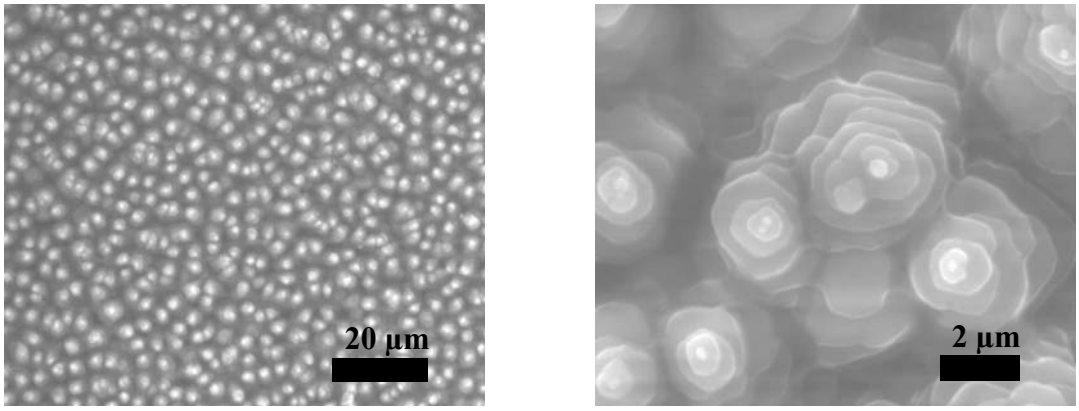

(a) (b)

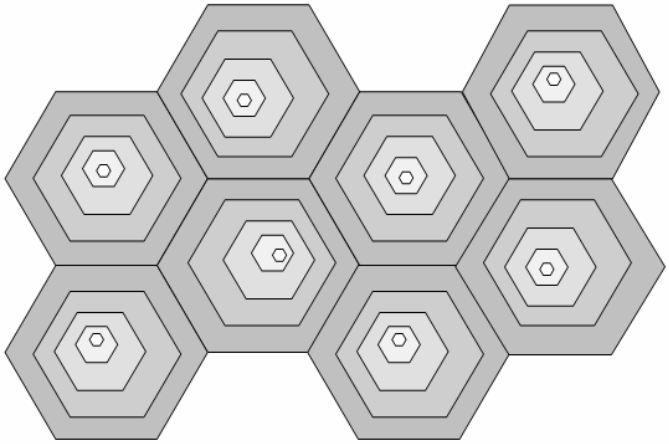

(c)

Figure 4.43 Growth on 15 mm slide after 24 days; (a) low magnification SEM; (b) high-magnification SEM; (c) Schematic drawing showing the same crystallographic orientation.

The "Christmas tree" like growth fields are associated with tiled aragonite growth [26,31,86,87] and can be seen in Figure 4.43. Figure 4.43 (a) shows a low magnification view, and it is seen that the ceramic phase nucleates randomly over the proteinaceous layer. Closer observation, shown in Figure 4.43 (b) reveals the "Christmas tree" pattern

described earlier by Shen et al. [48] and Fritz and Morse [87]. However, it should be noticed that the center-to-center distance is less than the tile size in natural abalone, which is 10 μm. It is possible that the glass from the implants provides greater areal density of nucleation sites; however, similar spacing was observed with the trepanning method [120]. A schematic drawing of adjacent "Christmas trees" is shown in Figure 4.43 (c). Each tile is smaller than the one below it.

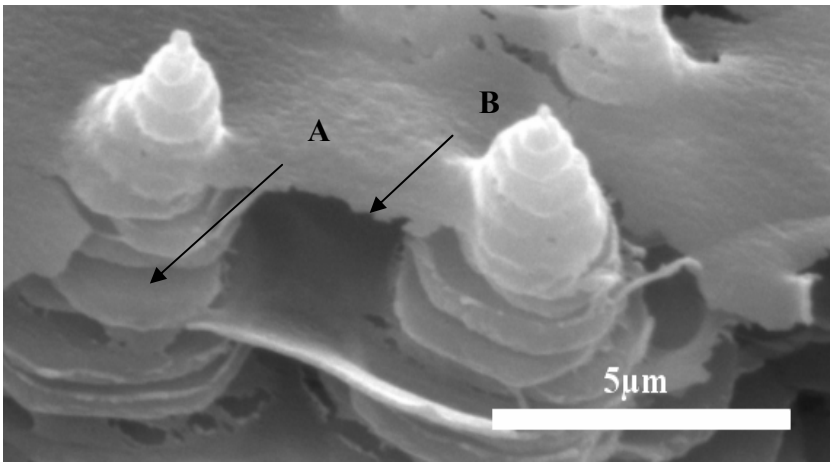

Figure 4.44 Growth of nacreous tiles by terraced cone mechanism; SEM of arrested growth showing partially grown tiles (arrow A) and organic layer (arrow B).

Electron microscopy of a fractured cross-section of the growth surfaces shows columns of sequential aragonite tiles during steady state growth (Figure 4.44). Partially grown tiles can be seen expanding along the a-b axis (marked by arrows A); they are separated by organic membranes which blanket the plane of the growth surface. These membranes are believed to separate the layers of tiles, while allowing mineral bridges to travel through and act as a nucleation site of subsequent aragonite layers.

Figure 4.45 (a) represents the possible sequence in which growth could occur through mineral bridges. The growth sequence is as follows; (i) organic scaffolding forms as interlamellar membranes between the layers of tiles arresting *c*-direction growth, (ii) a new tile begins growth through the porous membrane, (iii) the new tile grows in every direction, but faster along the *c*-axis, (iv) a new porous organic membrane is deposited, arresting *c*-axis growth of the new tile while allowing continued *a* and *b*-axis; growth, mineral bridges begin to protrude through the second organic membrane while sub-membrane tiles continue to grow along the *a* and *b*-axis, sub-membrane tiles abut against each other; a third tile begins to grow above the membrane. As shown, the bridges are believed to be the continuation of mineral growth in the *c*-axis from a previous layer of tiles. They protrude through the growth arresting layers of proteins, creating a site on the covering organic layer where mineralization can continue. These mineral bridges are the seed upon which the next tile forms.

A detailed view of mineral bridges enabling growth through a permeable organic membrane is shown in Figure 4.45 (b). Holes in the organic nanolayer, which have been identified by Schäffer et al. [105], are thought to be the channels through which growth continues. Mineral growth above the membrane is faster than growth in the membrane holes because of the increase in contact area with surrounding calcium and carbonate ions. Since these holes are small (30–50 nm diameter) the flow of ions is more difficult, resulting in a reduction of growth velocity to $V_1 << V_2$ (Figure 4.45 (b)). V_2 is the unimpeded growth velocity in the *c* direction.

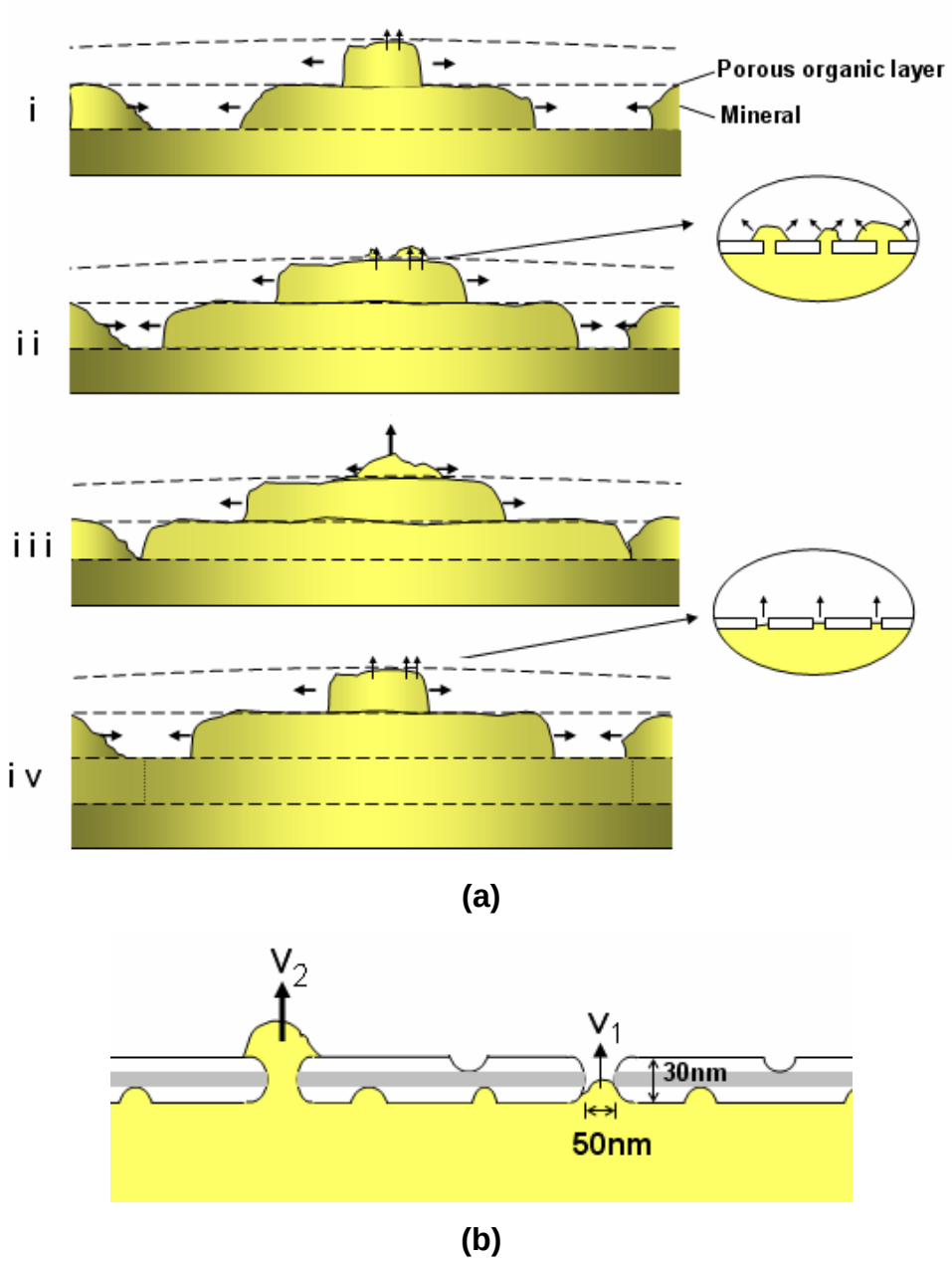

Figure 4.45 (a) Growth sequence through mineral bridges (b) Detailed view of mineral bridges forming through holes in organic membranes [120].

The supply of Ca^{2+} and CO_3^{2-} ions to the growth front is enabled by their flow through the holes in the membranes. This explains why the tiles have a width-to-

thickness ratio of approximately 20 whereas the growth velocity in the orthorhombic *c* direction is much higher than in the *a* and *b* direction.

4.2.2 Transmission Electron Microscopy:

To further prove the existence of mineral bridge-enabled tile growth, and to confirm results by Feng et al. [122], transmission electron microscopy (TEM) with selected area diffraction analysis was conducted across multiple layers of aragonite tiles. The TEM images of two samples with their respective diffraction patterns are seen in Figure 4.46. These results confirm a very high degree of crystallographic texture characterized by a nearly perfect "c-axis" alignment normal to the plane of the tiles, this is represented by the matching diffraction patterns across consecutive layers of mineral. The consistency of crystallographic orientation provides sufficient evidence to verify a mineral connection between consecutive layers of tiles, this could only be made possible through the existence of the above hypothesized mineral bridges.

It should be noted that crystallographic orientation alignment is observed in consecutive layers, and not along the "a-b axis" of adjacent neighboring tiles. This further strengthens the hypothesis of growth mechanics represented in Figure 4.45 (a), in which the intermittent deposition of protein layers mediates but does not completely terminate the c-axis mineral growth.

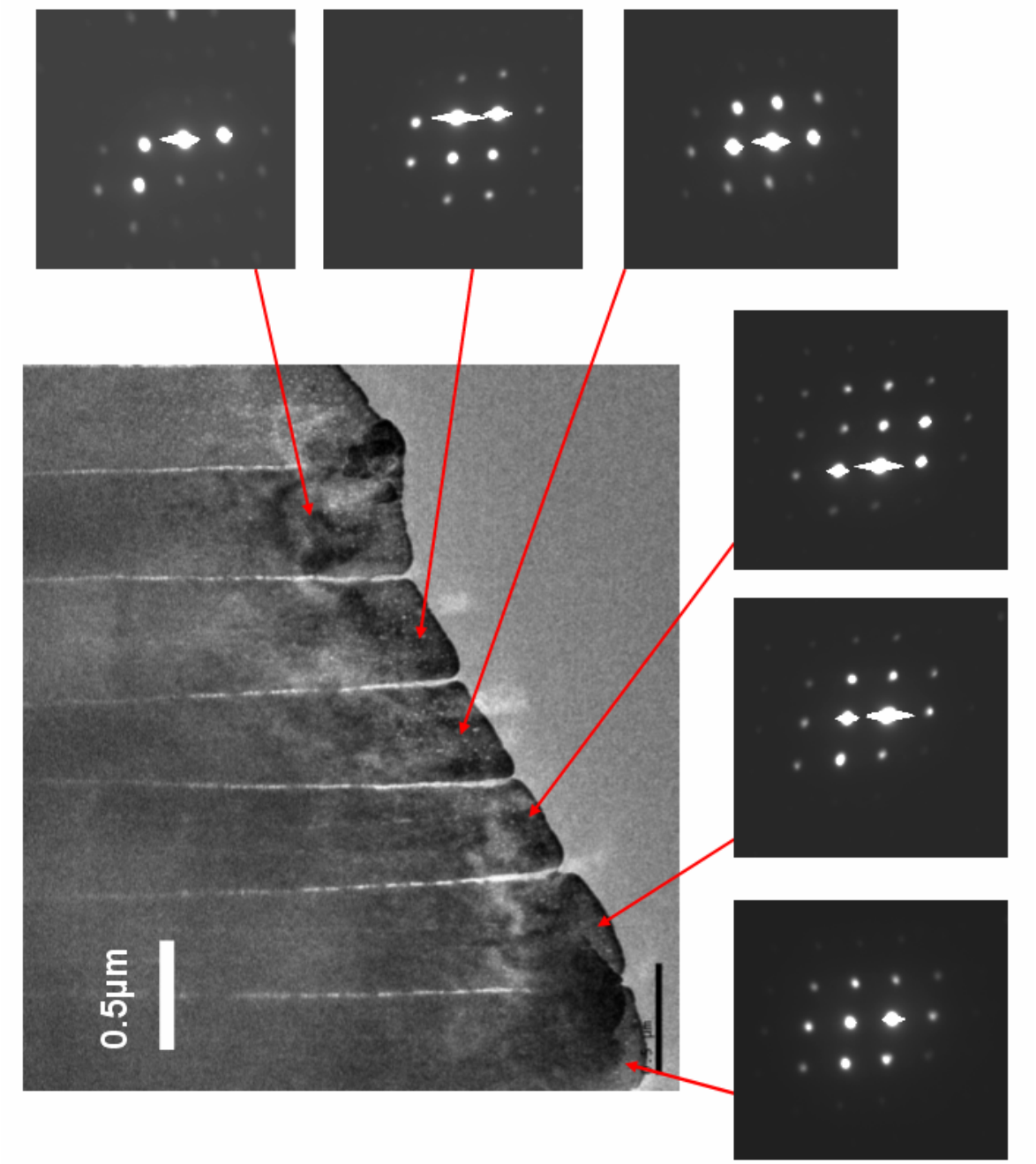

(a)

Figure 4.46 Transmission electron microscopy of tiled aragonite nacre with selected area diffraction.

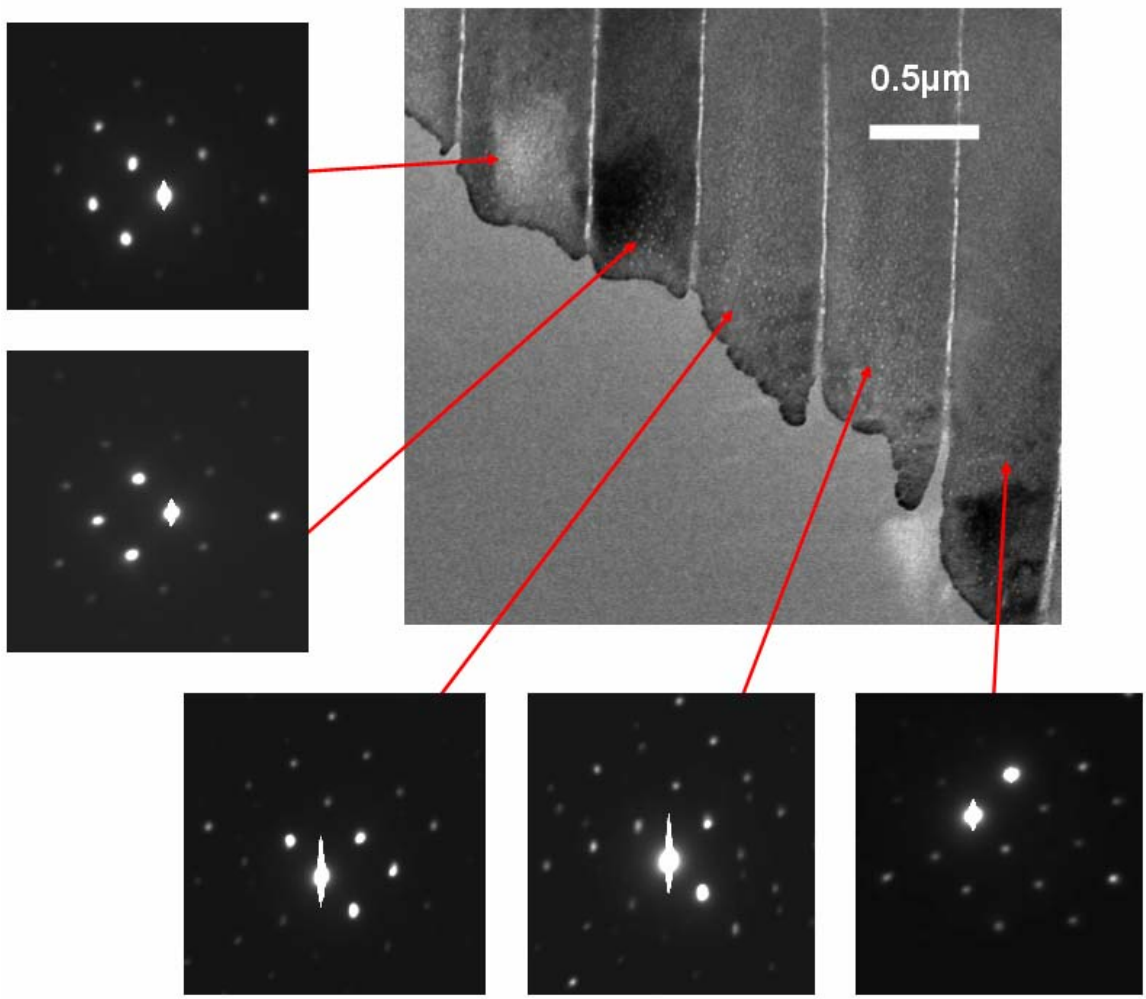

(b)

Figure 4.46 Continued.

Figure 4.47 (a) shows a more detailed view of the growth process. Two adjacent "Christmas trees" are seen. Their spacing, d, determines the tile size. Two growth velocities are indicated: V_{ab}, representing growth velocity in the basal plane (we assume that V_a=V_b) and V_c , the growth in the *c* axis direction. Since the growth in the *c* axis direction is mediated by organic layer deposition, the real growth direction, V_c, is

different from the apparent growth velocity, $V_c^{'}$. The apparent growth velocity (in the y direction) is:

$$V_c^{'} = \frac{dy}{dt} = \frac{c}{t_N + t_G} \tag{4.20}$$

where c is the tile thickness (=0.5 μm). t_N and t_G are the nucleation and growth times, respectively. The velocity of growth in the (a,b) directions is:

$$V_{ab} = \frac{dx}{dt} = \frac{b}{t_N + t_G} \tag{4.21}$$

where b is the increment in tile diameter from layer to layer. The actual growth velocity is given by:

$$V_c = \frac{c}{t_G} \tag{4.22}$$

The cone angle, α, is given by:

$$\tan\alpha = \frac{V_{ab}}{V_c^{'}} \tag{4.23}$$

It is possible to determine α from measurements made on the SEM micrographs of growing tiles (e.g., Figure 4.43 (b)). Measurements were made in several SEM micrographs and the results are plotted in Figure 4.47(b). But the number of unknowns in Eqn. 4.19 – Eqn. 4.22 still exceeds the number of variables; thus, two additional parameters are needed.

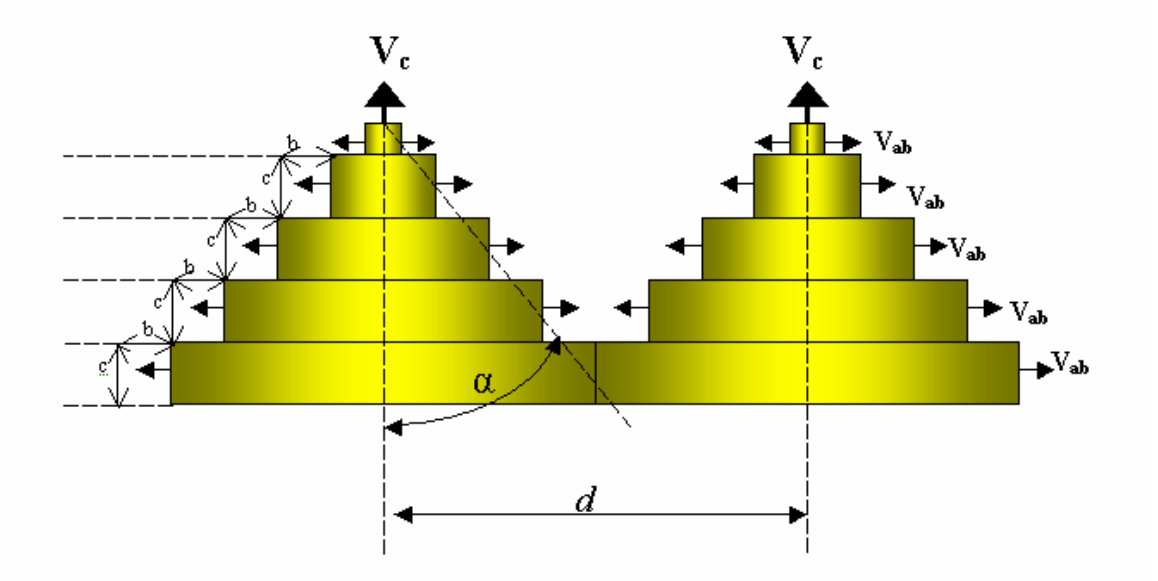

(a)

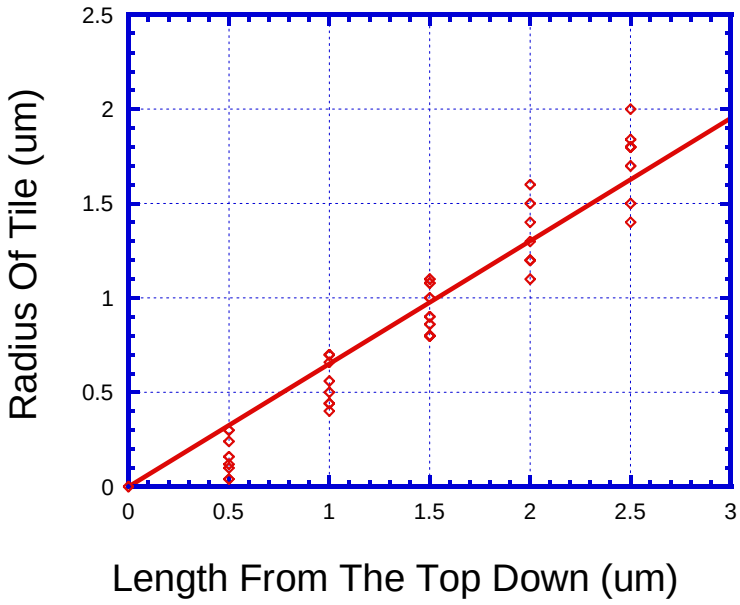

(b)

Figure 4.47 (a) Schematic representation of the growth of two adjacent "Christmas trees" with velocities V_c and V_{ab} along crystallographic axes (*a,b*) and *c* marked. (b) Measured tile sizes, d, for successive layers.

The experimental results obtained herein can serve to estimate the growth velocity, $V_c^{'}$. Approximately ten layers are observed in Figure 4.44 (b). This growth occurred from Day 14 to Day 24. This corresponds to a growth rate of one tile per day, or 0.5 μm/day (5.78x10^{-12} m/s). It should be mentioned that the growth rate in abalone can vary significantly. Lapota et al. [154] report growth rates for red and green abalone. They find seasonal variation in growth velocity, averaging 36 mm/year (in length) for red abalone and 60 mm/year for green abalone. The thickness/diameter ratio for abalone is approximately 1/50. Thus, one can estimate a growth rate $V_c^{'}$= 0.72 mm/year=1.97 μm/day (2.3 x10^{-11} m/s) (for a longitudinal growth velocity of 0.01 mm/day). Zaremba et al. [31] report maximum growth velocities of 5 μm/day, corresponding to 5.78x10^{-11} m/s. Fritz et al. [86] report a growth rate of approximately 14 μm/day on a flat pearl. They report that this is ~26 times the "normal" growth rate for pearls in bivalve mollusks, which would be 0.5 μm/day. This wide variation might be due to the fact that the growth of abalone is not coupled to tidal fluctuations; other mollusks show "growth bands" that correspond to tidal or daily cycles [156].

The uninhibited growth along the *c* axis, V_c, can be estimated from coral growth. Coral is the aragonitic form of calcium carbonate and its growth occurs without protein mediation. This growth takes place in an environment that is fairly close to the one inside the shell. A growth velocity V_c estimated [66] to be equal to 5 mm/year=13.7 μm/day, was used in the calculations below. This yields a growth velocity $V_c = 15x10^{-11} m/s$. For $V_c^{'}$, the value from Lapota et al. [154], which represents a good average, was used: 2.3 x10^{-11} m/s. The value of $\tan\alpha = 2/3$ is directly obtained from Figure 4.47 (b). By

inserting these parameters into Eqn. 4.19 – Eqn. 4.22, one obtains first estimates of the nucleation and growth times, t_N and t_G, respectively:

$$t_N = 16.4x10^3 s$$
$$t_G = 3.6x10^3 s$$

Thus, the time during which the protein is being deposited to arrest and reinitiate the process of biomineralization is approximately equal to five times the growth time. It is also possible to estimate V_{ab}. From Eqn. 4.19 one obtains V_{ab}=1.5x10^{-11} m/s. The ratio V_c / V_{ab} is approximately 10. Direct observations from Thompson et al. [157] give a ratio of approximately 5. It was possible to estimate the angle α measured from Figure 3 of Fritz et al. [87], which shows Christmas trees. Surprisingly, it is significantly lower (α =17^0) than the one measured here (α =34^0). The possible explanation is that the observation direction used by Fritz et al. [87] is oblique. Indeed, a 45^0 between the *c* axis of the tree (tree axis) and observation direction produces the required difference.

After 6 months of controlled culturing of the abalone, changes in growth patterns were observed. A change from tiled aragonite growth to a block-like structure occurred due to environmental changes in the circulating seawater of the holding tank. Su et al. [33] identified the block-like structure formed in the growth bands as aragonite. These changes, in contrast to specimens currently raised in constantly flowing seawater within our facilities at Scripps Institute of Oceanography, can be seen in Figure 4.48. It is estimated that the switch from aragonite growth to calcite growth occurred 6 months before the examination presented in Figure 4.48. This would indicate that the calcite grew an average distance of 40 μm over the span of 6 months along the vertical plane, or 0.22 μm/day. It should be noted that the sample was brittle in comparison to previous

samples that did not present this mesolayer. The cross-sectional view shown in Figure 4.48 reveals several columnar bands extending across the horizontal planes of the shell. It is believed that these bands represent fluctuations in the physical status of the animal.

In order to see whether the tile size was dependent on animal size, 10 mm and 100 mm diameter green abalone were obtained from Dr. Leighton. A 200 mm diameter pink abalone was also examined.

Figure **4.49** shows fracture surfaces for three sizes. The tiles are undistinguishable with the same 0.5 μm thickness and 10 μm diameters. The fracture could be seen to occur by pullout of the platelets in all samples.

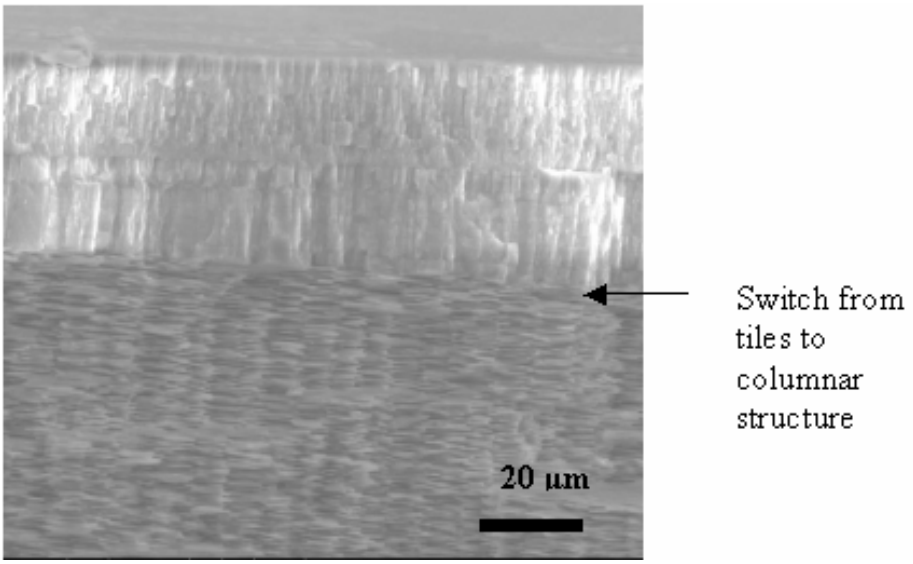

Figure 4.48 SEM micrograph of cross-sectional fracture surface of green abalone shell that has been cultured with environmentally-controlled variations in seawater content and feeding.

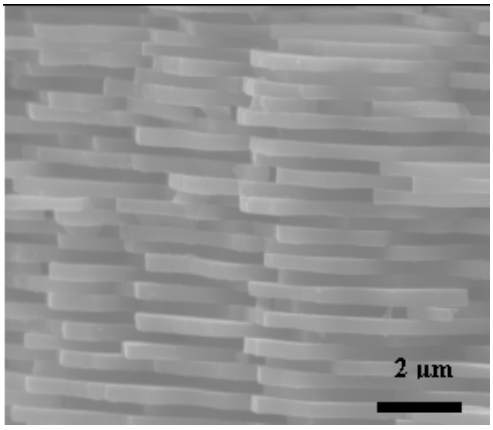

(a)

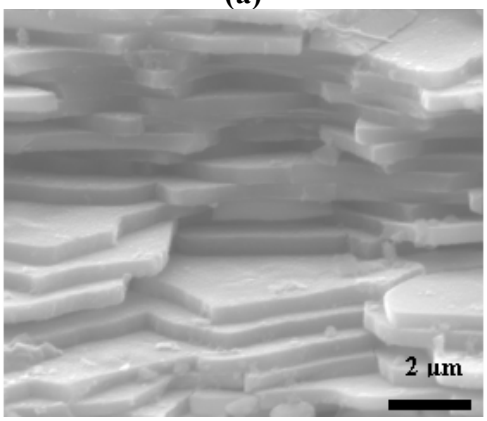

(b)

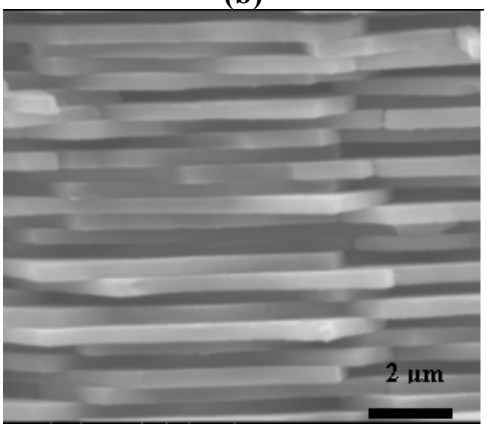

(c)

Figure 4.49. Tile configuration (on fractured surface) for shells having approximately 10, 100, and 200 mm length.

4.3 Functional Biological Materials

Materials in nature are required to serve crucial functional roles in order to avoid the chasm of Darwin's natural selection [201]. The following study examines various biological materials and the ingenious functions with which they are used.

4.3.1 Sharp Materials:

One important survival strategy of many animals is their ability to cut or puncture. This ability is based on sharp edges and serrations. These are important survival and predating mechanisms in a number of plants, insects, fishes, and mammals. Some plants (e.g., Pampas grass: *Cortaderia sclloara*) have sharp edges covered with serrations. The proboscis of mosquitoes and bee stinger are examples in insects. Serrations are a prominent feature in many fish teeth, for example, the piranha and various sharks all possess this feature. Rodents have teeth that are sharpened continuously, ensuring continuous sharpness and efficacy. Here we will examine a few of these sharp biological materials [196].

4.3.1.1 ***Plants: Razor grass***

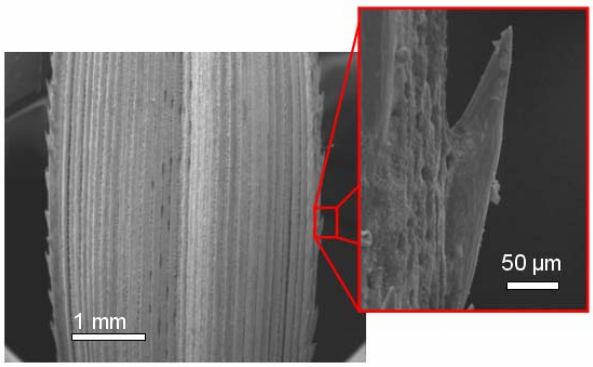

Figure 4.50. Pampas grass; note serrations at edges.

Figure 4.50 shows a blade of pampas grass (*Cortaderia selloana*) with serrations along its outer edge. Each serration is in the shape of a thorn protruding upward along the side of the blade. They extend approximately 50µm from the body of the leaf and form sharp points with an apex angle of roughly 20˚. This sharp cutting edge was evolutionarily designed as a defense mechanism against grazing animals. This feature is also prominent in other grasses, such as *Hypolitrium Sharaderenium*. Another example can be found in cactuses, which have bodies covered in thorns for protection

4.3.1.2 ***Insects: Mosquito and Bee***

Figure 4.51 shows the proboscis of the mosquito (*Culex pipiens*). The proboscis is composed of an outer sheath which is used to detect the surrounding environment such as temperature and chemical balance while there are two tubes which enters its unsuspecting prey. One of them is terminated with an inner stylet that is used to pierce through the skin and draw blood while the other injects an anticoagulant to keep the blood flowing. The figure shows that there are serrations on the edge of the stylet possibly designed to reduce nerve stimulation during a bite by increasing the efficiency of the cutting edge. This is in congruence with K. Oka et al. [197] who concluded that the initial bite of a mosquito is painless because of the highly serrated proboscis.

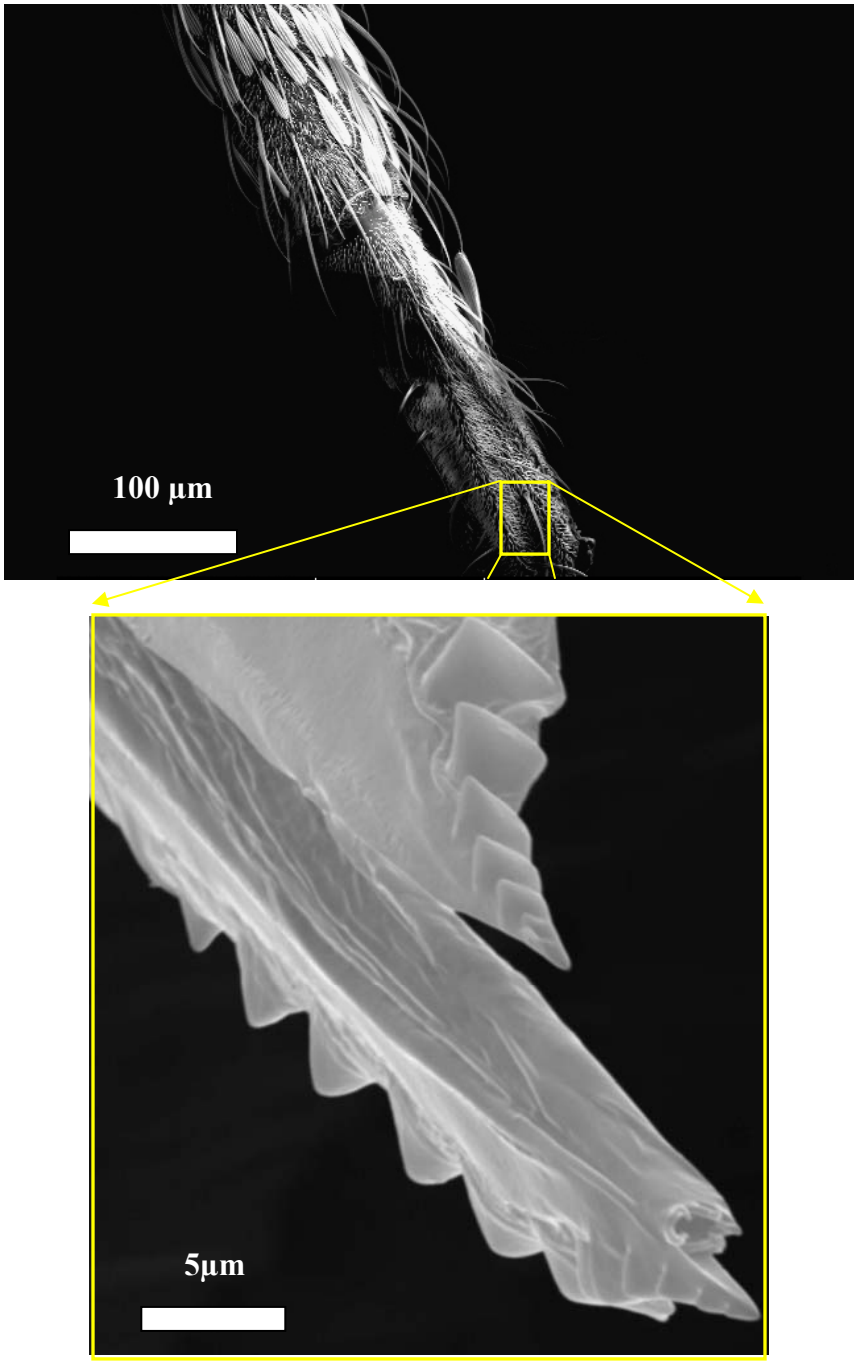

Figure 4.51 Scanning Electron Microscopy of mosquito proboscis; Top: proboscis covered with hairy sheath; bottom: serrated stylet designed to section tissue for dual needle penetration.

The stinger of the common bee (*Apis mellifera*) is yet another example of the efficiency of serrations. It is equipped with reverse facing barbs which are used to propel the needle deep into the tissue of its prey (seen in Figure 4.52). These backward facing barbs are on the scale of 10-20 µm in gauge length and run along the shaft of the stinger. When the insect has used its stinger it stays embedded in the skin.

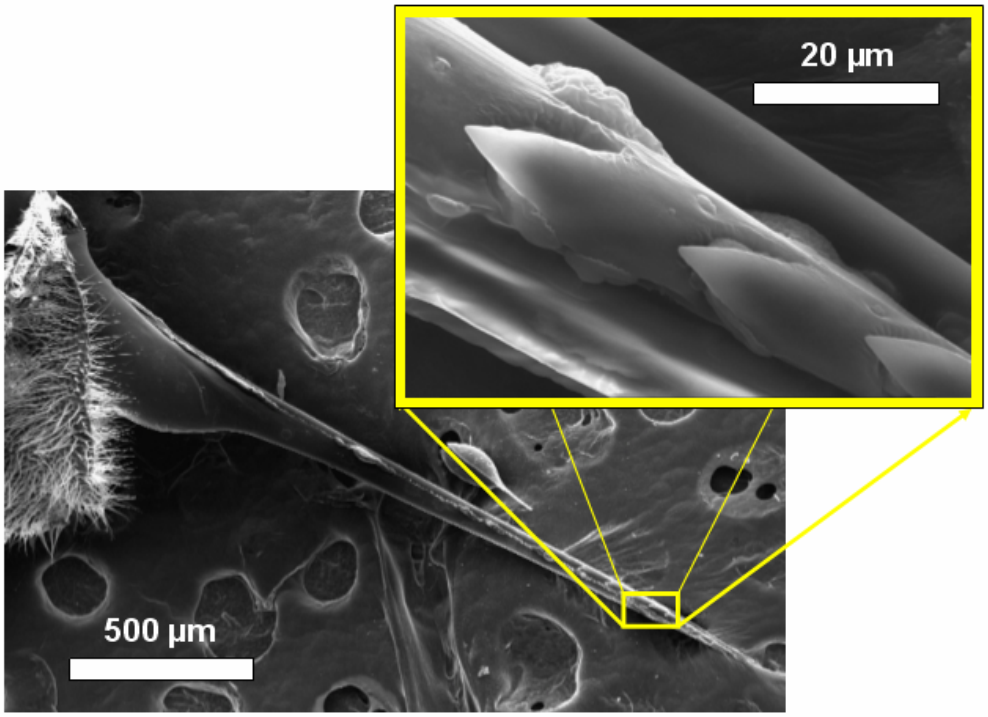

Figure 4.52 Bee (*Apis mellifera*) stinger

4.3.1.3 ***Fish teeth***

We discuss a few fish teeth with emphasis on their function. The "big teeth" of the Amazon dogfish has a piscivorous evolutionary design. They are used to puncture and hold prey and are thus designed in a hook-like fashion facing inward toward the mouth of the fish. This can be seen in Figure 4.53.

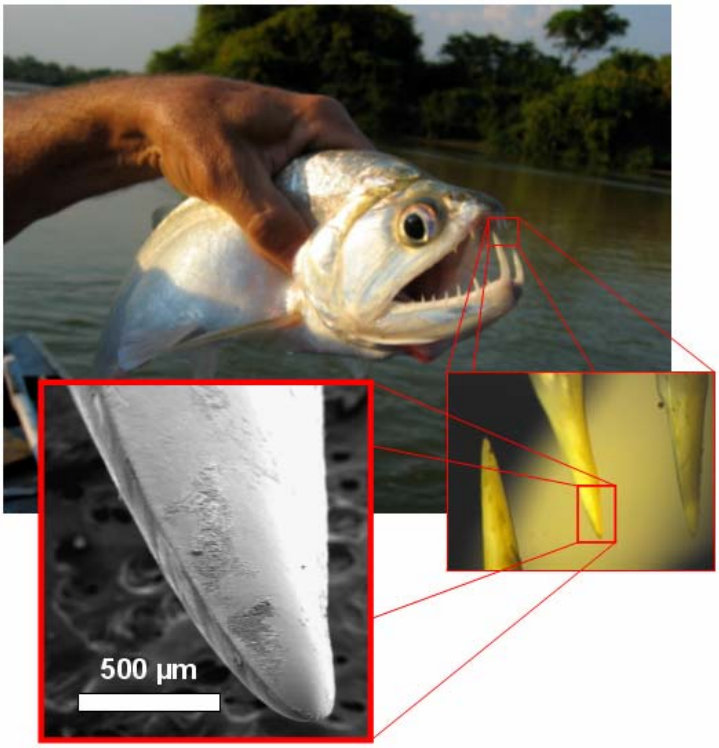

Figure 4.53 Dogfish and teeth.

Figure 4.54 (a) shows structural hierarchy of the cutting mechanisms found in the jaw of a piranha (*Serrasalmus manueli*). The jaw is designed with sharp triangular teeth aligned so that as the mouth of the fish closes the initial points of puncture of both the lower and upper jaw is superimposed. As the jaw further closes, any tissue caught in the trough of the aligned teeth are caught in a guillotine-like confinement of teeth. These serrations, approximately 10-15 µm in wavelength, are used to create a highly efficient cutting effect which converts some of the dragging force into normal force at localized points. This is shown in Figure 4.54 (b). There is a superimposed compression and shear which effectively cuts through skin and muscle. Each tooth exhibits microserrations along its cutting edge, seen in detail in Figure 4.54 (a).

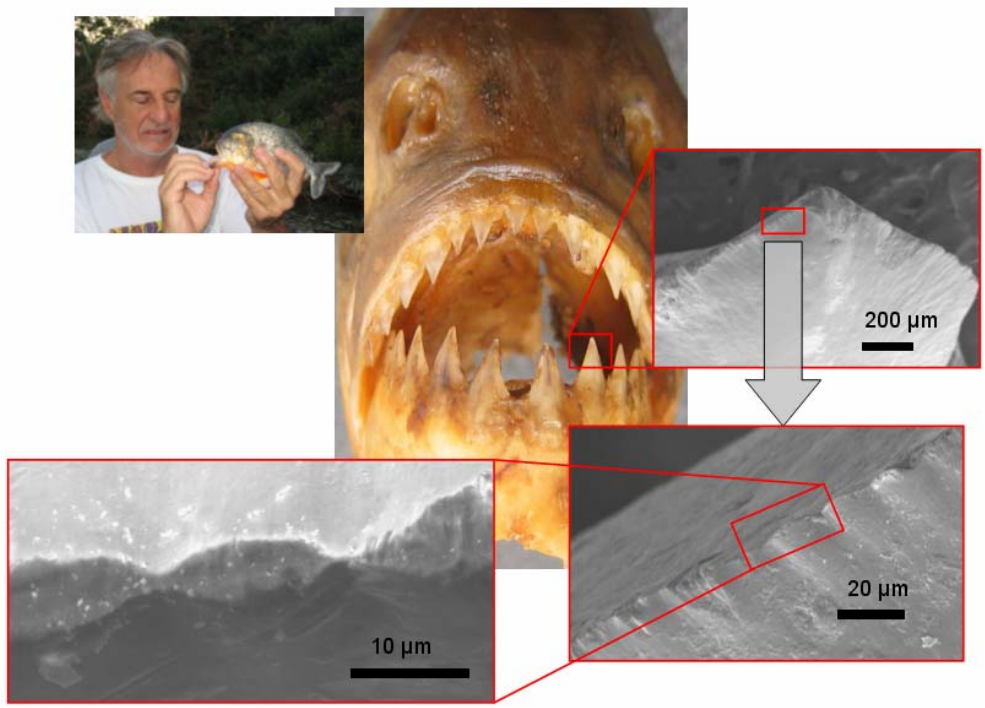

(a)

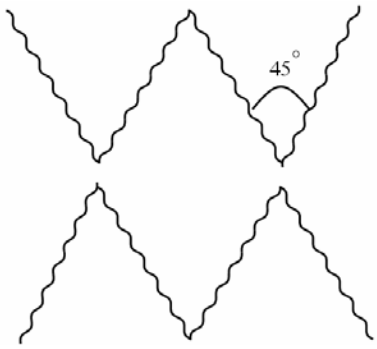

(b)

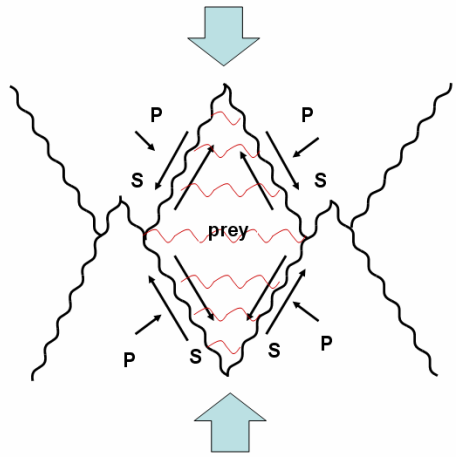

(c)

Figure 4.54 Piranha teeth: (a) hierarchical structure from jaw to single tooth to micro serrations; (b) and (c) diagram of guillotine-like confinement of material during the biting action of a piranha.

The Great White shark (*Carcaradon carcharinus*) evolved teeth from the scales of its ascendants. It uses these extremely sharp teeth to perform a very specific killing game. To avoid self-injury the Great White shark takes one efficiently large bite out of its prey then retreats and waits for its victim to undergo shock or hemorrhaging before final consumption. This bite takes only one second to complete [90] and thus extremely sharp teeth are required. Each tooth is outfitted with a line of large serrations, with up to 300 μm between points. The serrations are perfectly aligned along the cutting edge of the tooth, each creating a mini tooth on the side of its parent tooth. Similar to the piranha tooth the serrations on this edge maximize the efficiency of the drag force and convert it into points of normal force summed along the side of each serration. Figure 4.55 shows: (a) an optical image of the overall jaw of a Great White shark, with multiple rows of teeth, (b) a scanning electron micrograph of the cutting edge of the tooth with large serrations, (c) side view of serrations, (d) top down view of serrations.

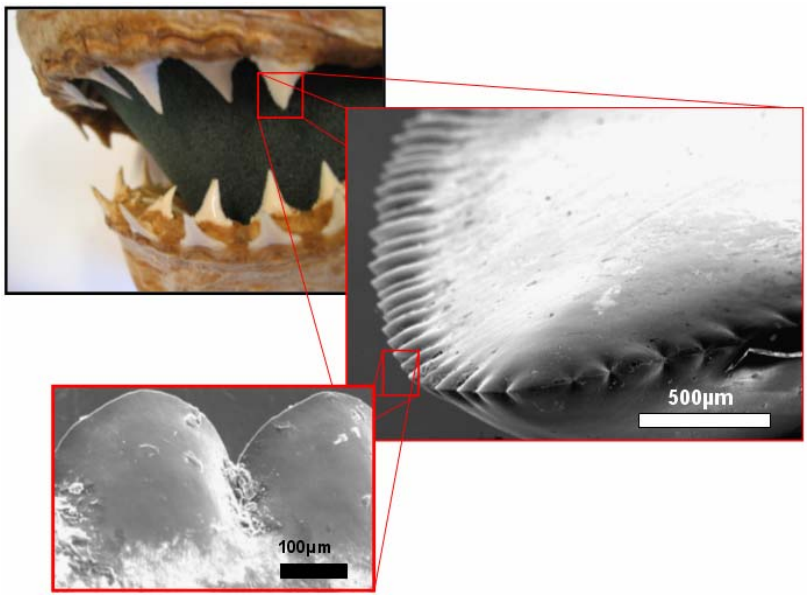

Figure 4.55 Great white shark (*Carcaradon carcharinus*) teeth.

Compared with Great White shark, there are no serrations on the edge of the Shortfin Mako shark (*Isurus oxyrinchus)* tooth. The teeth are slender and slightly curved in a hook-like fashion. The function of these teeth is primarily to puncture and capture prey while in the Great White shark the teeth are used more as cutting tools. It is clear in Figure 4.56 that the angle of the apex of the tooth of a Mako is much smaller then that of the great white. Again this sharp angle, similar to that of the dogfish is used to puncture and swallow pray in one bite.

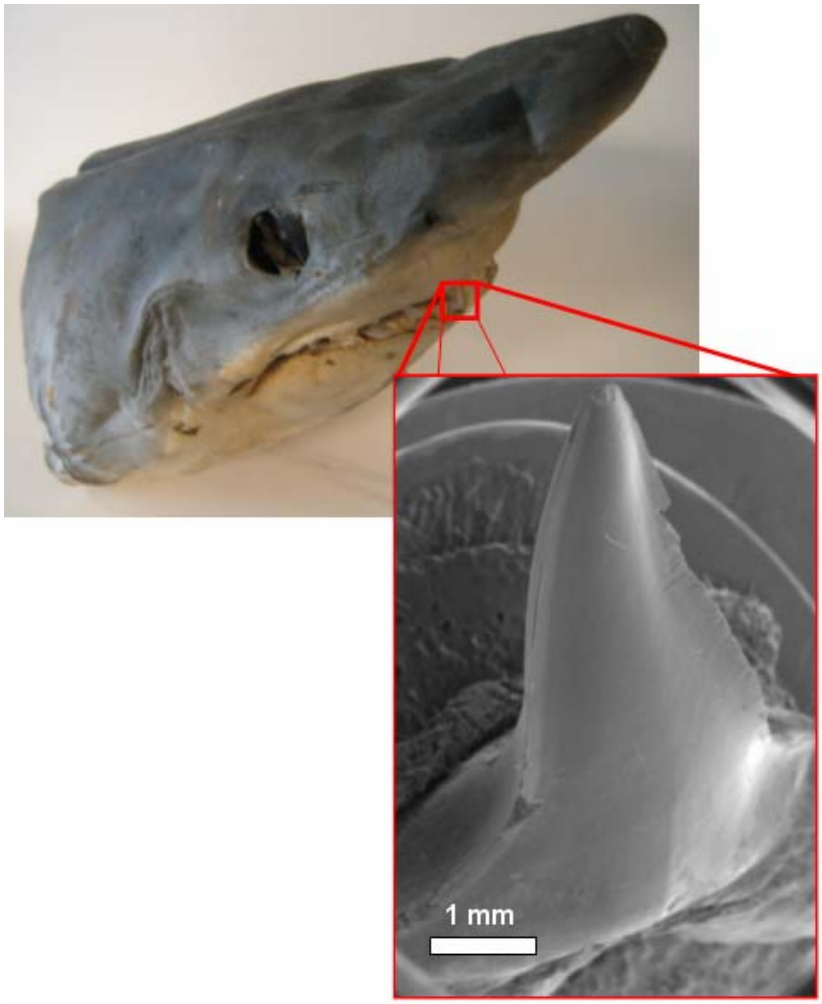

Figure 4.56 Mako Shark and tooth

4.3.1.4 ***Mammal Incisors***

The incisor teeth of animals such as the rabbit and rat (Figure 4.57) have been evolutionarily designed to "self-sharpen" through a process which takes advantage of natural wear and discrepancies in wear rates depending on the hardness of certain materials. These teeth are designed in a way so that a softer dentine backing is worn away at a faster rate then the hard enamel cutting edge. This action continuously exposes new sections of the enamel material, creating a self-sharpening effect.

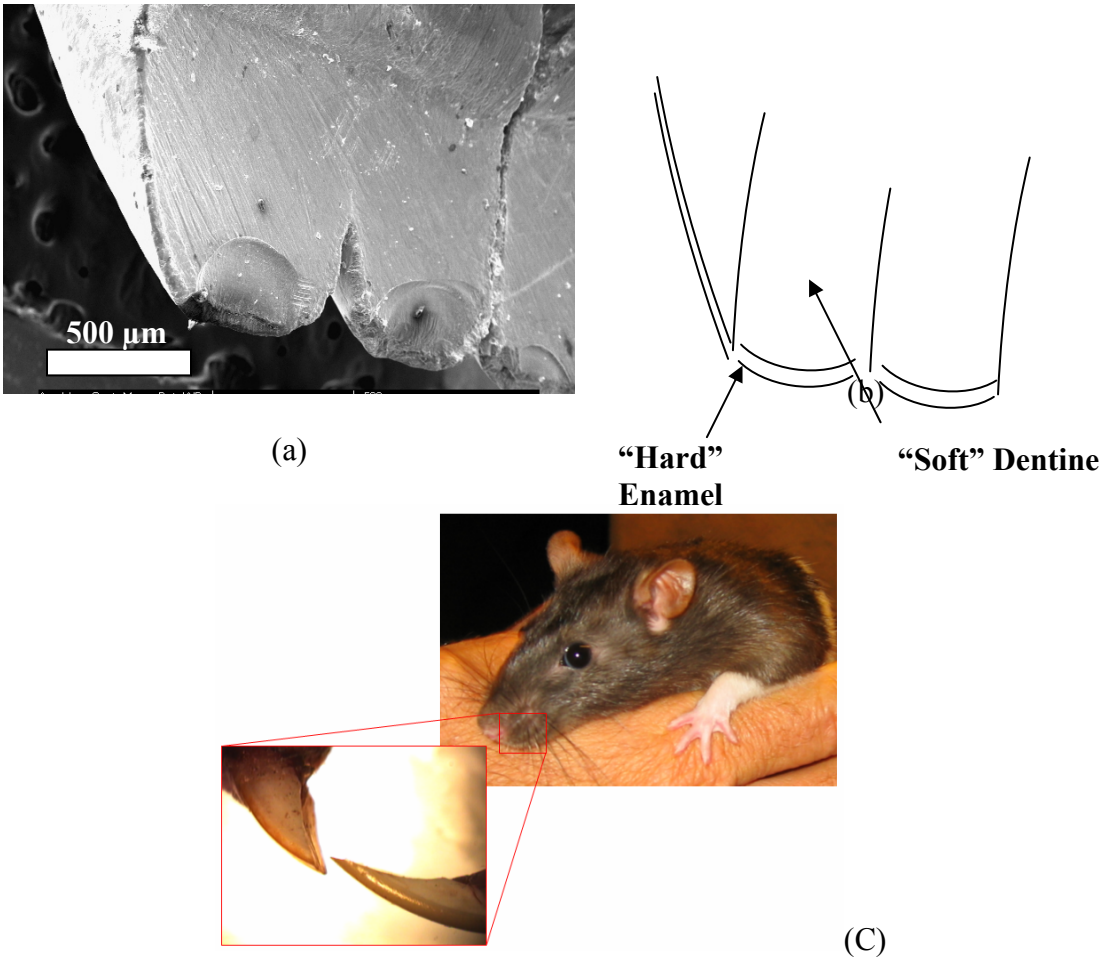

Figure 4.57 Rodent incisors: (a) rabbit teeth; (b) schematic; (c) rat teeth.

4.3.2 Attachment Device (Abalone foot):

As described in *Section 2.3.2* numerous organisms have the ability to functionally adhere to surfaces. Geckos, for example, have received significant attention for their ability to climb smooth vertical surfaces employing van der Waals and capillary forces generated by nanoscaled fibers on their feet [123,127,169,170]. Additionally, similar adhesive mechanisms have been found in a variety of other land animals such as tree frogs [171,172] and insects [173]. The reusability and versatility of these attachment devices on a variety of surfaces under varying conditions [174,145] has an efficiency not yet matched in modern technology. Thus, efforts to synthetically mimic these natural attachment devices are currently under way [134-140,175]. Complex fibrous hyper structures, which vary in hierarchy, dimensions, and material properties, are the key to these devices [148]. The structures have been found to produce intimate contacts with surfaces creating interactions at the molecular level. To date this specific mechanism in nature has only been observed in land species. Marine organisms such as mussels, octopi, and sea stars have been found to employ alternative mechanisms for adhesion, such as suction or quick acting protein based glues [176-180].

4.3.2.1 Characterization and theoretical evaluation

This research provides the first evidence that van der Waals forces acting in combination with capillary forces as a result of nanofibrils may contribute effectively to the strong adhesion exhibited by a marine species, the abalone. The scope of applications for future synthetic nanofibril attachment devices thus broadens to include use in wet

environments, opening the door to applications ranging from marine engineering to biomedical sciences. Furthermore, an observed convergence of evolution is presented in which this mechanism of attachment was independently developed in both terrestrial and aquatic environments.

The pedal foot of red abalone (*Haliotis rufescens*) is shown in Figure 4.58 a. The dark pedal folds, spaced approximately 0.5 mm apart, are the source of locomotion waves used in transportation [158, 159]. Figure 4.58 b shows an abalone supporting its own weight via a single contact point (a human finger). Figure 4.58 c shows a large magnification scanning electron microscopy (SEM) image of the cross-section of the sole tissue. Folds can be seen in greater detail as a mechanism in which the surface area of the foot can expand and contract allowing an increase or decrease in contact surface area and providing the mechanism for the propagation of waves on the ventral surface of the pedal muscle [158].

At higher magnification, Figure 4.59 a shows setae lining the outer surface of the tissue with a thickness of 1-2 μm. At their extremities (Figure 4.59 b), the setae separate into nanoscaled probes with hemispherical ends (Figure 4.59 c), averaging 150 nm in diameter and uniaxialy aligned perpendicular to the plane of the foot tissue. It is proposed that, as in the case of the gecko, these nanofibrils create intimate contacts at the molecular level to form van der Waals interactions which can be accumulated into a formidable macroscale effect.

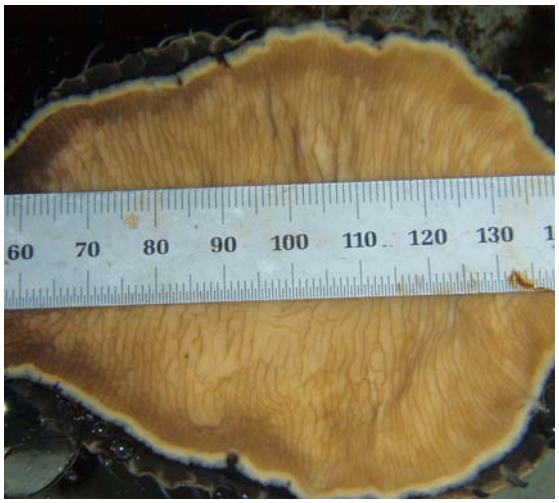

(a)

(b)

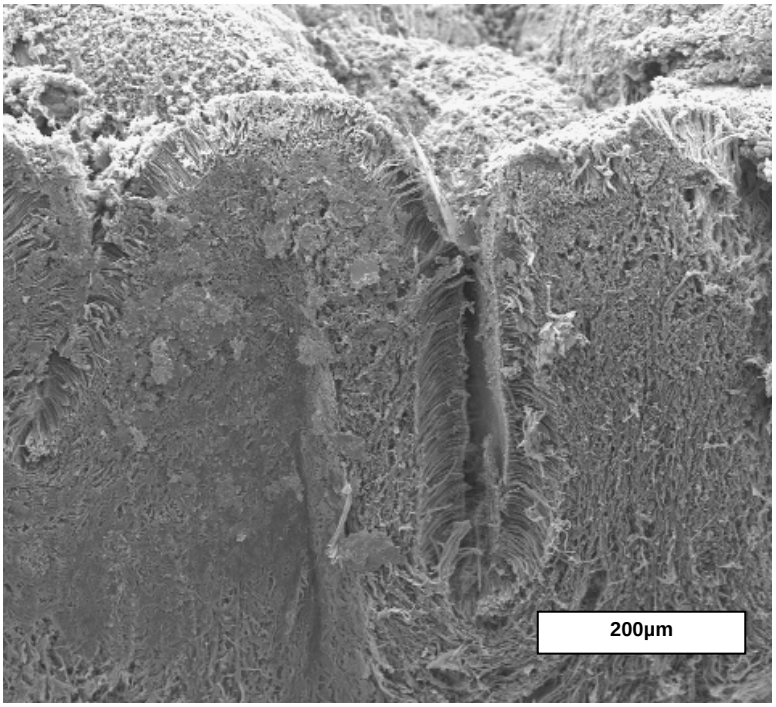

(c)

Figure 4.58 The pedal foot of the red abalone: (a) optical image of bottom surface of foot; (b) abalone supporting its own hanging weight through single contact point; (c) scanning electron microscopy of foot tissue cross-section, the top of the image represents the contact surface of the foot.

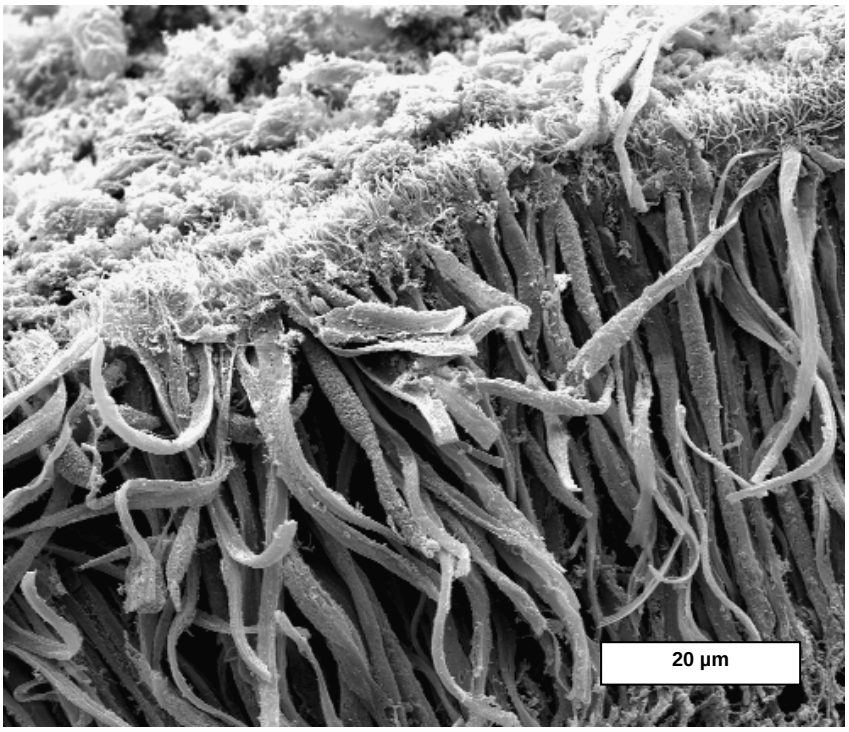

(a)

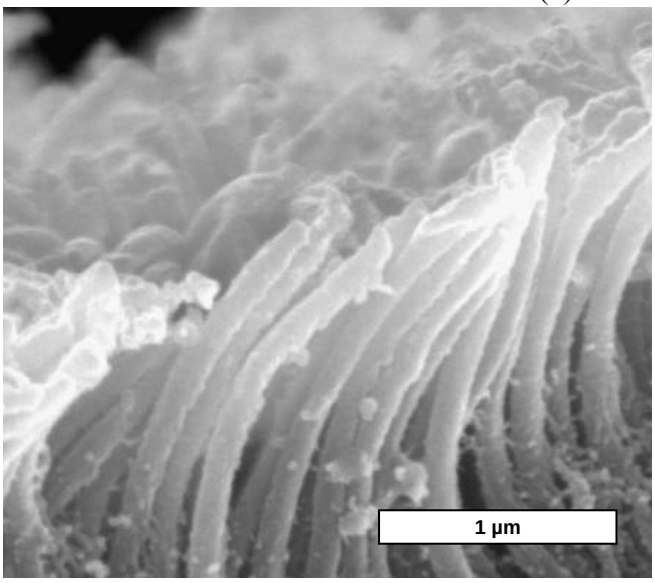

(b)

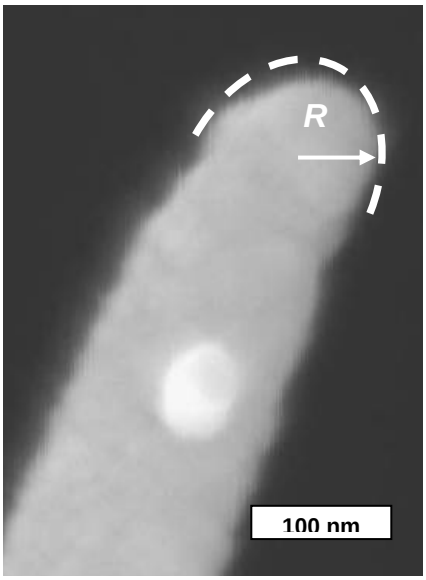

(c)

Figure 4.59 SEM characterization of abalone foot tissue: (a) seta lining the outer surface of the foot; (b) nanofibers uniaxially aligned on seta; (c) single nanofiber with hemispherical tip.

From Figure 4.59 b we observe the presence of roughly 25 effective nanofibrils per 1μm^2 giving an aerial density of 25 x 10^{12} nanofibrils/m^2. Thus, an abalone with an area of 5.5 x 10^{-3} m^2 contains approximately 1.38 x 10^{11} nanofibrils. This value can be used to predict the pull-off force of an abalone foot assuming the interactions between the nanofibrils and a substrate are the primary mechanism of adhesion. The Johnson, Kendall, and Roberts theory [160] allows calculation of the contact force between a sphere and a plane (a rough approximation of a nanofibril/substrate interface):

$$F_C = \frac{3}{2}\pi R\gamma \tag{4.24}$$

where R is the radius of the sphere (shown schematically in Figure 4.59 c), and γ is the surface energy. To estimate the contribution of the van der Waals interaction, the adhesion energy can be calculated as:

$$\gamma = \frac{A}{24\pi D_o^{\ 2}} \tag{4.25}$$

where A is the Hamaker constant and D_o is the cutoff distance [181]. Within a water medium these values are assumed to be 4.2 x 10^{-20} J and 0.2 nm, respectively, resulting in a surface energy of 14 mJ/m^2 [181].

Assuming a hemispherical tip (see Figure 4.59 c) with a radius of 75 nm, the contact force of a single nanofibril can thus be estimated as 5 nN. This corresponds to 300 nN for a seta of 2.5 μm^2 tip area. The total attractive force due to van der Waals interactions along the foot of a typical abalone of can be approximated by multiplying the force per nanofibril by the total number of nanofibrils. For a foot area of 5.5 x 10^{-3} m^2 this results in a total force of 0.7 kN, corresponding to a stress of approximately 123 kPa.

The angle of alignment of setae and nanofibrils relative to the attached substrate is critical in the validation of this theoretical model. Figure 4.60 provides a SEM image of a cleaved section of pedal foot tissue at the interface between tissue and an attached piece of kelp. The kelp extends downward from the upper right hand quadrant of the image, while setae can be observed to extend upward perpendicular to the interface. Figure 4.61 shows the alignment of the nanofibrils as they extend outward from setae, strong uniaxial alignment throughout the various levels of structural hierarchy can be observed.

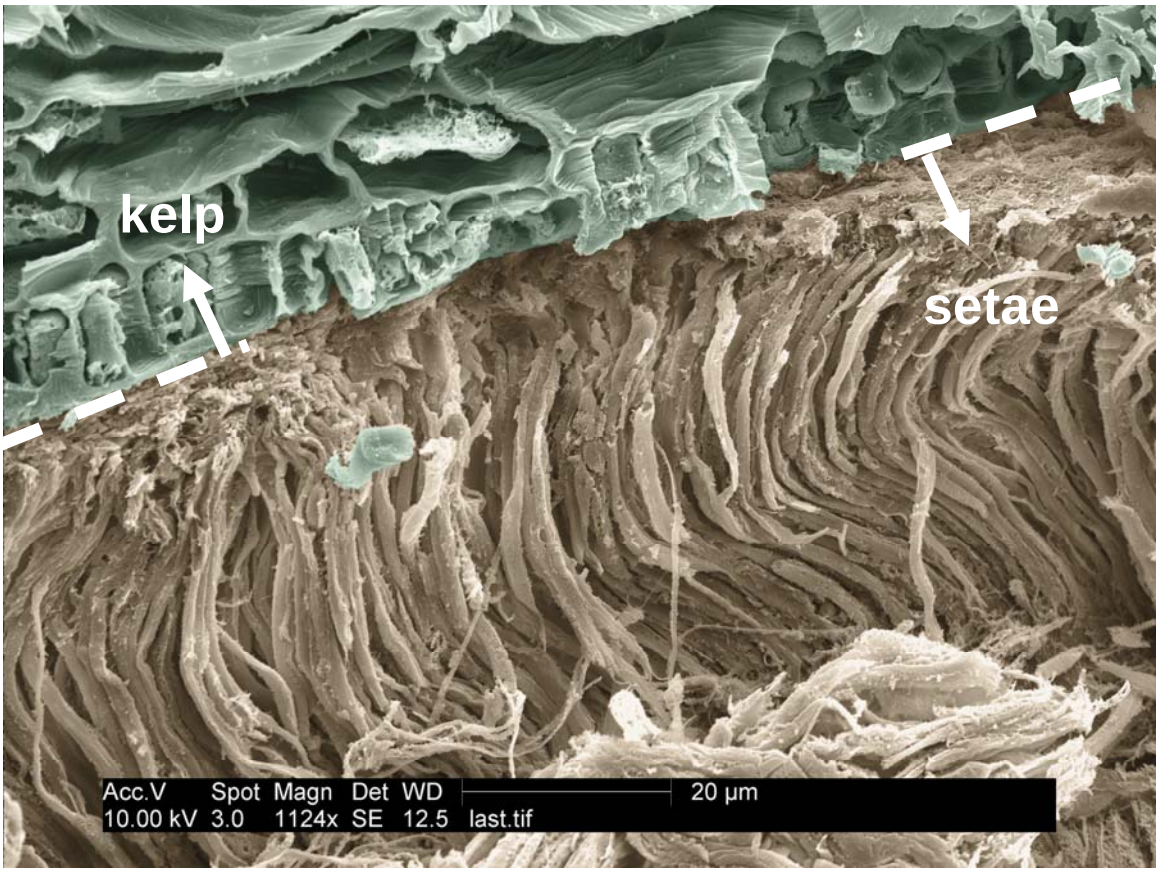

Figure 4.60 SEM image of cleaved section of pedal foot attached to kelp.

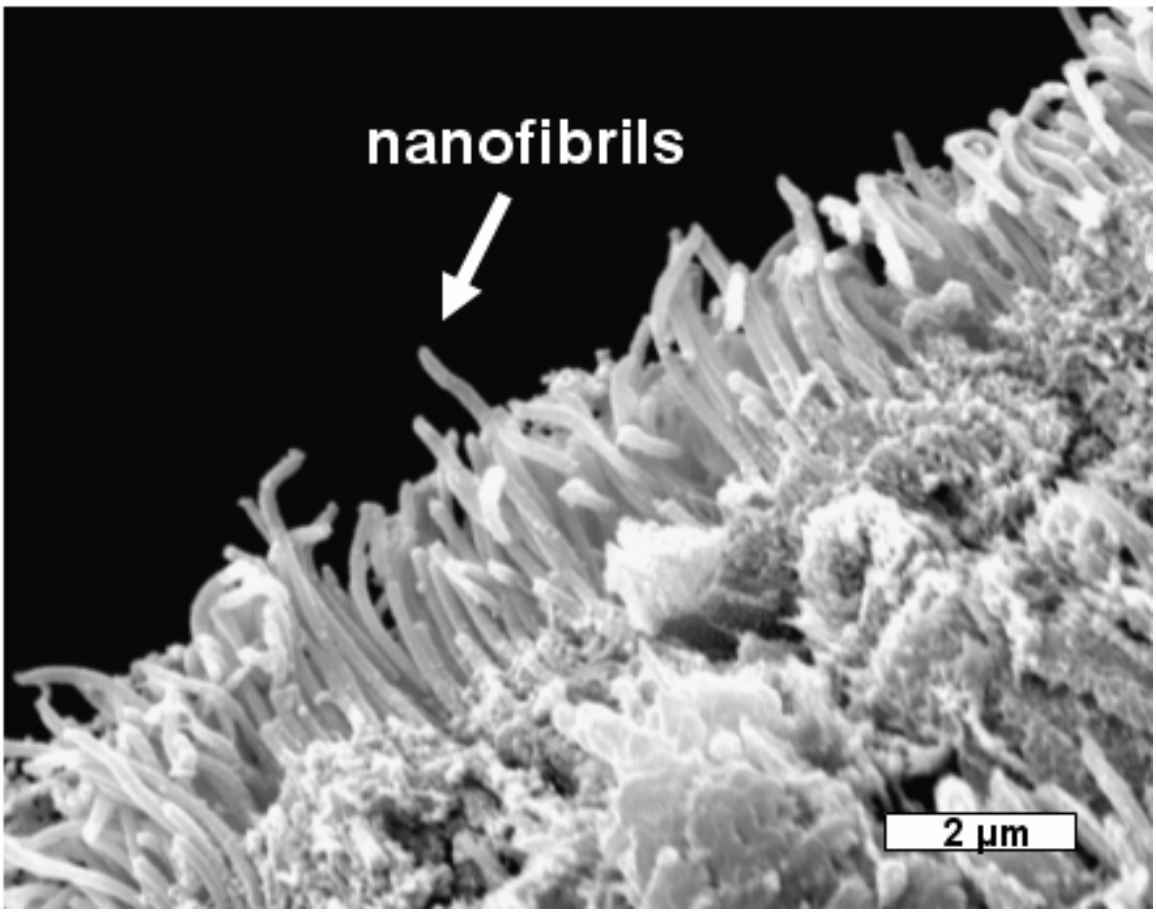

Figure 4.61 Nanofibrils uniaxially aligned along the outer surface of the foot tissue**.**

4.3.2.2 Bulk mechanical testing of pull-off force of the abalone foot

In vivo macro mechanical tests of the bulk pull-off force of adult abalone feet were performed. The tests were conducted on live abalone with an average foot area of 5.5×10^{-3} m^2. The animals were held in an open water facility in the Hubbs Hall Laboratory at the Scripps Institute of Oceanography, La Jolla, CA prior to bulk mechanical testing of the pull-off force. As described in chapter 3, a three pronged steel jaw was used to clamp the shell of abalones; its other end was attached to a cable that was

fed through a pulley to a platform on which the weights were incrementally placed. The detachment force was measured on a smooth, painted, tank in which the abalone had been held for over a year before testing. From seven samples an average pull off stress of 115 kPa with a standard deviation of 19 kPa was found. This is in close agreement with the theoretical stress of 123 kPa calculated from van der Waals forces.

4.3.2.3 Force estimation of a single seta during perpendicular pull-off using an AFM

In addition to bulk mechanical testing, atomic force microscopy (AFM) pull-off force measurements using force-distance curves of a single seta were conducted. These experiments, done in an environment with relative humidity less than 67%, provide evidence of van der Waals and capillary interactions as a possible mechanism of attachment.

The pull-off force for a single seta perpendicular to a hydrophilic (silicon oxide) and a hydrophobic (carbon coated thin film disks) substrate was measured using a contact silicon cantilever with a spring constant of 0.58 N/m. The AFM was placed in a sealed enclosure to allow controlled humidity variation within testing environment. The water contact angle was determined to be 48º for the hydrophilic material and 98º for the hydrophobic material. The RA roughness of the hydrophilic material was 0.8 nm and of the hydrophobic material was 0.4 nm.

Measurements were conducted for values between 10% and 67% humidity to study the effect of humidity on possible capillary forces. Dry nitrogen was introduced in the AFM chamber to reduce the humidity, which was measured by a hydroscope. From Figure 4.62 we observe that the pull-off force increases with increasing humidity for the

hydrophilic material while for the hydrophobic material the pull-off force remains constant.

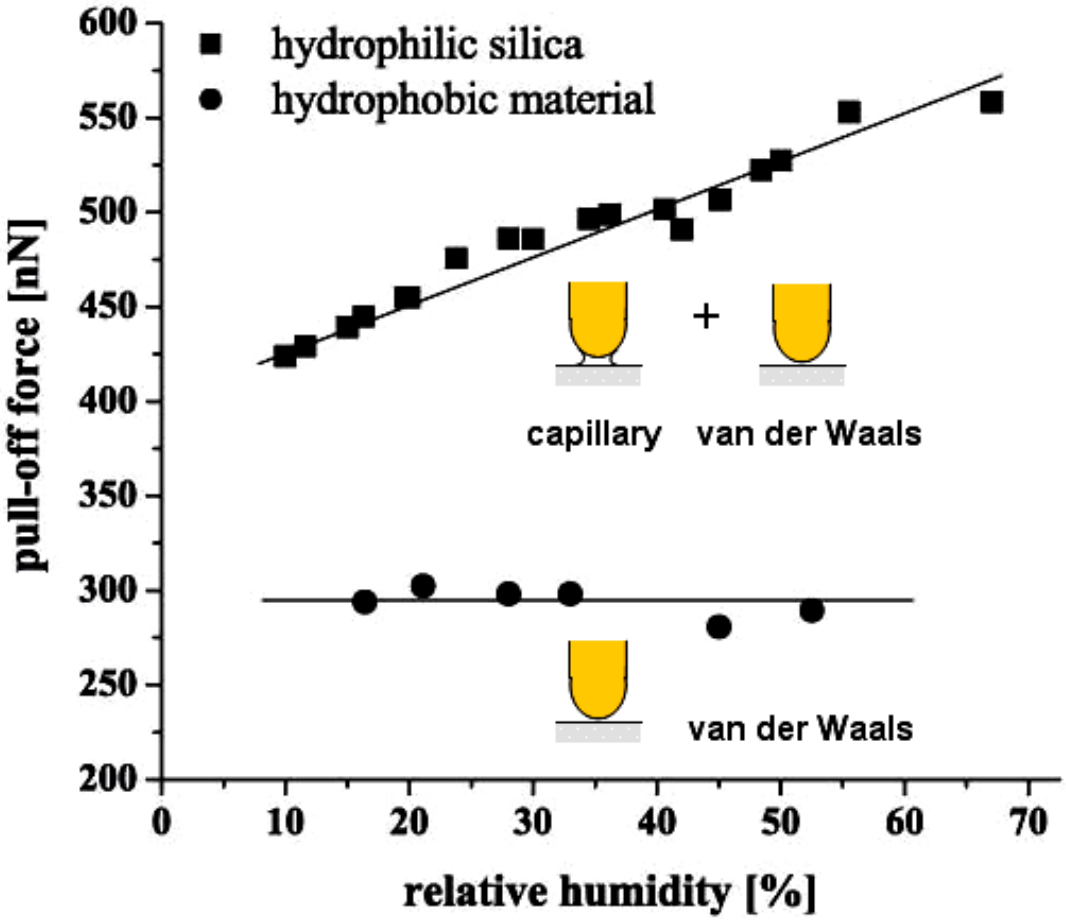

Figure 4.62 Pull-off force as a function of relative humidity of a single seta on a hydrophobic and a hydrophilic substrate.

In the case of the hydrophobic material the average pull-off force was determined to be 294 nN, remaining constant under varying humidity. If one assumes that 60 nanofibrils on a single seta are in contact with the surface, this would correspond to an

adhesion force of approximately 5 nN per nanofibril. This estimate is in exact agreement with the theoretical results of 5 nN calculated using the Johnson-Kendall-Roberts equation.

When the seta was tested on a hydrophilic substrate, at a relative humidity of 10%, the pull-off force was observed to be 424 nN before detachment. This represents an increased force of 130 nN relative to test on the hydrophobic substrate, which can be partially explained by the variation in surface energies for the two substrates (20 mJ/m^2 and 55.5 mJ/m^2 for the disk and silicon oxide, respectively). However, raising the relative humidity to 67% resulted in an additional increase in pull-off force to 558 nN. Similar to predictions by K. Autumn [169] and work by G. Huber et al. [174] for the gecko foot, this shows evidence of capillary interactions. The influence of a meniscus fluid between a fiber and a substrate is increasingly significant with decreased liquid-surface contact angle, i.e. a hydrophilic substrate would have more capillary interactions then a hydrophobic one. This is clearly seen in Figure 4.62.

4.3.2.4 Attachment hierarchy

Barnes [172] classifies attachment devices in animals into three classes: interlocking, friction, and bonding. Bonding may involve three mechanisms: wet adhesion, dry adhesion, and suction. The characterization of the abalone foot pedal and the mechanical tests suggest that the three mechanisms act cooperatively (and perhaps synergistically). Suction can generate attachment forces as explained schematically in Figure 4.63 a. It can be shown that the detachment force F_d is equal to (e. g., Popov [182]):

$$F_d = PA \tag{4.26}$$

where P is the pressure and A is the projected area of the abalone foot on the plane of the surface of attachment. Assuming that the effect of the water column is negligible, i.e., $P = P_{atm}$, we obtain the mean attachment stress as,

$$\sigma_d = P_{atm} = 101kPa \tag{4.27}$$

Figure 4.63 b and Figure 4.63 c show schematically how the three mechanisms can operate cooperatively to create the attachment stress on the same order of magnitude as the theoretical suction stress. The setae and nanofibrils maintain intimate contact with any irregular surface, closing possible channels and impending water penetration. The pressure at the interface, P_0, is equal to P_{atm} when no external detachment force is applied. As F_d increases, P_0 decreases. Once it becomes zero, detachment occurs. Figure 4.63 c shows the situation for a non-conforming material: A continuous fluid path to the interface region ensures pressure equilibration around the animal and effectively eliminates suction. It is proposed that capillarity and van der Waals forces can maintain the intimate contact between the ventral side of the foot pedal and the attachment surface; in this manner the suction force can reach and even exceed $P_{atm}A$.

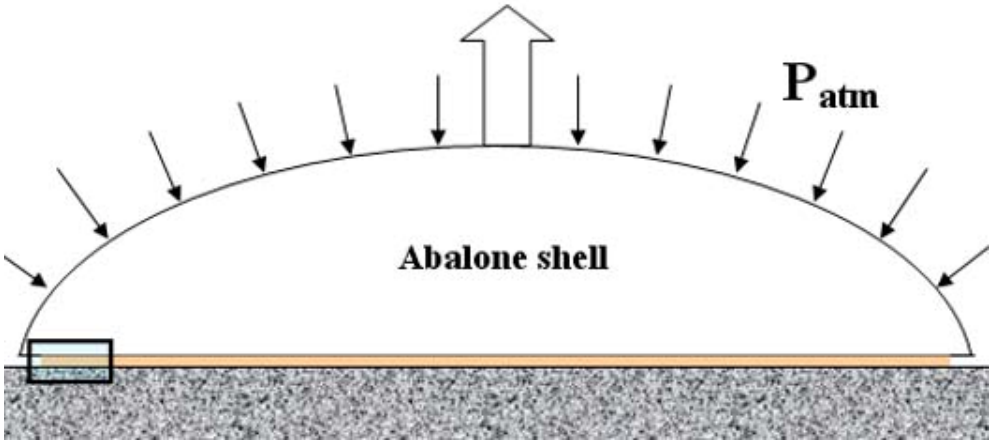

(a)

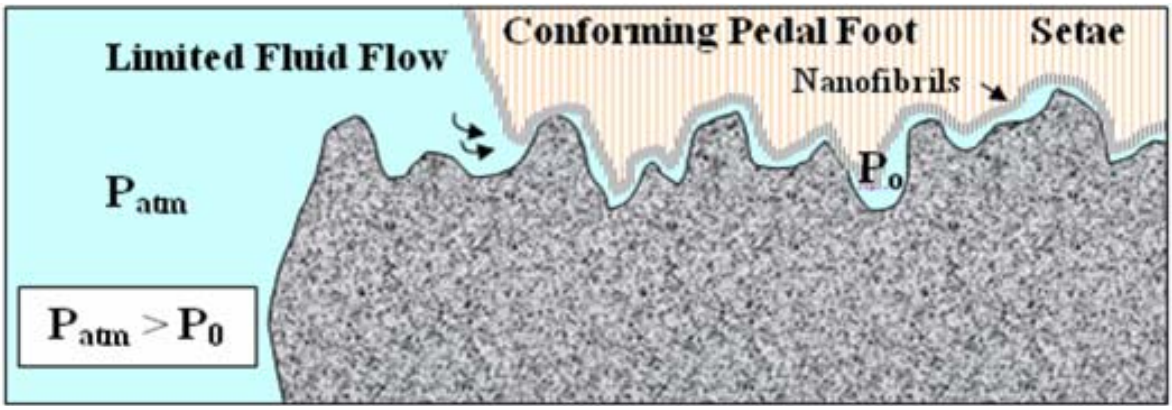

(b)

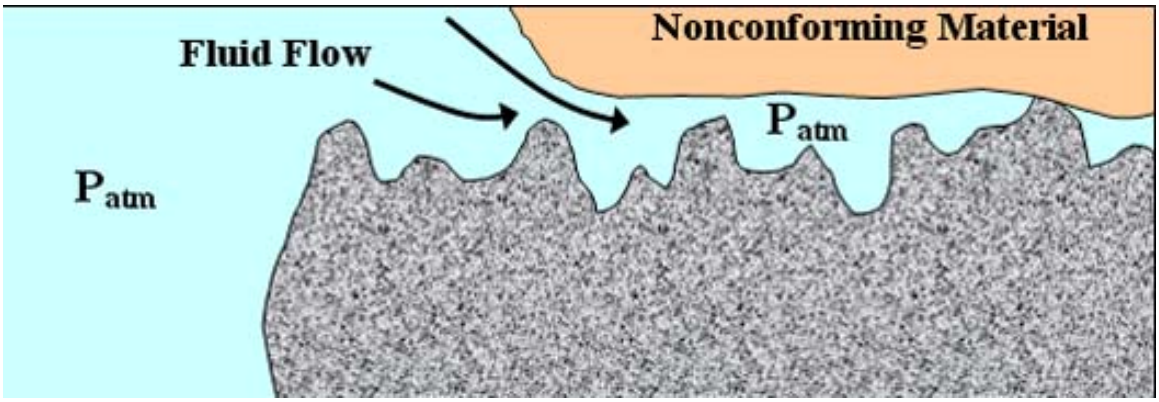

(c)

Figure 4.63 Schematic representation of how suction might generate attachment forces.

4.3.3 Attachment Devices (Tree Frog, Scinax perereca):

The toe pad of the Brazilian tree frog provides yet another example of functional adhesion in nature. This animal, which lives in the moist environment of the of a subtropical rain forest [183], is able to jump from surface to surface, and attach itself effectively through a variety of electro/mechanical/chemical action employed by the materials at the surface of its toe. Its movements are much more dynamic then those of the animals previously described in this thesis. The following section attempts to shed light on the mechanisms which enable such functionality.

Similarly to the gecko foot and the abalone foot described previously, the toe pad of the Brazilian tree frog is composed of aligned nanoscaled fibrils. The fibrils are sectioned into highly ordered hexagonal bundles. These bundles, described first in 1973 by Ernst [184] and Welsch et al. [185] and studied later by many others [186-201] are separated by canal-like spacing. More recent studies have been carried out by Barnes et al. [172] and Hanna et al. [171].

The structure of the toe pad is depicted in the schematic diagram presented in Figure 4.64. The diagram shows a tree frog attached to a glass substrate, with an illustration of the hexagonal subdivisions approximately 10 μm in diameters. These subdivisions are comprised of closely packed fibers approximately 100 nm in diameter. Each fiber terminates in cups of approximately 200 nm diameter. Each one of these cups is aligned beside its neighbor forming a flat surface.

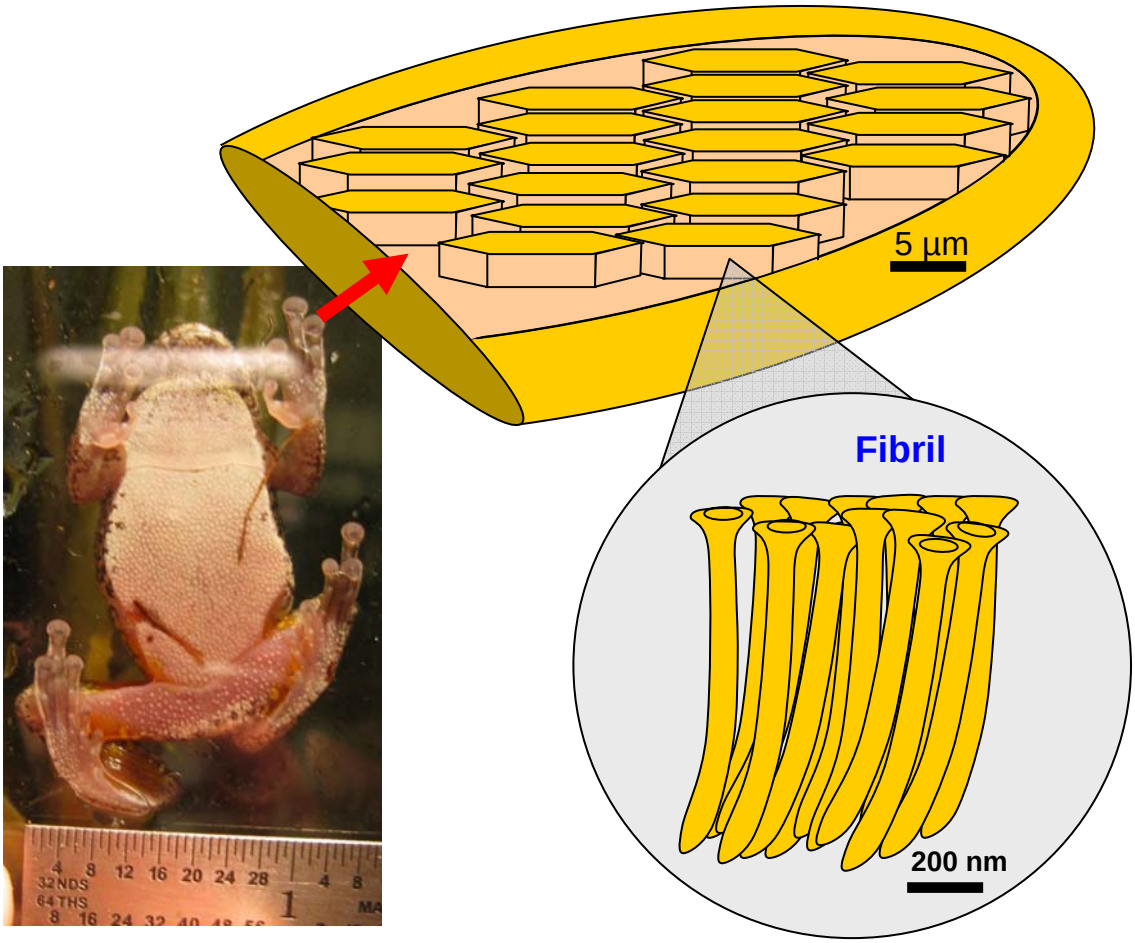

Figure 4.64 Schematic diagram of the structural hierarchy found in the toe pad of a Brazilian tree frog.

Figure 4.65 provides a scanning electron micrograph of a single toe at low magnification with an expanded view of the surface of the toe pad showing hexagonal subdivisions. A well defined circular pad of roughly 2.5 mm in diameter can be seen in the center of the toe. This area represents the surface of thousands of well packed pseudo hexagonal bundles as seen in the expanded caption of the figure.

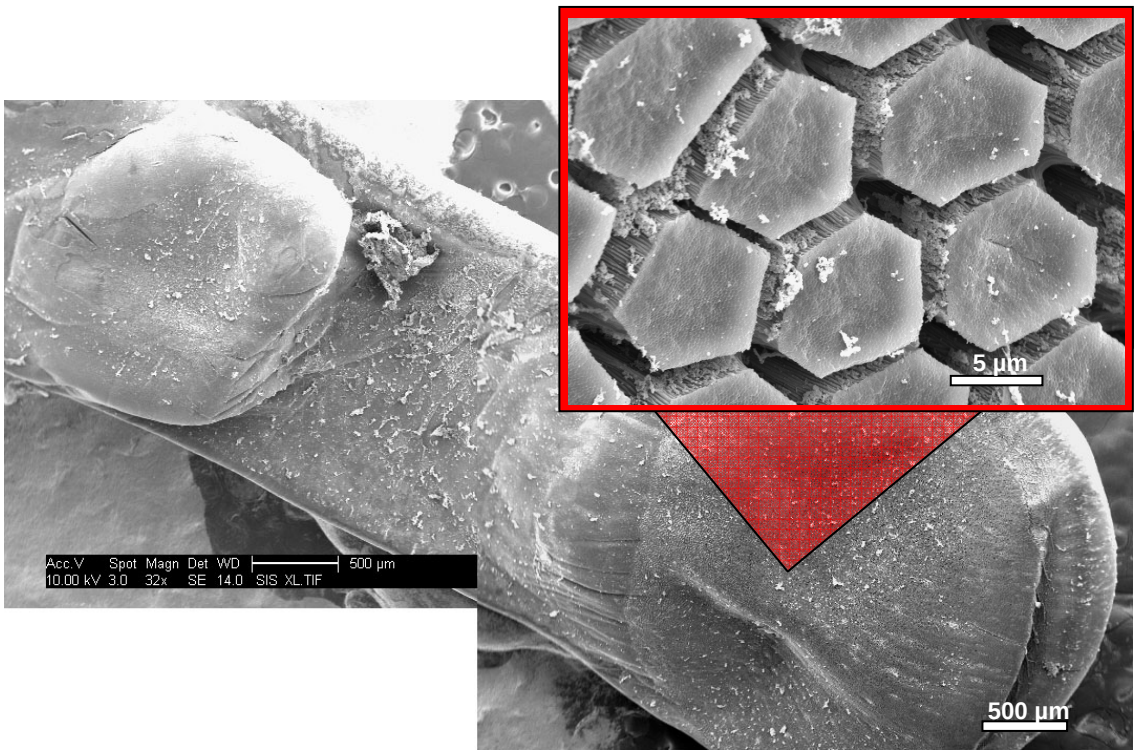

Figure 4.65 Scanning electron micrograph of the toe pad of a Brazilian tree frog; (a) low magnification view of single toe, (b) hexagonal subsections found on the contact surface of the toe pad.

It is believed that mucous glands excrete a viscous fluid which can be transported through the canals that exist between the hexagonal subsections [191]. It had been suggested that the fluid plays an essential role in adhesion [190], indicating a domination of wet adhesion mechanism, however this remains a topic of some debate [187,192-195]. It is proposed here that the contribution of molecular adhesion through van der Waals interactions between the nanofibril ends and a surface may have a place in the discussion of tree frog toe pad adhesion.

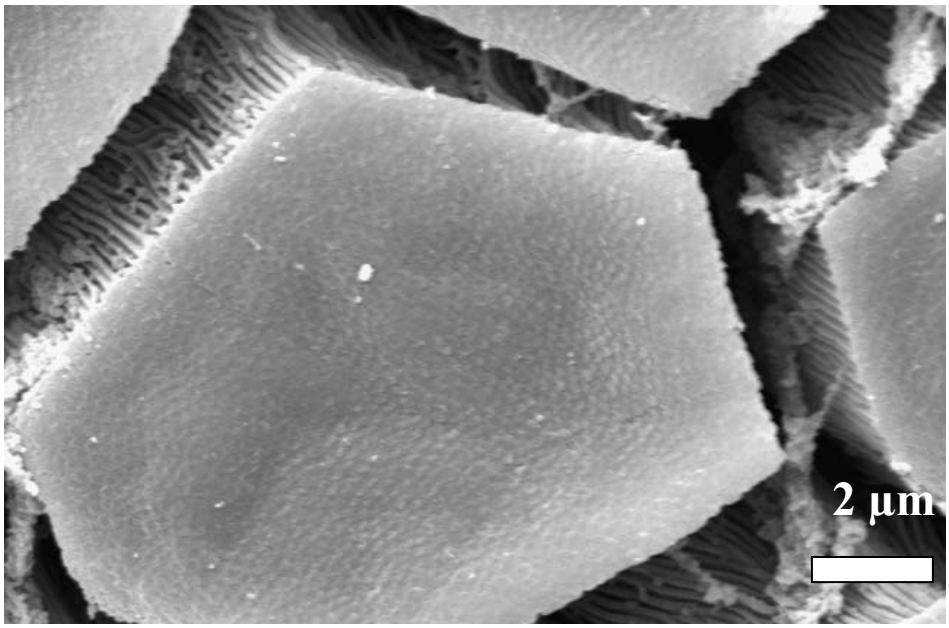

(a)

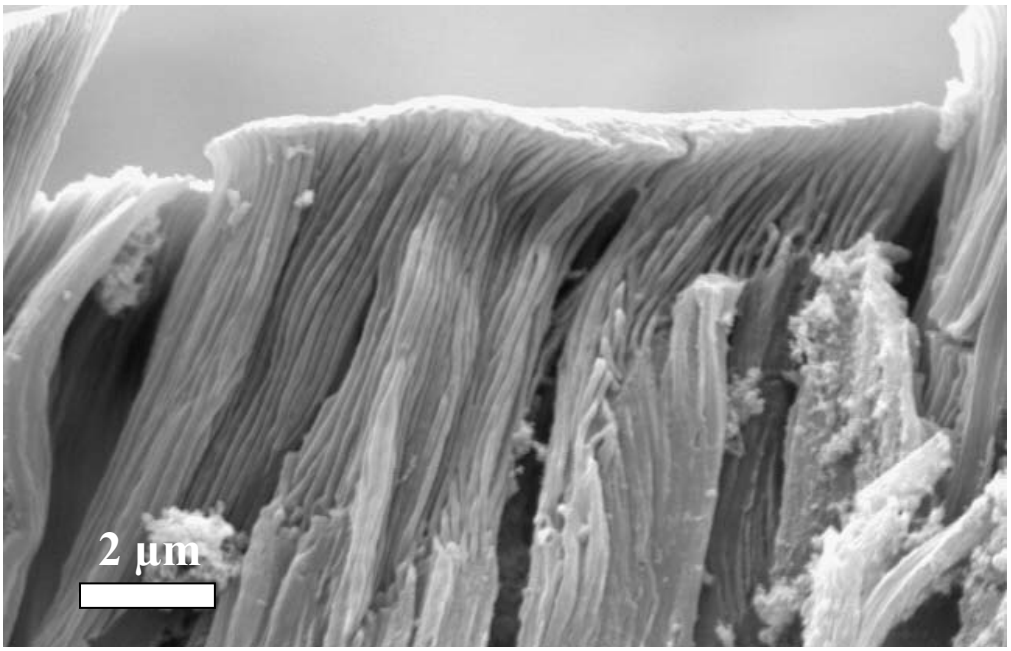

(b)

Figure 4.66 Scanning electron micrographs of hexagonal subdivisions: (a) top down view; (b) side view.

Figure 4.67 provides a; (a) top down, and (b) cross sectional view of an individual bundle. The tightly packed, well aligned fibers which comprise these bundles are shown in greater detail in Figure 4.67. The terminating cups on neighboring fibers are aligned closely against each other to create a smooth and consistent surface. As described in ***Section 2.3.2*** a contact tip shape such as that seen in the SEM image would be optimized to provide molecular adhesion. This is a mechanism which should be further investigated in future studies.

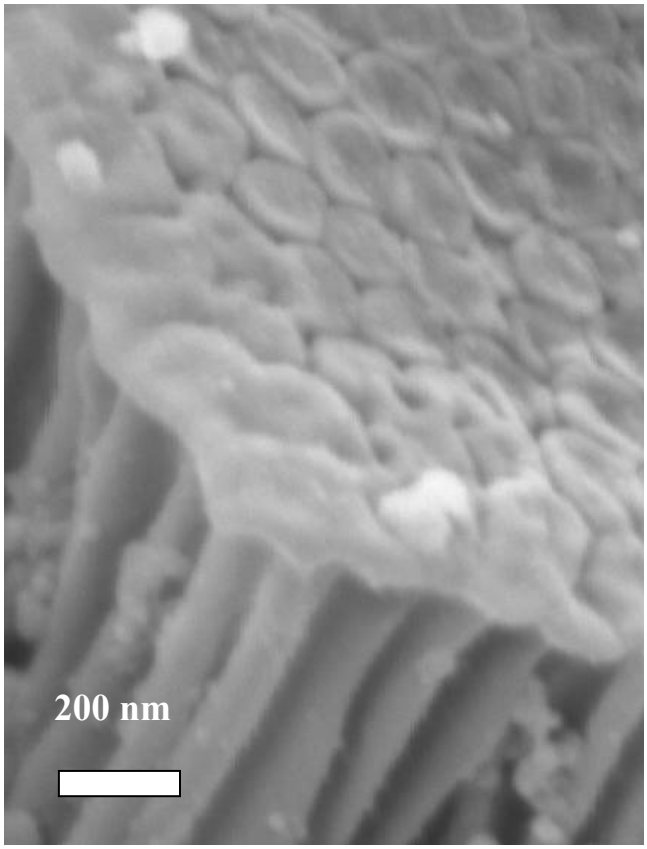

Figure 4.67 High magnification of individual fibers comprising the larger hexagonal subdivisions.

Content from the above chapter has been previously published in the following manuscripts:

Lin A, Meyers MA. Growth and structure in abalone shell. ***Materials Science and Engineering* A** 2005;390:27-41.

Lin AYM, Meyers MA, Vecchio KS. Mechanical properties and structure of Strombus gigas, Tridacna gigas, and Haliotis rufescens sea shells: A comparative study. ***Materials Science and Engineering C*** *2006;*16:1370-1389.

Lin AYM, Chen PY, Meyers MA. The Growth of Nacre in the Abalone Shell. ***Acta Biomaterialia*** 2008;4:131-138.

Lin AYM, Brunner R, Chen PY, Talke FE, Meyers MA. Abalone foot, underwater adhesion. Submitted

Meyers MA, Lin AYM, Chen PY, Muyco J. Mechanical strength of abalone nacre: role of the soft organic layer. ***Journal of the Mechanical Behavior of Biomedical Material. 2008;1:76-85.***

Meyers MA, Lin AYM, Lin YS, Olevsky EA, Georgalis S. The cutting edge: sharp biological materials. ***Journal of Metals*** March 2008;21.

CHAPTER 5

SUMMARY AND CONCLUSIONS

A three part study of lessons from nature has been presented through the examination of various biological materials, with an emphasis on materials from the mollusc *Haliotis Rufescens*, commonly referred to as the red abalone. Other biological materials from the pink conch (*Strombus gigas*), giant clam (*Tridacna gigas*), pampas grass (*Cortaderia selloana*), mosquito (*Culex pipiens*), bee (*Apis mellifera*), Amazon dog fish, piranha (*Serrasalmus manueli*), great white shark (Carcaradon carcharinus), shortfin mako shark (*Isurus oxyrinchus*), cotton tail rabbit, rat, and tree frog (*Scinax perereca*) have also been examined. The structural and mechanical properties, biomineralization, and functionality of these materials have been described and the following conclusions have been made.

The nacre from the shell of the abalone represents a biological composite of organic and inorganic phases which have structural hierarchies that range from the nano- to the macroscale. A strong anisotropy of mechanical strength is found in relation to the structure of the material. In compression perpendicular to the laminate structure a 50% failure probability was found to occur at approximately 250 MPa, significantly less then the previous results by Menig et al. [32] of 540MPa. This is nearly two orders of magnitude larger then the strength found in tension perpendicular to the layered structure, determined to be roughly 5 MPa. The strength of the material parallel to the tiled planes is found to be approximately 65 MPa in tension and 235 MPa in compression (compression results obtained from Menig et al. [32]). From these results it can be

concluded that the shell sacrifices tensile strength in the perpendicular direction to use it in the parallel direction.

A theoretical shear strength of the tile interface is calculated from the tensile tests parallel to tiled layers. This value of 50.9 MPa is in close agreement to experimental shear results which showed an average shear strength of 36.9 MPa.

Hardness and nanoindentation tests were performed on polished cross-sections of nacre, both perpendicular and parallel to the layered structure. In the tiled aragonite region of the shell a mean modulus and mean hardness of 94 GPa and 3.17 GPa was found, respectively. The organic growthbands showed a drastically lower value of 9.85 GPa and 0.56 GPa for mean modulus and mean hardness, respectively.

Efforts to characterize the structural components responsible for the mechanical response described above were conducted on the nano, micro, and macro scale. High resolution SEM images produced evidence of mineral bridges and nano asperities at the interface between tiles. Hydrazine-deproteination confirmed the mineral composition of these artifacts. These bridges were further confirmed with TEM, with an average diameter of 50 nm. A calculation of the theoretical strength of calcium carbonate and its relationship to a critical flaw size showed that the dimensions of the mineral bridges were just below that needed to allow failure by crack rupture. Thus it can be concluded that the scale of a material's subdivisions can be exploited to limit the size of internal flaws, thus reducing the possibility of crack propagation.

Structural characterization of fractured surfaces of nacre exposed the presence of organic sheets interleaved between aragonite tiles. These observations were used to predict the elastic modulus of the protein based sheets, which was found to be 100 Pa, a

value which would imply a limited role in the strengthening of the composite in various directions. Atomic force microscopy of EDTA demineralized nacre confirmed the sheets were composed of disordered layers of cross-linked protein chains. Demineralization also exposed larger growth bands, confirming their organic composition.

To further identify specific structural elements responsible for the mechanical toughening a comparative study of two other shells was provided, one with higher structural complexity (the pink conch, *Strombus gigas*) and one with lower structural complexity (the giant clam, *Tridacna gigas*). Quasi-static and dynamic compression results showed dramatic differences in strength between shells (all composed of the constituent material calcium carbonate). The giant clam showed the lowest strength of approximately 87 MPa and 123 MPa in quasi-static loading parallel and perpendicular to the layered structure, respectively. Results from the conch shell were obtained from Menig et al. [161] to be 166 MPa and 218 MPa, parallel and perpendicular to loading, respectively. These two materials show a strength approximately half that found in abalone nacre. Similar results were found in dynamic loading. It is proposed that an optimization of structural complexity is found in the nacre of abalone, and that an over- or underdeveloped structural hierarchy can reduce mechanical strength.

The process of steady state tiled aragonite growth is discussed in great detail. It is concluded through SEM and TEM observations that mineral bridges exist between the tile layer interfaces. Diffraction pattern analysis showed crystallographic orientation match between consecutive layers of tiles further confirming the existence of a mineral connection between layers. It is concluded that tile growth does not occur through the nucleation of new tiles following organic mediation, rather the deposition of the organic

inhibitor layer serves to arrest c-axis crystal growth however allow a limited continuation in the form of nanoscaled mineral bridges.

Two aspects of functionality were investigated in a variety of biological materials; their ability to cut, and their ability to attach. Observations on the sharp cutting edges of plants, insects, and teeth were performed through SEM. Two key elements of structural design were identified to contribute to these materials ability to cut through objects that are often stronger then their own constituent. Serrations were found to exist on a variety of animals with little scaling dependence on animal size. Rather, serration dimensions were observed to depend on the types of materials they were designed to cut. A second element was observed in the self sharpening ability of the incisors of the rat and the rabbit. A hard outer enamel layer supported by a softer, faster wearing dentine is found to provide a mechanism in which a sharp cutting edge of enamel is constantly being re-exposed.

Some of the attachment devices found in modern technology can trace their roots back to the earliest days of biomimetics, i.e. Velcro ®. This dissertation provides yet another example of an attachment mechanism in nature through the first study of the attachment of the abalone foot. Highly ordered rows of 1-2μm thick setae, terminating in bundles of aligned, 150 nm diameter nanofibers line the pedal muscle of the abalone. These structures show remarkable similarity to those found on the bottom of the gecko foot, elements which have been proven to employ van der Waals and capillarity forces for the purpose of adhesion. Theoretical estimations of van der Waals forces based on the dimensions of the observed abalone nanofibers predict a detachment force of 300 nN per seta corresponding to a pull-off stress of 123 kPa per foot. Experimental

conformation of these predictions was obtained through nanoscaled measurements on single setae using an atomic force microscope and through bulk mechanical testing on live abalone. Variations in relative humidity and testing substrates during atomic force pull-off tests showed evidence of capillary interactions. A base pull-off force on a hydrophobic substrate (in which capillarity would not play a role) was found to be approximately 300 nN, an exact match to the theoretical estimates. Bulk pull-off measurements on live abalone of various size showed an average pull-off stress of 115 kPa, also in close agreement with theoretical calculations.

Similar observations were found on the foot of the tree frog (*Scinax perereca*) in which pseudo hexagonal bundles of highly aligned nanofibers were confirmed through SEM.

The goal of this study is to contribute to the expanding knowledge base of biological systems with the hopes of inspiring innovative designs in technology. To ignore the lessons from nature would be to squander the greatest resource to man. The designs found in nature have evolved through millions of years of trial and error, thus it behooves us all to look towards them for inspiration.

REFERENCES

1. Thompson DW. *On growth and form.* 2nd ed., reprinted Cambridge: Cambridge University Press, 1968.

2. Vincent JFV. *Structural biomaterials*. Revised ed. New Jersey: Princeton Universtiy Press,1991.

3. Currey JD. *Bones: structure and mechanics*. New Jersey: Princeton University Press, 2002.

4. Arzt E. Mater Sci Eng C 2006;26:1245-50.

5. Meyers MA, Chen PY, Lin AYM, Seki Y. Progress in Materials Science 2008;53:1-206.

6. Sarikaya M. Microscopy research and technique 1994;27:360.

7. Srinivasan AV, Haritos GK, Hedberg FL. App Mech Rev 1991;44:463.

8. Zhang S, Marini DM, Hwang W, Santoso S. Current Opinion in Chemical Biology 2002;6:865-871.

9. Baer E, Hiltner A, Morgan RJ. Phy Today Oct 1992:60.

10. Heuer AH, Fink DJ, Laraia VJ, Arias JL, Calvert PD, Kendall K, Messing GL, Blackwell J, Rieke PC, Thompson DH, Wheeler AP, Veis A, Caplan AI. Science 1992;255:1098.

11. Laraia JV, Heuer AH. J Am Ceram Soc 1989;72:2177.

12. Weiner S, Wagner HD. An Rev Mater Sci 1998;28:271.

13. Weiner S, Addadi L. J Mater Chem 1997;7:689.

14. Vincent JFV, Owers P. J Zool (A) 1986.

15. Mayer G, Sarikaya M. Exper Mech 2002;42:395.

16. Kuhn-Spearing LF, Kessler H, Chateau E, Ballarin R, Heuer AH. J Mater Sci 1996;31:6583.

17. Sarikaya M, Aksay JA. In: *Results and Problems in Cell Differentiation in Biopolymers*. Case S. ed., Springer Verlag, Amsterdam, 1992 p.1.

18. Sarikaya M, Gunnison KE, Yasrebi M, Aksay JA. Mat Res Soc 1990;174:109

19. Currey JD, Kohn AJ. J of Mat Sci 1976;11:1614.

20. Currey JD, Taylor JD. J Zool 1974;173:395-406.

21. Lowenstam HA, Weiner S, *On Biomineralization*, Oxford University Press, New York, 1989.

22. Nicolis G, Prigogine I. *Self-Organization and Nonequilibrium Thermodynamics: from Dissipative Structures to Order through Fluctuation*s, Wiley, New York, 1977.

23. Whitesides G. Mat Res Bull Jan 2002:56.

24. Prigogine I, Stengers I. *Order Out of Chaos*, Bantam, 1984.

25. Simkiss K, Wilbur KM. *Biomineralization*, Academic Press, 1989.

26. Bauerlein E. ed., *Biomineralization,* Wiley-Interscience, Weinheim, Germany, 2000.

27. Mann S. *Biomineralization,* Oxford, 2001.

28. Vincent JFV. The Royal Soc, Philosophical Translations 2003;358:1597.

29. Feynman RP. Engineering and Science, 1960

30. Nakahara H, Bevelander G, Kakei M. Venus Jpn J Malac 1982;41:33-46.

31. Zaremba CM, Belcher AM, Fritz M, Li Y, Mann S, Hansma PK, and Morse DE. Chem Mater 1996;8:679.

32. Menig R, Meyers MH, Meyers MA, Vecchio KS. Acta Mater 2000;48:2383-2398.

33. Su XW, Belcher AM, Zaremba CM, Morse DE, Stucky GD, Heuer AH. Chem Mater 2002;14:3106-3117.

34. Erasmus J, Cook PA and Sweijd N. J Shellfish Res 1994;13:493-501.

35. Lin A, Meyers MA. Mater Sci Eng A 2005;390:27-41.

36. Voronoi G. Journal Fur die Reine und Angewandte Mathematik, 1907;133:97-178.

37. Currey JD. Proc Roy Soc Lond 1977;196: 443-463.

38. Jackson AP, Vincent JFV, Turner RM. Proc Roy Soc Lond B 1988;B234:415.

39. Sarikaya M, Gunnison KE, Yasrebi M, Aksay JA. Mater Res Soc 1990;174:109.

40. Jackson AP, Vincent JFV, Turner RM. Comp Sci and Tech 1989;36:255-266.

41. Weibull W. J Appl Mech 1951;18:293.

42. Argon AS. *Fracture of Composites. Treatise of Materials Science and Technology,* Academic Press, New York, 1972, p.1

43. Budiansky B. Comp Struct 1983;16:3.

44. Fleck NA, Deng L, Budiansky B. J Appl Mech 1995;62:329.

45. Jelf PM, Fleck NA. J Comp Mater 1992;26:18.

46. Meyers MA, Chawla KK. *Mechanical Behavior of Materials*, Prentice Hall Inc., Saddle River, NJ, 1999.

47. Sir Michel Ashby, Personal Communications.

48. Shen X, Belcher AM, Hansma PK, Stucky GD, Morse DE. J Biol Chem 1997;272:32472-81.

49. Meyers MA, Lin AYM, Chen PY, Muyco J. J Mech Biomed Biolog Mater 2007;1:76-85.

50. Bao G, Suresh S. Nature Materials 2003;2:715-725.

51. Belcher AM, Gooch EE. In: *Biomineralization: from biology to biotechnology and medical application*. ed. Bauerlein E, Germany: Wiley-Interscience, 2000, p.221.

52. Wustman BA, Morse DE, and Evans JS. Biopolymers 2004;74:262-276.

53. Weiner S and Hood L. Science 1975;190:987–989.

54. Weiner S. Biochem. 1983;22:4139–4144 (1983).

55. Weiner S, Talmon Y, Traub W. Int J Bio Macrom 1983;5: 325-328.

56. Nudelman F, Gotliv BA, Addadi L, Weiner S. J Struct Biol 2006;153:176-187.

57. Marin F and Luquet G. Mat Sci Eng C 2005;25:105-111.

58. Gilbert P, Abrecht M, Frazer BH. Rev in Mineral and Geochemistry 2005; 59:157-185.

59. Katti DR, Pradhan SM, Katti KS. Rev. on Advanced Materials Sci 2004;6:162-168.

60. Weiner S. Am Zool 1984;24:945-952.

61. Weiner S, Traub W. FEBS Letts 1982;111:311.

62. Weiner S. Cal Tissue Int 1979;29:163.

63. Addadi L, Weiner S. Proc Natl Acad Sci USA 1985;82:4110.

64. Vecchio KS, Unpublished results.

65. Nassif N, Pinna N, Gehrke N, Antonietti M, Jager C, Colfen H. Proc of the Natl Acad of Sci 2005;102:36.

66. Wang RZ, Suo Z, Evans AG, Yao N, Aksay IA. J Mater Res Soc 2001;16:2485.

67. Evans AG, Suo Z, Wang RZ, Aksay IA, He MY, Hutchinson JW. J Mater Res Soc 2001;16:2475.

68. Barthelat F, Li CM, Comi C, Espinosa HD. J Mater Res 2006;21:1977-1986.

69. Bruet BJF, Qi HJ, Boyce MC, Panas R, Tai K, Frick L, Ortiz C. J Mater Res 2005;20:2400-2419.

70. Gao HJ, Ji BH, Jäger IL, Arzt E, Fratzl P. Proc Natl Acad Sci USA 2003;100:5597-5600.

71. Ji BH, Gao HJ. J Mech Phy Solid 2004;52:1963-1990.

72. Ji BH, Gao HJ, Hsia KJ. Phil Mag Lett 2004;84:631-641.

73. Song F, Zhang XH, Bai YL. J Mater Res 2002;17:1567–70.

74. Song F, Soh AK, Bai YL. Biomaterials 2003;24:3623.

75. Smith BL, Schäffer TE, Viani M, Thompson JB, Frederick NA, Kindt J, Belcher A, Stucky GD, Morse DE, Hansma PK. Nature 1999;399:761.

76. Wada, K. Bull Japanese Soc Sci Fish 1958;24:421-427

77. Wada, K. Bull Japanese Soc Sci Fish 1959;25:342-345.

78. Watabe N, Wilbur KM. Nature 1960;188:334

79. Bevelander G, Nakahara H. Calc Tiss Res 1960;7:84-92.

80. Wise SW. Science 1970;167:1486-88.

81. Erben HK. Biomineral 1972;4:15-27.

82. Erben HK, Watabe N. Nature 1974; 248:128.

83. Belcher AM, Wu XH, Christensen RJ, Hansma PK, Stucky GD, Morse DE. Nature 1996;381:56-58.

84. Belcher AM, Ph.D. Thesis, University of California, Santa Barbara, 1996.

85. Belcher AM, Hansma PK, Stucky GD, Morse DE. Acta Mater 1997;46:733.

86. Fritz M, Belcher AM, Radmacher M, Walters DA, Hansma PK, Strucky GD, and Morse DE. Nature 1994;371: 49.

87. Fritz M, Morse DE. Col Int Sci 1998;3:55.

88. Mann S, Archibald DA, Didymus JM, Douglas T, Heywood BR, Meldrum FC, Reeves NJ. Science 1993;261:1286-92.

89. Ikeshoji T. *The Interface between Mosquitoes and Humans.* University of Tokyo Press, 1993;189-214.

90. Diamond JM. Nature (London) 1986;322:773-774.

91. Martin RA, Hammerschlag N, Collier RS, Fallows C. J Mar Biol Ass UK 2005;85: 1121-1135.

92. Frazzetta TH. Zoomorphology 1988;108:93-107.

93. Lucifora LO, Menni RC, Escalante AH. Cybium 2001;25(1):23-31.

94. Shimada K. Journal of Morphology 2002;251:38-72.

95. Addadi L, Moradian J, Shay E, Maroudas NG, Weiner S. Proc Natl Acad Sci USA 1987;84:2732

96. Addadi L, Raz S, Weiner S. Adv Mater 2003;15:959-970.

97. Hansma PK. Biophysical J 2000;79:3307-3312.

98. Politi Y, Arad T, Klein E, Weiner S, and Addadi L, Science 2004;306-1161-1164.

99. Colfen H, Mann S. Angew Chem Int ed. 2003;42:2350-2365.

100. Orme CA, Noy A, Wierzbickl A, McBride MT, Grantham M, Teng HH, Dove PM, DeYoreo JJ. Nature 2001;411:775-78.

101. Teng HH, Dove PM, Orme CA, DeYoreo JJ. Science 1988;282:724-7.

102. Nakahara H. Calcification of Gastropod Nacre. In: *Biomineralization and Biological Metal Accumulation.* ed. Westbroek P, De Jong EW. Dordrecht, Holland: D. Reidel Publishing Company, 1982, pp 225.

103. Nakahara H. Nacre Formation in Bivalve and Gastropod Molluscs. In: *Mechanisms and Phylogeny of Mineralizaion in Biological Systems*. ed. Suga S, Nakahara H. New York: Springer-Verlag,1991, pp 343.

104. Sarikaya M. Personal Communication, 1997.

105. Schäffer TE, Ionescu-Zanetti C, Proksch R, Fritz M, Walters DE, Almqvist N, Zaremba CM, Belcher AM, Smith BL, Stucky GD, Morse DE, Hansma PK. Chem Mater 1997;9:1731-1740.

106. Wang R, Feng Q, Cui F, Li H. Chinese J Of Materials Research 1996;10:95-100.

107. Sealy C. Materials today 2008;11:15.

108. Almqvist N, Thomson NH, Smith BL, Stucky GD, Morse DE, Hansma PK. Mater Science and Engineering C 1999;7:37-43.

109. Sellinger A, Weiss PM, Nguyen A, Lu Y, Assink RA, Gong W, Brinker CJ. Nature 1998;394:256-260.

110. Heuer AH, Fink DJ, Laraia VJ, Arias JL, Calvert PD, Kendall K, Messing GL, Blackwell J, Rieke PC, Thompson DH, Wheeler AP, Veis A, Caplin AI. 1992; 225:1098-1105.

111. Tompsia AP, Saiz E, Deville S. AIP Conference Proceedings 2007;916:560-572.

112. Xu G, Yao N, Aksay IA, Groves JT. Science 1994;120:11977-11985.

113. Veis A, In: *Biomineralization* 1989;189-222.

114. Deutsch D. Anat Rec 1989;224:189.

115. Caplan AI. Sci Am 1984;251:84.

116. Alper M, Calvert PD, Frankel R, Rieke PC, Tirrell DA, Eds., *Mateirls Synthesis Based on Biological Processes,* MRS, Pittsburgh, 1991.

117. Arias JL, Fernandez MS, Laraia VJ, Heuer AH, Caplan AI. *ibid*., pp193-201.

118. Arias JL, Fernandez MS, Dennis JE, Caplan AI. Connect Tissue Res 1991;26:37.

119. Caplin AI, Pechak DG. In: *Bone and Mineral Research.* ed. Peck WA, Elsevier, Amsterdam 1987:117-183.

120. Lin AYM, Chen PY, Meyers MA. Acta Biomaterialia 2008;4:131-138.

121. Cartwright JHE , Checa AG. J R Soc Interface 2007;4:491-504.

122. Feng QL, Li HB, Cui FZ, Li HD. J Mater Sci Lett 1999;18:1547-1549.

123. Autumn K, Liang Y, Hsieh ST, Zesch W, Chan WP, Kenny TW, Fearing R, Full RJ. Nature 2000;405:681.

124. Ruibal R, Ernst V. J Morphol 1965;117:271-93.

125. Meyers MA, Lin AYM, Chen P-Y. Unpublished result 2007.

126. Arzt E. Mater Sci Eng C 2006;26:1245-50.

127. Arzt E, Gorb S, Spolenak R. PNAS 2003;100:10603-10606.

128. Spolenak R, Gorb S, Arzt E. Acta Biom 2005;1:5.

129. Huber G, Mantz H, Spoolenak R, Mecke K, Jocobs K, Gorb SN, Arzt E. Proc Natl Acad Sci USA 2005;102:16293-96.

130. Autumn K, Dittmore A, Santos D, Spenko M, Cutkosky M. J of Exp Biology 2006;209:3569.

131. Autumn K, Hsieh ST, Dudek DM, Chen J, Chitaphan C, Full RJ. J Exp Biol 2006;209:260–272.

132. Chen JJ, Peattie AM, Autumn K, Full RJ. J Exp Biol 2006;209:249–259.

133. Spokenak R, Gorb S, Gao HJ, Arzt E. Proc R Soc A 2005;461:305-319.

134. del Campo A, Greiner C, Arzt E. Langmuir 2007;23:10235-10243.

135. Geim AK, Dubonos SV, Grigorieva IV, Novoselov KS, Zhukov AA, Shapoval SY. Nature Mateirals 2003; 2:461-463.

136. Majidi C, Groff RE, Maeno Y, Schubert B, Baek S, Bush B, Maboudian R, Gravish N, Wilkinson M, Autumn K, Fearing RS. Phys Rev Lett 2006;97:076103.

137. Kim S, Sitti M. Appl Phy Lett 2006;89:261911.

138. Gorb S, Varenberg M, Peressadko A, Tuma J. J Roy Soc, Interface 2006;1-6.

139. Glassmaker NJ, Jagota A, Hui CY, Noderer WL, Chaudhury MK. Proc Natl Acad Sci USA 2007;104:10786-10791.

140. Ge L, Sethi S Ci L, Ajayan PM, Dhinojwala A. Proc Natl Acad Sci USA 2007;104;10792-10795.

141. Ghatak A, Mahadevan L, Cheng JY, Chaudhury MK, Shenoy V. Proc Roy Soc London, Ser. A. 2004;460:2725-2735.

142. Tian Y, Pesika N, Zeng H, Rosenberg K, Zhao B, McGuiggan P, Autumn K, Israelachvili J. Proc Natl Acad Sci USA 2006;103:19320-19325.

143. Huber G, Gorb S, Spolenak R, Arzt E. Biol lett 2005;1:2-4.

144. Ciccottie M, Giorgini B, Vallet D, Barquins M. Int J Adhes Adhes 2004;24:143-151.

145. Persson BNJ, Gorb S. J Chem Phys 2003;119:11437-11444.

146. Kendall K. J Phys D: Appl Phys 1975;8:1449-1152.

147. Hui CY, Glassmaker NJ, Tang T, Jagota A. J Roy Soc Interface 2004;1-35-48.

148. Chan EP, Greiner C, Arzt E, Crosby AJ. MRS Bulletin 2007;32:497-503.

149. Gray GT. ASM Handbook 2000;8:462.

150. Asaro RJ. (unpublished data).

151. Ugural AC. *Stresses in Plates and Shells*. New York: McGraw-Hill, 1981, p 27.

152. Szilard R. *Theories and Applications of Plate Analysis*. New Jersey: John Wiley & Sons, 2004, p 57.

153. Bevelander G, Nakahara H. In: Omori M, Watabe N, editors. *The Mechanisms of Biomineralization in Animals and Plants*. Tokyo: Tokai University Press, 1980, pp 19-27.

154. Lapota D, Rosen G, Chock J, Liu CH. J Shellfish Res 2000;19:431.

155. Crisp DJ. In: Crick RE (ed.), *Origin, Evolution, and Modern Aspects of Biomineralization in Plants and Animals,* Plenum Press, New York, 1986, p. 103.

156. http://geology.uprm.edu/ Morelock/GEOLOCN_/rfbuild.htm

157. Thompson JB, Palczi CT, Kindt HK, Michenfelder M, Smith BL, Stucky G, Morse DE, Hansma PK. Bioophys J 2000;79:3307.

158. Donovan DA, Carefoot TH. J of Exp Bio 1997;200:1145-1153

159. Trueman ER, Hodgson AN. J Moll Stud 1990;56:221-228.

160. Johnson KL, Kendall K, Roberts AD. Proc Roy Soc London 1971;324:301-13.

161. Menig R, Meyers MH, Meyers MA, Vecchio KS. Mater Sci Eng A 2001;297:203-211.

162. Rosewater JR. Indo-pac. Mollusca 1965;1:347.

163. Moir BG. J Archaeol Sci 1990;17:329.

164. Kobayashim I. Am Zool 1969;9:633.

165. Lin AYM, Meyers MA, Vecchio KS. Materials Science and Engineering C 2006;16:1370-1389.

166. Tang Z, Kotov NA, Magonov S, Ozturk B. Nat Mater 2003;6:413-418.

167. Sellinger A, Weiss PM, Nguyen A, Lu Y, Assink RA. Nature 1998;394:256.

168. Bunker B. Science 1994;264:48-55.

169. Autumn K, Sitti M, Liang YA, Peattie AM, Hansen WR, Sponberg S, Kenny TW, Fearing R, Israelachvili JN, Full RJ. Proc Natl Acad Sci USA 2002;99:12252-12256.

170. Gao HJ, Wang X, Yao H, Gorb S, Arzt E. Mechanics of Mater 2005;37:275 -286.

171. Hanna G, Barnes WJP. J Exp Biol 1991:155;103-125.

172. Barnes WJP. MRS Bulletin 2007;32:479-485.

173. Scherge M, Gorb S, *Biological Micro- and Nanotribology*. Nanoscience and Technology Series, Springer, 2001.

174. Huber G, Mantz H, Spolenak R, Mecke K, Jacobs K, Gorb SN, Artz E. Proc Natl Acad Sci USA 2005;102(45):16293-16296.

175. Sitti M, Fearing RS. J Adhes Sci Tech 2003:17;1055-1077.

176. Waite JH, Tanzer ML. Science 1981:212;1038-1040.

177. Waite JH. Int J Adhesion and Adhesives 1987:7(1);9-14.

178. Santos R, Gorb S, Jamar V, Flammang P. Journal of Experimental Biology 2005:208;2555-2567.

179. Waite JH, Lichtenegger HC, Stucky GD, Hansma P. Biochemistry 2004:43;7653-7662.

180. Bell EYC, Gosline JM. J of Exp Bio. 1996:199;1005–1017.

181. Israelachvili JN. *Intermolecular and Surface Forces,* 2nd ed. Academic Press, San Diego, 1992.

182. Popov EP. *Engineering Mechanics of Solids*. Prentice Hall, NJ, 1999.

183. Pombal JP, Haddad CFB, Kasahara S. Journal of Herpetology 1995:29;1–6.

184. Ernst V. Tissue and Cell 1973a:5;83-96.

185. Welsch U, Storch V, Fuchs W. Cell Tiss Res 1974;148:407-416.

186. Green DM. Can. J Zool 1979;57:2033-2046.

187. Emerson SB, Diehl D. Biol J Linn Soc 1980;13:199-216.

188. McAllister W, Channing A. S Afr J Zool 1983;110-114.

189. Green DM, Simon MP. Aust J Zool 1986;34:135-145.

190. Hanna G, Barnes WJP. J Exp Biol 1991;155:103-125.

191. Ernst V. Tissue and Cell 1973b;5:97-104.

192. Noble GK, Jaeckle ME J. Morph 1928;45:259-292.

193. Peters JA. *Dictionary of Herpetology*. Hafner Publications, NY, 1964.

194. Nachtigall W. *Biological Mechanisms of Attachment*. Springer-Verlag, Germany, 1974.

195. Green DM. Copeia 1981; 790-796.

196. Meyers MA, Lin AYM, Lin YS, Olevsky EA, Georgalis S. JOM March 2008;21-26.

197. Oka K, Aoyagi S, Arai Y, Isono Y, Hashiguchi G, Fujita H. Sensors and Actuators A 2002;97:478–485.

198. Harach DJ and Vecchio KS. Metallurgical and Materials Transactions 2001;32A:1493-1505.

199. Forster-Miller, Inc., *Cost Effective Advanced Ceramic Armor*, Waltham, MA, 1995.

200. Mahdavi A, Ferreira L, Sundback C, Nichol JW, Chan EP, Carter DJD, Bettinger CJ, Patanavanich S, Chignozha L, Ben-Joseph E, Galakatos A, Pryor H, Pomerantseva I, Masiakos PT, Faquin W, Zumbuehl A, Hong S, Borenstein J, Vacanti J, Langer R, and Karp JM. PNAS 2008;105:2307-2312.

201. Darwin C. *The Origin of Species by Means of Natural Selection*. ed. John Murray, London, 1859.